Chemical Reactors

Chemical Reactors

H. Scott Fogler, EDITOR

The University of Michigan

Based on a symposium

sponsored by the Division of

Industrial and Engineering Chemistry

at the Second Chemical Congress

of the North American Continent

(180th ACS National Meeting),

Las Vegas, Nevada,

August 25–26, 1980.

ACS SYMPOSIUM SERIES **168**

ACS Symposium Series

M. Joan Comstock, *Series Editor*

FOREWORD

The ACS SYMPOSIUM SERIES was founded in 1974 to provide
a medium for publishing symposia quickly in book form. The
format of the Series parallels that of the continuing ADVANCES
IN CHEMISTRY SERIES except that in order to save time the
papers are not typeset but are reproduced as they are sub-
mitted by the authors in camera-ready form. Papers are re-
viewed under the supervision of the Editors with the assistance
of the Series Advisory Board and are selected to maintain the
integrity of the symposia; however, verbatim reproductions of
previously published papers are not accepted. Both reviews
and reports of research are acceptable since symposia may
embrace both types of presentation.

PREFACE

The symposium upon which this volume is based focused on three areas in reaction engineering: fluidized bed reactors, bubble column reactors, and packed bed reactors. Each area comprises a section of this book. Professor J. R. Grace chaired and coordinated the fluidized bed sessions; Professors Y. T. Shah and A. Bishop, the bubble column reactor session; and Professor A. Varma, the packed bed reactor session. Each section in this book opens with a brief review chapter by the session chairman that includes an overview of the chapters in each session.

Fluidized bed reactors have received increased interest in recent years owing to their application in coal gasification. The section on fluidized beds discusses critical areas in fluid bed reactor modeling. Computer simulation of both solid-catalyzed gas phase reactions as well as gas–solid reactions are included.

In the section on bubble column reactors, the hydrodynamic parameters needed for scale-up are presented along with models for reaction and heat transfer. The mixing characteristics of columns are described as are the directions for future research work on bubble column reactors.

The packed bed reactors section of this volume presents topics of catalyst deactivation and radial flow reactors, along with numerical techniques for solving the differential mass and energy balances in packed bed reactors. The advantages and limitations of various models (e.g., pseudo-homogeneous vs. heterogeneous) used to describe packed bed reactors are also presented in this section.

H. SCOTT FOGLER

The University of Michigan

Ann Arbor, MI 48109

June 1, 1981

Fluidized Bed Reactor Modeling

An Overview

J. R. GRACE

Department of Chemical Engineering, University of British Columbia,
Vancouver, Canada V6T 1W5

Critical areas in fluid bed reactor modeling are dis-
cussed in the light of papers in this symposium.
There continues to be a wide diversity of assumptions
underlying models. However, it is now clear that pre-
dictions are generally much more sensitive to some
assumptions than to others. For example, proper mod-
eling of interphase exchange is generally more criti-
cal than the assumptions adopted to describe axial
gas dispersion in the dense or emulsion phase. For
the 1980's advances are looked for in a number of
areas, especially in more sophisticated computer mod-
els, unsteady state representations suitable for con-
trol purposes, models which describe high velocity
regimes of fluidization, inclusion of grid and free-
board effects, and study of radial gradients.

This volume brings together a number of papers under the
theme of fluidized bed reactor modeling. This field is of rela-
tively recent origin. Table I gives the emphasis in research in
successive decades beginning with the 1940's. It is seen that
early research was devoted primarily to practical problems associ-
ated with the operation of fluidized bed reactors and to very
simple models. With the passage of time models have been devised
which are increasingly sophisticated. Reviews of the commercial
development of fluidized beds as reactors have been prepared by
Geldart (1,2). In the 1970's there were a number of reviews (3-7)
which considered fluidized bed reactor modeling.

In order to be able to represent the behaviour of fluidized
bed reactors with confidence, one must have a thorough understand-
ing of the bed hydrodynamics and of the reaction kinetics. Almost
all of the reactions carried out in fluidized beds are either
solid-catalysed gas phase reactions or gas-solid reactions. (We
will not consider here homogeneous gas phase reactions, reactions
in liquid fluidized beds or reactions in three phase fluidized
beds.) While the chemical kinetics can often be highly complex,

for example in the gasification or combustion of coal, the hydro-
dynamic aspects have given the greatest difficulty and have been
subject to the greatest debate. While considerable progress has
been made in achieving an understanding of many aspects of bed
behaviour, there are many features which remain poorly under-
stood. Some of these (e.g. regimes of bed behaviour, gas mixing
patterns, and exchange of gas between phases) can affect pro-
foundly the nature of the model adopted.

Table I: Focus of Research on Fluidized Bed Reactors

Decade	Emphasis
1940's	Practical design and operation problems. Single phase models only.
1950's	Simple two-phase models for gas-phase solid-catalysed reactions.
1960's	Incorporation of properties of single bubbles. Early models for gas-solid reactions.
1970's	Addition of end (grid and freeboard) effects. More sophisticated models for specific gas-solid reactions including energy balances. Consideration of complex kinetics.
1980's	? Probable emphasis on non-bubbling (turbulent and fast fluidization) regimes. Probable consideration of effects of aids to fluidization (e.g. centrifugal, magnetic and electrical fields, baffles). Increasing emphasis on more complex hydrodynamics and kinetics, with models requiring computers for solution.

The papers presented at the Las Vegas symposium, most of
which are reproduced in this volume, both illustrate the diver-
sity of modeling approach and show some new directions for reactor
modeling in the 1980's. Before turning to these matters in de-
tail, it is necessary to discuss briefly three of the papers
which are fundamentally different in focus from the other eight.
The paper by Ramírez et al (8) considers the important ques-
tion of particle-to-gas heat transfer in fluidized beds. In ad-
dition to the importance of this question in its own right, par-
ticle-to-gas heat transfer can be important for fluid bed reac-
tors, for example in determining thermal gradients in the entry
(grid) region, in establishing the surface temperature of parti-
cles undergoing reactions, and via the analogous case of gas-to-
particle mass transfer. There has been considerable controversy
over the fact that Nusselt and Sherwood numbers have been found
to fall well below 2, the lower limit for a single sphere in a
stagnant medium. Ramírez et al produce further evidence of Sh
<< 2 and Nu << 2 and consider these results in the light of
transfer models in the literature.
The paper by Blake and Chen (9) represents an extension of

the novel approach adopted by the Systems, Science and Software group. In what must be the most ambitious and comprehensive fluidization modeling effort to date, this group has used modern computational techniques to solve a set of equations representing the physics and chemistry of fluidized bed coal gasifiers. Hydrodynamic fixtures are represented by a set of continuum equations and constitutive relationships, while chemical kinetics equations are written for key heterogeneous and homogeneous reactions based on studies reported in the literature. In previous papers, the authors have shown that the model gives a realistic simulation of a jet of gas issuing into a bed of solids. In the present paper they seek to duplicate results obtained in the IGT and Westinghouse pilot scale reactors. The results are of considerable interest, giving a good match with most of the experimental results.

A further paper by Gibbs (10) deals with design and modeling of centrifugal fluidized beds. In this case gas is fed radially inwards into a spinning bed. On account of the greatly augmented effective gravity force, greater through-puts of gas can be accommodated and entrainment is greatly lowered. This new technique has received attention in the late 1970's especially in connection with coal combustion. Some unique problems are encountered, e.g. the minimum fluidization velocity becomes a function of bed depth, while particles ejected into the "freeboard" by bubbles bursting at the bed surface travel initially nearly at right angles to the gas exit direction. This paper gives a preliminary scheme for dealing with some of these problems.

Classification of Reactor Models

There are many choices to be made in fluid bed reactor modeling and little unanimity among those who devise such models on the best choices. Table II lists some of the principal areas for decision and the corresponding choices of the other eight papers at this symposium (11-18).

Phases. Both two-phase and three-phase representations are widely used as shown schematically in Figure 1. In two-phase representations the dilute phase may represent bubbles alone, jets (in the grid region), or bubbles plus clouds. Three-phase representations generally use the scheme followed by Kunii and Levenspiel (19) whereby bubbles, clouds, and "emulsion" (i.e. that part of the non-bubble bed not included in the clouds) are each treated as separate regions. As shown in Table II, all of these possibilities are represented in the models adopted by the authors in this symposium. There appears, however, to be an increasing tendency to adopt three phase models, probably as a result of experimental results (20) which showed that the Kunii and Levenspiel model gave a better representation of measured concen-
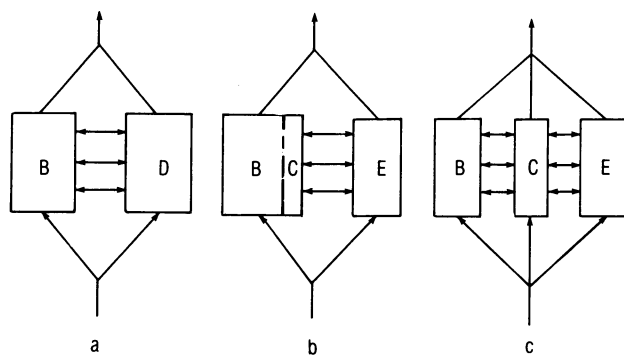
Figure 1.   Schematic of two-phase and three-phase representations for fluidized beds operating in the bubble regime: B, bubble phase; C, cloud phase; D, dense phase; E, emulsion phase: Two-phase models, a and b; three-phase models, c

tration profiles for a particular particle size than other models
tested. The bubbles themselves are usually treated as being com-
pletely devoid of particles, but it is important (21) that solids
dispersed in the bubbles be included with the bubble phase for
fast reactions, even though their concentration is small (typi-
cally < 1% by volume).

Gas Mixing in the Dense or Emulsion Phase. No other feature
of fluidized bed reactor modeling has been subjected to so many
alternative assumptions as axial mixing in the dense phase. At
least eight possibilities have been tried as shown in Figure 2.
These range from upward plug flow, through perfect mixing and
stagnant gas, to downflow. Intermediate degrees of mixing have
been represented by axial dispersion models and well-mixed
stages in series. As shown in Tabe II many of these possibili-
ties have been covered in the present symposium.

In view of the large number of disparate representations of
dense phase axial mixing, one might easily conclude that this is
one of the more important modeling features. In practice this is
not the case, unless high conversions (e.g. 90% or greater in a
single stage) are sought. For lower conversions, overall reactor
performance tends to be insensitive to the pattern of axial mix-
ing adopted (21). There are several illustrations of this point
in this symposium. In the paper by Jayaraman _et al_ (16), re-
placement of the downflow condition adopted by Fryer and Potter
(22) by perfect mixing in the emulsion led to conversions which
were barely distinguishable from those given by the earlier mod-
el. (At the same time solution became much simpler.) Jaffres _et
al_ (15) show that the two extreme cases of perfect mixing and
plug flow in the Orcutt models (23) lead to similar results. (In
their case, however, bubble properties were varied together with
kinetic constants in their optimization so it is harder to dis-
tinguish the influence of the mixing assumptions alone.) Elna-
shaie and Elshishini (12) further show that the effect of axial
dispersion is not only relatively slight in terms of overall con-
version, but that dense phase mixing also plays a relatively
minor role in determining selectivity for consecutive reactions
and multiplicity of steady states.

In almost all previous modeling work, one-dimensional flow
has been assumed in each phase, radial gradients being taken as
negligible. There is some experimental evidence (24) that sub-
stantial radial gradients may exist, however. Radial gradients
are especially important for fluid bed combustors with in-bed
feeding of fresh coal via a series of nozzles. In this case the
rapid devolatilization reactions will occur close to the distri-
buted feed points, and radial dispersion of volatiles away from
these points and oxygen towards them will be extremely important
if the volatiles are to burn out within the bed. Fan and Chang
(13) have considered this problem, coupling an assumption of per-
fect axial mixing with a diffusion-type mixing model in the ra-

Table II: Key features of models used in this symposium

	de Lasa et al (11)	Elnashaie & Elshishini (12)	Fan & Chang (13)	Fogler & Brown (14)
Phases	2: Bubble (or jet) & dense or 1: (CSTR)	2: Bub/Cloud & emulsion or 3: Bubble, cloud & emulsion	2: Bubble & dense	3: Bubble, cloud and emulsion
Gas mixing in dense or emulsion phase	perfect mixing	perfect mixing or plug flow upward	perfect axial mixing + radial dispersion	stagnant
Interphase transfer	jet/dense: Behie (43) bub/dense: (27) or (19)	(37) or (19)	K-L (19)	K-L (19)
Distribution of flow between phases	Two phase theory	2-ϕ theory + cloud or U_{mf} A through emulsion	Two phase theory	Two phase theory
Bubble size	Basov equation (constant)	Kept as parameter (constant)	Kept as parameter (constant)	Mori & Wen (varies)
Heat balance?	Yes	Yes	Yes	No
Time variation	steady	steady	unsteady	steady
Reaction	gas-solid	catalytic	gas-solid	catalytic
Application	Catalyst regenerator	consecutive reactions	Coal combustion	general
Experimental data	large unit	none	none	none

Table II: Key features of models used in this symposium (Continued)

	Jaffres et al (15)	Jayaraman et al (16)	Peters et al (17)	Rehmat et al (18)
Phases	2: Bubble & dense	3: Bubble, cloud & emulsion	3: Bubble, cloud & emulsion	3: Gas, char & limestone
Gas mixing in dense or emulsion phase	plug flow or perfect mixing	perfect mixing	compartments in series	all gas in plug flow upward
Interphase transfer	D-H (27)	K-L (19)	K-L (19)	N.A.
Distribution of flow between phases	Two phase theory	as Fryer and Potter	New approach	N.A.
Bubble size	Mori & Wen & fitted values (constant)	specified value (constant)	Mori & Wen (varies)	N.A.
Heat balance?	Yes	No	No	Yes
Time variation	unsteady	steady	steady	steady
Reaction	catalytic	catalytic	pseudo-catalytic	gas-solid
Application	Maleic anhydride	general	Aerosol filtration	Coal combustion
Experimental data	cf. earlier data	none	cf. earlier data	none
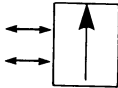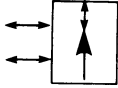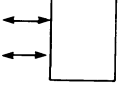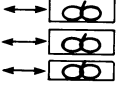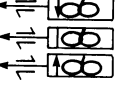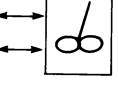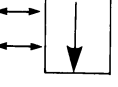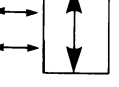
ASSUMPTION	SCHEMATIC	EXAMPLES
Plug flow		Orcutt et al (23) Partridge and Rowe (37)
Dispersed plug flow		May (45)
Stagnant		Kunii and Levenspiel (19)
Well-mixed tanks in series		Kato and Wen (46)
Tanks in series with net outflow and flow reversal		Peters et al (40)
Perfect mixing		Orcutt et al (23) Avedesian and Davidson (49)
Downflow		Fryer and Potter (21)
Bubble-induced turbulent fluctuations		Bywater (47)

Figure 2.   Alternative schemes used in reactor models to represent axial dispersion of gas in the dense or emulsion phase

dial direction. Although the underlying assumptions of diffusion-
type models often seem inappropriate to axial mixing in fluidized
beds (25), there is some evidence (e.g. 26) that lateral mixing
can be described in this manner. Hence the paper of Fan and
Chang (13) may represent a useful approach to the description of
an important problem.

   Interphase Gas Transfer. From the heavy reliance in this
symposium (see Table II) on the mass transfer equations proposed
by Davidson and Harrison (27) and by Kunii and Levenspiel (19),
one might reasonably conclude that these approaches have been sup-
ported by at least the majority of experimental evidence. Nothing
could be further from the truth.
   The Davidson and Harrison approach concentrates solely on the
resistance at the bubble/cloud boundary (or bubble/dense phase
boundary for $\alpha < 1$). The transfer coefficient, referred to bubble
surface area, is

$$k_{bc} = 0.75\ U_{mf} + 0.975[g\mathcal{D}^2/d_b]^{\frac{1}{4}} \qquad (1)$$

Alternatively, on a bubble volume basis, this becomes

$$k_{bc}' = 4.5\ U_{mf}/d_b + 5.85\ [g\mathcal{D}^2/d_b^5]^{\frac{1}{4}} \qquad (2)$$

The first term in each case arises from bulk flow of gas into the
floor of an isolated bubble and out the roof, as required by the
hydrodynamic model of Davidson and Harrison (27). The weight of
experimental evidence, from studies of cloud size (28,29), from
chemical reaction studies (e.g. 30), and from interphase transfer
studies (e.g. 31,32), is that this term is better described by the
theory proposed by Murray (33). The latter leads to a reduction
in the first term by a factor of 3. Some enhancement of the bulk
flow component occurs for interacting bubbles (34,35), but this
enhancement for a freely bubbling bed is only of the order of 20-
30% (35), not the 300% that would be required for the bulk flow
term Equations (1) and (2) to be valid.
   The second term in Equations (1) and (2) accounts for diffu-
sional transfer across the bubble boundary. (A factor $\epsilon_{mf}/(1+\epsilon_{mf})$
is sometimes (e.g. 49) included in the bracket of Eq. 2 to account
for the dense phase diffusional resistance.) There is some ques-
tion (30) of the extent to which there is interference between
the bulk flow and diffusion terms. Nevertheless, most experiment-
al evidence suggests that the two terms are additive and that the
diffusional term is described by the penetration theory. With
these changes, and including a small enhancement factor for bubble
interaction, Sit and Grace (35) have recommended the following
equations as being in best accord with existing experimental data:

$$k_{bc} = U_{mf}/3 + [4\mathcal{D}\epsilon_{mf}\bar{u}_b/\pi\bar{d}_b]^{\frac{1}{2}} \qquad (3)$$

or $\qquad k_{bc}' = 2U_{mf}/\bar{d}_b + 12 \; [\mathcal{D}\epsilon_{mf}\bar{u}_b/\pi\bar{d}_b^{\;3}]^{\frac{1}{2}}$ $\qquad\qquad$ (4)

Kunii and Levelspiel ($\underline{19}$) again use Equation (2) to describe bubble/cloud transfer. Based on the penetration theory, they propose the following expression for cloud/emulsion transfer:

$$k_{ce}' = 6.78 \; [\mathcal{D}\epsilon_{mf}u_b/d_b^{\;3}]^{\frac{1}{2}} \qquad\qquad (5)$$

Equation (5) considers gas diffusion to be the only mechanism of transfer across the outer cloud boundary. In practice there are at least three other important mechanisms not accounted for: (a) The cloud boundary is a streamline for gas elements but not for solid particles. Particles entering and leaving the cloud boundary will carry adsorbed species with them. (b) There is strong evidence of shedding of elements from the wakes. Photographs ($\underline{28}$) indicate that these shed elements results in transfer of cloud gas to the emulsion. (c) The concept of the cloud is based on steady state analyses ($\underline{27},\underline{33}$). While a mantel of gas appears to remain associated with bubbles as they coalesce, these "clouds", like the bubbles themselves, distort and undergo volume changes during bubble interaction and coalescence ($\underline{28},\underline{36}$). This no doubt further enhances cloud/emulsion transfer.

For most practical conditions, a comparison of k_{bc}' and k_{ce}' from Equations (4) and (5) would suggest that the principal resistance to transfer resides at the outer cloud boundary. However, when (a), (b) and (c) are taken into account, this is no longer the case. In fact, experimental evidence (e.g. $\underline{30},\underline{31},\underline{32}$) indicates strongly that the principal resistance is at the bubble/cloud interface. With this in mind, it is probably more sensible to include the cloud with the dense phase (as in the Orcutt ($\underline{23}$, $\underline{27}$) models) rather than with the bubbles (as in the Partridge and Rowe ($\underline{37}$) model) if a two-phase representation is to be adopted (see Figure 1). If three-phase models are used, then Equations (2) and (5) appear to be a poor basis for prediction. Fortunately the errors go in opposite directions, Equation (2) overpredicting the bubble/cloud transfer coefficient, while Equation (5) underestimates the cloud/emulsion transfer coefficient. This probably accounts for the fact that the Kunii and Levenspiel model ($\underline{19}$) can give reasonable predictions in specific instances (e.g.20).

Flow Distribution between Phases. One of the principal assumptions underlying many of the models of fluidized bed reactors is the "two-phase theory of fluidization". This theory, really no more than a postulate, holds that the flow beyond that required for minimum fluidization passes through the bed as translating void units. Although not included in what the originators of this postulate ($\underline{38}$) appeared to have in mind, the two phase theory is often held to imply, in addition, that the dense phase voidage remains constant and equal to ϵ_{mf} for all $U > U_{mf}$. Much has been written and said about the two phase theory

(e.g. see 39). For our purposes here it suffices to note that
there is very little evidence indeed that the flow distribution
really follows the theory. In fact, the weight of evidence (see
39) suggests that the theory seriously overestimates the flow ac-
counted for by translation of bubbles, except in the limit as slug
flow conditions are approached. Yet, despite all this evidence,
the two phase theory continues as an underpinning for much of the
serious modeling work, as is again evident from Table II. There
are several probable reasons for the continuing popularity of the
two phase theory in the face of contradicting evidence:

    (i)   There is a lack of alternative approaches.

    (ii)   There is confusion between "visible" and "invisible"
(i.e. bulk flow or "throughflow") terms. Toomey and Johnstone
(38) appeared to have in mind only the "visible" (i.e. flow due to
void unit translation) term. As noted above, the theory then
overestimates the bubble flow. However, if the bubble flow is
taken to include the invisible throughflow, the theory may do
better and may even underestimate the bubble flow. Many workers
fail to distinguish clearly whether they are talking of visible or
total bubble flow.

    The paper by Peters et al (17) is welcome in that it attempts
a new approach to the two phase flow distribution problem. Fur-
ther details are given in another paper by the same authors (40).
However, the authors fail to distinguish clearly between "visible"
and invisible flow components in the bubble and cloud phases. At
this time their approach must be regarded as a purely empirical
method which appears to give a reasonable match with selected ex-
perimental data.

    Bubble Size. A number of empirical and semi-empirical ap-
proaches are available for predicting mean bubble size as a func-
tion of height and other conditions in gas fluidized beds. Judg-
ing from Tabe II, the approach followed by Mori and Wen (41) ap-
pears to have become the favored method of predicting d_b. This
equation is semi-empirical; predictions are bounded between an
initial size produced at a distributor and a maximum size achiev-
ed only under slug flow conditions. Another recent mechanisti-
cally based equation due to Darton et al (42) is also receiving
considerable attention, but has not been tested by any of the au-
thors in this symposium. Both approaches seem to represent marked
improvements over previous equations of a solely empirical nature
in the literature. A method is still required for predicting
bubble sizes in beds containing tubes as in the Type B combustor
considered by Fan and Chang (13).

    Five of the papers surveyed in Tabe II treat the bubble size
as if it were independent of height. In two cases (14, 17) d_b is
allowed to vary with height. While the latter assumption is cer-
tainly more realistic, assumption of a constant bubble size is de-
fensible on the grounds of simplicity and limited sensitivity rel-
ative to some of the other assumptions discussed in this paper.

    Heat Balance. For many years it has been customary to treat

fluid bed reactors as isothermal and to ignore energy balances in
the modeling process. Recent emphasis on coal combustion and
other gas-solid reactions with high heats of reaction has led to
the inclusion of heat balances with more and more models. Heat
balances are ignored in only three of the eight papers surveyed
in Table II confirming this trend.

Steady versus Unsteady State Models. Until very recently,
fluidized bed reactor models have dealt almost exclusively with
steady state conditions. Steady state models are unsuitable for
control purposes, for load following in fluid bed combustors, and
for start-up and shutdown purposes. It is a welcome sign that
two of the papers in this symposium (13,15) derive models which
are potentially suitable for these purposes.

Type of Reaction and Application. An increased emphasis on
gas-solid reactions has been evident for about a decade. Three
of the papers in this symposium treat gas-solid reactions, two
(13,18) dealing with coal combustion and the other (11) with cat-
alyst regeneration. Of the four papers which consider solid-cat-
alysed gas-phase reactions, one (15) deals with a specific appli-
cation (production of maleic anhydride), and one (12) treats an
unspecified consecutive reaction of the type A → B → C; the other
two (14,16) are concerned with unspecified first order irreversi-
ble reactions. The final paper (17) considers a relatively re-
cent application, fluidized bed aerosol filtration. Principles
of fluid bed reactor modeling are directly applicable to such a
case: Aerosol particles disappear by adsorption on the collector
(fluidized) particles much as a gaseous component disappears by
reaction in the case of a solid-catalysed reaction.

Experimental Data. While the emphasis in this session was
on reactor modeling, models can only ultimately prove successful
if they are compared to experimental data. This point may seem
obvious, but it is worth making since modeling efforts too often
seem to be intellectual exercises rather than efforts to represent
reality. While there is a need to verify some of the models pre-
sented at this symposium, it is gratifying that three of the pa-
pers (11,15,17) have already been exposed to the test of experi-
mental data.

Other Model Features

Some of the principal features common to the different models
are discussed above. In this section some further features of re-
actor models are considered briefly with reference to individual
papers in this symposium.

Only the paper by de Lasa et al (11) explicitly treats the
entry or grid region as a non-bubbling region. This region is
modeled in terms of discrete gas jets, an idea originated by Be-
hie and Kehoe (43), but contested actively by Rowe et al (44). As
indicated in the papers by Jaffres et al (15) and Rehmat et al
(18), the grid region is clearly a zone of effective gas-solid

contacting, but considerable work is required to achieve an understanding of the hydrodynamics and gas exchange processes therein.

None of the papers in this session explicitly considers the freeboard region although both de Lasa et al (11) and Jaffres et al (15) refer to previous work which has shown that the freeboard can play an important role in determining the overall reactor performance. None of the papers treats directly flow regimes other than the bubbling regime, although Rehmat et al (18) mention the turbulent flow regime (together with rapid interphase exchange in the grid region) as justification for using a model which treats the gas as a single phase in plug flow. As already suggested in Table I, efforts to model turbulent and fast fluidized beds are likely to be important features of the 1980's.

In modeling gas-solid reactions in fluid beds, provision must be made for dealing with particle size distributions and with solids mixing. Solids mixing is usually adequately described in terms of perfect mixing. To account for size distribution effects, population balances are generally required. These must take into account the size distribution of the feed, elutriation and losses of fines, attrition (if appreciable), and any changes in particle size due to chemical reaction. The paper by Rehmat et al (18) illustrates how these factors can be taken into account. Overall solid reaction rates must be determined by summing over all particle sizes, and conversion must be related to gas conversion via the stoichiometry of the reactions.

Concluding Remarks

It is clear that there are many unresolved questions in the field of fluidized bed reactor modeling. Only the bubble and slug flow regimes have received significant attention. While end effects (grid zone and freeboard region effects) are beginning to be treated, almost no efforts have been made to model high velocity fluidized beds operating in the turbulent and fast fluidization regimes. These regimes are of great importance industrially and for future applications. Even in the bubble flow regime, where there is a wealth of hydrodynamic and other data, some of the key aspects of behavior remain poorly understood.

It is clear from previous work and from the papers in this symposium that models are much more sensitive to assumptions in some areas than in others. For very slow reactions, rates become controlled by chemical kinetics and insensitive to whatever hydrodynamic assumptions are adopted (14,48). For intermediate reactions, interphase transfer generally becomes the key factor controlling the reactor performance, with the distribution of gas between phases also playing a significant role. As outlined above, advances have been made in understanding both areas, but models have generally been slow to adopt changes in the basic assumptions used in early bubble models. For fast reactions, the

extent of axial mixing of gas in the dense or emulsion phase and
the fraction of solids assigned to the dilute phase also become
important. However, axial gas mixing is less important in gener-
al than might be indicated by the degree of attention devoted to
this feature. On the other hand, radial mixing has received too
little attention.

The papers presented in this symposium point to a number of
advances that will be important in the 1980's. These include:
(a) fundamentally new types of models using the power of modern
computers to solve comprehensive governing equations (9);
(b) continuing strong attention on gas-solid reactions as well as
gas-phase solid-catalysed reactions; (c) unsteady state models
suitable for control purposes (13,15); (d) attention to rate-
limiting steps and to sensitivity analyses; (e) inclusion of grid
and freeboard effects; (f) inclusion of energy balances; and
(g) study of radial gradients and radial dispersion (13). Multi-
phase reactor models have chiefly been useful in the past as an
educational tool in aiding understanding of fluid bed processes
and, to a limited extent, for simulation of existing reactors and
chemical processes. If these models are to become useful also for
design, scale-up and control of new equipment and processes, ad-
vances in all of these areas may be very helpful.

Legend of Symbols

$\mathcal{D}$	molecular diffusivity
d_b	bubble diameter
$\bar{d}_b$	mean bubble diameter
g	acceleration of gravity
k_{bc}	bubble/cloud mass transfer coefficient based on bubble surface area
k_{bc}'	bubble/cloud mass transfer coefficient based on bubble volume
k_{ce}'	cloud/emulsion mass transfer coefficient based on bubble volume
Nu	Nusselt number
Sh	Sherwood number
U	superficial gas velocity
U_{mf}	superficial gas velocity at minimum fluidization
u_b	bubble rise velocity
$\bar{u}_b$	bubble rise velocity corresponding to $\bar{d}_b$
α	ratio of bubble velocity to remote interstitial velocity,$= u_b \varepsilon_{mf}/U_{mf}$
ε_{mf}	bed void fraction at minimum fluidization

Acknowledgement

Literature Cited

1. Geldart, D. Chem. and Ind. 1967, 1474-1481.
2. Geldart, D. Chem. and Ind. 1968, 41-47.
3. Grace, J.R. AIChE Symp. Ser. 1971, 67, No. 116, 159.
4. Pyle, D.L. Adv. Chem. Ser. 1972, 109, 106.
5. Rowe, P.N. "Proc. 5th Europ./2nd Intern. Symp. on Chem. Reaction Engng.", Elsevier, Amsterdam, 1972, p.A9.
6. Yates, J.G. Chemical Engineer (London) Nov. 1975, 671.
7. Bukur, D.; Caram, H.S.; Amundson N.R. "Chemical Reactor Theory: a Review", ed. L. Lapidus and N.R. Amundson, Prentice-Hall, Englewood Cliffs, N.J., 1977, p.686.
8. Ramírez, J.; Ayora, M.; Vizcarra, M. This symposium volume.
9. Blake, T.R.; Chen, P.J. This symposium volume.
10. Gibbs, B.M. Paper presented at A.C.S. symposium, Las Vegas, 1980.
11. de Lasa, H.I.; Errazu, A.; Barreiro, E.; Solioz, S. Paper given at A.C.S. symposium, Las Vegas, 1980, and to be published in Can. J. Chem. Eng.
12. Elnashaie, S.S.E.H.; Elshishini, S.S. Paper presented at A.C.S. symposium, Las Vegas, 1980.
13. Fan, L.T.; Chang C.C. This symposium volume.
14. Fogler, H.S.; Brown, L.F. This symposium volume.
15. Jaffres, J.L.; Chavarie, C.; Patterson, W.I.; Laguerie, C. This symposium volume.
16. Jayaraman, V.K.; Kulkarni, B.D.; Doraiswamy, L.K. This symposium volume.
17. Peters, M.H.; Fan, L-S.; Sweeney, T.L. This symposium volume.
18. Rehmat, A.; Saxena, S.C.; Land, R. This symposium volume.
19. Kunii, D.; Levenspiel, O. "Fluidization Engineering", Wiley, New York, 1969.
20. Chavarie, C.; Grace, J.R. Ind. Eng. Chem. Fund. 1975, 14, 79.
21. Grace, J.R. Chapter 11 in "Gas Fluidization", ed. D. Geldart, Wiley, New York, 1982.
22. Fryer, C.; Potter, O.E. Ind. Engng. Chem. Fund., 1972, 11, 338.
23. Orcutt, J.C.; Davidson, J.F.; Pigford, R.L. Chem. Engng. Progr. Symp. Series 1962, 58, No. 38, 1.
24. Chavarie, C. Ph.D. thesis, McGill University, 1973.
25. Mireur, J.P.; Bischoff, K.B. A.I.Ch.E. Journal 1967, 13, 839.
26. Reay, D. "Proc. 1st International Symp. on Drying", ed. A.S. Mujumdar, Science Press, Princeton, 1978, p. 136.
27. Davidson, J.F.; Harrison, D. "Fluidized Particles", Cambridge University Press, Cambridge, England, 1963.
28. Rowe, P.N.; Partridge, B.A.; Lyall, E. Chem. Eng. Sci. 1964, 19, 973.

29. Anwer, J.; Pyle, D.L. "La Fluidisation et ses Applications",
     Soc. Chim. Ind., Paris, 1974, p.240.
30. Walker, B.V. Trans. Instn. Chem. Engrs., 1975, 53, 255.
31. Chavarie, C.; Grace, J.R. Chem. Eng. Sci. 1976, 31, 741.
32. Sit, S.P.; Grace, J.R. Chem. Eng. Sci. 1978, 33, 1115.
33. Murray, J.D. J. Fluid. Mech. 1965, 21, 465 & 22, 57.
34. Pereira, J.A.F. Ph.D. dissertation, University of Edinburgh,
     1977.
35. Sit, S.P.; Grace, J.R. Effect of bubble interaction on inter-
     phase mass transfer in gas fluidized beds, Chem. Eng. Sci.
     1981, 36, 327.
36. Clift, R.; Grace, J.R.; Cheung, L.; Do, T.H. J. Fluid Mech.
     1972, 51, 197.
37. Partridge, B.A.; Rowe, P.N. Trans. Instn. Chem. Engrs. 1966,
     44, 335.
38. Toomey, R.D.; Johnstone, H.P. Chem. Eng. Progr. 1952, 48,220.
39. Grace, J.R.; Clift, R. Chem. Eng. Sci. 1974, 29, 327.
40. Peters, M.H.; Fan, L-S.; Sweeney, T.L. A.I.Ch.E. National
     Meeting, Chicago, November, 1980.
41. Mori, S.; Wen, C.Y. A.I.Ch.E. Journal 1975, 21, 109.
42. Darton, R.C.; Lanauze, R.D.; Davidson, J.F.; Harrison, D.
     Trans. Instn. Chem. Engrs., 1977, 55, 274.
43. Behie, L.A.; Kehoe, P. A.I.Ch.E. Journal 1973, 19, 1070.
44. Rowe, P.N.; MacGillivray, H.J.; Cheesman, D.J. Trans Instn.
     Chem. Engrs. 1979, 57, 194.
45. May, W.G. Chem. Engng. Progr. 1959, 55, No. 12, 49.
46. Kato, K.; Wen, C.Y. Chem. Eng. Sci. 1969, 24, 1351.
47. Bywater, R.J. A.I.Ch.E. Symposium Series 1978, 74, No. 176,
     126.
48. Grace, J.R. AIChE Symp. Series 1974, 70, No. 141, 21.
49. Avedesian, M.M.; Davidson, J.R. Trans. Instn. Chem. Engrs.
     1973, 51, 121.

An Initial Value Approach to the Counter-Current Backmixing Model of the Fluid Bed

V. K. JAYARAMAN, B. D. KULKARNI, and L. K. DORAISWAMY

National Chemical Laboratory, Poona 411 008 India

The counter-current backmixing model of Fryer and Potter has been modified by assuming mixed flow in the emulsion phase. The terminal conversions obtained with the present model are compared with those of the original model and found to agree well except at very low values of bubble diameter. The assumption of complete mixing in the emulsion phase converts the original two-point boundary value problem into a simpler initial value problem, thereby considerably reducing the mathematical complexity.

The intensive gas mixing that occurs in a fluid bed due to the presence of bubbles and the associated circulatory movement of solids has been recognized for quite some time ($\underline{1}$, $\underline{2}$). The rising bubbles carry wakes of solids along with them and release them subsequently on bursting at the surface ($\underline{3}$, $\underline{4}$, $\underline{5}$). The released solids then move downwards for reasons of continuity and a simple circulatory pattern of movement of solids is set up. The studies on particle movement in deep fluidized beds ($\underline{6}$) have indicated that solids move upwards in the center region of the bed and downwards at the periphery. The intensity of circulation of solids increases with increase in the fluidizing gas velocity, and at a critical velocity U_{cr} the velocity of down flowing solids exceeds the interstitial gas velocity, so that the interstitial gas is carried downwards as described by ($\underline{7}$-$\underline{10}$). A simple mechanism for gas mixing therefore seemed possible and several models - the so-called counter-current backmixing models that take into account this flow reversal - have been proposed ($\underline{8}$, $\underline{11}$, $\underline{12}$).

It should, however, be noted that the solids movement pattern as mentioned above has been observed in beds with sufficiently large values of length to diameter ratio ($L_f/d_t \gg 1$). Industrial fluid beds normally operate with L_f/d_t values less than or close to unity and the solids flow pattern could be entirely different. More recent experimental studies such as

those of Okhi and Shirai (13) in shallow beds indicate a
different flow pattern. Their experimental measurements have
confirmed the fact that solids move downward in the central
region of the bed. Earlier, Whitehead et al (14) had also made
measurements of solids movement and demonstrated in some cases a
strong down flow of solids in a small area at the center of the
bed. Such solids circulatory pattern has also been reported by
Werther (15) and Schmalfeld (16). Nguyen and Potter (9, 10)
experimenting with a 30 cm diameter column have also observed
that gas mixing is at its maximum in the center. Bubbles move
in the area between the center and the wall, forcing the solids
and the backmixed gas to move downwards in the central and near-
to-wall region. The more recent experiments of Nguyen et al (17)
in a large scale fluidized bed confirm this fact; however at very
high velocities the stream becomes more unstable and flow is
difficult to define.

It is clear from the foregoing discussion that a consider-
able extent of gas backmixing results due to the presence of
bubble tracks and the associated solids movement. Besides this,
the industrial   units are normally operated with baffles and
internals to remove the heat of reaction. The hinderances from
these would lead to further enhancement of gas mixing in the
emulsion phase. The common assumption of plug flow in the
emulsion phase therefore seems incompatible with the situation
prevailing in industrial reactors, and in the present work the
original Fryer-Potter model (12) has been modified to take this
reality into account. This has the additional advantage of
converting the boundary value nature of the Fryer-Potter
representation into an initial value problem, thus considerably
simplifying the mathematical treatment.

Theoretical Development

Let us consider a simple reaction A ⟶ R and make the
following assumptions: the bubbles are uniform in size and free
of particles. The emulsion phase voidage is constant, with the
voidage of the bubbling bed equal to that at incipient
fluidization. The voidage in the cloud is the same as in the
emulsion. Plug flow prevails in the bubble and cloud phases, with
the emulsion phase completely mixed. With these assumptions the
material balance equations may be written as follows:

$$- U_{Gb} \frac{dC_b}{dz} + \epsilon_b K_{bc} (C_c - C_b) = 0 \qquad (1)$$

$$-U_{Gc} \frac{dC_e}{dz} + \epsilon_b K_{bc} (C_b - C_c) + \epsilon_b K_{ce} (C_e - C_c)$$
$$- kf_w \epsilon_b C_c = 0 \qquad (2)$$

$$-U_{Ge} (C_c(1) - C_e) + K_{ce}\epsilon_b \int_0^{L_f} (C_c - C_e) \, dz$$

$$-k (1-\epsilon_b(1+f_w)) L_f C_e = 0 \qquad (3)$$

The appropriate initial conditions can be written as

$$C_b(0) = C_o \qquad (4)$$

$$(U-U_{Gb}) C_o + (-U_{Ge}) C_e(0) = U_{Gc} C_c(0) \qquad (5)$$

Equations 1-5 can be written in dimensionless forms as

$$- \frac{dC_1}{dl} + A_1 (C_2 - C_1) = 0 \qquad (6)$$

$$- \frac{dC_2}{dl} + A_2(C_1 - C_2) + A_3(C_3 - C_2) - A_4 C_2 = 0 \qquad (7)$$

$$- (C_2(1) - C_3) + A_5 \int_0^1 (C_2 - C_3) \, dl - A_6 C_3 = 0 \qquad (8)$$

where the constants $A_1 - A_6$ are defined as follows :

$$A_1 = \frac{\epsilon_b K_{bc} L_f}{U_{Gb}} \qquad A_2 = \frac{\epsilon_b K_{bc} L_f}{U_{Gc}}$$

$$A_3 = \frac{\epsilon_b K_{ce} L_f}{U_{Gc}} \qquad A_4 = \frac{kf_w \epsilon_b L_f}{U_{Gc}}$$

$$A_5 = \frac{\epsilon_b K_{ce} L_f}{U_{Ge}} \qquad A_6 = \frac{k (1-\epsilon_b(1+f_w))L_f}{U_{Ge}} \qquad (9)$$

The set of Equations 6-8 is accompanied by initial conditions

$$C_1 = 1 \text{ at } l = 0 \qquad (10)$$

$$1 + B_1 C_3 = B_2 C_2 \text{ at } l = 0 \qquad (11)$$

where

$$B_1 = \frac{-U_{Ge}}{(U-U_{Gb})} \quad \text{and} \quad B_2 = \frac{U_{Gc}}{(U-U_{Gb})} \qquad (12)$$

The assumption of complete mixing in the emulsion phase renders the concentration C_3 constant in the bed, and Equations 6 and 7 can be rearranged as

$$D^2C_1 + (A_1+A_2+A_3+A_4)\ DC_1 + A_1(A_3+A_4)\ C_1 - A_1A_3C_3 = 0 \qquad (13)$$

where the operator D refers to $d/d\ell$. The solution to this equation can be readily obtained as

$$C_1 = R_1 e^{\lambda_1 \ell} + R_2 e^{\lambda_2 \ell} + R_3 \qquad (14)$$

where λ_1 and λ_2 are the roots of Equation 13 with the constant term $(A_1A_3C_3)$ removed, and R_3 is the particular solution of Equation 13 given by

$$R_3 = \frac{A_3}{A_3 + A_4}\ C_3 \qquad (15)$$

Equation 14 can be substituted in Equation 6 to obtain

$$C_2 = R_1\alpha_1 e^{\lambda_1 \ell} + R_2\alpha_2 e^{\lambda_2 \ell} + R_3 \qquad (16)$$

where the $\alpha's$ are defined as

$$\alpha_1 = \frac{\lambda_1 + A_1}{A_1} \quad \text{and} \quad \alpha_2 = \frac{\lambda_2 + A_1}{A_1} \qquad (17)$$

It is interesting to note that Equations 14 and 16 require a knowledge of C_3 which can be obtained after some algebraic manipulations by substituting these equations in 8 as

$$C_3 = A_7A_8R_1 + A_7A_9R_2 \qquad (18)$$

where A_7, A_8 and A_9 are constants defined as

$$A_7 = \left[1-A_6-A_5 + \frac{A_5A_3}{A_3+A_4} - \frac{A_3}{A_3+A_4} \right]^{-1}$$

$$A_8 = \alpha_1 e^{\lambda_1} + \frac{A_5 \alpha_1}{\lambda_1}(1 - e^{\lambda_1})$$

$$A_9 = \alpha_2 e^{\lambda_2} + \frac{A_5 \alpha_2}{\lambda_2}(1 - e^{\lambda_2}) \tag{19}$$

Equations 14 and 16 along with 18 give the concentration profiles in the bubble and cloud phases. The constants R_1 and R_2 appearing in these equations can be evaluated subject to initial conditions given by Equations 9 and 10 and can be written in matrix form as

$$\begin{bmatrix} B_3 & B_4 \\ B_5 & B_6 \end{bmatrix} \begin{bmatrix} R_1 \\ R_2 \end{bmatrix} = \begin{bmatrix} 1 \\ 1 \end{bmatrix} \tag{19a}$$

where parameters $B_3 - B_6$ are defined as

$$B_3 = 1 + \frac{A_3 A_7 A_8}{A_3 + A_4} \qquad B_4 = 1 + \frac{A_3 A_7 A_9}{A_3 + A_4}$$

$$B_5 = B_2 \alpha_1 + A_8 \left(\frac{B_2 A_3 A_7}{A_3 + A_4} - B_1 A_7 \right)$$

$$B_6 = B_2 \alpha_2 + A_9 \left(\frac{B_2 A_3 A_7}{A_3 + A_4} - B_1 A_7 \right) \tag{20}$$

The gas concentration at the bed exit is given by

$$C(1) = \frac{U_{Gb}}{U} C_1(1) + \left(1 - \frac{U_{Gb}}{U} \right) C_2(1) \tag{21}$$

The concentration profiles in the bubbles, cloud and emulsion phases are plotted in Figure 1 for a set of parameter values. For the sake of comparison, the profiles for the same values of parameters obtained using the Fryer-Potter model are shown in Figure 2. Figures 3-6 show the influence of parameters such as bubble diameter, U/U_{mf}, H_o and rate constant on the extent of
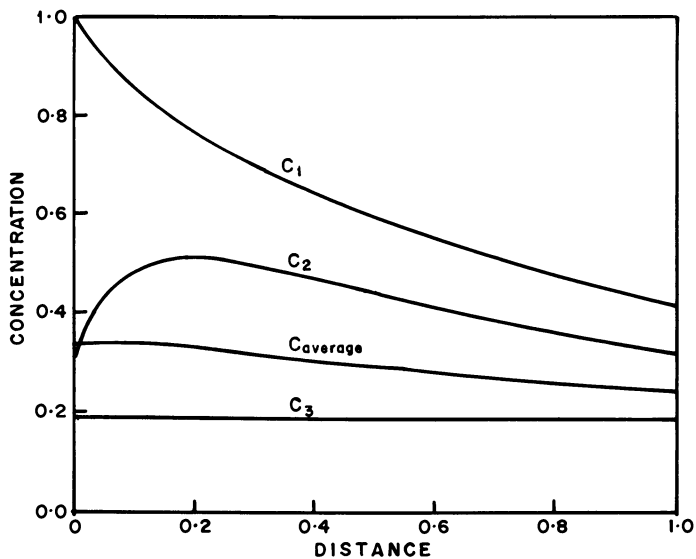
Figure 1.   Concentration profiles using present model: $H_o = 50$ cm, $d_b = 5$ cm, $U = 10$ cm/s, $U_{mf} = 1$ cm/s, $k = 0.5$ s^{-1}, $\epsilon_{mf} = 0.5$, $D_e = 0.2$ cm^2/s
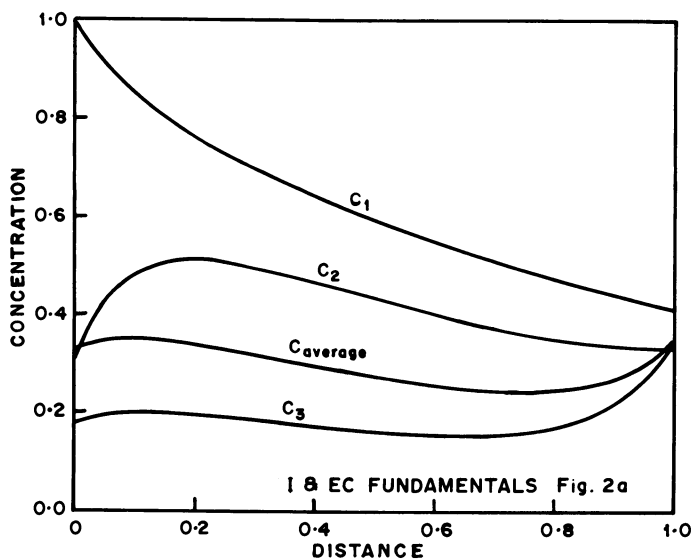
Figure 2.   Concentration profiles using Fryer–Potter model (12): $H_o = 50$ cm, $d_b = 5$ cm, $U = 10$ cm/s, $U_{mf} = 1$ cm/s, $k = 0.5$ s^{-1}, $\epsilon_{mf} = 0.5$, $D_e = 0.2$ cm^2/s
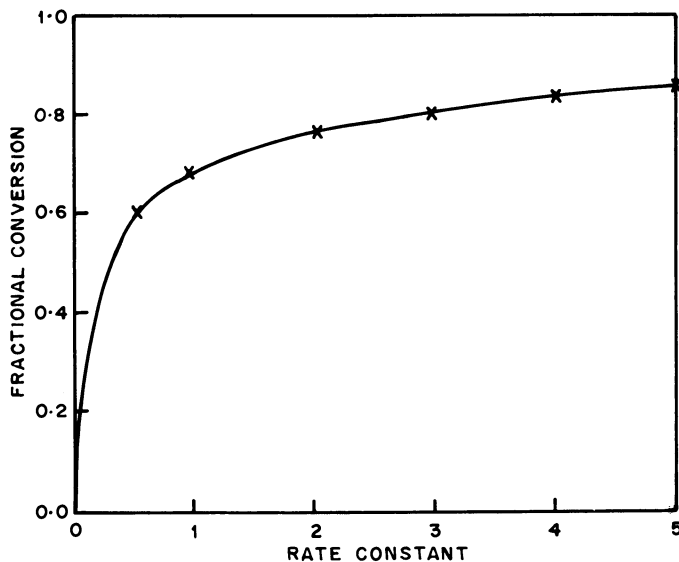
Figure 3. Comparison of the present and the FP model effect of rate constant:
$H_o = 50$, $d_b = 5$ cm, $U = 10$ cm/s, $U_{mf} = 1$ cm/s, $D_e = 0.2$ cm²/s, $\epsilon_{mf} = 0.5$,
(×) FP model, (———) present model
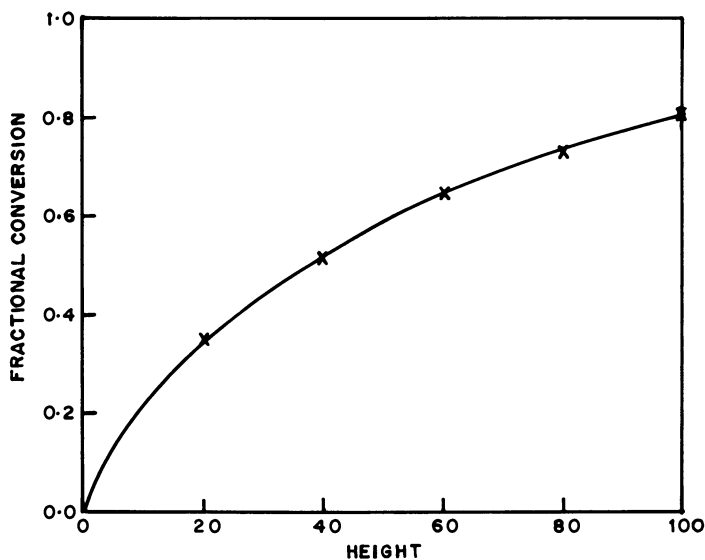
Figure 4. Comparison of the present and the FP model effect of the bed height:
$d_b = 5$ cm, $U = 10$ cm/s, $U_{mf} = 1$ cm/s, $\epsilon_{mf} = 0.5$, $D_e = 0.2$ cm²/s, $k = 0.5$ s⁻¹,
(×) FP model, (———) present model

Figure 5.   Comparison of the present and the FP model effect of U/U_{mf} on conversion: $H_o = 50$ cm, $d_b = 5$ cm, $U_{mf} = 1$ cm/s, $D_e = 0.2$ cm²/s, $k = 0.5$ s⁻¹, $\epsilon_{mf} = 0.5$, (×) FP model, (——) present model

Figure 6.   Effect of bubble diameter on conversion: $H_o = 50$ cm, $k_1 = 0.5$ s⁻¹, $D_e = 0.2$ cm²/s, $U = 10$ cm/s, $U_{mf} = 1$ cm/s, $\epsilon_{mf} = 0.5$, (×) FP model, (——) present model
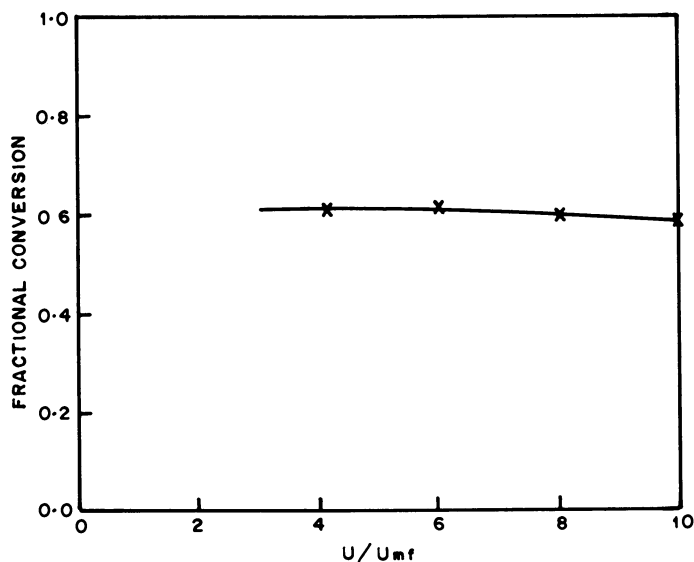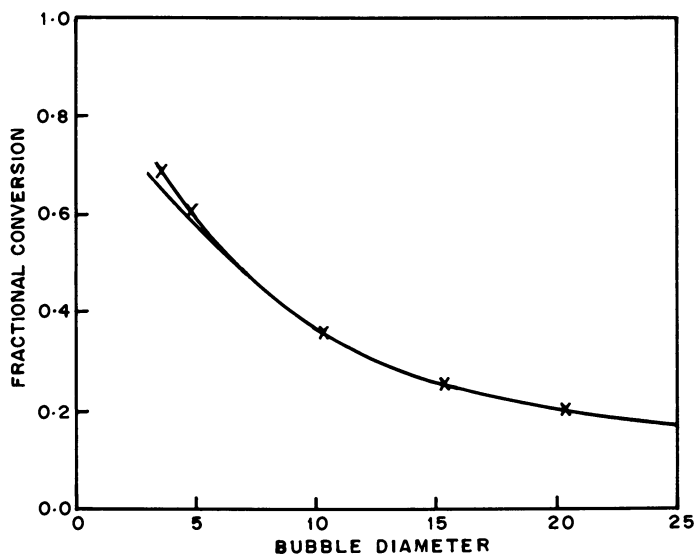
conversion. Again, for the sake of comparison, the results
obtained using the Fryer–Potter model are also presented.

It can be seen from these figures that the results obtained
using the two models are almost indistinguishable from each
other except at smaller values of d_b. The smaller bubble
diameters are however unlikely in large industrial fluid beds,
and therefore for all practical purposes the predictions of the
two models are identical.

The large industrial fluid beds are normally operated with
U/U_{mf} exceeding 10, so that a large portion of the gas bypasses
the bed in the form of bubbles. Also the diameter of the
bubbles is fairly large, so that interphase mass transport is
small compared to the rate of reaction. Under these conditions
the extent of mixing in the emulsion phase is rather an unimport-
ant parameter as far as the prediction of conversion is concern-
ed. It would, however, have significant influence when non
first–order reactions are involved.

The formulation of the model as above has the advantage
that mathematically it picturizes the bed as an initial value
problem in contrast to the more complicated boundary value
representation of the Fryer–Potter model. The implications of
this reduced complexity become more evident (and considerably
more important) when the reactions involved are nonlinear.
While the initial value problem can be readily solved for such
a case, the boundary value presentation leads to severe
stability and convergence problems.

Conclusions

The behavioural features of the fluidized bed have been
modeled based on a modified representation of the Fryer–Potter
model. The restrictive assumption of plug flow of the emulsion
gas has been removed, and model equations developed based on
complete mixing of the emulsion gas. This simplification, in
addition to bringing the model closer to reality, has led to the
conversion of a boundary value problem (Fryer–Potter model) to
a simpler initial value problem. Except at very low bubble
diameters, the predictions of the two models (based on terminal
conversion) agree closely with each other. On the other hand,
agreement between the average concentration profiles in the bed
predicted by the two models is less satisfactory. While
therefore the modified model proposed in this work has the
advantage of simplicity and is perhaps closer to reality,
further experimental work on industrial size equipment is
necessary for a firmer opinion on the latter (nature of gas
flow in the emulsion phase).

Legend of Symbols

A_1 to A_6	constants defined by Equation (9)
A_7 to A_9	constants defined by Equation (19)
B_1, B_2	constants defined by Equation (12)
B_3 to B_6	parameters defined by Equation (20)
C_b, C_c, C_e	concentration in the bubble, cloud-wake and emulsion phase respectively
C_1, C_2, C_3	dimensionless concentration in the bubble, cloud and emulsion
$C_1(1)$, $C_2(1)$	dimensionless bubble phase and cloud-wake phase concentration at the bed exist
$C(1)$	dimensionless gas concentration at the exit
d_b	bubble diameter cm
d_t	diameter of the bed cm
f_w	ratio of wake volume to bubble volume
H_o	height of the bed at incipient fluidization
K_{bc}	volumetric rate of gas exchange between bubble and cloud-wake per unit bubble volume s^{-1}
K_{ce}	volumetric rate of gas exchange between cloud-wake and emulsion per unit volume s^{-1}
L_f	height of bubbling bed cm
ℓ	dimensionless height above distributor
k	first order reaction rate constant, based on unit volume of dense phase, s^{-1}
R_1, R_2	parameters defined by Equation (19a)
R_3	parameter defined by Equation (15)
U	superficial gas velocity cm s^{-1}
U_{cr}	critical velocity cm s^{-1}
U_{Gb}	superficial velocity in bubble phase cm s^{-1}
U_{Gc}	superficial velocity in cloud-wake phase cm s^{-1}
U_{Ge}	superficial velocity in emulsion phase cm s^{-1}
z	length parameter along the bed height

Greek Letters

α_1, α_2	constants defined by Equation (17)
ϵ_b	fraction of bed volume occupied by bubbles
λ_1, λ_2	roots of Equation (13)
ϵ_{mf}	void fraction in bed at minimum fluidization conditions

Acknowledgement

Literature Cited

1. Gilliland, E.R.; Mason, E.A. Ind. Eng. Chem. 1949, 41, 1191.
2. Gilliland, E.R.; Mason, E.A. Ind. Eng. Chem. 1952, 44, 218.
3. Noble, P.J. "Mineral Dressing Research Symposium Annual Conference"; Australian Instn. Min. Met. 1962.
4. Rowe, P.N. Trans. Inst. Chem. Engrs. 1961, 39, 175.
5. Woollard, I. N. M.; Potter, O.E. AIChE J. 1968, 14, 388.
6. Marscheck, R.M.; Gomezplata, A. AIChE J. 1965, 11, 167.
7. Stephens, G.K.; Sinclair, R.J.; Potter, O.E. Powder Tech. 1967, 1, 157.
8. Latham, R.L.; Hamilton, C.J.; Potter, O.E. Brit. Chem. Eng. 1968, 13, 666.
9. Nguyen, H.V.; Potter, O.E. "Advances in Chemistry Series No.133"; American Chemical Society : Washington, DC. 1974; p 290.
10. Nguyen, H.V. Ph.D. thesis, Monash University, Australia, 1975.
11. Kunii, D.; Levenspiel, O. Ind. Eng. Chem. Fundam. 1968, 7, 446.
12. Fryer, C.; Potter, O.E. Ind. Eng. Chem. Fundam. 1972, 11, 338.
13. Ohki, K.; Shirai, T. "Fluidization Technology I"; Hemisphere Publishing Corporation : Washington DC, 1976; p 95.
14. Whitehead, A.B.; Gartside, G.; Dent, D.C. Chem. Eng. J. 1970, 1, 175.
15. Werther, J. Preprint, paper presented at GVC/AIChE Meeting, Munchen, 1974.
16. Schmalfeld, V.J. V.D.I-Z. 1976, 118, 65.
17. Nguyen, H.V.; Whitehead, A.B.; Potter, O.E. AIChE J. 1977, 23, 913.

Predictions of Fluidized Bed Operation Under Two Limiting Conditions: Reaction Control and Transport Control

H. S. FOGLER

Department of Chemical Engineering, The University of Michigan, Ann Arbor, MI 48109

L. F. BROWN

Department of Chemical Engineering, The University of Colorado, Boulder, CO 80309

Some aspects of fluidized-bed reactor performance
are examined using the Kunii-Levenspiel model of
fluidized-bed reactor behavior. An ammonia-oxi-
dation system is modeled, and the conversion pre-
dicted is shown to approximate that observed ex-
perimentally. The model is used to predict the
changes in conversion with parameter variation
under the limiting conditions of reaction control
and transport control, and the ammonia-oxidation
system is seen to be an example of reaction con-
trol. Finally, it is shown that significant dif-
ferences in the averaging techniques occur for
height to diameter ratios in the range of 2 to 20.

There has been increased interest in recent years in the
science and engineering of fluidized-bed reactors. Part of this
interest can be attributed to the projected extensive use of
fluidized-bed coal gasifiers, but the development of magnetically-
stabilized fluidized beds and centrifugal beds also has contrib-
uted significantly to rejuvenating fluidized-bed research and
modeling. Some of the many recent reviews and evaluations of
fluidized-bed modeling are those of Bukur (1974), Chavarie and
Grace (1975), Yates (1975), Van Swaaif (1978), Weimer (1978), and
Potter (1978). Of these, Yates gives an unusually good compari-
son of the theoretical similarities and differences among cur-
rently popular models, while Chavarie and Grace compare the pre-
dictions of various models with the experimentally-observed
internal behavior of a fluidized-bed reacting system. These
latter authors conclude that the Kunii-Levenspiel (K-L) model
gives the most realistic estimate of behavior within a fluidized
bed. Yates points out that the countercurrent-backmixing model
of Fryer and Potter, not considered by Chavarie and Grace, is
more rigorously founded than the K-L model. On the other hand,
Potter shows that when the average bubble size is smaller than
8-10 cm, there is little difference between the countercurrent-

backmixing and the K-L models, both of which give good predic-
tions of fluidized-bed performance.

The K-L model, because of its greater simplicity, thus seems
to be the model of choice for systems with smaller bubbles. In
this paper we shall show how the K-L model can be used to predict
the experimental results obtained by Massimilla and Johnstone
(1961) on the catalytic oxidation of ammonia. It will be seen
that the performance of their system was largely controlled by
reaction limitations within the bed's phases. The effects of
various parameters on bed performance are examined for such a
reaction-limited system, and then the effects of these parameters
for a transport-limited system are also discussed. Finally, we
consider the effect of using average values of the bubble diam-
eter and transport coefficients on model predictions.

Applying the Kunii-Levenspiel Model

The Kunii-Levenspiel Model will be used in conjunction with
the correlations of Broadhurst and Becker (1975) and Mori and Wen
(1975) to analyze the ammonia oxidation of Massimilla and John-
stone (1961). The reaction

$$4NH_3 + 7O_2 \rightarrow 4NO_2 + 6H_2O$$
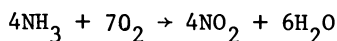
was carried out in an 11.4 cm diameter fluidized-bed reactor con-
taining 4kg of catalyst particles. The particles had a diameter,
d_p, of 105 μm, and a density, ρ_p, of 2.06 g/cm^3. The particle
sphericity, ψ, was taken to be 0.6 as is typical of published
values (Kunii and Levenspiel, 1969).

A mixture of 90% oxygen and 10% ammonia was fed to the reac-
tor at a rate of 818 cm^3/s, a temperature of 523 K, and a pressure
of 0.11 MPa (840 torr). The reaction is first order in ammonia.
The reaction is apparently zero order in oxygen owing to the
excess oxygen. Thus

$$-r_A = k_{cat}C_A \tag{1}$$

From fixed-bed studies, k_{cat}=0.0858 cm^{3}gas/[(cm^3 catalyst)(s)].

The catalyst weight, W, and corresponding expanded bed
height, h, necessary to achieve a specified conversion, X, are

$$W = Ah(1-\varepsilon_{mf})(1-\delta)\rho_p \tag{2}$$

$$h = \frac{u_b}{k_{cat}K_R} \ell n(\frac{1}{1-X}) \tag{3}$$

in which

A   is the cross-sectional area
K_R is the overall dimensionless reaction rate constant
u_b is the velocity of bubble rise, cm/s
ε_{mf} is the bed porosity at minimum fluidization condi-
        tions
δ is the fraction of the column occupied by bubbles

Calculating the Fluidization Parameters.   The porosity at
minimum fluidization is obtained from the Broadhurst and Becker
correlation (1975):

$$\varepsilon_{mf} = 0.586\psi^{-0.72}\left[\frac{\mu^2}{\rho_g \eta d_p^3}\right]^{0.029}\left(\frac{\rho_g}{\rho_p}\right)^{0.021} \qquad (4)$$

resulting in ε_{mf}=0.657. At first sight, this value appears
higher than void fractions of 0.35-0.45 normally encountered in
packed beds (Drew et al., 1950). The catalyst used by Massimilla
and Johnstone used an impregnated cracking catalyst, however, and
a value of ε_{mf} of 0.657 is consistent with the numbers reported
for materials of this type by Leva (1959) and by Zenz and Othmer
(1960).
     The corresponding minimum fluidization velocity is

$$u_{mf} = \frac{(\psi d_p)^2 \eta}{150 \mu} \frac{\varepsilon_{mf}^3}{1-\varepsilon_{mf}} \qquad \begin{array}{l} Re < 20 \\ (Kunii~and \\ Levenspiel, 1969) \end{array} \qquad (5)$$

which gives $u_{mf} = 1.48$ cm/s.
     The entering volumetric flow rate of 818 cm^3/s corresponds
to a superficial velocity of 8.01 cm/s. Therefore

$$\frac{u_o}{u_{mf}} = 5.4$$

     In order to calculate the expanded bed height, h, for the
given catalyst weight of 4 kg, one needs to calculate the frac-
tion of bed occupied by bubbles, δ. From the K-L model

$$\delta = \frac{u_o - u_{mf}}{u_b - u_{mf}(1+\alpha)} \qquad (6)$$

For 0.1 mm particles, Kunii and Levenspiel (1969) state that
$\alpha = 0.4$ is a reasonable estimate.
     At this point, however, there is a difficulty. To calculate
the velocity of bubble rise, u_b, the bubble diameter at the
midpoint in the column, d_b, is required:

$$u_b = u_o - u_{mf} + u_{br} \tag{7}$$

and

$$u_{br} = (0.71)(gd_b)^{1/2} \quad (u_{br} = \text{rise velocity of a single bubble})$$

In Mori and Wen's (1975) correlation, the bubble diameter is a function of distance up the column, L:

$$d_b = d_{bm} - (d_{bm} - d_{bo})[\exp(-0.3L/D)] \tag{8}$$

Thus, in order to obtain the bubble diameter at L=h/2, the height of the expanded bed, h, is needed. Equation (8) also contains a maximum bubble diameter, d_{bm},

$$d_{bm} = (0.652)[A(u_o - u_{mf})]^{0.4} \tag{9}$$

(A in cm^2, u's in cm/s, and d_{bm} in cm)

and a minimum diameter for a porous plate:

$$d_{bo} = (0.00376)(u_o - u_{mf})^2 \tag{10}$$

(u's in cm/s, and d_{bo} in cm)

Equations (6) and (2) are used to obtain h, and the bubble-rise velocity u_b, appears in Eq. (6). Consequently, we see a predicament has arisen, in that h is needed to calculate d_b, which is needed to calculate u_b, which in turn is needed to calculate h.

To overcome this difficulty, the sequence in Figure 1 is normally adopted. The unexpanded bed height was 39 cm, so the expanded bed height will probably be around 60 cm and the average bubble size will first be calculated at L = h/2 = 30 cm. Using Eqs. (9) and (10),

$$d_{bo} = 0.16 \text{ cm}$$

and

$$d_{bm} = 8.79 \text{ cm}$$

The bubble diameter at L = h/2 calculated from Eq. (8) is 4.87 cm. Using this value, one can now calculate u_b, δ, and h using Eqs. (2), (6) and (7). These values are given in Table 1.
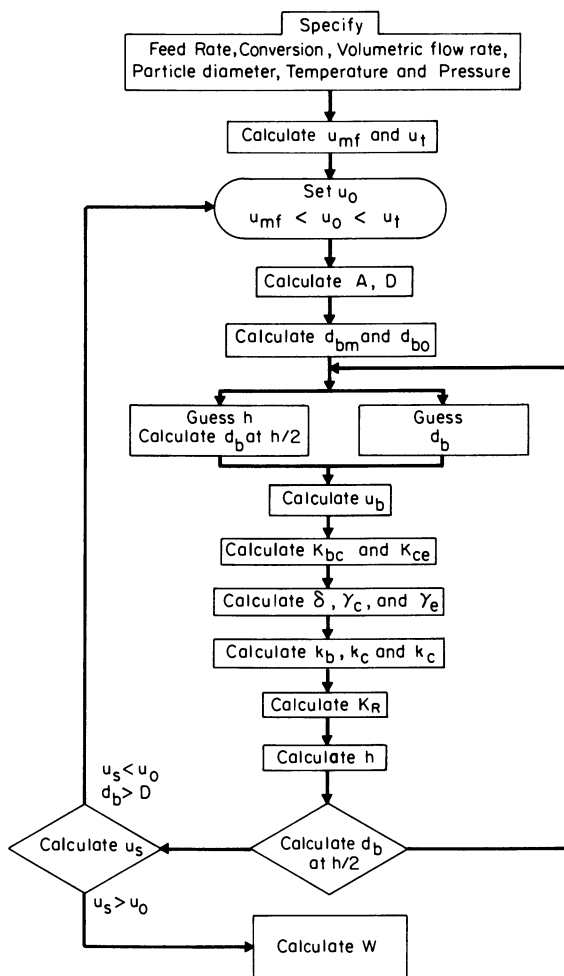
Figure 1. Computational algorithm for fluid bed reactor design

Table I
Fluidized-Bed Characteristics of Ammonia Oxidation Reactor

u_o = 8.01 cm/s d_{bo} = 0.16 cm

ε_{mf} = 0.657 d_{bm} = 8.79 cm

u_{mf} = 1.48 cm/s d_b = 4.87 cm

α = 0.4 u_b = 55.6 cm/s

δ = 0.122 h = 63.2 cm

Since the estimated bed height of 60 cm is sufficiently close to the calculated value of 63.2 cm, we can proceed in the calculations without making a new estimate of h. The only remaining parameter needed to calculate the conversion is the overall dimensionless reaction rate constant K_R.

Calculating The Reaction Parameters. The overall dimensionless rate constant is expressed in terms of exchange coefficients between the bubble, cloud, and emulsion, and in terms of the volumes of catalyst per volume of bubble in the bubble, cloud, and emulsion:

$$K_R = \gamma_b + \cfrac{1}{\cfrac{k_{cat}}{K_{bc}} + \cfrac{1}{\gamma_c + \cfrac{1}{\cfrac{1}{\gamma_e} + \cfrac{k_{cat}}{K_{ce}}}}} \tag{11}$$

The exchange coefficients between the bubble and the cloud, K_{bc}, and the cloud and the emulsion, K_{ce}, are respectively

$$K_{bc} = (4.5)\left(\frac{u_{mf}}{d_b}\right) + (5.85)\left(\frac{D_{AB}^2 g}{d_b^5}\right)^{1/4} \tag{12}$$

$$K_{ce} = (6.78)\left(\frac{\varepsilon_{mf} D_{AB} u_b}{d_b^3}\right)^{1/2} \tag{13}$$

Using these formulas, we obtain

$$K_{bc} = 4.92 \ s^{-1}$$
$$K_{ce} = 3.00 \ s^{-1}$$

The 0.618 cm^2/s used for the value of D_{AB}, the molecular diffusivity, in Eqs. (12) and (13) was calculated from the Fuller, Schettler, and Gidding correlation (Reid et al., 1977). The volumes of catalyst particles per volume of bubble in the bubble phase, γ_b, the cloud phase, γ_c, and the emulsion phase, γ_e, are given by the equations

$$\gamma_b = 0.01 \text{ cm}^3 \text{ of catalyst in bubbles/cm}^3 \text{ of bubble} \tag{14}$$

(this is a typical value which is frequently assumed)

$$\gamma_c = (1-\varepsilon_{mf}) \left[\frac{\left(\frac{3u_{mf}}{\varepsilon_{mf}} \right)}{\left(u_{br} - \frac{u_{mf}}{\varepsilon_{mf}} \right)} + \alpha \right] \tag{15}$$

$$\gamma_e = (1-\varepsilon_{mf}) \left(\frac{1-\delta}{\delta} \right) - \gamma_c \tag{16}$$

Substituting the indicated values into the equations yields

$$\gamma_c = 0.187 \text{ cm}^3 \text{ catalyst in clouds and wakes/cm}^3 \text{ of bubble}$$

and

$$\gamma_e = 2.28 \text{ cm}^3 \text{ catalyst in emulsion/cm}^3 \text{ of bubble}$$

When the values obtained from Eqs. (12) through (16) are substituted into Eq. (11),

$$K_R = 0.01 + \cfrac{1}{\cfrac{0.0858}{4.92} + \cfrac{1}{0.187 + \cfrac{1}{\cfrac{1}{2.28} + \cfrac{0.0858}{3.0}}}}$$

$$K_R = 0.01 + \cfrac{1}{0.0174 + \cfrac{1}{0.187 + \cfrac{1}{0.4386 + 0.0286}}}$$

Solving this equation gives the numerical value of the dimensionless reaction rate constant

$$K_R = 2.25$$

Equation (3) may be solved for the conversion, X:

$$X = 1 - \exp\left(\frac{k_{cat}K_R h}{u_b}\right) \qquad (17)$$

Substituting the values we have determined into this equation gives

$$X = 0.197$$

The 20% conversion calculated using the Kunii-Levenspiel model compares quite well with the experimental value of 22% measured by Massimilla and Johnstone.

Limiting Situations. As engineers, it is important to deduce how a bed will operate if one were to change operating conditions such as gas flow rate, catalyst particle size, etc. To give some general guides as to how changes will affect bed behavior, we shall consider the two limiting circumstances of reaction control and transport control.

In the K-L model, reaction occurs within the bed's phases, and material is continuously transferred between the phases. Two limiting situations thus arise. In one, the interphase transport is relatively fast and transport equilibrium is maintained, causing the system performance to be controlled by the rate of reaction. In the other, the reaction rate is relatively fast and the performance is controlled by interphase transport. It will be shown that the ammonia oxidation example used above is essentially a reaction-limited system.

The overall reaction rate in the bed is proportional to K_R, so the reciprocal of K_R can be viewed as an overall resistance to the reaction. The different terms and groups on the RHS of Eq. (11) can be viewed as individual resistances which can be arranged in series or parallel to give the overall resistance.

$$R_o = \frac{1}{K_R} = \cfrac{1}{\cfrac{1}{\cfrac{1}{\gamma_b}} + \cfrac{1}{\cfrac{1}{\cfrac{k_{cat}}{K_{bc}}} + \cfrac{1}{\cfrac{1}{\cfrac{1}{\gamma_c}} + \cfrac{1}{\cfrac{1}{\cfrac{1}{\gamma_e}} + \cfrac{k_{cat}}{K_{ce}}}}} \qquad (18)$$

$$R_o = \cfrac{1}{\cfrac{1}{R_{rb}} + \cfrac{1}{R_{tbc} + \cfrac{1}{\cfrac{1}{R_{rc}} + \cfrac{1}{R_{re} + R_{tce}}}}} \qquad (19)$$

in which:

$$R_{rb} = \frac{1}{\gamma_b} = \text{resistance to reaction in the bubble}$$

$$R_{tbc} = \frac{k_{cat}}{K_{bc}} = \text{resistance to transfer between bubble and cloud}$$

$$R_{rc} = \frac{1}{\gamma_e} = \text{resistance to reaction in cloud}$$

$$R_{re} = \frac{1}{\gamma_e} = \text{resistance to reaction in the emulsion}$$

$$R_{tce} = \frac{k_{cat}}{K_{ce}} = \text{resistance to transfer between cloud and emulsion}$$

The analog electrical resistance for the system is shown in Figure 2 along with the corresponding resistances for this reaction. As with its electrical analog, the reaction will pursue the path of least resistance, which in this case is along the right hand side branch of Figure 2. If the major resistance in this side, the resistance to reaction in the emulsion, R_{re}, could be reduced, a greater conversion could be achieved for a specified catalyst weight. To reduce R_{re}, one needs to look for ways of increasing γ_e

$$\gamma_e = (1-\varepsilon_{mf})\left[\frac{1-\delta}{\delta} - \frac{\dfrac{3u_{mf}}{\varepsilon_{mf}}}{(.71d_b g)^{1/2} - (u_{mf}/\varepsilon_{mf})} - \alpha\right] \qquad (20)$$

Examination of equation (20) shows that decreasing the bubble size, d_b, and fraction, δ, while decreasing the minimum fluidization velocity would increase γ_e and hence the conversion. The minimum fluidization velocity could be decreased by decreasing the particles size. We now will investigate how the various parameters will affect the conversion for different limiting situations.

The Slow Reaction. In addition to the obvious way of increasing the temperature to increase the conversion, there are other ways the conversion may be increased when the reaction is slow. From equation (3) we know the conversion depends upon h, k_{cat}, u_b and K_R. We will first determine K_R under this situation. For a slow reaction, k_{cat} is small when compared to K_{bc} and K_{ce}, so that resistance to transport is essentially zero, i.e.
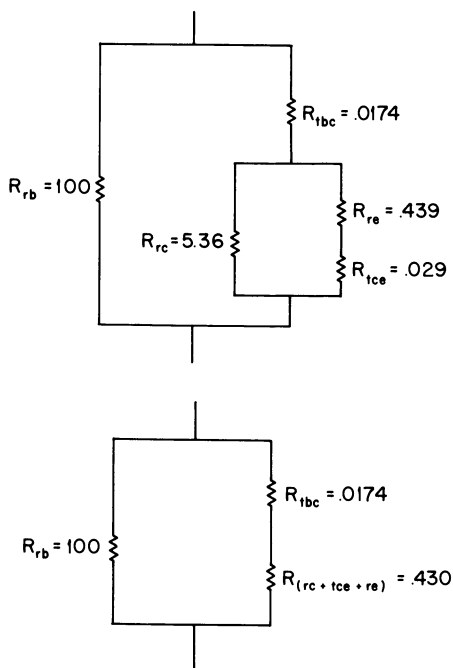
*Figure 2.   Electrical analog of transport and reaction resistances in the Kunni–
Levenspiel model using the data of Massimillia and Johnstone (9)*

$$\frac{k_{cat}}{K_{bc}} \simeq 0$$

and

$$\frac{k_{cat}}{K_{ce}} \simeq 0$$

then

$$K_R = \gamma_b + \cfrac{1}{0 + \cfrac{1}{\gamma_c + \cfrac{1}{\cfrac{1}{\gamma_e} + 0}}} = \gamma_b + \gamma_c + \gamma_e \qquad (21)$$

Using Eq. (16) to substitute for γ_e we have

$$K_R = \gamma_b + (1-\epsilon_{mf}) \left(\frac{1-\delta}{\delta}\right) \qquad (22)$$

neglecting γ_b w.r.t. the second term gives

$$K_R = (1-\epsilon_{mf}) \left(\frac{1-\delta}{\delta}\right) \qquad (23)$$

Consequently we see that K_R can be increased by decreasing δ, the volume fraction of bubbles. For the ammonia oxidation example, this would give

$$K_R \simeq 2.47$$

or about 11% higher than the value obtained by the more elaborate calculations which included the transport. This would predict a conversion of 21.4%, very close to the 19.7% given by the method which includes the transport limitations. Thus the ammonia oxidation system of Massimilla and Johnstone is essentially a reaction-limited system.

The conversion and catalyst weight are related by

$$W = Ah\rho_p (1-\epsilon_{mf}) (1-\delta) = \frac{Au_b \rho_p (1-\epsilon_{mf}) (1-\delta)}{k_{cat} K_R} \ell n \frac{1}{1-X} \qquad (24)$$

Substituting for K_R

$$W = \frac{A\rho_p u_b \delta}{k_{cat}} \ell n \left(\frac{1}{1-X}\right) \qquad (25)$$

Recalling

$$\delta = \frac{u_o - u_{mf}}{u_b - u_{mf}(1+\alpha)} \tag{6}$$

In most all instances u_b is significantly greater than $u_{mf}(1+\alpha)$ so that Equation (6) is approximately

$$\delta = \frac{u_o - u_{mf}}{u_b} \tag{26}$$

combining Eq. (24) and (25)

$$W = \frac{A\rho_p (u_o - u_m)}{k_{cat}} \ell n \frac{1}{1-X} \tag{27}$$

Therefore one observes that to reduce the catalyst weight for a specified conversion, u_o and u_{mf} should be as close as possible. One can now ask what ways may the catalyst weight be reduced for a specified conversion. The answer to this question is the same as to the question, "How may one increase the conversion for a fixed catalyst weight?"

For example, suppose you are operating at 5 times the minimum fluidization velocity, $u_o = 5u_{mf}$.

Case 1

$$W_1 = \frac{A\rho_p 4u_{mf1}}{k_{cat}} \ell n \frac{1}{1-X_1} \tag{28}$$

What would be the effect of doubling the particle diameter on the catalyst weight for the same throughput and conversion?

Case 2

$$W_2 = \frac{\rho_p A(u_{o2} - u_{mf2})}{k_{cat2}} \ell n \frac{1}{1-X_2} \tag{29}$$

Since the temperature $k_{cat1} = k_{cat2}$, the throughput $(u_{o1} = u_{o2})$, and conversion $(X_1 = X_2)$ are the same for Cases 1 and 2, the ratio of equation (28) and (29) yield

$$\frac{W_2}{W_1} = \frac{u_{o1} - u_{mf2}}{4u_{mf1}} = \frac{5u_{mf1} - u_{mf2}}{4u_{mf1}} \tag{30}$$

Recalling Eq. (5)

$$u_{mf} = \frac{(\psi d_p)^2 \eta}{150\mu} \frac{\varepsilon_{mf}^3}{1-\varepsilon_{mf}} \tag{5}$$

and neglecting the dependence of ε_{mf} on d_p we see that the only parameters which vary between Case 1 (d_p) and Case 2 $(d_{p2}=2d_{p1})$ are u_{mf} and W.

$$\frac{u_{mf2}}{u_{mf1}} = \left(\frac{d_{p2}}{d_{p1}}\right)^2 = \left(\frac{2d_{p1}}{d_{p1}}\right)^2 = 4$$

and therefore

$$\frac{W_2}{W_1} = \frac{5u_{mf1}-4u_{mf1}}{4u_{mf1}} = 0.25$$

Thus in the situation we have postulated, with a first-order re-action and reaction limiting the bed behavior, doubling the parti-cle size will reduce the catalyst by approximately 75% and still maintain the same conversion.

The slow-reaction situation has been treated before (Grace, 1974), using a model of bed performance developed well before the K-L model (Orcutt et al., 1962). This earlier work concluded that when the reaction was very slow, the hydrodynamics and the way the hydrodynamics were modeled were unimportant. The analysis given above, using the more sophisticated K-L model, shows that the hy-drodynamics can be very important indeed, even when the reaction is slow. In the situation cited, a reduction of 75% in catalyst requirement can be attained by expoitation of the bed hydrodynam-ics.

The Rapid Reaction. To analyze this limiting situation we shall assume the particles are sufficiently small so that the effectiveness factor is essentially one and that the rate of transfer from the bulk fluid to the individual catalyst particles is rapid in comparison with the rate of transfer between the fluidization phases. For the case of rapid reaction

$$\frac{k_{cat}}{K_{bc}} \text{ and } \frac{k_{cat}}{K_{ce}} \gg 1$$

Using these approximations in the equation for K_R which is

$$K_R = \gamma_b + \cfrac{1}{\cfrac{k_{cat}}{K_{cb}} + \cfrac{1}{\gamma_c + \cfrac{1}{\cfrac{k_{cat}}{K_{ce}} + \gamma_e}}} \qquad (11)$$

one observes the first term to be neglected is

$$\frac{1}{\cfrac{k_{cat}}{K_{ce}} + \cfrac{1}{\gamma_e}} \qquad \frac{1}{(\text{Large No.}) + \cfrac{1}{\gamma_e}} \approx 0$$

Then neglecting the reciprocal of γ_c w.r.t. k_{cat}/K_R gives

$$K_R \cong \gamma_b + \cfrac{1}{\cfrac{k_{cat}}{K_{bc}} + \cfrac{1}{\gamma_c}} \approx \gamma_b + \frac{K_{bc}}{k_{cat}} \qquad (31)$$

There are two situations one can analyze here

Situation 1: $\gamma_b \ll \dfrac{K_{bc}}{k_{cat}}$ Resistance to transport small w.r.t. resistance to reaction inside the bubble

Situation 2: $\gamma_b \gg \dfrac{K_{bc}}{k_{cat}}$ Resistance to transport large w.r.t. resistance to reaction inside the bubble

Only situation 1 will be analyzed in the test and the analysis of situation 2 is left as an exercise for the interested reader.
     Assuming very few particles are present in the bubble phase

$$K_R \cong \frac{K_{bc}}{k_{cat}} \qquad (32)$$

The catalyst weight is given by combining Eqs. (2) and (32)

$$W = \frac{Au_b \rho_p (1-\delta)\ (1-\varepsilon_{mf})\rho_p}{K_{bc}}\ \ell n\left(\frac{1}{1-X}\right) \qquad (33)$$

Neglecting δ w.r.t. 1 in the numerator

$$W = \frac{Au_b \rho_p (1-\epsilon_{mf})}{k_{cat} K_{bc}} \ln\left(\frac{1}{1-X}\right) \tag{34}$$

On observing the equation for K_{bc}, Eq. (12) is the sum of two terms A and B

$$K_{bc} = 4.5\frac{u_{mf}}{d_b} + 5.85\frac{D_{AB}^{1/2} g^{1/4}}{d_b^{5/4}} \tag{12}$$

$$K_{bc} = A_0 + B_0$$

One finds the problem can be further divided.

Case A: $A_0 >> B_0$

Case B: $B_0 >> A_0$

Only Case A will be considered here and Case B again will be left as an exercise for the interested reader.

For Case A

$$K_{bc} \cong 4.5\frac{u_{mf}}{d_b} \tag{35}$$

Then

$$W = \frac{u_b d_b}{4.5 u_{mf}} \rho_p A(1-\epsilon_{mf}) \ln\left(\frac{1}{1-X}\right) \tag{36}$$

Recalling the equation for u_b and neglecting other terms in the equation w.r.t. the velocity of rise of a single bubble, i.e.,

$$u_b \cong u_{br}$$

and

$$u_{br} = 0.71 g^{1/2} d_b^{1/2}$$

$$W = \frac{0.71 g^{1/2} d_b^{3/2}}{4.5 u_{mf}} A\rho_p (1-\epsilon_{mf}) \ln\left(\frac{1}{1-X}\right)$$

$$W = 4.9 \frac{d_b^{3/2}}{u_{mf}} A\rho_p (1-\epsilon_{mf}) \ln\left(\frac{1}{1-X}\right) \tag{37}$$

The average bubble diameter is a function of the tower diameter (thus A), height, u_o, and u_{mf}. As a first approximation, we assume the average bubble diameter is some fraction, (say 0.75) of the maximum bubble diameter.

$$d_b = 0.75 \, d_{bm}$$

Then, from Eq. (9),

$$d_b = (0.75)(0.652)\left[A(u_o-u_{mf})\right]^{0.4} \tag{38}$$

and

$$W = 1.69 \frac{A^{1.6}(u_o-u_{mf})^{0.6}}{u_{mf}} \rho_p(1-\varepsilon_{mf})\ln(\frac{1}{1-X}) \tag{39}$$

We again consider the effect of doubling particle size while keeping all other variables the same.

$$\frac{W_2}{W_1} = \frac{(u_{o2}-u_{mf2})^{0.6}}{(u_{o1}-u_{mf1})^{0.6}} \frac{u_{mf1}}{u_{mf2}} \tag{40}$$

Recalling

$$u_{o2} = u_{o1} = 5u_{mf1}$$

$$u_{mf2} = 4u_{mf1}$$

then

$$\frac{W_2}{W_1} = \left(\frac{5u_{mf1}-4u_{mf1}}{5u_{mf1} - u_{mf1}}\right)0.6 \frac{u_{mf1}}{4u_{mf1}} \tag{41}$$

or

$$\frac{W_2}{W_1} = 0.11 \tag{42}$$

In this case we see that doubling the particle diameter decreases the catalyst weight by 89% while still maintaining the same conversion. However, for a fast reaction, a significant decrease in effectiveness factor could offset this advantage.

It may be noted that the situation considered here, in which the bulk flow term >> diffusion term in Eq. (12), is a somewhat restricted one. For A_O >> B_O in small-particle systems, the binary diffusion coefficient must be on the order of 0.01 cm^2/s or less. Systems involving heavy hydrocarbons frequently have diffusion coefficients this low, but systems with lighter components do

not. Systems using larger particles also have $A_0 \gg B_0$, but then
Re > 20, Eq. (5) cannot be used, and the example analysis given
above is not directly applicable. Thus the example is limited to
systems with small particles and low binary diffusion coefficients.

  Evaluation of the Average Transport Coefficient and Bubble
Size. A constant bubble size is used when evaluating the proper-
ties of the fluidized bed, and since bubbles in real beds vary in
size, it is important to ask what bubble size should be used.
Fryer and Potter (1972), using the model of Davidson and Harrison,
reported that a bubble size found at about 0.4h could be used as
the single bubble size in that model. Earlier in this paper, the
bubble size found at 0.5h was used arbitrarily in calculating the
conversion in an ammonia oxidation system using the K-L model.
  The average bubble size $\bar{d}_b$ in a bed can be found using
Eq. (8):

$$\bar{d}_b - d_{bo} = (d_{bm} - d_{bo}) \int_o^h (1-e^{-0.3L/D})dL \Big/ \int_o^h dL \qquad (43)$$

Integrating:

$$(\bar{d}_b - d_{bo})/(d_{bm} - d_{bo}) = 1 - [(1-e^{-0.3h/D})/(0.3h/D)]$$

$$= 1 - (1-e^{-\beta})\beta \qquad (44)$$

At midpoint, $(\hat{d}_b - d_{bo})/(d_{bm} - d_{bo}) = 1-e^{-\beta/2}$, and therefore

$$(\bar{d}_b - d_{bo})/(\hat{d}_b - d_{bo}) = [1 - (1-e^{-\beta})/\beta]/(1-e^{-\beta/2}) \qquad (45)$$

A plot of the ratio of the mean bubble size to the bubble size
evaluated at the midpoint in the column is shown in Fig. 3 as a
function of h/D. The mean bubble size is at least 90% of the
bubble size evaluated at h/2 for almost all the height-to-diameter
ratios of practical interest.

Evaluation of the Transport Coefficient

  We now wish to determine the difference between the average
exchange coefficient evaluated at the midpoint in the columns.
The dependence of the transport coefficient between the bubble
and the cloud on the bubble diameter,

$$K_{bc} = \left[4.5 u_{mf} + 5.85 \left(\frac{D_{AB}\, g}{d_b} \right)^{1/4} \right] \frac{1}{d_b} \tag{46}$$

will be approximated as

$$K_{bc} \cong \frac{A_1}{d_b} \tag{47}$$

owing to the weak dependence of K_{bc} and d_b in the second term in Eq. (46). From the Mori and Wen correlation

$$d_b = d_{bm} - (d_{bm} - d_{bo}) e^{-\beta x} \tag{48}$$

where $x = L/h$. The local transport coefficient takes the form

$$K_{bc} = \frac{A_1}{d_{bm} - (d_{bm} - d_{bo}) e^{-\beta x}} = \frac{A_2}{1 - (1 - \frac{d_{bo}}{d_{bm}}) e^{-\beta x}} \tag{49}$$

At the midpoint in the column, $L = h/2$, $x = 1/2$

$$\hat{K}_{bc} = \frac{A_2}{1 - (1 - \frac{d_{bo}}{d_{bm}}) e^{-\beta x}} \cong \frac{A_2}{1 - (1 - \frac{d_{bo}}{d_{bm}}) e^{-\beta/2}} \tag{50}$$

The average transport coefficient

$$\overline{K}_{bc} = \frac{\int_0^1 K_{bc}\, dx}{\int_0^1 dx} \tag{51}$$

$$\overline{K}_{bc} = A_2 \int_0^1 \frac{dx}{1 - (1 - \frac{d_{bo}}{d_{bm}}) e^{-\beta x}} \tag{52}$$

$$\overline{K}_{bc} = A_2 \left[1 + 1/\beta \ln \left[\frac{d_{bm}}{d_{bo}} - \left(\frac{d_{bm}}{d_{bo}} - 1 \right) e^{-\beta} \right] \right] \tag{53}$$

Taking the ration of Eq. (50) to Eq. (50) and letting r be the ration of maximum to minimum bubble diameter, $r = \dfrac{d_{bm}}{d_{bo}}$,

$$\frac{\overline{K}_{bc}}{\hat{K}_{bc}} = \left[1+1/\beta \ln[r-(r-1)e^{-\beta}]\right] \; [1-(1-1/r)e^{-\beta/2}] \qquad (54)$$

as $\beta \to \infty$

$$\frac{\overline{K}_{bc}}{\hat{K}_{bc}} \cong 1.0 \qquad (55)$$

A plot of the ratio of the transport coefficients is shown in Figure 4 as a function of β for various values of the parameter r. For the ammonia oxication discussed earlier,

$$r = \frac{d_{bm}}{d_{bo}} = 55 \qquad (56)$$

For large values of r

$$\frac{\overline{K}_{bc}}{\hat{K}_{bc}} \cong \left[1 + 1/\beta \ln[r(1-e^{-\beta})]\right] \; (1-e^{-\beta/2}) \qquad (57)$$

and for larger values of β

$$\frac{\overline{K}_{bc}}{\hat{K}_{bc}} \cong 1 + 1/\beta \ln r \qquad (58)$$

One notes the greatest disparity between the two transport coefficients for large ratios of the maximum to minimum bubble diameter and for columns with h/D ratios in the range of 2 to 20 $(.6<\beta<6)$.

    The exchange coefficient between the cloud and the emulsion is

$$K_{ce} = 6.78 \left(\frac{\varepsilon_{mf} D_{AB} u_o}{d_b^3}\right)^{1/2}$$

    We have shown that one can make the approximation
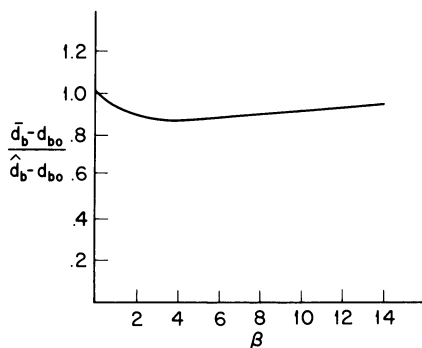
$$u_b \cong u_{br}$$

Figure 3.   Ratio of the average bubble diameter to the bubble diameter evaluated at h/2 as a function of the aspect ratio, $\beta = .3h/D$
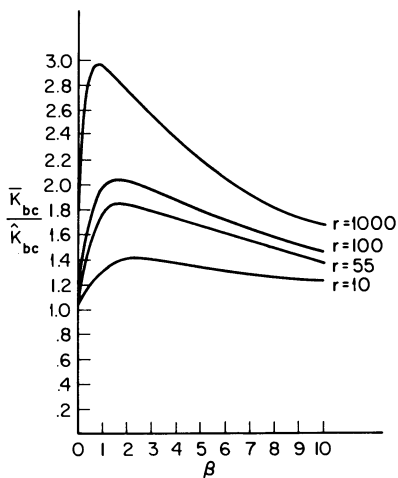

Figure 4.   Ratio of the average bubble-cloud transport coefficient to the transport coefficient evaluated at h/2 as a function of the aspect ratio for various ratios the maximum to minimum bubble diameter, r

consequently

$$u_b \cong d_b^{1/2}$$

then

$$K_{ce} = A_3 \left[\frac{d_b^{1/2}}{d_b^3} \right]^{1/2} = A_3 \frac{1}{d_b^{5/4}} \qquad (59)$$

$$K_{ce} = \frac{A_3}{d_b^{1/4}} \left(\frac{1}{d_b} \right) \qquad (60)$$

Since the 1/4 power is a relatively weak functional dependence, we will consider the term

$$A_4 = \frac{A_3}{d_b^{1/4}} \qquad (61)$$

to be a constant, in which case the averaging technique for

$$K_{ce} = \frac{A_4}{d_b} \qquad (62)$$

gives the same result as obtained for K_{bc}, i.e.

$$\frac{\overline{K}_{ce}}{\hat{K}_{ce}} = \left[1 + 1/\beta \ln[r - (r-1)e^{-\beta}] \right] [1 - (1-1/r)e^{-\beta/2}] \qquad (63)$$

for the ammonia oxidation, r = 55 and

$$\beta = \frac{(.3)(63.2)}{(11.4)} = 1.66$$

then

$$\frac{\overline{K}_{ce}}{\hat{K}_{ce}} = 2.1$$

The average transport coefficients, K_{bc} and K_{ce} are twice the coefficient used in the L-K model when evaluated at h/2. The corresponding values of K_r and conversion are

$$K_r = 2.33$$

$$X = 0.204$$

Owing to the fact that the ammonia oxidation is mostly reaction limited, the correction factor for using the averaging technique is slight. However, in cases of rapid reaction, the two techniques $\hat{K}_{bc}$ will give significantly different results.

Summary

In this paper we have shown that the Kunii-Levenspiel model can be used to accurately predict the results of Massimilla and Johnstone. In addition, we have used the K-L model to predict the changes in conversion with parameter variation under the limiting conditions of reaction control and transport control. Finally, we have shown that significant differences in the averaging techniques occur for height to diameter ratios in the range of 2 to 20.

A	cross-sectional area of column, cm^2
	collection of terms in Eq. (12), cm/s
C	concentration, $gmoles/cm^3$
d	diameter, cm
D	diameter of column or bed, cm
	molecular diffusivity, cm^2/s
g	gravitational constant, cm/s^2
h	height of expanded bed, cm
k	reaction rate constant, s^{-1}
K	overall dimensionless reaction rate constant
	exchange coefficient between phases, s^{-1}
L	distance up the bed from distributor plate, cm
r	reaction rate, $gmoles/(cm^3)$ (s)
Re	Reynolds number, dimensionless
u	axial velocity, cm/s
	superficial axial velocity, cm/s
W	mass of catalyst, g
x	dimensionless distance from distributor plate, L/h
X	fractional conversion, dimensionless

Greek

α	volume of wake per volume of bubble, dimensionless
β	dimensionless collection of terms in Eq. (44), 0.3h/D
γ	volume of catalyst in a particular phase per volume of bubble, dimensionless
δ	fraction of total bed in bubble phase (not including wakes), dimensionless
ε	void fraction of bed, dimensionless

η group of terms, $g(\rho_p - \rho_g)$, $g/(cm^2)(s^2)$
μ viscosity of gas, poise
ρ density, g/cm^3
ψ sphericity of particle, dimensionless

Subscripts
A   of substance A
AB   of substance A through substance B
b   of bubbles or of bubble phase
bc   between bubble phase and cloud phase
bm   of bubbles at the maximum point
bo   of bubbles at the distributor plate
br   of a bubble in isolation from other bubbles
c   of the cloud phase
cat   of the catalyst
ce   between cloud phase and emulsion phase
e   of emulsion phase
g   of gas
mf   at minimum fluidization conditions
o   at distributor plate
p   of solid particle
R   referring to reaction rate
s   referring to slugging conditions

Superscripts
^   evaluated at midpoint in column
–   average value

Literature Cited
 1. Broadhurst, T. E.; Becker, H. A. AIChE J. 1975, 21, 238-247.
 2. Bukur, D. B.; Wittman, C. V.; Amundson, N. R. Chem. Eng. Sci.
     1974, 29, 1173-1192.
 3. Chavarie, C.; Grace, J. R. Ind. Eng. Chem. Fundam. 1975, 14,
     79-86.
 4. Drew, T. B.; Dunkle, H. H.; Genereaux, R. P. in "Chemical
     Engineers' Handbook," 3rd ed. (J. H. Perry, Ed.), McGraw-
     Hill, New York, 1950, p. 394.
 5. Fryer, C.; Potter, O. E. Powder Technol. 1972, 6, 317-322.
 6. Grace, J. F. AIChE Symp. Ser. 1974, 70, No. 141, 21-6.
 7. Kunii, D.; Levenspiel, O. "Fluidization Engineering," Wiley,
     New York, 1969.
 8. Leva, M. "Fluidization," McGraw-Hill, New York, 1959, p. 21.
 9. Massimilla, L.; Johnstone, H. F. Chem. Eng. Sci. 1961, 16,
     105-112.
10. Mori, S.; Wen, C. Y. "Estimation of Bubble Diameter in
     Gaseous Fluidized Beds," AIChE J. 1975, 21, 190-115.
11. Orcutt, J. C.; Davidson, J. F.; Pigford, R. L. Chem. Eng.
     Progr. Symp. Ser. 1962, 58, No. 38, 1-15.
12. Potter, O. E. Catal. Rev.-Sci. Eng. 1978, 17, 155-202.

13. Reid, R. C.; Prausnitz, J. M.; Sherwood, T. K. "The Proper-
     ties of Gases and Liquids," 3rd ed. McGraw-Hill, New York,
     19 77.
14. Weimer, A. W. M.S. Thesis, University of Colorado, Boulder,
     CO, 1978.
15. Yates, J. G. Chem. Eng. (London) 1975, 671-677.
16. Zenz, F. A.; Othmer, D. F. "Fluidization and Fluid-Particle
     Systems," Reinhold, New York, 1960, pp. 231, 234.
17. van Swaaij, W. P. M. in "Chemical Reaction Engineering
     Reviews-Houston" (D. Luss and V. W. Weekman, Eds.), ACS
     Symposium Series #72, American Chemical Society, Washington,
     DC, 1979, pp. 193-222.

Simulation of a Fluidized Bed Reactor for the Production of Maleic Anhydride

J. L. JAFFRÈS, W. IAN PATTERSON, C. CHAVARIE, and C. LAGUÉRIE[1]

Ecole Polytechnique, Montréal, Canada

The simulation of a fluidized bed preheater-fluidized bed reactor system for the catalytic oxidation of benzene to maleic anhydride was attempted. The experimental apparatus and results of Kizer et al (7) together with the kinetics proposed by Quach et al (8) formed the basis for the simulation. It was determined that the rate constants and activation energies would not successfully describe the experimental results, and these parameters were estimated using a portion of the results. The rate constants and activation energies found in this manner were close to those reported by other workers for similar catalysts. The simulation using these estimated parameters gave reasonable agreement with the complete experimental results for conversion and selectivity as functions of temperature, air flow rate and bed height, except for selectivity versus bed height. An unsteady-state simulation agreed qualitatively with the limited data available.

The production of maleic anhydride by the catalytic oxidation of benzene is an established industrial process. While C_4 hydrocarbons are often suggested as a feedstock, it has been pointed out recently by De Maio (1) that they are an alternative but not necessarily a substitute. The benzene oxidation is done commercially in fixed bed reactors and, because of its exothermicity, is difficult to control in any optimal sense. The process is thus a natural candidate for a fluidized-bed reactor. The reaction has been studied in both fixed bed (2, 3) and fluidized bed (4-7) reactors. These studies, with the exception of that of Kizer et al (7) do not give sufficient information for simulation purposes. The availability of the reaction data of Kizer et al and the kinetic studies of Quach et al (8) using a similar catalyst suggested the possibility of simulating the process.

[1] Institut du génie chimique, Toulouse, France

Reaction Kinetics

   The key to good reactor simulation is undoubtedly a knowled-
ge of the reaction kinetics. The kinetics of the catalytic oxi-
dation of benzene to maleic anhydride has been studied for diffe-
rent catalysts and conditions by many workers (8-13) however
only Quach et al (8) examined a catalyst, FX203, of a type simi-
liar to that employed by Kizer et al (FB203-S). Both catalysts
are fabricated by Halcon Catalyst Industries, but are of different
formulation.
   Quach et al studied the catalyst (in the form of 0.4 cm gra-
nules) in a Carberry-type reactor. Reaction conditions were: a
temperature range of 280°C to 430°C and a benzene to air feed
ratio variation of 0.45 to 8.23 mol percent. Their results dic-
tated a two-step oxidation of the form:

$$C_6H_6 + 4O_2 \rightarrow C_4H_2O_3 + CO + CO_2 + 2H_2O \qquad\qquad (1)$$
$$C_4H_2O_3 + 2O_2 \rightarrow 2CO + 2CO_2 + H_2O$$
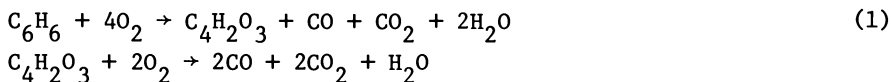
Both reactions are exothermic and essentially irreversible. The
maleic anhydride formation occurs only at the catalyst surface
while its degradation takes place in the gas phase (8). It is
therefore expected that the selectivity and the conversion will be
equally important in the operation of fluidized bed reactor.
Quach et al found that the benzene conversion rate was best des-
cribed by the Langmuir-Hinshelwood relation:

$$r_B = \frac{k_B k_O p_B p_O^{1/2}}{k_O p_O^{1/2} + 4 k_B p_B} \quad ; \quad \begin{array}{l} k_B = 5.01 \exp(-24600/RT) \\[4pt] k_O = 3490 \exp(-64300/RT) \end{array} \qquad (3)$$

where: r_B = reaction rate in gmol $\cdot$ g^{-1} $\cdot$ h^{-1}

The form of equation (3) indicates that oxygen dissociation occurs
before its adsorption on the catalyst. When the reaction has a
large excess of air ($\frac{benzene}{air} \approx 1$ mol %) equation (3) can be re-
written as:

$$r_B = \frac{k_B p_B}{1 + 4\dfrac{k_B p_B}{k_O p_O^{1/2}}} = k_B' \, p_B \qquad\qquad (4)$$

and first order kinetic behaviour will be observed.
   The gas phase degradation of the maleic anhydride is descri-
bed by:

$$r_M = k_M p_M^{1/2} \quad ; \quad k_M = 90000 \exp(-33400/RT) \qquad (5)$$

where r_M = reaction rate in gmol $\cdot$ m^{-3} $\cdot$ h^{-1}

Pilot Reactor

The reactor used by Kizer and simulated in this work is illustrated in Figure 1. It consists of a fluidized bed preheater section feeding directly the fluidized bed reactor section. Each section was a 0.4 m high cylinder of 0.184 m diameter. The preheater contained sand and was heated by an external electrical element. The FB203S catalyst is a powder of 0.173 mm diameter particles (weight average) and has a minimum fluidization velocity, U_{mf}, of 0.021 m · s^{-1} at normal temperature and pressure. The reactor was cooled by ambient air blown through a jacket. The reactor distributor was made from a 50 mm thick fixed bed of 5 mm diameter pebbles supported on a perforated plate with the benzene introduced at its centre. Nickel particles (0.53 mm diameter) to a depth of 25 mm on top of a second perforated plate formed a second fixed bed and completed the distributor. The reactor was completely insulated with glass wool.

Experimental Results

The effects of the reaction temperature, T, the air flow rate F_a (reported at 20°C and 1 atm), the depth of the catalyst bed, H_{mf}, and the molar concentration of benzene, c, on the conversion, selectivity and production were reported by Kizer et al (14). The experiments were performed according to a factorial plan of 2^4 experiments within the following limits:

$430°C \leqslant T \leqslant 490°C$

$4 \leqslant F_a \leqslant 8$ m^3 · h^{-1}

$3 \leqslant H_{mf} \leqslant 7$ cm

$0.5 \leqslant c \leqslant 1.5$ mol percent, $\dfrac{C_6H_6}{air}$

The results for conversion, selectivity and production were expressed as:

$$Y_c = 74.79 + 0.29(T - 460) - 10.52(c - 1) - 3.91(F_a - 6) + 3.83(H_{mf} - 5) \tag{6}$$

$$Y_s = 51.34 - 0.22(T - 460) - 3.48(F_a - 6) - 3.76 (H_{mf} - 5) \tag{7}$$

$$Y_p = 38.11 - 6.40(c - 1) \tag{8}$$

Reactor Model

The fluidized bed characteristics of high solids heat capacity, large interfacial heat transfer area, and good solids mixing allow the assumptions of thermal equilibrium between the solids and the gas, uniform bed temperature and negligible heat capacitance of the gas. An additional assumption required to use equation (9) is that the reactions do not change the gas volume.
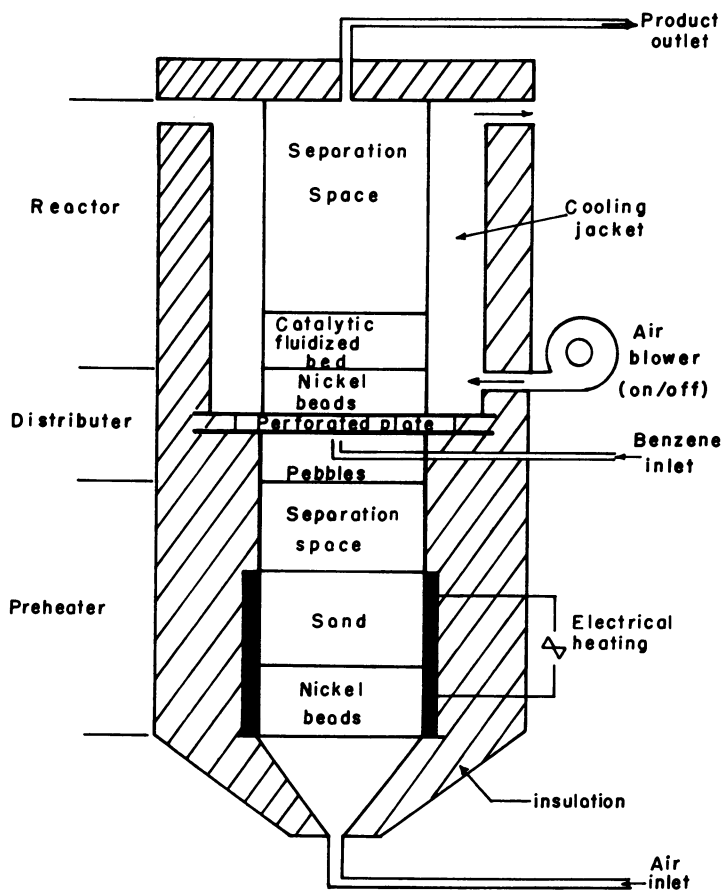The reactor and preheater each divide naturally into three types of thermal zone. These are:

Figure 1. Experimental apparatus: preheater–reactor system

1) the fluidized beds of sand (preheater) or catalyst (reactor),
2) the fixed distributor beds and
3) the separation space above the fluidized beds.

Some of these zones have been divided into isothermal regions. This is shown in Figure 2 which shows that the preheater consists simply of the above three zones whereas the reactor distributor and separation space have been represented by three and five regions respectively. The reactor was cooled by forced air from a fan controlled in an on-off manner. Heat transfer to the cooling air was modelled as either forced or natural convection depending on whether the fan was on or off.

The reactor was simulated for both steady and transient behaviour. The steady-state model is straightforward and will not be discussed in detail. The unsteady-steady state simulation took advantage of the fact that the rate of reaction is much faster than the thermal response rate. The concentration transient response can thus be modelled as pseudo-steady state in the actual fluidized bed; this pseudo-steady state then follows the slowly changing temperature profile. A mass balance on the species, j, for each region (see Figure 2) is written as:

$$-(\frac{\partial c_i}{\partial t}) V_R = 0 = \sum_i V_R \nu_{ij} r_{ij} + Fc_{i,in} - Fc_i \qquad (9)$$

where: i refers to the reacting species
j refers to the product species.

Reaction Considerations

The reaction kinetics suggest the separation of the reactor into the fluidized-bed and separation space zones. The conversion of benzene to maleic anhydride and the degradation of the maleic anhydride both occur within the fluidized bed. Only the degradation reaction takes place in the space above the bed which has been divided into five regions, each of which is treated as a perfectly mixed, homogeneous gas-phase reactor.

It has been shown by Chavarie and Grace (15) that the decomposition of ozone in a fluidized-bed is best described by Kunii and Levenspiel's model (16) but that the Orcutt and Davidson models (17) gave the next best approximation for the overall behaviour and are easier to use and were chosen for the simulation. They suppose a uniform bubble size distribution with mass transfer accomplished by percolation and diffusion. The difference between the two models is the presumption of the type of gas flow in the emulsion phase: piston flow, PF, for one model and a perfectly mixed, PM, emulsion phase for the other model. The two models give the following expressions at the surface of the fluidized bed for first-order reaction mechanism:
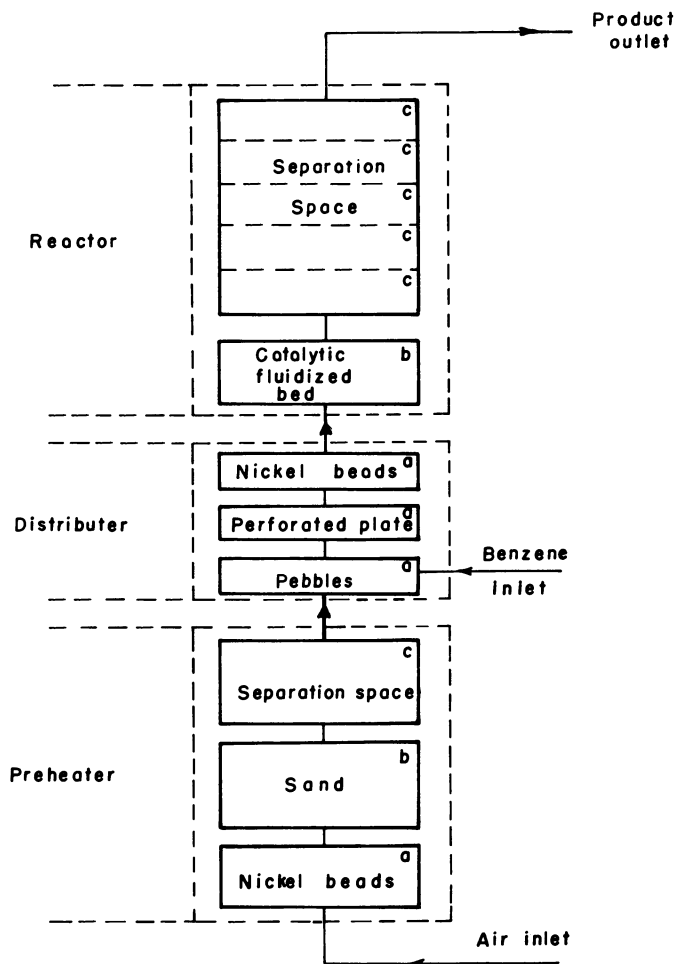
Figure 2.   Physical model of the preheater–reactor system. Isothermal regions are indicated as: a, fixed beds; b, fluidized beds; c, gaseous regions.

PM: $\quad Y_c = 1 - \left[\beta e^{-X} + \dfrac{(1 - \beta e^{-X})^2}{1 + K' - \beta e^{-X}} \right]$ (10)

PF: $\quad Y_c = 1 - \left[\dfrac{1}{m_2 - m_1} \; (m_2 e^{-m_1 H}(1 - \dfrac{m_1 H U_{mf}}{XU}) - m_1 e^{-m_2 H}(1 - \dfrac{m_2 H U_{mf}}{XU}) \right]$

(11)

where m_1 and m_2 are the roots of:

$(1 - \beta) \, m^2 H^2 - (X + K') \, mH + XK' = 0$ (12)

Kinetics other than first-order require the numerical integration of the differential mass balances and the conversions cannot be expressed in simple equations.

The fluidized bed reactor model requires a description of the bubble diameter, D_b. The relationship of Mori and Wen (18) was chosen using the D_{bo} of a porous plate distributer:

$$\frac{D_{bm} - D_b}{D_{bm} - D_{bo}} = \exp \left(\frac{-0.3H}{D_R} \right)$$ (13)

Equation (13) was checked using the expression of Yacono (19) which was obtained from a distributor configuration similar to that employed by Kizer. Values from the two relationships were compared at bed mid-height, H/2, for typical reaction conditions and differed by 3%.

Reactor Simulation: Thermal Aspects

The energy balances on the different zones and regions of the preheater-reactor system yield the following types of terms:
I. heat introduced by convection from the zone $(\alpha - 1)$ to the zone α, ΔQ_c;

$\Delta Q_c = F_\alpha \rho_\alpha \left[\sum_i \tilde{H}_{i\alpha} c_{i\alpha} \right] - F_{(\alpha-1)} \rho_{(\alpha-1)} \left[\sum_i \tilde{H}_{i(\alpha-1)} c_{i(\alpha-1)} \right]$

II. heat lost to the surroundings, ΔQ_ℓ;

$\Delta Q_\ell = ha\Delta T$

III. heat introduced by the chemical reactions of species i producing j, ΔQ_R;

$\Delta Q_R = \sum_i \nu_{ij} r_{ij} \Delta H_{ij} V_R$

IV. accumulation;

$\dfrac{\partial Q}{\partial t} = \dfrac{\partial}{\partial t} \left[(W_s C_s + V_R \sum_i C_i c_i) T_\alpha \right]$

which comprise the thermal balance:

$$-\frac{\partial Q}{\partial t} = \Delta Q_c + \Delta Q_\ell + \Delta Q_R \tag{14}$$

The simplifying assumption that the properties of the reaction mixture are those of air is justified by the maximum benzene concentration of 1.5 mol percent. It has also been assumed that the gas volume is unchanged by the reactions. Heat transfer to the walls from the distributer was evaluated by Froment's expression for fixed beds [20]:

$$\frac{hD_R}{\lambda_f} = 0.813 \left[\frac{D_p G}{\mu_f}\right]^{0.9} \exp(-6D_p/D_R) \tag{15}$$

while that of Wen and Leva was used for the fluidized bed [21]:

$$\frac{hD_p}{\lambda_f} = 0.16 \left[\frac{C_f \mu_f}{\lambda_f}\right]^{0.4} \left[\frac{D_p \rho_f U}{\mu_f}\right]^{0.76} \left[\frac{\rho_p C_p}{\rho_f C_f}\right]^{0.4} \left[\frac{U^2}{gD_p}\right]^{-0.2} \left[\frac{\eta}{\xi}\right]^{0.36} \tag{16}$$

The relationship of Pohlhausen was used for the heat transfer in the separation space [22]:

$$Nu = \frac{RePrD_R}{4H_S} \ln \left[1 - \frac{1}{Pr^{0.167}\left[\dfrac{RePrD_R}{H_S}\right]^{0.5}} \right] \tag{17}$$

The relationship of Mac Adams was used to estimate the heat transfer due to natural convection [23]:

$$h = 1.42 \left[\frac{\Delta T}{H_R}\right]^{0.25} \tag{18}$$

Activating the cooling blower causes air to enter the jacket tangentially to the wall of the reactor and is assumed to follow a helical path to the exit. The heat transfer coefficient was calculated from Perry [24]:

$$h = h_{av} \left[1 + 3.5 \frac{D_{in}}{D_m}\right] \tag{19}$$

The thermal simulation was verified by choosing a benzene concentration of zero (no reaction) and natural convection cooling only. An ambient temperature of 20°C was assumed and, to minimise calculation time, the accumulation terms in the separation regions were neglected. For a 1.2 kW power input, the model predicted a steady-state catalyst temperature of 473°C which was reached about seven hours after heating was begun. A temperature loss of 42°C between the pebble benzene mixer and the catalyst was predicted while the difference between the catalyst and the fluidized bed preheater was 57°C. This loss was attributed to the increased

heat transfer through the flanges used to attach the preheater
to the reactor. The simulation results agreed to within 10%
with the observed behaviour of the apparatus and are presented in
Figure 3.

Reactor Simulation: Steady State

The results of the thermal simulation were sufficiently en-
couraging for us to proceed to the reactor simulation for a number
of steady-state operating conditions, but neglecting the maleic
anhydride degradation in the fluidized bed. Both the simplified
kinetic expression (equation (4)) and the more exact equation (3)
were used and the results are shown in Table I as Case 1 and
Case 2 respectively.

TABLE I
PREDICTED CONVERSIONS: ORCUTT-DAVIDSON PM MODEL

T (^{o}C)	X	βe^{-X}	Conversion given by Kizer's model	Case 1		Case 2	
				K'	Y_c	K'	Y_c
430	2.10	0.113	66%	0.364	27%	0.327	25%
460	1.91	0.138	76%	0.432	30%	0.398	29%
490	1.73	0.165	83%	0.506	33%	0.475	32%

Operating conditions: c = 1%, H_{mf} = 5 cm, F_a = 6 m^3h^{-1},

D_{bo} = 0.9 cm

It is obvious that the simulation predicts conversions for
below those obtained by Kizer and this cannot be due solely to
the neglect of the maleic anhydride degradation. There may be
several possible causes for the low predicted values: the Orcutt-
Davidson PM model may not be sufficiently accurate or the bubble
size estimate may be incorrect. Alternatively, neither equation
(3) nor (4) correctly describe the reactor kinetics. The number
of possibilities may be reduced by considering Figure 4 which
plots conversion versus the non-dimensional reaction rate cons-
tant, K', with βe^{-X} as a parameter. Two possible zones of opera-
tion are shown in the figure, zones A and B. Zone A is bounded
by the Orcutt-Davidson PF model and the values of βe^{-X} from Table
1 together with Quach's kinetics allowing for a 10% error in the
kinetic parameters. Zone B is delineated by the PF model, the
maximum value of βe^{-X} from Table 1 and the values of conversion
obtained by Kizer. Evidently an increase in K' is required to
allow the two regions to overlap and furthermore, for the range of
βe^{-X} reported in Table 1, both kinetics and bed hydrodynamics
(bubble diameter) play a significant role in determining reactor
conversion.

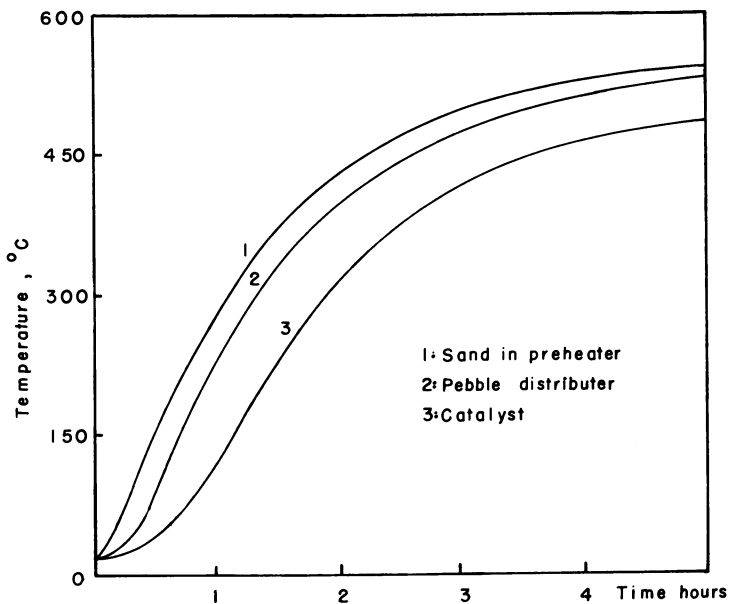It was at this point that the simulation, per se, was

Figure 3.   Thermal unsteady response of the apparatus during reactor start-up:
1, sand in preheater; 2, pebble distributer; 3, catalyst
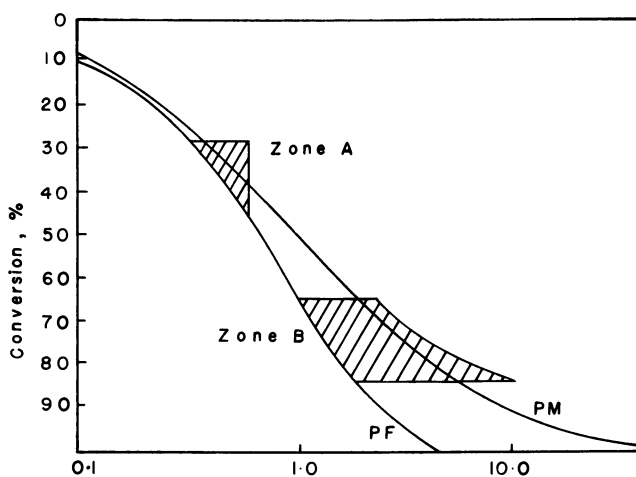

Figure 4.   Conversion vs. nondimensional reaction rate constant, K'.   The two
limiting cases of one phase (Orcutt–Davidson) PM and PF models are the solid
lines.   Zone A is the limit of operation allowing for a 10% error in the kinetic
parameters of Quach et al.   Zone B is the experimental limit of operation.

abandoned. The previously cited results of other workers gave evidence that the form of the kinetic expression of Quach et al was probably adequate to simulate Kizer's reactor. Thus, we undertook to force the conversions obtained from the "simulation" to coincide with those obtained experimentally by Kizer for a number of operating conditions. The Marquardt (25) algorithm was chosen for this non-linear least-squares minimization problem in which the rate constants, activation energies and initial bubble diameter were the variables manipulated to obtain the minimal deviations for three combinations of reactor regime and kinetic expressions (cases A, B and C) as shown in Table II. It is seen that, for a given set of kinetic parameters the value of D_{bo} is almost independent of the gas flow rate and the assumption of first-order kinetics (equation (4)) gives a conversion that is independent of the benzene concentration in the feed. This latter feature significantly reduced the computation time and was retained for the selectivity and transient behaviour calculations. This was justified by the agreement of the conversions over the range of operating conditions.

The simulation could now be advanced to include the maleic anhydride degradation. This gas phase reaction takes place only in the bubble phase, the interstitial gas and the separation space. The interstitial gas and the bubbles account for about 15% of the total free volume of the reactor and therefore cannot be neglected. Moreover the degradation kinetics depend on a fractional power of the maleic anhydride concentration (equation (5)); hence the fluidized bed cannot be integrated analytically to yield a simple relationship. However, it has been shown by Grace (26) that for a fast reaction the major part of conversion occurs in the first few millimeters close to the distributer. The maleic anhydride concentration in the bed is thus very nearly constant and can be estimated from the conversion since the degradation reaction is relatively slow. This permits the fluidized bed to be modelled as a bipartite reactor as shown in Figure 5, and avoids the computer-time consuming subdivision of the bed into regions.

Despite this simplistic treatment the simulation has become quite complex and yielded selectivity and production values that differed significantly from those obtained by Kizer. Again, it was apparent that the kinetic parameters for equation (5) needed adjustment to reconcile the differences. This was done by a simple trial and error method.

Discussion and Conclusions: Kinetics

It was possible to determine a set of kinetic relations which gave the best possible simulation of the reported results. These relations are:

TABLE II
RESULTS OF OPTIMIZATION OF MODEL PARAMETERS

Kizer's data Y_c, %	75	66	83	83	67	67	82	80	69	Optimized parameters
Operating conditions c(mol %)	1*	1	1	1	1	1	1	0.5	1.5	
H_{mf}	5	5	5	5	5	3	7	5	5	
F_a(m³h⁻¹)	6	6	6	8	4	6	6	6	6	
T(°C)	460	430	490	460	460	460	460	460	460	
Case A Orcutt-Davidson PM Eq. 4 Y_c	75	66	82	68	82	65	80	75	75	f_B =37500 E_B =66800 D_{bo}=0.043
D_b(cm)	1.22	1.18	1.25	0.93	1.49	0.82	1.59	1.22	1.22	
Case B Orcutt-Davidson PF Eq. 4 Y_c	75	67	80	87	65	65	80	75	75	f_B =10260 E_B =60000 D_{bo}=0.420
D_b(cm)	1.53	1.49	1.56	1.25	1.79	1.13	1.89	1.53	1.53	
Case C Orcutt-Davidson PF Eq. 3 Y_c	75	66	80	87	65	62	81	77	72	f_B =11900 E_B =58100 f_O =2900 E_O =65900 D_{bo}=0.643
D_b(cm)	1.71	1.68	1.75	1.44	1.97	1.32	2.08	1.71	1.71	

Kinetics: Eq. 3 $r_B = \dfrac{k_B k_O P_B P_O}{k_O P_O^{1/2} + 4k_B P_B}^{1/2}$; $k_B = f_B\, e^{-E_B/RT}$ $k_O = f_O\, e^{-E_O/RT}$

Eq. 4 $r_B = k'_B P_B$

* These conditions are the central point of the factorial plan and are counted four times for the purposes of optimization.
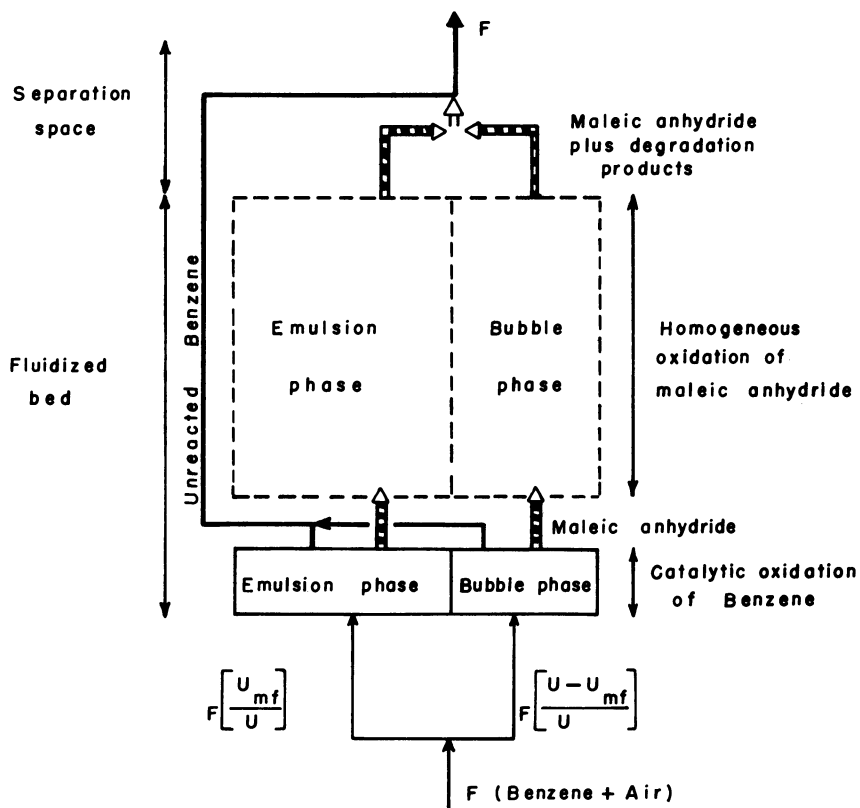
Figure 5. Model of the fluidized bed. Benzene flow is shown by the heavy solid line and maleic anhydride is represented by the heavy dashed line.

$$r_B = \frac{k_B k_O p_B p_O^{1/2}}{k_O p_O^{1/2} + 4 k_B p_B} \quad , \quad \text{where } \begin{array}{l} k_B = 11900 \ e^{-58100/RT} \\ k_O = 2900 \ e^{-65900/RT} \end{array} \tag{20}$$

for the catalytic oxidation, and

$$r_M = k_M p_M^{1/2}, \text{ where } k_M = 237000 \ e^{-30000/RT} \tag{21}$$

Implicit in these equations are the successive oxidations of benzene and maleic anhydride. The direct oxidation of benzene to water and carbon oxides is not permitted.

The optimization results reported in table II indicate that the activation energies are almost independent of the model chosen to represent the fluidized bed reactor. Furthermore, the activation energy obtained in this manner agree with those reported by Holsen, Steger and Germain et al while those given by Quach are much smaller. The data are summarized in table III below. Moreover, it is known from the catalyst fabricator that fixed bed reactors having an inlet benzene concentration of 1.5% and a residence time of 0.72 s. give conversions on the order of 93 to 95%. The kinetics required for this result coincide with the kinetics obtained from the numerical experimentation. Finally, we note that the energy of activation for the homogeneous decomposition of maleic anhydride obtained from the optimization is in good agreement with the work of Quach et al.

<center>TABLE III
COMPARISON OF ACTIVATION ENERGIES</center>

Worker	Catalyst	Temperature range $^\circ C$	Activation energy kJ/mole
Holsen	V_2O_5/Al_2O_3	325–450	81–82
Steger	Ag_2O, V_2O_5, MoO_3, Al_2O_3/SiC	450–530	63
Germain et al	V_2O_5/MoO_3	380–500	92–42
Quach et al	V_2O_5/SiO_2	280–430	24
Our numerical optimization	V_2O_5/SiO_2	430–490	60–67

Discussion and Conclusion: Fluidized Bed Model

The optimized values given in table II include the values of the mean bubble diameter. These values are consistently smaller than those calculated from the Mori and Wen equation. For example, at the central point of the factorial plan, a value of $D_b = 2.1$ cm is predicted by Mori and Wen's equation while the "optimized"

values for D_b vary between 1.22 and 1.71 cm depending on the simulation case.

This discrepancy is not entirely unexpected since the bubble diameters identified from the fluidized bed models are apparent or effective values intimately linked to the mass transfer mechanism of the model. The smaller bubble size values obtained by our procedure may simply mean that the actual mass transfer is larger than that suggested by the Orcutt-Davidson models. This is compatible with the fast reaction assumption that implies a disproportionately high conversion close to the distributer and a much higher mass transfer rate in this zone. Calculations of conversion and selectivity have good general agreement with Kizer's results as shown in Figure 6. An exception is the selectivity-bed height relationship. Our calculations show selectivity to be insensitive to bed height, but Kizer found a strong inverse relation between selectivity and H_{mf}. Kizer explains this by proposing a direct oxidation of benzene to water and carbon oxides which is in competition with the oxidation to maleic anhydride. We note that the heterogeneous depletion of maleic anhydride may also explain the above behaviour.

Kizer et al (14) claimed that the combined effects of bed height and flow rate could be replaced by the residence time. This implies that simple fixed bed models could be used to adequately describe this reactor. Table II and Figure 4 shows that this could be the case for the Orcutt-Davidson PM model, however the model demands the unrealistic value of $D_{bo} = 0.043$ cm (case A). The PF model requires operation away from the limiting conversions and is thus in conflict with Kizer's claim, although more realistic values of D_{bo} are estimated. It seems probable that the reactor operation is somewhere between that of a single-phase perfectly mixed reactor and plug flow in the same reactor. It is precisely in this region that both bed hydrodynamics and kinetics are important. Thus, it is not useful to further analyse our results without possessing independant knowledge of the hydrodynamic or kinetic parameters.

A number of points have become apparent as a result of our efforts to simulate the fluidized-bed reactor-preheater system studied by Kizer. Two of the most important are: it is imperative to have good kinetic data for the reaction(s) that occur. It has been demonstrated that the interpretation of the results is profoundly affected by relatively small changes in the kinetics. The second important point is the recognition that there are regions of operation where both the reaction kinetics and the bed hydrodynamics influence the overall performance of the reactor. The coupling of kinetic and hydrodynamic effects is strong such that both must be known to properly describe the reactor behaviour.

We note that this model is not suited to process control purposes. The computational resources and time required are simply too great to allow real-time control algorithms to use this
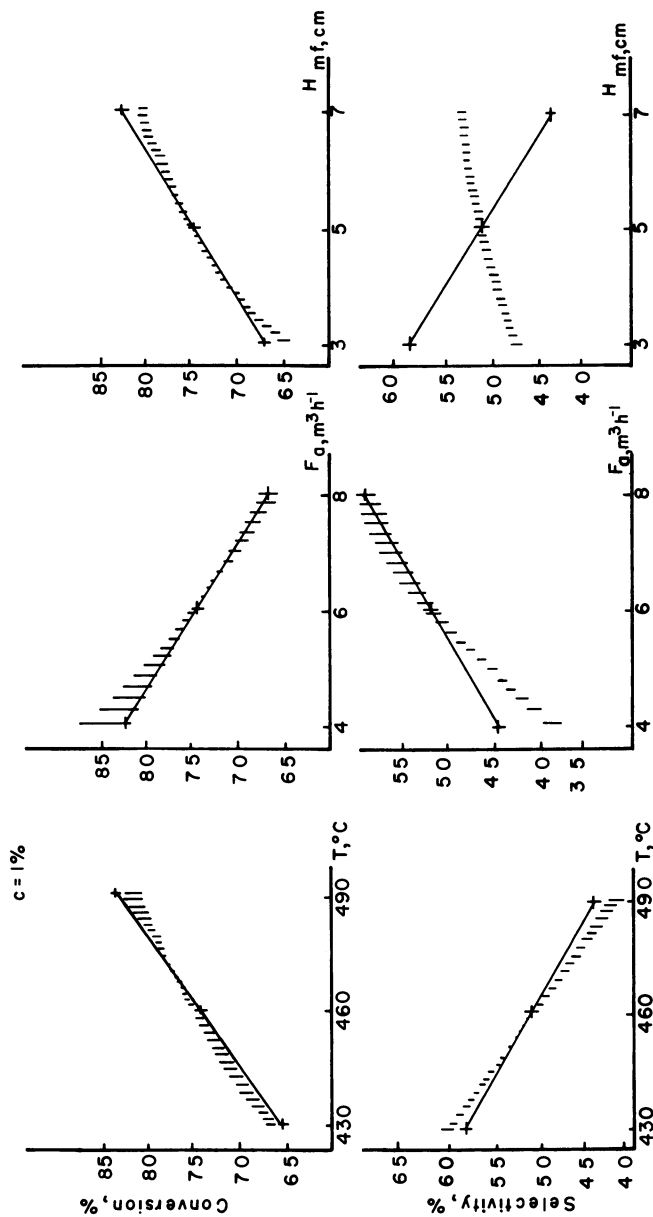
Figure 6. *Conversion and selectivity vs. catalyst temperature, air flowrate, and bed height. The results of Kizer et al. are the solid lines and our calculations are shown as the hatched area. Operating conditions are:* $F_a = 6 m^3 h^{-1}$, $H_{mf} = 5$ cm, T = 460°C, *benzene concentration, c = 1 mol percent except when the variable appears on the abscissa.*

model in spite of the many simplifying assumptions made to reduce
the computer load.

Legend of Symbols

A	– cross-sectional area of reactor, m^2
a	– heat-transfer area, m^2
C	– specific heat, $cal \cdot g^{-1}$
c	– concentration, mol percent
D	– diameter, m
E	– activation energy, $J \cdot mol^{-1}$
F, f	– volumetric flow rate, $m^3 \cdot h^{-1}$
G	– mass flow rate, $g \cdot h^{-1}$
h	– heat transfer coefficient, $cal \cdot m^{-2} \cdot s^{-1} \cdot {}^oC^{-1}$
$\tilde{H}$	– enthalpy, $cal \cdot g^{-1}$
H	– height, m
ΔH	– heat of reaction, $cal \cdot mol^{-1}$
K'	$= (k_B' RTW_s)/(AU)$, dimensionless reaction rate
k, k'	– reaction rate constant, sec^{-1}
Pr	– Prandtl number, dimensionless
p	– (partial) pressure, $N \cdot m^{-2}$
Q	– heat, cal
Re	– Reynolds' number, dimensionless
R	– gas constant
r	– reaction rate, $mol \cdot h^{-1}$
T	– temperature, ^oC
U	– velocity, $m \cdot sec^{-1}$
V	– volume, m^3
w	– mass, g
X	$= (xH)/(U_b V_b)$, number of transfer units, equations (10) and (11)
x	– overall rate of exchange between bubble and dense phase
Y_c, Y_p, Y_s	– reactor conversion, production and selectivity
β	$= 1 - (U_{mf}/U)$, equations (10) and (11), dimensionless
η	– parameter of equation (16)
λ	– thermal conductivity, $cal \cdot sec^{-1} \cdot m^{-1} \cdot {}^oC^{-1}$
μ	– viscosity, $Pa \cdot sec^{-1}$
ν	– stoichiometric coefficient, dimensionless
ξ	– parameter of equation (16)
ρ	– density, $g \cdot cm^{-3}$

Subscripts

a	– air (at NTP; 20^oC and 1 atm)
B	– benzene
b, bo, bm	– bubble, initial, mean
c	– convection
f	– fluid
in	– inlet

i, j	– summation indices
ℓ	– lost
M	– maleic anhydride
m	– mean
mf	– minimal fluidization
p	– particle
R	– reactor, reaction
S	– separation
s	– solid

Acknowledgements

The authors gratefully acknowledge the research grants provided by the Province of Quebec (FCAC), the Natural Sciences and Engineering Research Council of Canada and the Institut du génie chimique de Toulouse.

Literature Cited

1. De Maio, D.A., "Will Butane Replace Benzene as a Feedstock for Maleic Anhydride", Chem. Eng., 1980, May 19, p. 104.
2. Germain, J.E., Graschka, F., Mayeux, A., "Cinétique de l'oxydation catalytique du benzène sur oxydes de vanadium-molybdène", Bull. Soc. Chim. Fr., 1965, p. 1445.
3. Vaidyanathan, K., Doraiswamy, L.K., "Controlling Mechanism in Benzene Oxidation", Chem. Eng. Sci., 1968, 23, 537.
4. Badarinarayana, M.C., Ibrahim, S.M., Kuloor, N.R., "Single Step Catalytic Vapor Phase Oxidation of Benzene", Ind. J. Techn., 1967, 5, 314.
5. Kullavinajaya, P., "Statistical Study of the Benzene Oxidation Process in a Fluidized Bed Reaction", Ph.D. thesis, Ohio State University, Columbus, 1966.
6. Ahmad, S.I., Ibrahim, S.M., Kuloor, N.R., "Kinetic Studies on the Oxidation of Maleic Anhydride", Ind. J. Techn., 1971, 9, 251.
7. Kizer, O., Laguérie, C., Angelino, H., "Experimental Study of the Catalytic Oxidation of Benzene to Maleic Anhydride in a Fluidized Bed", Chem. Eng. Journal, 1977, 14, 205.
8. Quach, T.Q.P., Rouleau, D., Chavarie, C., Laguérie, C., "Catalytic Oxidation of Benzene to Maleic Anhydride in a Continuous Stirred Tank Reactor", Can. J. Chem. Eng., 1978, 56, 72.
9. Hammar, C.G.B., "Reaction Kinetics of the Catalytic Vapor-Phase Oxidation of Benzene to Maleic Anhydride", Svensk. Kem. Tid., 1952, 64, 165.
10. Holsen, J.N., "An Investigation of the Catalytic Vapor Phase Oxidation of Benzene", Ph.D. thesis, Washington University, St.Louis, Missouri, 1954.

11. Ioffe, I.I., Lyubarski, A.G., "Kinetics of Catalytic Oxidation of Benzene to Maleic Anhydride", Kin. i Kat., 1963, 3, 261.
12. Dmuchovsky, B., Freerks, M.C., Pierron, E.D., Munch, R.H., Zienty, F.B., "Catalytic Oxidation of Benzene to Maleic Anhydride", J. Catalysis, 1965, 4, 291.
13. Steger published in Catalysis, edited by P.H. Emmet, Reinhold, New York, 7, Chap. 3, 1960, pp. 186-194.
14. Kizer, O., Chavarie, C., Laguérie, C., Cassimatis, D., "Quadratic Model of the Behaviour of a Fluidized Bed Reactor: Catalytic Oxidation of Benzene to Maleic Anhydride", Can. J. Chem. Eng., 1978, 56, 716.
15. Chavarie, C., Grace, J.R., "Performance Analysis of a Fluidized Bed Reactor", IEC Fund., 1975, 14, 75, 79, 86.
16. Kunii, D., Levenspiel, O., "Bubbling Bed Model for Kinetic Processes in Fluidized Bed-Gas-Solid Mass and Heat Transfer and Catalytic Reactions", IEC Proc. Des. Dev., 1968, 7, 481.
17. Orcutt, J.C., Davidson, J.F., Pigford, R.L., "Reaction Time Distributions in Fluidized Catalytic Reactors", Chem. Eng. Progr. Symp. Ser., 1962, 58, 1.
18. Mori, S., Wen, C.Y., "Estimation of Bubble Diameter in Gaseous Fluidized-Beds", AIChE Journal, 1975, 11, 109.
19. Yacono, C., Angelino, H., "The Influence of Gas Distributor on Bubble Behaviour; Comparison between Ball Distributor and Porous Distributor", published in Fluidization, Cambridge University, Cambridge, 1978, p. 25.
20. Froment, G.F., "Fixed-Bed Catalytic Reactors - Current Design Status", Ind. Eng. Chem., 1967, 59, 18.
21. Wen, C.Y., Leva, M., "Fluidized-Bed Heat Transfer - a Generalized Dense Phase Correlation", AIChE Journal, 1956, 2, 482.
22. Pohlhaussen, K. published in Principles of Heat Transfer, 3rd ed. Intext Press, New York, 1976, p. 442.
23. Mac Adams, W.H., Heat Transmission 2nd ed. MacGraw Hill Book Company, New York, 1942, p. 241.
24. Perry, R.M., Chilton, C.H., Chemical Engineers Handbook, 5th ed., 1973, p. 10-15.
25. Marquardt, D.W., "An Algorithm for Least Squares Estimation of Non-Linear Parameters", Journ. Soc. Ind. Appl. Math., 1963, 11, 431.
26. Grace, J.R., De Lasa, H.I., "Reaction near the Grid in Fluidized Beds", AIChE Journal, 1978, 24, 364.

A Model for a Gas–Solid Fluidized Bed Filter

MICHAEL H. PETERS, THOMAS L. SWEENEY, and LIANG-SHIH FAN

Department of Chemical Engineering, The Ohio State University, Columbus, OH 43210

A general mathematical model for simulating parti-
culate removal in gas-solid fluidized beds is pre-
sented. Model predictions of the fluidized bed fil-
tration efficiencies, which include the possibility
of electrical effects, are shown to compare well to
the experimental results of various investigators.
Because of the general formulation of the proposed
model it is believed to be applicable in the design
of both single and multistage fluidized bed filters.

Fluidized beds have been employed in many industrial process-
es such as coal combustion, gasification and liquefaction, solid
residue pyrolysis, catalytic cracking and reforming, and polymer
production. In addition, the possibility of using fluidized beds
for fine particulate removal has recieved growing attention over
recent years (1 - 12). Typically, the fluidized bed is of the gas-
solid type and the particulates may be liquid or solid aerosols.
Note that in this application the bed medium solids function as
the collecting medium and particle removal is accomplished through
particle-collector contacting.
    Our approach to the problem of predicting the performance of
fluidized bed filters involves logically coupling models that de-
scribe the flow behavior of the fluidized state with models that
describe the mechanisms of particle collection. The collection
mechanisms analysis leads to expressions for determining the col-
lection efficiency of a single filter element. An example of a
collection mechanism is inertial impaction by which a particle de-
viates from the gas stream lines, due to its mass, and strikes a
collector. It should be noted that because particle collection
mechanisms are functions of the fluid flow behavior in the vicin-
ity of a collector, there exists an interdependency between fluid-
ization mechanics and particle collection mechanisms.
    In a previous paper, the importance of fluidization mechanics
on the performance of fluidized bed filters was demonstrated (13).
To accomplish this, classical methods were employed for evaluating

the single spherical collector efficiencies. In the present paper our analysis is extended by considering more realistic methods for estimating particle removal efficiencies for a single collector element.

Model Background

The model presented here for quantitatively describing the mechanics of the fluidization process is a simplified version of a more complex scheme recently proposed by Peters et al (14), and is largely based on bubble assemblage concepts (15). In brief, the bubble assemblage concept considers an aggregative fluidized bed to be divided axially into a number of compartments. Each compartment consists of a bubble, cloud, and emulsion phase. The size of each compartment, which varies throughout the fluidized bed, is based on the cloud diameter computed at a given bed height. The key features of the present analysis lie in the reduction in independencies among the relationships as well as elimination of major two phase theory assumptions (14).

Model

Figure 1 shows the present model representation of the gas-solid fluidized bed. Making a steady-state material balance on particulates over the nth compartment results in the equation

$$\bar{U}_{is} S (C_{i_{n-1}} - C_{i_n}) + F_{i(i+1)_n} V_{1_n} (C_{i+1_n} - C_{i_n})$$

$$+ F_{(i-1)i_n} V_{1_n} (C_{i-1_n} - C_{i_n}) = \eta_{i_n} C_{i_n} \bar{U}_{is} \frac{3(1-\varepsilon_i) V_{i_n}}{2D_c} \tag{1}$$

Where, $i = 1$ for the bubble phase, $i = 2$ for the cloud phase, and $i = 3$ for the emulsion phase. Note from the term on the right-hand side of Eqn. (1) that a first order rate equation for particulate collection is assumed (10). The inlet gas corresponds to the zeroth compartment, thus,

$$C_{1_o} = C_o$$

$$C_{2_o} = C_o \tag{2}$$
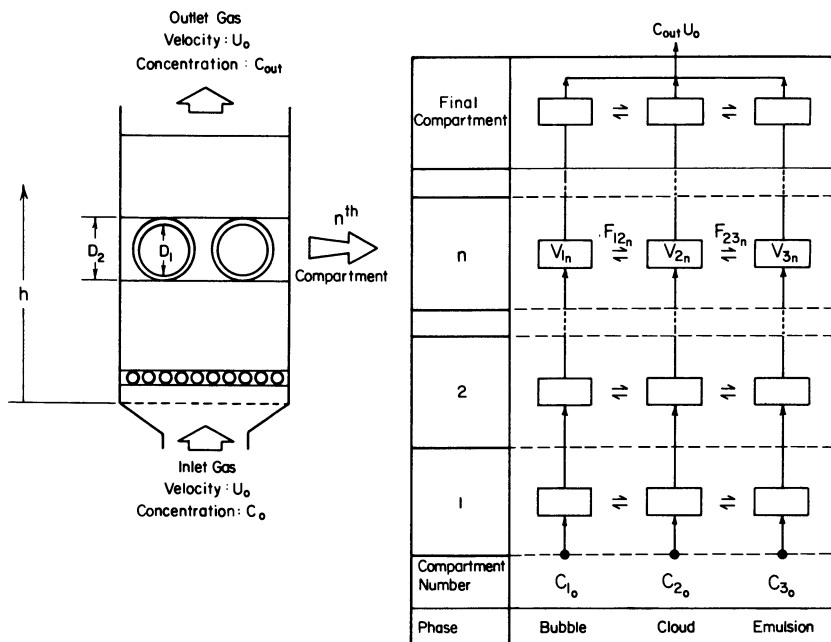
$$C_{3_o} = C_o$$

Figure 1. Schematic of the present model

Estimation of the Parameters of the Model

As presented below, the parameters in the model may be estimated in terms of a relatively small number of fundamental parameters that characterize either the bubbling phenomenon, mass conservation, or particulate collection mechanisms. For those parameters not based on average properties the subscript n has been omitted for clarity in many cases.

A.   Superficial gas velocity, U_o. The superficial gas velocity can be expressed as

$$U_o = \overline{U}_{1s} + \overline{U}_{2s} + \overline{U}_{3s} \tag{3}$$

where $\overline{U}_{1s}$, $\overline{U}_{2s}$, and $\overline{U}_{3s}$ are based on average properties in the fluidized bed.

B.   Superficial gas velocity in the bubble phase, $\overline{U}_{1s}$. The superficial gas velocity in the bubble phase is related to the average linear bubble phase gas velocity and the average bubble phase volume fraction by

$$\overline{U}_{1s} = \overline{U}_1 \, \overline{\delta}_1 \, \varepsilon_1 \tag{4}$$

where $\overline{U}_1$ and $\overline{\delta}_1$ are computed from the relationships given in sections E. and M., respectively. Note that Eqn. (4) represents the so-called visible bubble flow rate.

C.   Superficial gas velocity in the cloud phase, $\overline{U}_{2s}$. Since a bubble and its associated cloud rise together at the same linear velocity, the superficial gas velocity in the cloud phase is given by

$$\overline{U}_{2s} = \frac{\overline{\delta}_2}{\overline{\delta}_1} \frac{\varepsilon_2}{\varepsilon_1} \overline{U}_{1s} \tag{5}$$

where $\overline{\delta}_2/\overline{\delta}_1$ is given in section F.

D.   Superficial gas velocity in the emulsion phase, $\overline{U}_{3s}$. Substituting Eqns. (4) and (5) into Eqn. (3) gives the superficial gas velocity in the emulsion phase, as

$$\overline{U}_{3s} = U_o - \overline{U}_1 \, (\overline{\delta}_1 \varepsilon_1 + \overline{\delta}_2 \varepsilon_2) \tag{6}$$

subject to the stipulation that

$$U_o > \overline{U}_1 \, (\overline{\delta}_1 \varepsilon_1 + \overline{\delta}_2 \varepsilon_2) \tag{7}$$

E.   Linear gas velocity in the bubble phase, U_1. The linear gas velocity in the bubble phase may be computed from the commonly accepted relationship proposed by Davidson and Harrison (16).

$$U_1 = (U_o - U_{mf}) + 0.71 \sqrt{GD_1} \tag{8}$$

The average linear gas velocity in the bubble phase may be expressed as

$$\overline{U}_1 = (U_o - U_{mf}) + 0.71 \sqrt{G\overline{D}_1} \tag{9}$$

F.   Volume ratio of cloud to bubble phases, δ_2/δ_1. The volume ratio of the cloud phase to the bubble phase may be estimated from the model of Murray (17)

$$\frac{\delta_2}{\delta_1} = \frac{U_{mf}}{\varepsilon_{mf} U_1 - U_{mf}} \tag{10}$$

and the average volume ratio may be expressed as

$$\frac{\overline{\delta_2}}{\overline{\delta_1}} = \frac{U_{mf}}{\varepsilon_{mf} \overline{U}_1 - U_{mf}} \tag{11}$$

G.   Bubble Diameter, D_1. A recent correlation by Mori and Wen (18), which considers the effects of bed diameters and distributor types, is utilized. This correlation, based on the bubble diameter data appearing in the literature prior to 1974 is

$$\frac{D_{1_m} - D_1}{D_{1_m} - D_{1_o}} = \exp\,(-0.3h/D_R) \tag{12}$$

where

$$D_{1_m} = 0.652 \left[S\,(U_o - U_{mf}) \right]^{2/5} \tag{13}$$

and

$$D_{1_o} = 0.347 \left[\frac{S\,(U_o - U_{mf})}{N_D} \right]^{2/5} \tag{14}$$

(for perforated distributer plates)

$$D_{1_o} = 0.00376\,(U_o - U_{mf})^2 \tag{15}$$

(for porous distributor plates)

This correlation is valid over the following variable ranges:

$$0.5 < U_{mf} < 20 \qquad , \text{cm/s}$$

$$0.006 < D_c < 0.045 \qquad , \text{cm}$$

$$U_o - U_{mf} < 48 \qquad , \text{cm/s}$$

$$D_R < 130 \qquad , \text{cm}$$

H.   Gas interchange coefficients. Gas interchange coefficients given here are based on the Murray model (12). The analysis parallels the two step transfer mechanism proposed by Kunii and Levenspiel (19) which is based on the Davidson model (16). Assuming an average bubble throughflow (20) and neglecting the film diffusional contribution between bubble and cloud phases, which is usually small compared to the bulk flow term, the gas interchange coefficients can be expressed as

$$F_{12} = 1.5 \left(\frac{U_{mf}}{D_1}\right) \tag{16}$$

and

$$F_{23} = 6.78 \left(\frac{D_G \, \epsilon_{mf} \, U_1}{D_1^3}\right)^{1/2} \tag{17}$$

Note that these expressions have been previously given from an overall standpoint by Chavarie and Grace (21).
I.   Expanded Bed Height. The height of bed expansion can be approximated as (14)

$$L = L_{mf} + \frac{Y L (U_o - U_{mf})}{U_o - U_{mf} + 0.71 \sqrt{G \overline{D}_1}} \tag{18}$$

where

$$\overline{D}_1 = D_{1_m} - (D_{1_m} - D_{1_o}) \exp\left(-0.15 \, L_{mf}/D_R\right), \tag{19}$$

and

$$Y = 0.76$$

J.   Volume Fraction Gas in Each Phase. The volume fraction of gas in the cloud and emulsion phases is assumed to be equal to that at

minimum fluidization throughout the entire bed:

$$\varepsilon_2 = \varepsilon_3 = \varepsilon_{mf} \tag{21}$$

The model assumes a value of 1.0 for the volume fraction of gas in the bubble phase.

K.   Cloud diameter, D_2. The diameter of the cloud may be easily obtained by rearranging Eqn. (10) to give

$$\left(\frac{D_2}{D_1}\right)^3 = \frac{\varepsilon_{mf} U_1}{\varepsilon_{mf} U_1 - U_{mf}} \tag{22a}$$

as well as the average cloud diameter as

$$\left(\frac{\overline{D}_2}{\overline{D}_1}\right)^3 = \frac{\varepsilon_{mf} \overline{U}_1}{\varepsilon_{mf} \overline{U}_1 - U_{mf}} \tag{22b}$$

L.   Number of Bubbles in a Compartment, N. With compartment height based on the diameter of the cloud, the number of bubbles can be computed from material balance considerations as well as some assumptions concerning the average solids volume fraction in the bed (14)

$$N = \frac{6 S D_{2_n} (\varepsilon - \varepsilon_{mf})}{\pi D_{1_n}^3 (1 - \varepsilon_{mf})} \tag{23}$$

where

$$1 - \varepsilon = \frac{L_{mf}}{L} (1 - \varepsilon_{mf}) \tag{24}$$

for $h \leq L_{mf}$

and

$$1 - \varepsilon = \frac{L_{mf}}{L} (1 - \varepsilon_{mf}) \left\{ \exp \left[-\left(\frac{h - L_{mf}}{L - L_{mf}}\right) \right] \right\} \tag{25}$$

for $L_{mf} \leq h$

M.   Volume fraction of each phase, δ_i. The volume fraction of the bubble, cloud and emulsion phases may be computed as

$$\delta_{i_n} = V_{i_n} / SD_{2_n} \tag{26}$$

where i = 1 for the bubble phase, i = 2 for the cloud phase, i = 3 for the emulsion phase, and

$$V_{1_n} = N (1/6) \pi D_{1_n}^3 \tag{27}$$

$$V_{2_n} = V_{1_n} \left[\frac{U_{mf}}{\varepsilon_{mf} U_1 - U_{mf}} \right] \tag{28}$$

$$V_{3_n} = SD_{2_n} - V_{2_n} - V_{1_n} \tag{29}$$

Note that,

$$\overline{\delta}_1 = \overline{V}_1 / S\overline{D}_2 \tag{30}$$

and

$$\overline{V}_1 = \overline{N} (1/6) \pi \overline{D}_1^3 \tag{31}$$

where $\overline{N}$ is evaluated at $h = L_{mf}/2$ and $\overline{D}_1$ is given by Eqn. (19).
N. Single Spherical Collector Efficiencies. Four collection mechanisms are considered in the present analysis: inertial impaction, interception, Brownian movement and Coulombic forces. Although in our previous analysis the electrical forces were considered to be of the induced nature (13), there is evidence that it is the Coulombic forces which dominate the electrical interactions between the particle and collector (7, 12, 22). Taking the net effect as the simple summation of each collection mechanism results in the single spherical collector efficiency equation,

$$\eta_i = \eta_{IMP} + \eta_{INT} + \eta_{BD} + \eta_E \tag{32}$$

where

$$\eta_{IMP} = -0.19133 + 1.7168 \, Stk - 1.2665 \, Stk^2$$

$$+ 0.31860 \, Stk^3 \tag{33}$$

for $\varepsilon_i \cong 0.4$ and $Stk_c \cong 0.12$

$$\eta_{INT} = 1.5 \left(\frac{1.31}{\epsilon_i}\right)^3 N_R^2 \tag{34}$$

$$\eta_{BD} = 4 \left(\frac{1.31}{\epsilon_i}\right) Pe^{-2/3} \tag{35}$$

$$\eta_E = 4.4 K_c^{0.87} \tag{36}$$

for $\epsilon_i \tilde{=} 0.4$

The particle diffusion coefficient is calculated from the Stokes-Einstein equation (24)

$$D_G = \frac{KT}{6 \pi \mu r_p} \left\{ 1 + \frac{\lambda}{r_p} \left[1.257 + 0.4 \exp{(-1.10 \, r_p/\lambda)} \right] \right\} \tag{37}$$

Equations (33) – (35) are taken from Tardos et al (23), and are based on a low Reynold's number analysis. Eqn. (33) is the result of a "best-fit" of the theoretically computed values taken from Figure 7 of that same work. Similarly, Eqn. (36) for the electrical deposition, is obtained from a "best-fit" of the theoretically computed values taken from Figure 3 of Tardos and Pfeffer (21). Note that if the particle and collector charges are of the same sign, the electrical deposition efficiency becomes the negative of Eqn. (36). Consistent with the flow field models used in the development of Eqns. (33) – (36), the velocity employed is an assembly averaged velocity for each phase. For the multi-phase situation that exists in the fluidized bed, this is given by the superficial or empty-tower velocity divided by the phase volume fraction,

$$\hat{U}_i = \frac{\overline{U}_{is}}{\delta_i} \tag{38}$$

Note from Eqn. (38) that since the volume fraction of each phase varies throughout the bed, so will the assembly average velocities and hence, the single collector efficiencies.
0.   Volumetric average particulate concentration at the exit of the bed, C_{out}, and the overall collection efficiency, X.
     The volumetric average particulate concentration at the exit of the bed is expressed by

$$C_{out} = C_1 \frac{\overline{U}_{1s}}{U_o} + C_2 \frac{\overline{U}_{2s}}{U_o} + C_3 \frac{\overline{U}_{3s}}{U_o}, \tag{39}$$

and the overall collection efficiency, in percent, is defined as

$$X = 100 \left(\frac{C_o - C_{out}}{C_o} \right) \qquad (40)$$

At ratios of superficial to minimum fluidization velocities great-er than three to five, local flow reversal of gas in the emulsion phase can occur (14). In the present analysis the divisions of gas flow among the phases are based on average values, and thus are taken to be constant throughout the fluidized bed. Equation (7) states that only an average upward flow of gas in the emulsion phase is considered here. It is assumed that the equations de-scribing the flow of gas in a fluidized bed are also applicable to the flow of particulates, and that the particulates contacting a collector adhere to it and are not re-entrained by the gas flow. Relative changes in particle velocities due to the motion of the collectors in the fluidized bed are neglected.

Method of Solution

Calculations of the overall collection efficiency for the fluidized bed filter begin with specification of the values of the superficial gas velocity, U_O, minimum fluidization velocity, U_{mf}, bed height at minimum fluidization, L_{mf}, void fraction at minimum fluidization, ε_{mf}, column diameter, D_R, gas viscosity, μ, collec-tor diameter, D_c, density of particulate, ρ_p, and particulate di-ameter, D_p. There are no adjustable parameters in the present mo-del. The charge acquired on both the particulates and collectors, Q_p and Q_{AC}, respectively, remain as experimentally determined in-put parameters in the present analysis.

Because bubble diameter is a function of the height from the distributor, and the height from the distributor is taken to the center of the bubble in question, an iterative procedure is used to determine D_1. The initial guess is taken to be the bubble dia-meter computed for the previous compartment. For each compartment there are three material balance equations with three unknowns, the concentrations in each phase (bubble, cloud and emulsion). The total number of equations then is three times the total number of compartments. These may be solved by a matrix reduction scheme or a trial and error procedure. The average superficial gas veloci-ties in each phase are first determined from Eqns. (4) – (6). The computational sequence for the remaining parameters in Eqn. (1) is given in Table 1.

It is assumed here that the size of the last compartment is determined from the difference between the cummulative compart-ments size and the height of the expanded bed. However, for con-sistency, gas interchange coefficients and the linear bubble phase gas velocity are based on a hypothetical bubble diameter predicted from Eqn. (12). The computational scheme also takes into consid-eration the possibility of only two phases in any compartment. This can result from both cloudless and cloud overlap compartments,

Table I.   Computational sequence for parametric evaluation at the nth compartment.

Sequence	Eqn. Number	Calculated Parameter
1	12	D_1
2	8	U_1
3	10	δ_2/δ_1
4	22a	D_2
5	24, 25	ϵ
6	23	N
7	27, 28, 29	V_1, V_2, V_3
8	26	δ_i
9	16, 17	F_{12}, F_{23}
10	38	$\hat{U}_2, \hat{U}_3$
11	32	n_i

typically occuring for larger minimum fluidization velocities. Figure 2 shows a typical situation that can occur along with the appropriate simplified equations. Gas interchange in a two phase compartment is taken to be solely Eqn. (16), based on the so-called invisible bubble flow rate. The unsteady-state diffusional contribution, Eqn. (17), is neglected.

Results and Discussion

     The potency of the present model lies in predicting the performance of fluidized bed filters over a relatively wide range of operating conditions. Our previously reported sensitivity studies and comparisons with experimental results (13) are extended here.

     Comparisons with the Experimental Results of Tardos et al (12).

     Figure 3 shows a comparison of the model prediction of the overall collection efficiency as a function of superficial gas velocity versus the experimental data of Tardos et al (12). Since the charge acquired on the collectors was not reported, assumed values shown in Figure 3 were employed. It should be noted that this assumed functional dependency between Q_{AC} and U_0 was not entirely arbitrary, but qualitatively suggested by experimental measurements of the electric potential in the fluidized bed (12). An important aspect of Figure 3 is both the model prediction and experimental
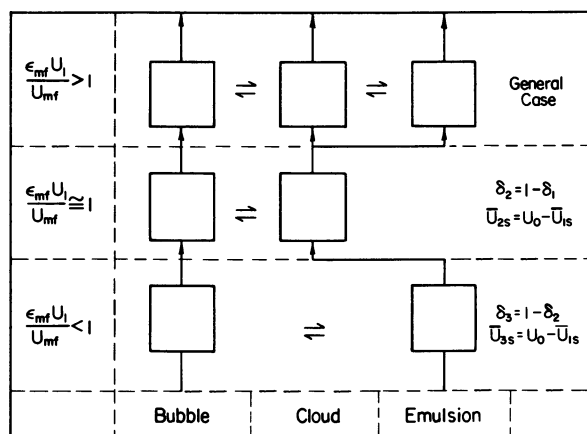
Figure 2.   Compartments representation of cloudless and cloud overlap compartments
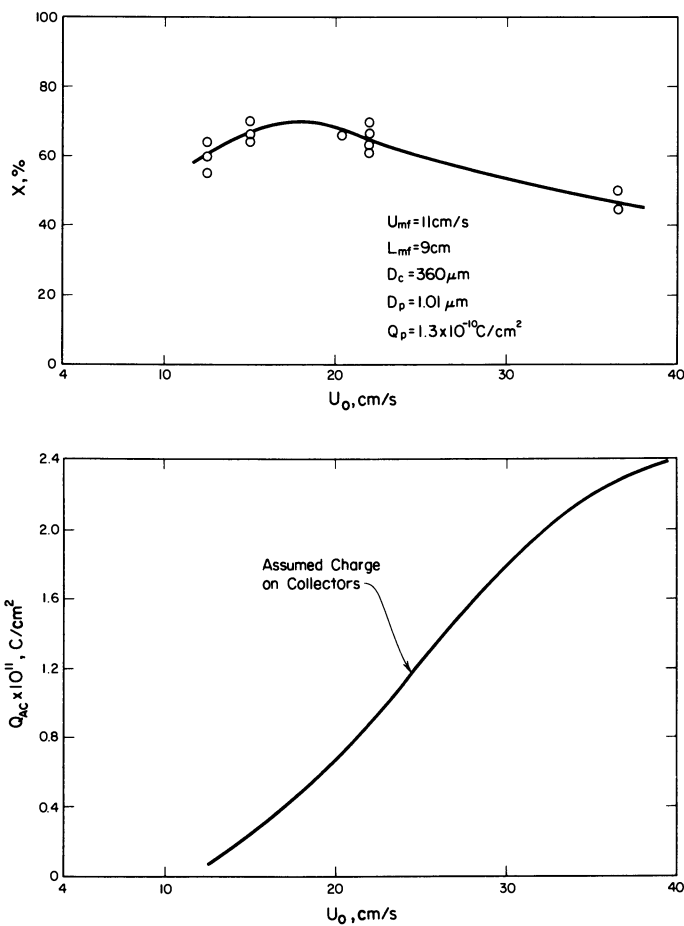
Figure 3. Comparison of (———) model prediction and (○) experimental data (12) for the overall collection efficiency as a function of superficial gas velocity: $D_p = 1.01 \ \mu m$

observation of a maximum in the overall collection efficiency as a
function of superficial gas velocity. Model analysis shows that
this is due to the competing effects of electrostatic collection
and gas by-passing. In Figure 4, the same charge distribution as-
sumed in Figure 3 is employed for comparisons at a slightly larger
particle diameter. Model analysis indicates that the higher effi-
ciencies observed in Figure 4 over Figure 3 are due solely to the
higher predicted interception efficiencies. Increases in the sin-
gle collector efficiencies due to increases in the specific charge
density outweigh gas by-passing effects up to a superficial gas
velocity of about 18 cm/s in Figures 3 and 4.

Comparisons with the Experimental Results of Gutfinger and Tardos (11).

In addition to the effects of superficial gas velocity on the
overall collection efficiency, the direct effects of particle dia-
meter are also of importance. Figure 5 shows the present model
predictions of the overall collection efficiency as a function of
particle diameter compared to the experimental data of Gutfinger
and Tardos (11). Since experimental care was taken to neutralize
electrical effects for this system, these were not included in the
model predictions. Thus, only three mechanisms were considered in
Figure 5, namely, inertial impaction, interception and Brownian mo-
tion. In Figure 5 reasonable agreement is seen at small particle
diameters (< 0.3 µm) where Brownian motion is predominant, and at
large particle diameters (> 3 µm) where interception effects are
controlling. In the vicinity of the minimum overall collection ef-
ficiency (~ 1 µm) the agreement is not as good. It is also in this
region that the predicted results are very sensitive to the values
of the single collector efficiencies. In Figure 5 the experiment-
al data would indicate higher single collector efficiencies in the
vicinity of the minimum than predicted by the equations employed
here.
    For completeness it should be noted that the minimum overall
collection efficiencies in Figures 3 and 4 occur for particle dia-
meters less than 0.5 µm. Thus, the particle diameters employed in
Figures 3 and 4 are sufficiently displaced from the minimum so that
the results are not considered fortuitous.

Comparisons with the Multistage Efficiencies of Patterson and Jackson (8).

For highly reactive systems in which the majority of particu-
late collection in the emulsion phase occurs in a relatively short
distance from the distributor plate, multistage fluidized beds
have been employed (8, 4). Because of the general formulation of
the present model, it may be employed for determining multistage
fluidized bed filtration efficiencies. This includes a variation
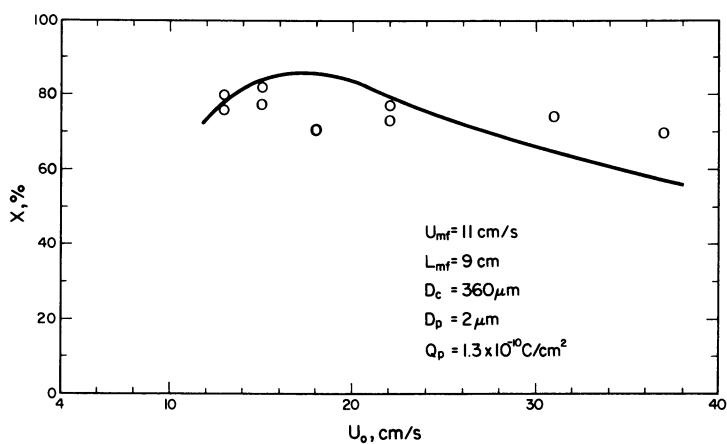in the characteristics of each stage such as bed depth and collector size.

Figure 4. Comparison of (———) model prediction and (○) experimental data (12) for the overall collection efficiency as a function of superficial gas velocity:
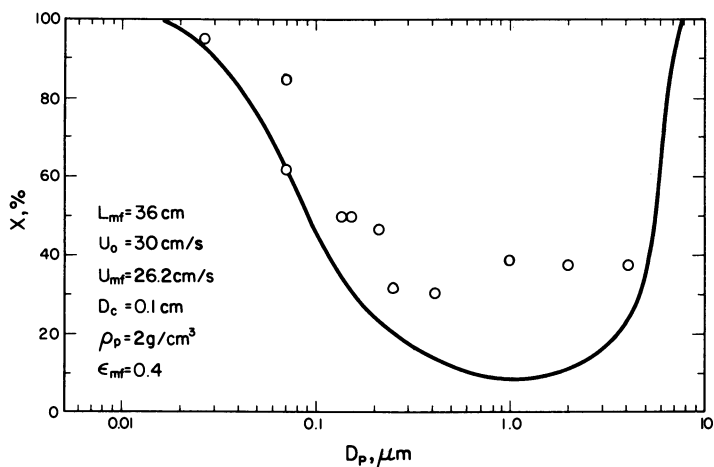$$D_p = 2 \ \mu m$$

Figure 5. Comparison of (———) model prediction and (○) experimental data (11) for the overall collection efficiency as a function of particle diameter
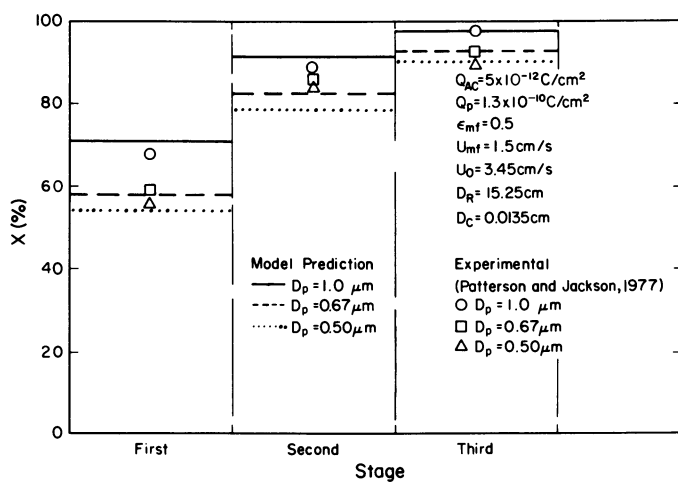
Figure 6.   Comparison of the predicted multistage efficiencies and the experimental results (8). Model prediction: (———) $D_p = 1.0$ μm; (– – –) $D_p = 0.67$ μm; (· · ·) $D_p = 0.50$ μm. Experimental: (○) $D_p = 1.0$ μm; (□) $D_p = 0.67$ μm; (△) $D_p = 0.50$ μm.

Under the simplifications that each stage has identical characteristics and that the particulates are of a single size, model predictions of the single stage efficiencies may be directly used to calculate multistage efficiencies by (8)

$$X_M = 100 \left[1 - (1 - \frac{X_1}{100})^M \right] \qquad (41)$$

In Fig. 6 the present model predictions of the multistage efficiencies calculated from Eqn. (41) are shown to compare closely to the experimental data of Patterson and Jackson (8). Because of the importance of electrical effects noted for this system, (12) the Coulombic force term in Eqn. (32) was included. Values of Q_P and Q_{AC} were arbitrarily set as shown in Figure 5. It should be noted that along with pressure drop information the present model may be used for optimizing the depths of each stage in a multistage fluidized bed filter.

Conclusion

In the present paper our previous analysis of fluidized bed filtration efficiencies has been extended by considering more realistic methods for estimating the single collector efficiencies as well as more recently reported experimental results. In general the predicted values of the fluidized bed filtration efficiencies compare favorably to the experimental values. For electrically active fluidized beds, direct measurements of the particle and collector charges would be necessary to substantiate the results given here.

The present model appears to be useful in the design of fluidized bed filters. It does not address questions concerning the quality of fluidization, stickiness of the particles, solids regeneration rates and agglomeration effects. In order to optimize the fluidized bed filter these effects must be considered in conjunction with those aspects to the problem elucidated here.

Legend of Symbols

C_{i_n} = concentration of particles in n^{th} compartment in phase i, g/cm^3

C_o = inlet particle concentration, g/cm^3

C_{out} = outlet particle concentration, g/cm^3

D_c = collector diameter, cm

D_G = molecular diffusion coefficient of particulate, cm^2/s

D_P = particulate diameter, cm

D_R = fluid bed diameter, cm

D_1 = equivalent spherical bubble diameter having the same volume as that of a bubble, cm

D_2 = equivalent spherical cloud diameter, cm

$\overline{D}_1$ = average equivalent spherical bubble diameter, cm

$\overline{D}_2$ = average equivalent spherical cloud diameter, cm

D_{1_o} = initial bubble diameter, cm

D_{1_m} = maximum bubble diameter, cm

F_{12} = gas interchange coefficient between phase 1 and phase 2 per unit volume of phase 1, 1/s

F_{23} = gas interchange coefficient between phase 2 and phase 3 per unit volume of phase 1, 1/s

G = gravitational acceleration, cm/s^2

h = height from distributor plate, cm

K = Boltzman's Constant, 1.38×10^{-16} erg/molecule ^oK

K_C = dimensionless characteristic particle mobility for Coulombic force,

$$\frac{D_P \, Q_{AC} \, Q_P}{3 \mu \, \hat{U}_i \, \varepsilon_f}$$

L = expanded bed height, cm

L_{mf} = bed height at U_{mf}, cm

N = number of bubbles in a compartment

$\overline{N}$ = average number of bubbles in a compartment

N_D = number of orifice openings on the distributor

Pe = Peclet number, $\hat{U}_i D_c/D_G$

N_R = dimensionless interception parameter, D_p/D_c

Q_{AC} = charge on collector, C/cm^2, $\Bigg\}$ assumed of opposite signs throughout this work

Q_P = charge on particle, C/cm^2

r_p = particle radius, cm

S = cross sectional area of bed, cm^2

Stk = Stoke's number

$$\frac{1}{9} \, \frac{D_p^2 \, \hat{U}_i \rho_p}{\mu D_c}$$

Stk_c = critical Stoke's number, below which there can be no collection by inertial impaction

$\hat{U}_i$ = assembly averaged velocity of gas in phase i, cm/s

$\overline{U}_1$ = average linear gas velocity in bubble phase, cm/s

$\overline{U}_{is}$ = average superficial velocity of gas in phase i, cm/s

U_{mf} = minimum fluidization velocity, cm/s

U_o = superficial gas velocity, cm/s

V_i = volume of phase i in n^{th} compartment, cm^3

$\overline{V}_1^n$ = average volume of bubble phase, cm^3

X = overall collection efficiency (%)

X_M = overall collection efficiency for M^{th} stage (%)

Greek Symbols

ε_i = void fraction of gas in phase i

ε_{mf} = void fraction in bed at U_{mf}

ε_f = permittivity of free space, 8.85×10^{-21} $c^2/dyne - cm^2$

δ_i = volume fraction of bed occupied by phase i

$\overline{\delta}_1$ = average bubble phase volume fraction

η_i = single spherical collector efficiency in phase i

η_{BD} = single spherical collector efficiency for Brownian motion

η_{IMP} = single spherical collector efficiency for impaction

η_{INT} = single spherical collector efficiency for interception

η_E = single spherical collector efficiency for Coulombic forces

ρ_p = particle density, g/cm^3

ρ = gas density, g/cm^3

μ = gas viscosity, g/cm-s

λ = mean free path of gas, $\sim 6.5 \times 10^{-6}$ cm for air at 20°C

Acknowledgements

Literature Cited

1. Knettig, P.; Beeckmans, J.M. Can. J. Chem. Eng. 1974, 52, 703.
2. Tardos, G.; Gutfinger, C.; Abuaf, N. Israel J. Tech. 1974, 12, 184.

3. McCarthy, D.; Yankel, A.J.; Patterson, R.G.; Jackson, M.L.
    Ind. Eng. Chem. Proc. Des. Dev. 1976, 15, 266.
4. Svrcek, W.Y.; Beeckmans, J.M. Tappi 1976, 59, 79.
5. Tardos, G.; Gutfinger, C.; Abuaf, N. AIChE J. 1976, 22, 1147.
6. Zahedi, K.; Melcher, J.R. J. Air Poll. Cont. Ass. 1976, 26,
    345.
7. Ciborows, J.; Zakowski, L. Int. Chem. Eng. I. 1977, 17, 529.
8. Patterson, R.G.; Jackson, M.L. AIChE Symp. Ser. No. 161
    1977.
9. Zahedi, K.; Melcher, J.R. Ind. Eng. Chem. Fund 1977, 16,
    248.
10. Doganoglu, Y.; Jog, V.; Thambimuthu, D.V.; Clift, R. Trans.
    Int. Chem. Eng. 1978, 56, 239.
11. Gutfinger, C.; Tardos, G.I. Atm. Env. 1979, 13, 853.
12. Tardos, G.; Gutfinger, C.; Pfeffer, R. Ind. Eng. Chem. Fun.
    1979, 18, 433.
13. Peters, M.H.; Fan, L.-S.; Sweeney, T.L. AIChE J. 1981, (in
    press).
14. Peters, M.H.; Fan, L.-S.; Sweeney, T.L. Reactant Dynamics in
    Catalytic Fluidized Bed Reactors with Flow Reversal of Gas in
    the Emulsion Phase, presented at 1980 AIChE Meeting, Chicago,
    Ill.
15. Kato, K.; Wen, C.Y. Chem. Eng. Sci. 1969, 24, 1351.
16. Davidson, J.F.; Harrison, D., "Fluidized Particles," 1963,
    Cambridge University Press.
17. Murray, J.D. J. Fluid Mech. 1965, 21, 465.
18. Mori, S.; Wen, C.Y. AIChE J. 1975, 21, 109.
19. Kunii, D.; Levenspiel, O. Ind. Eng. Chem. Fund. 1968, 7, 446.
20. Lockett, M.J.; Davidson, J.F.; Harrison, D. Chem. Eng. Sci.
    1967, 22, 1059.
21. Chavarie, C.; Grace, J.R. Chem. Eng. Sci. 1976, 31, 741.
22. Tardos, G.I.; Pfeffer, R. Proc. 2nd World Filt. Cong. Sept.
    18-20, 1979, London, U.K.
23. Tardos, G.I.; Yu, E.; Pfeffer, R.; Squires, M. J. Coll. Int.
    Sci. 1979, 71, 616.
24. Friedlander, S.K. J. Coll. Int. Sci. 1967, 23, 157.

Modeling and Simulation of Dynamic and Steady-State Characteristics of Shallow Fluidized Bed Combustors

L. T. FAN and C. C. CHANG

Department of Chemical Engineering, Kansas State University, Manhattan, KS 66506

The dynamic and steady-state characteristics of a
shallow fluidized bed combustor have been simulated
by using a dynamic model in which the lateral solids
and gas dispersion are taken into account. The
model is based on the two phase theory of fluidiza-
tion and takes into consideration the effects of
the coal particle size distribution, resistance due
to diffusion, and reaction. The results of the
simulation indicate that concentration gradients
exist in the bed; on the other hand, the tempera-
ture in the bed is quite uniform at any instant in
all the cases studied. The results of the simula-
tion also indicate that there exist a critical
bubble size and carbon feed rate above which
"concentration runaway" occurs, and the bed can
never reach the steady state.

Fluidized bed combustion is believed to be one of the most
promising methods for direct burning of coal in an environmentally
acceptable and economically competitive manner. Many mathematical
models have been proposed to predict the performance of fluidized
bed combustors (see, e.g., 1-7). A review of the models has been
presented by Carretto (8). Most of these models are steady-state
ones, and, furthermore, assume that concentration and temperature
variations do not exist in the lateral direction of the bed. How-
ever, it has been shown that there could be significant variation
in the carbon concentration across a large fluidized bed reactor
(9). Fan et al. (10) have proposed an isothermal dynamic model
for estimating the lateral carbon concentration distribution in a
shallow fluidized bed combustor. Simulation based on the model
has indicated that an appreciable carbon concentration gradient
can exist in the lateral direction in the bed. The objective of
this work is to improve the model by eliminating the assumption of
isothermal condition in the bed.

In the present work, the transient and steady-state character-
istics of a fluidized bed combustor are studied by solving numeri-
cally a dynamic model in which lateral solids and gas dispersion,
lateral temperature distribution and wide size distribution of
coal feed are taken into account. The influences of bubble size,
excess air rate, specific area of heat exchangers and coal feed
rate on the performance of the fluidized combustor are examined by
means of simulation with the model.

Mathematical Formulation

Let us consider a shallow fluidized bed combustor with mul-
tiple coal feeders which are used to reduce the lateral concentra-
tion gradient of coal (11). For simplicity, let us assume that
the bed can be divided into N similar cylinders of radius R_B, each
with a single feed point in the center. The assumption allows us
to use the symmetrical properties of a cylindrical coordinate sys-
tem and thus greatly reduce the difficulty of computation. The
model proposed is based on the two phase theory of fluidization.
Both diffusion and reaction resistances in combustion are consid-
ered, and the particle size distribution of coal is taken into
account also. The assumptions of the model are: (a) The bed con-
sists of two phases, namely, the bubble and emulsion phases. The
voidage of emulsion phase remains constant and is equal to that at
incipient fluidization, and the flow of gas through the bed in
excess of minimum fluidization passes through the bed in the form
of bubbles (12). (b) The emulsion phase is well mixed in the axial
direction, and the solids mixing can be described by the diffusion
equation in the lateral direction (9). The bed can be character-
ized by an effective bubble size, and the bubble flow is of the
plug type (10). (c) No elutriation occurs. (d) The convective
transport of coal particles in the lateral direction can be ne-
glected. (e) Ash is continuously withdrawn from the bed at the
same rate as that in the feed. (f) The only combustion reaction is

$$C + O \longrightarrow CO_2$$

(g) The solids and gas are at the same temperature. (h) The size
distribution of coal particles in the bed is the same as that in
the feed; the sizes of coal particles are widely distributed (1).
These assumptions give rise to the following equations:

Material balances in the emulsion phase

$$\frac{\partial [CP_b(R)]}{\partial t} = \Psi_F P_o(R) + \frac{1}{r}\frac{\partial}{\partial r}\left(rD_s \frac{\partial [CP_b(R)]}{\partial r}\right)$$

$$+ \frac{\partial [CP_b(R)S(R)]}{\partial R} - \frac{3CP_b(R)}{R}S(R) \qquad (1)$$

$$\frac{\partial C}{\partial t} = \Psi_F + \frac{1}{r}\frac{\partial}{\partial r}(rD_s\frac{\partial C}{\partial r}) - \int_0^{R_{max}}\frac{3S(R)}{R}CP_b(R)dR \qquad (2)$$

$$\varepsilon_{mf}\frac{\partial C_{ae}}{\partial t} = \frac{U_{mf}}{(1-\delta_b)L}(C_{ao} - C_{ae}) + \frac{1}{r}\frac{\partial}{\partial r}(rD_{ae}\frac{\partial C_{ae}}{\partial r})$$

$$+ \frac{\delta_b}{1-\delta_b}\frac{1}{L}\int_0^L K_{be}[C_{ab}(z) - C_{ae}]dz$$

$$- \int_0^{R_{max}}\frac{3S(R)}{RM_C}CP_b(R)dR \qquad (3)$$

Material balance in the bubble phase

$$\frac{\partial C_{ab}}{\partial t} = -U_b\frac{\partial C_{ab}}{\partial z} - K_{be}(C_{ab} - C_{ae}) \qquad (4)$$

Energy balance

$$\rho_m C_{pm}\frac{\partial T}{\partial t} = \frac{1}{r}\frac{\partial}{\partial r}(rk_e\frac{\partial T}{\partial r}) + \frac{U_g\rho_g C_{pg}}{L}(T_{go} - T) + \Psi_F(1-\delta_b)C_{ps}(T_{so}-T)$$

$$+ \{(1 - \delta_b)\int_0^{R_{max}}\frac{3S(R)}{R}CP_b(R)\ dR\}(-\Delta H)$$

$$- ha(T - T_w) + \Phi(t) \qquad (5)$$

where

$$\rho_m C_{pm} = \rho_g C_{pg}\delta_g + \rho_s C_{ps}(1 - \delta_g)$$

The appropriate initial and boundary conditions are

$$t = 0;\quad C_{ab} = C_{ae} = C_{ao},\quad T = T_o,\quad C = 0$$

$$t > 0;\quad C_{ab} = C_{ao}\quad \text{at } z = 0$$

$$\frac{\partial C}{\partial r} = \frac{\partial C_{ab}}{\partial r} = \frac{\partial C_{ae}}{\partial r} = \frac{\partial T}{\partial r} = 0\quad \text{at } r = 0$$

$$\frac{\partial C}{\partial r} = \frac{\partial C_{ab}}{\partial r} = \frac{\partial C_{ae}}{\partial r} = \frac{\partial T}{\partial r} = 0\quad \text{at } r = R_B$$

The feeding rate function, Ψ_F, is defined as:

$$\Psi_F \begin{cases} = \dfrac{F}{\pi r_f^2 (1 - \delta_b)L} = \dfrac{F}{\pi r_f^2 L_{mf}} & \text{at } 0 \leq r \leq r_f \\[20pt] = 0 & \text{at } r_f < r \leq R_B \end{cases}$$

and the size reduction function of coal particles is defined as:

$$S(R) = -\frac{dR}{dt}$$

The unreacted core shrinking model gives rise to the size reduction function of the following form (13);

$$S(R) = -\frac{dR}{dt} = \left(\frac{1}{\dfrac{1}{k_g} + \dfrac{1}{k_s}}\right)\frac{C_{ae}M_c}{\rho_c} \qquad (6)$$

The heat source function, $\Phi(t)$, is defined as:

$$\Phi(t) = Q[U(t) - U(t - t_s)] \qquad (7)$$

A fluidized bed combustor can be used as a process heater (the type A combustor) or a steam generator (the type B combustor) as shown in Fig. 1. The combustor usually has no built-in heat exchangers when it is used as a process heater, and it operates with a very high excess air flow rate.

Numerical Simulation

Numerical calculation has been carried out using a software interface which is based on the so-called "Method of lines" (14). Gear's backward difference formulas (15) are used for the time integration. A modified Newton's method with the internally generated Jacobian matrix is utilized to solve the nonlinear equations.

To simulate the start-up of the combustor, an external heat source with a constant strength of 30 cal/sec-cm^2, i.e., Q = 30 in equation (7), is applied to the system at the onset of operation. The coal particles are fed into the bed when the bed temperature reaches 1300°K, and the heat source is removed ten seconds later. Thus,

$$\Phi(t) = 30[U(t) - U(t - 10)]$$

Coal

hot
gas ←

oil burner for
starting up

A.Process Heater

air

Coal

hot
gas ←

oil burner for
starting up

heat exchanger

B.Steam Generator

air
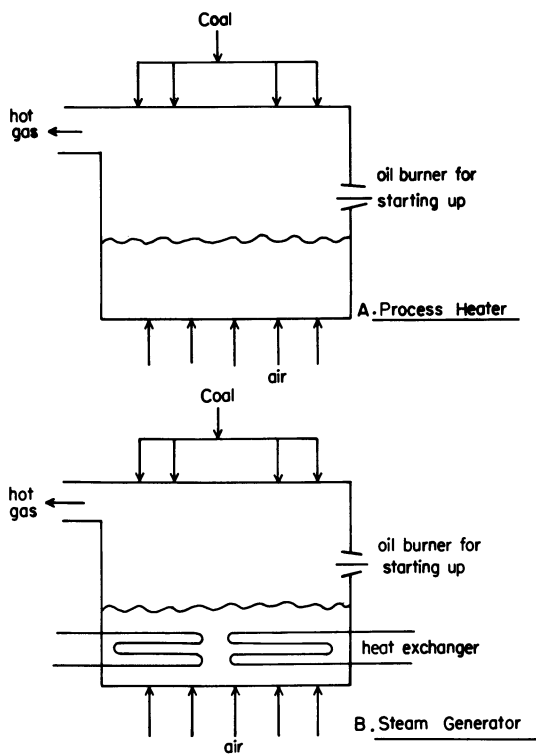
Figure 1. *Two types of shallow fluidized bed combustor*

It is assumed that circulation of the cooling steam through the
heat exchangers is started fifty seconds after feeding of the coal
particles into the bed is initiated. The functional relationships
among variables and the nominal values of various parameters
employed in numerical computation are listed in Table I and II,
respectively. Numerical simulation has been carried out sepa-
rately for the type A combustor and the type B combuster in order
to emphasize the differences between them.

Results and Discussion

        Type A combustor [see Figure 1; no heat exchangers in the bed,
i.e., a = 0 in equation (5)].
        Figure 2 shows the effect of bubble size on the steady-state
carbon concentration and bed temperature profiles. The concentra-
tion profiles are similar to those obtained previously (10) in that
an appreciable carbon concentration gradient is generated along
the lateral direction, and large bubbles can reduce this concentra-
tion gradient. Furthermore, the temperature profiles are almost
flat, indicating that the superior heat transfer property of a
fluidized bed overcomes the poor lateral mixing effect and that an
isothermal model is probably adequate for representing the steady-
state characteristics of a fluidized bed combustor.
        The effect of excess air rate on the steady-state carbon
concentration and temperature profiles is shown in Figure 3. As
can be seen, the effect of excess air rate on the carbon concentra-
tion profiles is not profound. On the other hand, even though the
steady-state bed temperature profiles are essentially flat, the
temperature level is strongly influenced by the excess air rate.
It is usually desirable to operate the combustor at certain optimal
temperature ranges in order to control the emission of NO_x and SO_2
or to obtain the maximum combustion efficiency. This can probably
be accomplished through the control of excess air flow rate.
        Figure 4 shows the effect of bubble size on the transient,
average carbon concentration. Note that a critical bubble size
exists, above which a concentration runaway occurs, i.e., the bed
cannot reach a steady state. This is the result of an insufficient
rate of oxygen transfer from the bubble phase to the emulsion
phase. It can also be seen in the figure that the steady-state
average carbon concentration is strongly influenced by the bubble
size; it increases sharply when the bubble size exceeds a certain
value, e.g., 5 cm in this case.
        The effects of bubble size and excess air rate on the tran-
sient average bed temperature are illustrated in Figure 5. The
effect of bubble size is almost negligible under stable operating
conditions, while the effect of excess air has a strong influence
on the temperature change. It can be seen in both Figures 4 and 5
that the bed reaches a steady state at about 2000 s after initi-
ation of the operation. This value is very different from the
value, 200 s, obtained based on an isothermal dynamic model (10).

Table I. Variable Relationships

$$U_{mf} = (\frac{\mu}{d_p \rho_g}) \{[33.7^2 + 0.0408 d_p^3 \rho_g (\rho_s - \rho_g) g/\mu^2]^{0.5}$$

$$- 33.7\} \ cm/s \qquad (\underline{16})*$$

$$\delta_b = \frac{U_0 - U_{mf}}{U_b} = \frac{L - L_{mf}}{L}$$

$$U_b = U_0 - U_{mf} + 0.711 \ (g d_B)^{0.5} \ cm/s$$

$$K_{be} = \frac{K_1 K_2}{K_1 + K_2} \ 1/s$$

$$\text{where } K_1 = 4.5 \ \frac{U_{mf}}{d_B} + 5.85 \ (\frac{D^{0.5} g^{0.25}}{d_B^{1.25}})$$

$$K_2 = 6.78 \ (\frac{\varepsilon_{mf} D U_b}{d_B^3})^{0.5} \qquad (\underline{17})*$$

$$D_s = 0.187 \ \delta_b U_{mf} \ \frac{d_B}{(1 - \delta_b) \varepsilon_{mf}} \ cm^2/s \qquad (\underline{18})*$$

$$k_e = D_s (\rho_s \ C_{ps}) \ \frac{cal}{cm \cdot s \cdot °K} \qquad (\underline{17})*$$

$$P_o(R), \ P_b(R) \sim N(\mu_c, \ \sigma_c)$$

$$\frac{\mu_1}{\mu_2} = (\frac{T_1}{T_2})^{1/2}$$

$$D = \frac{10^{-3} T^{1.75} (1/M_{air} + 1/M_{O_2})^{0.5}}{P[(\Sigma v)_{air}^{1/3} + (\Sigma v)_{O_2}^{1/3}]} \ cm^2/s \qquad (\underline{19})*$$

$$\frac{\rho_{g_1}}{\rho_{g_2}} = \frac{T_2}{T_1}$$

*References

Table II. Numerical Values of Parameters
Used in Computation

C_{ao} = 2.38 x 10^{-6} mole/cm^3

C_{pg} = 0.238 + 1.753 x 10^{-3} (T-273) cal/g°C

C_{ps} = 0.215 cal/g°C

d_B = 2, 5, 10 cm

d_p = 0.05 cm

Excess
air = 100, 150, 200% (Type A combustor); 5, 10, 20%
(Type B combustor)

$(-\Delta H)$ = 7831 cal/g

L_{mf} = 15 cm

R = 40 cm

T_o = 1300°K

T_{go} = T_{so} = 300°K

T_w = 600°K

ε_{mf} = 0.5

ρ_s = 1.4 g/cm^3

Ψ_F = 0.02, 0.03, 0.04, 0.05 (Type A combustor)
0.01, 0.02, 0.03, 0.04 (Type B combustor)
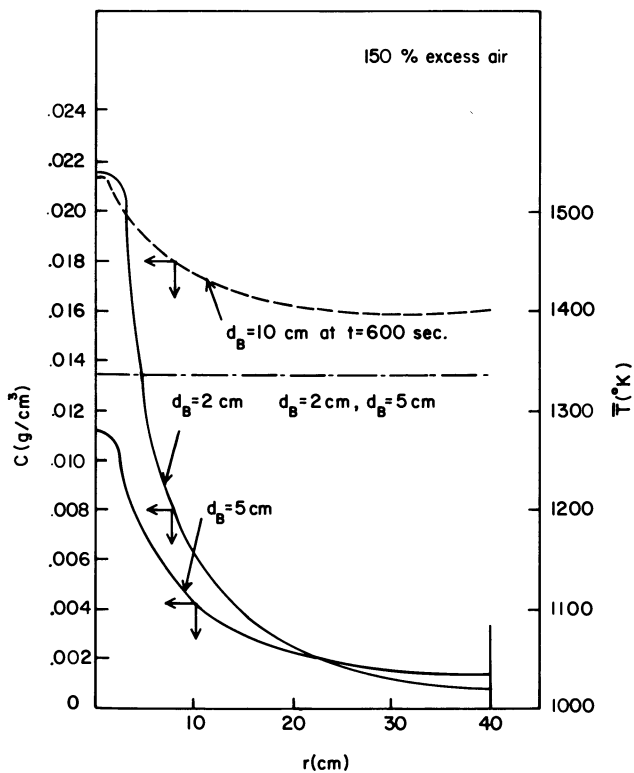
Figure 2. Effect of bubble size on the (———) steady-state carbon concentration and (– – –) bed temperature profiles in the type A combustor
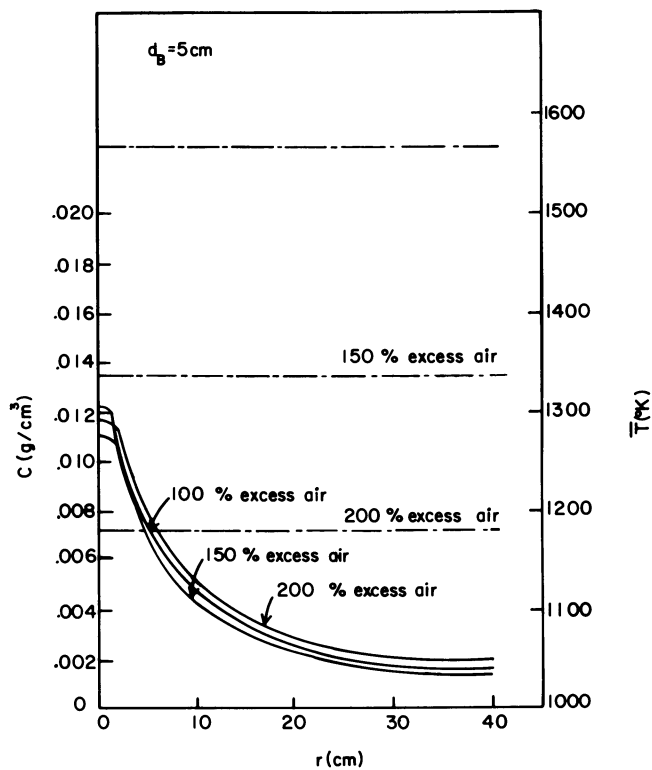
Figure 3.   Effect of excess air rate on the (———) steady-state carbon concentration and (— – —) bed temperature profiles in a type A combustor
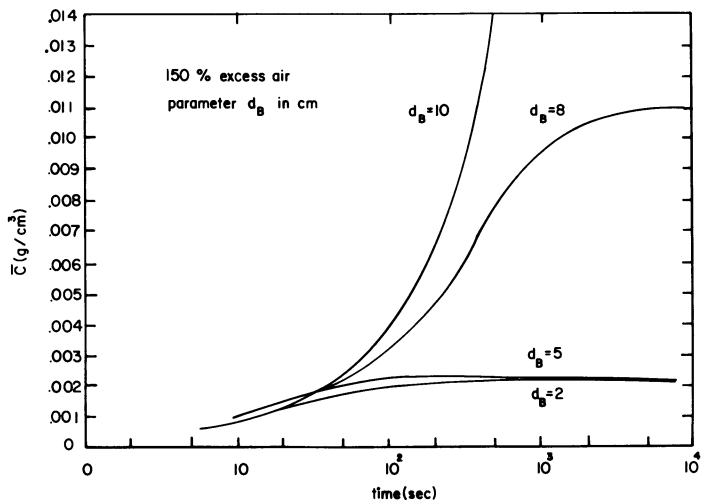
Figure 4.   *Effect of bubble size on the transient average carbon concentration in the type A combustor*
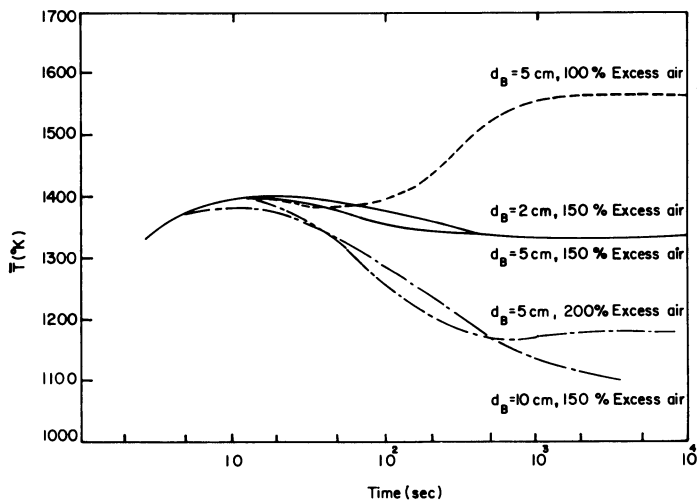
Figure 5.   *Effect of bubble size and excess air rate on the transient average bed temperature in the type A combustor*

This implies that even though the bed temperature is fairly uniform, an isothermal dynamic model can not represent sufficiently well the temperature transient of a fluidized bed combustor, and therefore, a nonisothermal dynamic model is necessary.

The effect of carbon feed rate, as expressed in terms of the carbon feed rate function, Ψ_f, on the steady-state carbon concentration and bed temperature profiles is presented in Figure 6. It can be seen that the shapes of the concentration profiles remain almost unchanged. This appears to indicate that the carbon feed rate has a negligible effect on the concentration gradient; it only influences the average amount of carbon in the bed. This result was also observed in a previous study (11).

In Figure 7 the effects of carbon feed rate and bubble size on the steady-state average carbon concentration are shown. The existence of critical bubble size for a fixed carbon feed rate can clearly be observed in this figure. It can also be observed that a critical carbon feed rate exists above which concentration runaway occurs, and a stable or steady-state condition can not be reached for a given bubble size. The value of the critical feed rate increases with a decrease in the bubble size. Under the critical condition, the maximum attainable rate of oxygen transfer from the bubble phase to the emulsion phase is reached, and it becomes the rate determining step for combustion as explained previously. To increase the carbon feed rate to a fluidized bed combustor, either the oxygen concentration in the air (gas) stream or the rate of mass transfer between the bubble and emulsion phase needs to be increased.

It should be noted that a carbon concentration of 0.014 g/cm^3 corresponds to 1% by weight in the present study, indicating that the steady-state carbon concentrations in all cases studied are far less than 1% by weight for the type A combustor.

Type B combustor [see Figure 1: with heat exchangers in the bed, i.e., a ≠ 0 in equation (5)].

The effects of bubble size and specific area of heat exchangers on the steady-state carbon concentration and bed temperature profiles are shown in Figure 8. Obviously, the carbon concentration gradient in the type B combustor is much greater than that in the type A combustor. The result might imply that more feeders are needed for the type B combustor than for the type A combustor, provided that their sizes are the same. The bed temperature is again quite uniform, and the temperature level in the type B combustor appears to be largely dependent on the characteristics of the heat exchangers instead of the excess air rate, as in the case of the type A combustor.

The effects of bubble size and specific areas of heat exchangers on the transient average carbon concentration and bed temperature are presented in Figure 9. It can be seen that the critical bubble size is about 5 cm, which is much smaller than that for the type A combustor. This is because of the relatively small excess air rate used and the large carbon concentration gradient
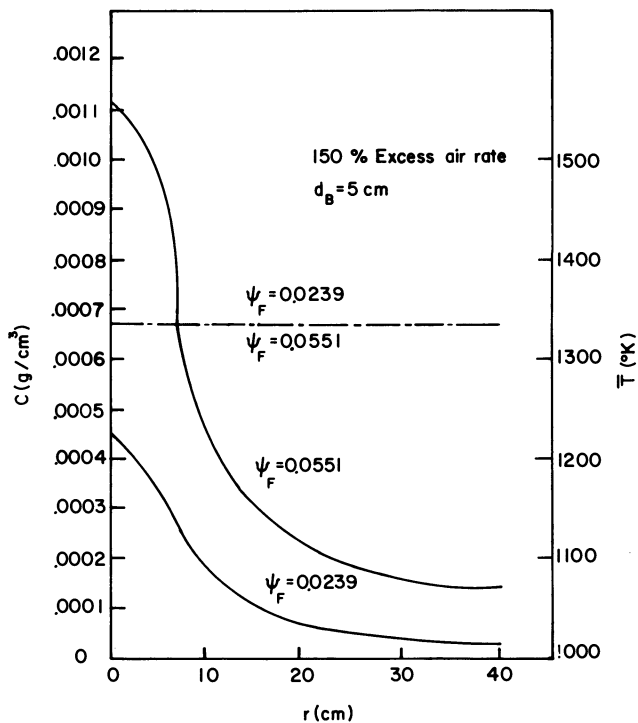
Figure 6. Effect of carbon feed rate on the (———) steady-state carbon concentration and (– – –) bed temperature profiles in the type A combustor
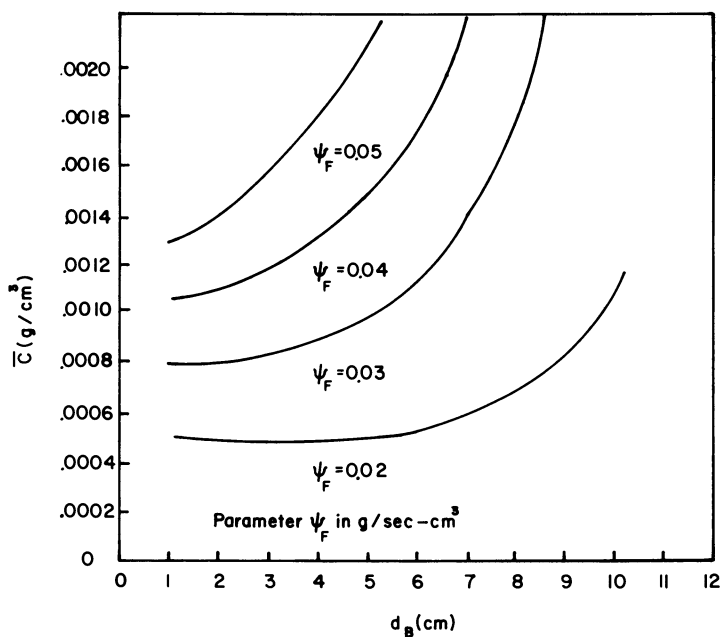
Figure 7.   Effect of carbon feed rate and bubble size on the steady-state average carbon concentration in the type A combustor
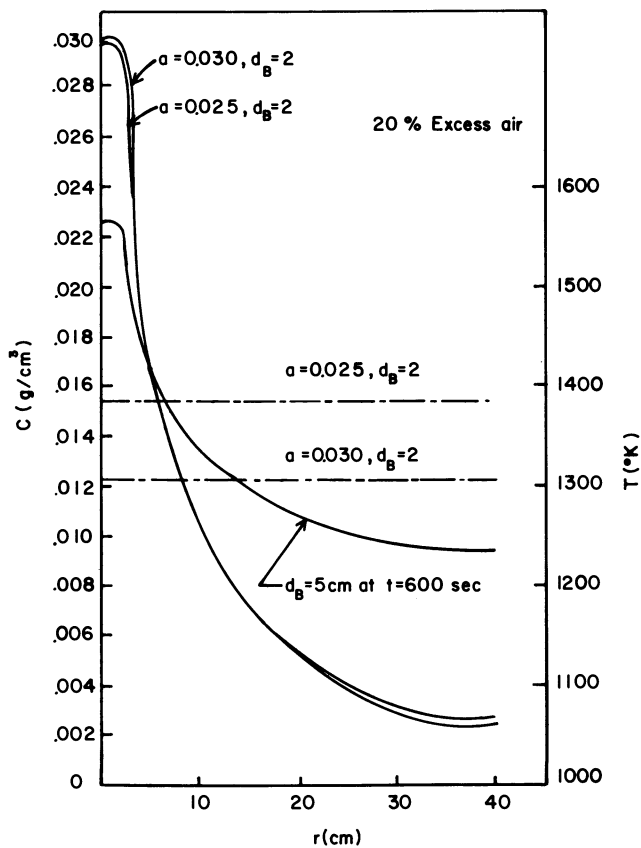
Figure 8. Effect of bubble size and specific area of heat exchangers on the (————) steady-state carbon concentration and (— — —) bed temperature profiles in the type B combustor
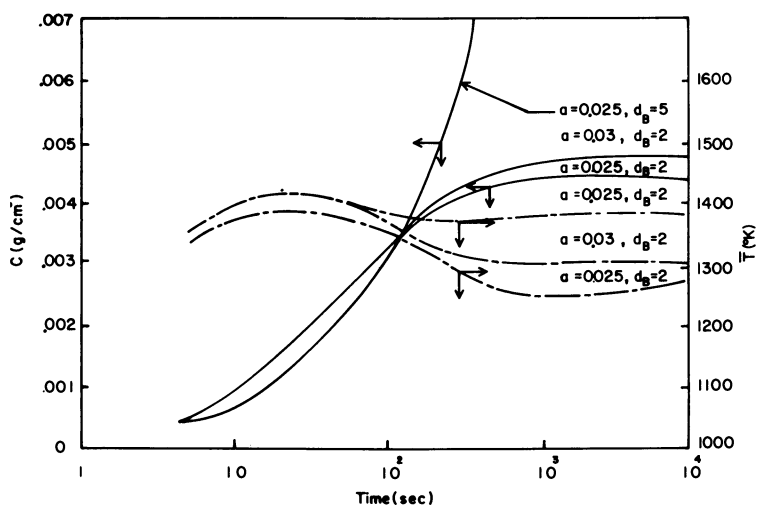
*Figure 9.   Effect of bubble size and specific area of heat exchangers on the (———)
transient average carbon concentration and (— — —) bed temperature in the type
B combustor*

obtained. Since most of the heat generated in the type B com-
bustor is removed through the heat exchangers, the excess air rate
can usually be kept low to save the blowing costs and the elutri-
ation loss. Therefore, the excess air rate should be controlled
so that it is neither too large nor too small.

A parametric study on the carbon feed rate was also made for
the type B combustor. The results obtained for the effect of
carbon feed rate on the steady-state carbon concentration and bed
temperature profiles are similar to those in the type A combustor
and will not be presented here. The effects of carbon feed rate
and bubble size on the steady-state average carbon concentration
are shown in Figure 10. It shows that the average carbon concen-
tration in the type B combustor is much higher than that in the
type A combustor for the given values of the carbon feed rate
function and bubble size. Apparently, both the critical bubble
size and carbon feed rate in the type B combustor are smaller than
those in the type A combustor under the same set of operating con-
ditions except the excess air rate. This indicates the perfor-
mance of a fluidized bed combustor with built-in heat exchangers
is much more sensitive to variations in the operating conditions;
greater effort is required to ensure its smooth operation.

The assumption (d) imposed in deriving the model appears to
be valid for both types of combustors since the feed rate of coal
is relatively small under normal operating conditions. The order
of magnitude analysis shows that the convective flux, uc, is
indeed much smaller than the dispersion flux, $-D \frac{\partial c}{\partial r}$, under the
conditions simulated.

Conclusion

A non-isothermal dynamic model has been developed for a
shallow fulidized bed combustor, which can be used to predict, at
least qualitatively, the transient and steady-state characteris-
tics of such systems. Parametric studies have been conducted to
examine the effects of excess air flow rate, bubble size and car-
bon feed rate. It has been shown that an appreciable carbon con-
centration gradient does exist in the bed. This explains why it
is necessary to use multiple feed points in large fluidized bed
combustors. A surprising result obtained is that the temperature
in the bed is essentially uniform under all conditions studied
even though the carbon concentration is not uniform laterally.

For a combustor without heat exchangers, the bed temperature
is strongly influenced by the excess air flow rate. On the other
hand, for a combustor with heat exchangers, the bed temperature
is mainly dependent on the characteristics of the heat exchangers.

It has been illustrated that the bubble size has strong
influences on both the transient and steady-state carbon concentra-
tions. The effects of the carbon feed rate, expressed as the car-
bon feed rate function, on the steady-state carbon concentration
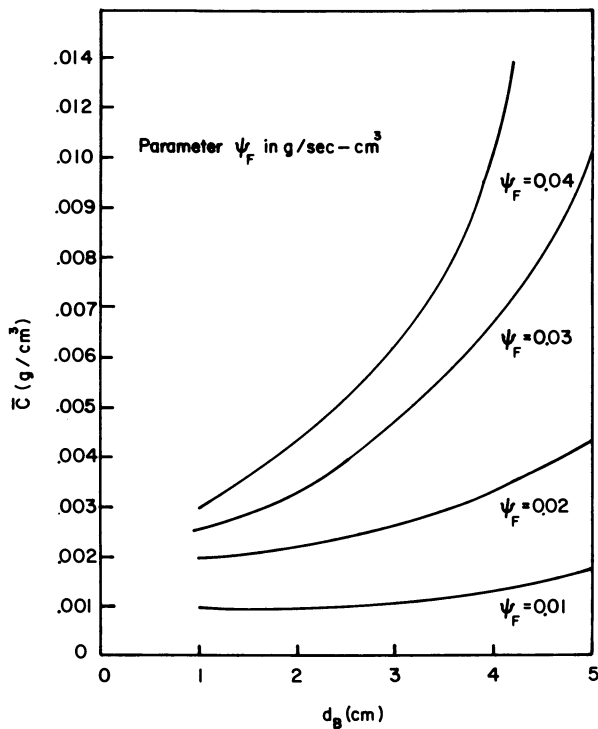and bed temperature profiles are negligible under the conditions

Figure 10. Effect of carbon rate and bubble size on the steady-state average carbon concentration in the type B combustor; 20% excess air, a = 0.025 cm²/cm³

simulated. It has also been illustrated that a critical bubble size and a critical carbon feed rate exist, above which a stable steady-state operating condition can never be attained. Such critical values for a combustor with heat exchangers (type B) have been found to be much smaller than those for the corresponding combustor without heat exchangers (type A).

Nomenclature

a = surface area of the heat exchanger per unit bed volume, cm^{-1}

C = carbon concentration in the emulsion phase, g/cm^3

C_{ab} = oxygen concentration in the bubble phase, mol/cm^3

C_{ae} = oxygen concentration in the emulsion phase, mol/cm^3

C_{ao} = initial oxygen concentration in the feed gas, mol/cm^3

C_{pg} = heat capacity of gas, $cal/g°K$

C_{ps} = heat capacity of the bed solid particles (limestone or dolomite), $cal/g°K$

D = gas diffusivity in the solid-gas boundary, cm^2/s

D_{ae} = effective dispersion coefficient of oxygen in the emulsion phase, cm^2/s

D_s = effective dispersion coefficient of solids, cm^2/s

d_B = bubble diameter, cm

F = feeding rate of coal particles, g/s

$(-\Delta H)$ = heat of reaction, cal/g

K = gas interchange coefficient, 1/s

k_e = effective thermal conductivity, $cal/cm·s·°K$

k_g = oxygen mass transfer coefficient in the solid-gas boundary, cm/s

L = bed height, cm

L_{mf} = bed height at minimum fluidization, cm

M_c = molecular weight of carbon, g/mole

$P_b(R)$ = coal size distribution function in the bed, –

$P_o(R)$ = coal size distribution function in the feed stream, –

Q = magnitude of the external heat source, $cal/s·cm^2$

R = radius of the coal particles, cm

R_B = radius of equivalent bed radius per feed point, cm

r = coordinate in the radial direction, cm

r_f = radius of the feeder, cm

Sh = Sherwood number, –

S(R) = rate of particle shrinkage as defined in equation (6), cm/s

T = bed temperature, °K

T_{go} = temperature of the air in the feed stream, °K

T_o = initial bed temperature, °K

T_{so} = temperature of the coal particles in the feed stream, °K

t = time, s

t_s = time interval in which the external heat source is applied during start-up, s

U_b = bubble velocity, cm/s

U_g = superficial velocity of gas, cm/s

U_{mf} = incipient fluidization velocity, cm/s

U(t) = step function, –

z = coordinate in the axial direction, cm

δ_b = fraction of the bubble phase, –

δ_g = fraction of the gas phase in the bed, –

ε_{mf} = incipient void fraction of the emulsion phase, –

μ = gas viscosity, g/cm s

ρ_c = density of the coal particles, g/cm^3

ρ_s = density of the bed solid particles, g/cm^3

ρ_g = density of the gas mixture in the bed, g/cm^3

$\Phi(t)$ = external heat source function, cal/s·cm^2

$\Psi_F(t)$ = carbon feed rate function, g/s·cm^3

Acknowledgement

Literature Cited

1. Gibbs, B.M., Paper A-5 Institute of Fuel Symposium Series, 1975.
2. Gordon A. L., Amundson, N. R., Chem. Eng. Sci., 1976, 31, 1163.
3. Beer, J. M., paper presented at 16th Symposium on Combustion, The Combustion Institute, 1976; p. 439.

4. Horio, M., Rengarajan, P., Krishnan, R., Wen, C. Y.,
    "Fluidized Bed Combustor Modeling", Report to NASA Lewis
    Research Center: Cleveland, January, 1977.
5. Baron, R. E., Hodges, J. L., Sarofim, A. F., paper presented
    at AIChE 70th Annual Meeting: New York, November, 1977.
6. Borghi, G., Sarofim, A. F., Beer, J. M., paper presented at
    the AIChE 70th Annual Meeting: New York, November, 1977.
7. Horio, M., Wen, C. Y., <u>AIChE Symposium Series</u>, 1977 (161),
    <u>73</u>, 9.
8. Caretto, L. S., paper presented at the 1977 Fall Meeting,
    Western States Section/The Combustion Institute: Stanford
    University, October, 1977.
9. Highley, J., Merrick, D., <u>AIChE Symposium Series</u>, 1971 (116),
    <u>69</u>, 219.
10. Fan, L. T., Tojo, K., Chang, C. C., <u>Ind. Eng. Chem. Process
    Des. Dev.</u>, 1979, <u>18</u>, 333.
11. Tojo, K., Chang, C. C., Fan, L. T., paper submitted to <u>Ind.
    Eng. Chem. Process Des. Dev.</u>, for publication, 1979.
12. Davidson, J. F., Harrison, D., "Fluidized Particles," Cam-
    bridge University Press: New York, NY, 1963.
13. Yagi, S., Kunii, D., <u>5th Symposium (International) on Com-
    bustion</u>: Reinhold, New York, 1955; p. 231.
14. Sincovec, R. F., Madsen, N. K., <u>ACM Trans. Math. Software</u>,
    1975, <u>1</u>, 232.
15. Gear, C. W., "Numerical Initial Value Problems in Ordinary
    Differential Equations"; Chapter 9, Prentice-Hall: Englewood
    Cliffs, N.J., 1971.
16. Wen, C. Y., Yu, Y. H., <u>AIChE J.</u>, 1966, <u>12</u>, 610.
17. Kunii, D., Levenspiel, P., <u>J. Chem. Eng. Jpn.</u>, 1969, <u>2</u>, 122.
18. Kunii, D., "Kagaku Kikai Gijutsu"; Maruzen, 1966 (18), p. 161.
19. Fuller, E. N., Schettler, P. D., Giddings, J. G., <u>Ind. Eng.
    Chem.</u>, 1966, <u>58</u>, 18.

Modeling of Fluidized Bed Combustion of Coal Char Containing Sulfur

A. REHMAT[1], S. C. SAXENA[2], and R. H. LAND

Argonne National Laboratory, 9700 South Cass Avenue, Argonne, IL 60439

A mathematical model is developed for coal char combustion with sulfur retention by limestone or dolomite in a gas fluidized bed employing noncatalytic single pellet gas-solid reactions. The shrinking core model is employed to describe the kinetics of chemical reactions taking place on a single pellet whose changes in size as the reaction proceeds are considered. The solids are assumed to be in back-mix condition whereas the gas flow is regarded to be in plug flow. The model is strictly valid for the turbulent regime where the gas flow is quite high and classical bubbles do not exist. Formulation of the model includes setting up heat and mass balance equations petaining to a single particle exposed to a varying reactant concentration along the height of the bed with accompanying changes in its size during the course of reaction. These equations are then solved numerically to account for particles of all sizes in the bed to obtain the overall carbon conversion efficiency and resultant sulfur retention. In particular, the influence of several fluid-bed variables such as oxygen concentration profile, additive particle size, reaction rate for sulfation reaction, sulfur absorption efficiency are examined on additive requirement.

[1] Current Address: Institute of Gas Technology, Chicago, IL
[2] Current Address: University of IL at Chicago Circle, Chicago, IL

Many models have been used to describe fluidized-bed oper-
ation (1-7). Several additional models have been proposed during
the last three years and these will be referred to later in this
report. It is commonly assumed that the bed is composed of two
distinct phases, viz., a dense phase (emulsion) consisting of
solid particles and interstitial gas, and a bubble phase con-
sisting of rising voids with almost no solids. The most advanced
models (1, 2, 3) also consider additional phases, viz., a cloud
and wake associated with each bubble. Further variations appear
in the characterization of gas flow within each phase, and mode
of exchange among the phases, and the bubble shapes, velocities,
and growth rates. It is generally assumed that in the two-phase
theory of fluidization (8), the flow rate of bubble voids through
the fluidized bed is equal to the excess gas flow rate above that
required for minimum fluidization. Chemical reactions in the bed
are assumed to occur entirely in the emulsion phase.

In the present analysis, we shall develop a basic model for
fluidized bed operation by extending our earlier analysis (9, 10,
11) for a single pellet reaction to model the noncatalytic
gas-solid reactions taking place in a fluidized bed. The earlier
results have been derived with the assumption of constant
gaseous reactant concentration surrounding the pellet. However,
in a fluidized bed, the pellet encounters a considerable variation
in the gaseous reactant concentration due to its movement. Also,
the fluidized bed is composed of particles of different sizes,
each of which will behave differently. The solid material in the
bed is constantly being consumed due to chemical reactions and is
being depleted by entrainment and overflow. This solid material
should be replenished continuously by feeding fresh reactant
particles. In order to develop a realistic model, the particle
size distribution of the feed and the bed must be taken into
account as also the fact that the fluidized bed operates in a
continuous mode with solids addition to the bed by feed and
removal by overflow and elutriation.

The model presented here takes into account the changes in
the size of a particle as a result of chemical reactions in a
fluidized bed. A number of modeling studies related to the
noncatalytic reactions and to coal combustion in particular,
taking place in a fluidized bed have been reported (2-25). A
review of these studies indicate that the coal combustion process
is primarily diffusion controlled. The amount of gaseous reactant
diffusing through the gas film surrounding the particle, will
depend on its size. In most of the models referred to above, the
particle size is assumed to be constant throughout the reaction
insofar as the mass transfer process is concerned. The shrinkage
of particles in those cases where either no solid product is
formed or ash is flaked off from the surface is used only in
calculating the particle size distribution in the bed, carryover,
and overflow streams.

To account for particle growth or shrinkage as the reaction
progresses in the reactor, a parameter, Z, is introduced. The

theory developed by Kunii and Levenspiel (1) is for a reacting
system in which the particles maintain a constant size (Z = 1).
It (1) deals with the derivation of relations giving the particle
size distribution in the bed, overflow, and carryover streams and
their respective weights. This theory will be extended to
include the effects of particle growth or shrinkage (Z>1 or Z<1).
For typical combustion of char containing sulfur followed by
sulfur dioxide absorption by limestone, relations will be derived
to determine the extent of sulfur retention. The reaction,
carryover, and overflow rates will be evaluated with particular
attention to their dependence on Z.

Description of Char Particle Combustion

The combustion of sulfur-rich char is accompanied by the
production of an undesirable reaction product, viz., sulfur
dioxide. However, most of the sulfur dioxide should be removed
from the combustion gases before they leave the combustor. This
may be accomplished by the introduction into the combustor of
suitable additives which can absorb sulfur dioxide. Limestone is
such an additive. The limestone reacts with sulfur dioxide in
the presence of oxygen to form calcium sulfate, which is a solid
product and can be easily removed from the reactor. In this
work, a model is proposed for the prediction of sulfur dioxide
removal from the combustion gases, based on knowledge of gas-solid
reactions taking place on a single pellet.
    The kinetics of gas-solid reactions obtained from single-
particle studies are utilized to calculate the generation and
utilizaton of sulfur dioxide for many particles present in a
fluidized-bed reactor. For simplicity, char (i.e., coal with
almost all volatiles removed) will be the basic feed to the
reactor and it is assumed to contain carbon, ash, and sulfur.
Carbon and sulfur react with oxygen to form their respective
oxides. Sulfur dioxide subsequently reacts with limestone and
excess oxygen to form calcium sulfate. Char and limestone
particles undergo change in size as they react, and this will be
included in obtaining average conversions. Ultimately, this
model predicts the average concentration of sulfur dioxide in the
combustion gas stream, solid flow rates, and the particle size
distributions in the reactor and in the streams leaving the
reactor.
    The following assumptions are made in the mathematical
formulation of the process:
    1. The particles are completely mixed in the reactor.
    2. Gases do not mix vertically, i.e., the gas flow through
       the bed is in plug flow. Further, no gas concentration
       gradients exist transverse to the direction of flow.
    3. The gas flow is statistically uniform over the bed
       cross section at a given bed height and is equal to a
       certain mean value.

4. The temperature is uniform throughout the bed.
5. The reactor is operated in the steady state mode.
6. Sulfur is uniformly distributed in the coal char
    particles.
7. Combustion and consequent generation and absorption of
    sulfur dioxide occur throughout the bed.
8. The reaction rates are independent of reaction product
    concentrations.
9. The gas-solid reaction follows a shrinking core model.

Char and limestone (calcium carbonate) particles are fed to
the reactor continuously at rates, F_1 and F_1', respectively, and
their particle size distributions in the feed are given by $P_1(\xi_s)$
and $P_1'(\xi_s')$, respectively. The mass of these solid components
in the bed, the overflow and the carryover rates, and their
respective size distributions are shown in Figure 1. The carry-
over and the overflow particles are not recycled. The following
reactions are considered to take place in the fluidized bed. The
subscripts by which the reactants and products are referred to
throughout in this work are given in parentheses.

$$\text{carbon (J) + oxygen (A)} \xrightarrow{k_1} \text{carbon dioxide (D)} \tag{1}$$

$$\text{sulfur (S) + oxygen (A)} \xrightarrow{k_2} \text{sulfur dioxide (B)} \tag{2}$$

$$\text{calcium carbonate (N) + sulfur dioxide (B) + oxygen (A)} \xrightarrow{k_3}$$
$$\text{calcium sulfate (E) + carbon dioxide (D)} \tag{3}$$
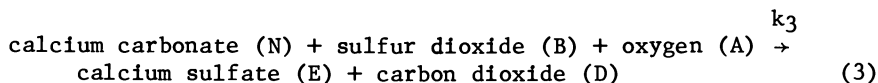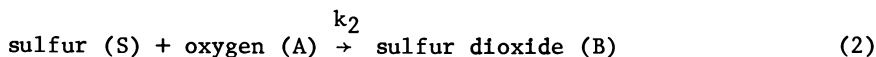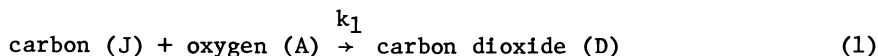
When char reacts with oxygen, solid product ash is formed
and it adheres to the particle. Similarly, in the case of
limestone, the solid product calcium sulfate adheres to the
limestone particle. The change in the overall size of the
particle depends on the amount of solid formed and is related to
the amount of solid reactant consumed in the following manner:

$$Z = \frac{\text{volume of solid product formed}}{\text{volume of solid reactant consumed}} \tag{4}$$

The average radius, $\bar{r}$, is defined as follows:

$$\bar{r} = \frac{1}{\Sigma_i (w_i'/r_i)} \tag{5}$$

and is employed to normalize the distances from the center of the
pellet.

In the following sections, the equations for a single pellet
involving one and two independent reactions are presented.
First, we shall derive equations pertaining to a single reaction

and then extend the derivation to the two gas-solid reactions
taking place with one gas and two solids. Gas-solid reactions
given by Eqs. 1, 2, and 3 will be used.

Single Pellet: One Reaction. The sulfation reaction which
is considered here for calcium carbonate is given by Eq. 3, and
the temperature and concentration profiles of a typical growing
limestone particle are shown in Figure 2. The rate of dis-
appearance of sulfur dioxide is assumed to be the first order and
is given by

$$-r_B = k_3(T_c') \, C_{NO} C_{BC} \tag{6}$$

The differential equation for the mass balance of gaseous
reactant B reacting with a pellet of radius R_0' under the pseudo-
steady-state assumption is

$$\frac{d}{d\xi'} \left[\xi'^2 \frac{d\omega_B}{d\xi'} \right] = 0 \tag{7}$$

with the following boundary conditions:

at $r' = R'$, i.e., at $\xi' = \xi_s'$,

$$\left. \frac{d\omega_B}{d\xi'} \right|_{\xi' = \xi_s'} = N_{SH\overline{r}}' (\omega_{BH} - \omega_{BS}) \tag{8}$$

at $r' = r_c'$, i.e., at $\xi' = \xi_c'$,

$$\left. \frac{d\omega_B}{d\xi'} \right|_{\xi' = \xi_s'} = \phi_{3\overline{r}} \frac{(\omega_{BC})}{U_c'} \exp\left\{ \frac{E_3}{\overline{R}T_0} \left(1 - \frac{1}{U_c'} \right) \right\} \tag{9}$$

The solution of the above Equation 7 gives

$$\frac{\omega_{BH}}{\omega_{BC}} = \left[1 + \frac{\phi_{3\overline{r}} \xi_c'^2 \exp\left\{ \frac{E_3}{\overline{R}T_0} \left(1 - \frac{1}{U_c'} \right) \right\}}{U_c' \, N_{SH\overline{r}} \, \xi_c'^2} + \frac{\phi_{3\overline{r}} \xi_c' \left(1 - \frac{\xi_c'}{\xi_s'} \right)}{U_c'} \right.$$

$$\left. \cdot \exp \frac{E_3}{\overline{R}T_0} \left\{ \left(1 - \frac{1}{U_c'} \right) \right\} \right] \tag{10}$$

The heat balance is

$$\frac{d}{d\xi'} \left[\xi'^2 \frac{dU'}{d\xi'} \right] = 0 \tag{11}$$
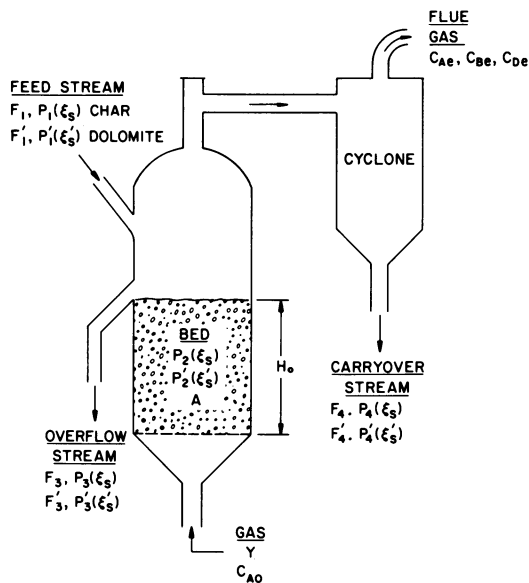
Figure 1.   Feed and exit streams of the fluidized-bed combustor
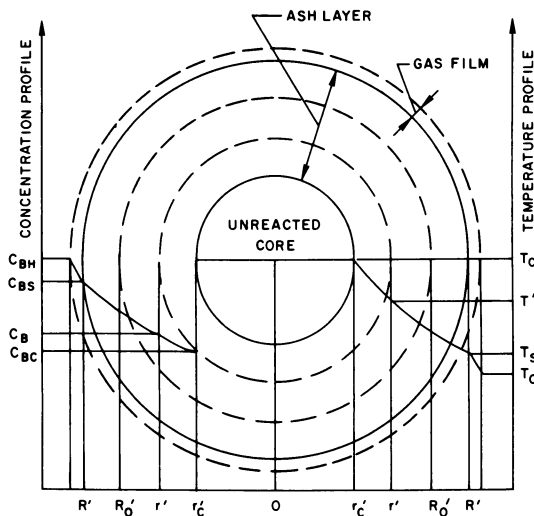
Figure 2.   Gas–solid reaction of a growing limestone particle at height **H** *in the fluidized bed: concentration and temperature profiles*

with the following boundary conditions:

at $r' = R'$, i.e., $\xi' = \xi_s'$,

$$-\left.\frac{dU'}{d\xi'}\right|_{\xi' = \xi_s'} = N_{Nur}' \, (U_s' - 1) \tag{12}$$

and at $r' = r_c'$, i.e., $\xi' = \xi_c'$

$$-\left(\frac{\bar{R}T_o}{E_3}\right)\left(\frac{dU'}{d\xi'}\right)\bigg|_{\xi' = \xi_c'} = \phi_{3\bar{r}}\beta_3 \left(\frac{\omega BC}{U_c'}\right) \exp\left\{\frac{E_3}{\bar{R}T_o}\left(1 - \frac{1}{U_c'}\right)\right\} \tag{13}$$

U_c' is then given by the following expression:

$$U_c' - 1 = \phi_{3\bar{r}}\beta_3 \frac{\omega BC}{U_c'} \frac{E_3}{\bar{R}T_o} \exp\left\{\frac{E_3}{\bar{R}T_o}\left(1 - \frac{1}{U_c'}\right)\right\} \cdot$$

$$\cdot \left[\frac{1}{N_{Nur}'} \frac{\xi_c'^2}{\xi_s'^2} + \xi_c'\left(1 - \frac{\xi_c'}{\xi_s'}\right)\right] \tag{14}$$

If we assume that the gas in the reactor is ideal and the gas pressure is constant, the following relation holds true throughout the reactor:

$$CT = \text{constant} \tag{15}$$

Thus, we can write the expression for the rate of conversion for the pellet in terms of its core radius as follows:

$$-\frac{d\xi_c'}{d\theta_3} = \frac{\omega BC}{U_c'} \exp\left\{\frac{E_3}{\bar{R}T_o}\left(1 - \frac{1}{U_c'}\right)\right\} \tag{16}$$

where

$$\tau_3 = \frac{\rho_N \bar{r}}{M_N k_3(T_o) C_{NO} C_{AO}} \tag{17}$$

and $\theta_3 = \dfrac{t}{\tau_3}$ \tag{18}

Since the behavior of the fluidized bed depends upon the overall particle size, it is necessary to derive an expression for $d\xi_s'/d\theta_3$. It is shown (9) that for spherical particles,

$$\frac{d\xi_s'}{d\theta_3} = (1 - Z') \frac{\xi_c'^2}{\xi_s'^2} \frac{d\xi_c'}{d\theta_3} \tag{19}$$

Substituting the expression for $d\xi_c/d\theta_3$ from Eq. 16 into Eq. 19, we get the required relation, <u>viz.</u>,

$$\frac{d\xi'_s}{d\theta_3} = (1 - Z') \frac{\xi_c'^2}{\xi_s'^2} \cdot \frac{\omega_{BC}}{U_c'} \left\{ \exp \frac{E_3}{RT_0} \left(1 - \frac{1}{U_c'} \right) \right\} \tag{20}$$

<u>Single Pellet: Two Independent Reactions</u>. The two independent reactions considered for char combustion are given by Eqs. 1 and 2, and their respective rates of reaction are

$$r_D = k_1 C_{JO} C_{AC}, \text{ and} \tag{21}$$

$$r_B = k_2 C_{SO} C_{AC} \tag{22}$$

Reactions 1 and 2 take place independently within a single pellet which contains both of the solid reactants, J and S.

The material balance for the gaseous reactant A in the ash layer of the pellet under the pseudo-steady-state assumption is represented by:

$$\frac{d^2\omega_A}{d\xi^2} + \frac{2}{\xi} \frac{d\omega_A}{d\xi} = 0 \tag{23}$$

The boundary condition at $\xi = \xi_s$ is

$$\left. \frac{d\omega_A}{d\xi} \right|_{\xi = \xi_s} = N_{SH\bar{r}}(\omega_{AH} - \omega_{AS}) \tag{24}$$

and at $\xi = \xi_c$ is

$$\left. \frac{d\omega_A}{d\xi} \right|_{\xi = \xi_c} = \phi_{1\bar{r}} \left(\frac{\omega_{AC}}{U_c} \right) \exp \left\{ \frac{E_1}{RT_0} \left(1 - \frac{1}{U_c} \right) \right\}$$

$$+ \phi_{2\bar{r}} \left(\frac{\omega_{AC}}{U_c} \right) \exp \left\{ \frac{E_2}{RT_0} \left(1 - \frac{1}{U_c} \right) \right\} \tag{25}$$

Solution of the above equations gives the following result for ω_{AC}:

$$\frac{\omega_{AH}}{\omega_{AC}} = 1 + \frac{1}{U_c} \left[\phi_{1\bar{r}} \exp \left\{ \frac{E_1}{RT_0} \left(1 - \frac{1}{U_c} \right) \right\} + \phi_{2\bar{r}} \exp \left\{ \frac{E_2}{RT_0} \left(1 - \frac{1}{U_c} \right) \right\} \right]$$

$$\left[\frac{1}{N_{SH\bar{r}}} \frac{\xi_c^2}{\xi_s^2} + \xi_c \left(1 - \frac{\xi_c}{\xi_s} \right) \right] \tag{26}$$

The heat balance equation is

$$\frac{d^2U}{d\xi^2} + \frac{2}{\xi} \frac{dU}{d\xi} = 0 \tag{27}$$

with the following boundary conditions:
At $\xi = \xi_s$

$$-\frac{dU}{d\xi}\bigg|_{\xi = \xi_s} = N_{Nu\bar{r}} (U_s - 1) \tag{28}$$

and at $\xi = \xi_c$

$$-\left(\frac{\bar{R}T_0}{E_1}\right)\left(\frac{dU}{d\xi}\right)\bigg|_{\xi = \xi_c} = \left(\frac{\omega_{AC}}{U_c}\right)\left[\phi_{1\bar{r}}\beta_1 \exp\left\{\frac{E_1}{\bar{R}T_0}\left(1 - \frac{1}{U_c}\right)\right\} + \phi_{2\bar{r}}\beta_2\left(\frac{E_2}{E_1}\right)\right.$$

$$\left. \exp\left\{\frac{E_2}{\bar{R}T_0}\left(1 - \frac{1}{U_c}\right)\right\}\right] \tag{29}$$

U_c is obtained from the following expression:

$$U_c - 1 = \frac{\omega_{AC}}{U_c}\left[\frac{1}{N_{Nu\bar{r}}}\frac{\xi_c^2}{\xi_s^2} + \xi_c\left(1 - \frac{\xi_c}{\xi_s}\right)\right]\phi_{1\bar{r}}\beta_1 \frac{E_1}{\bar{R}T_0} \exp\left\{\frac{1}{\bar{R}T_0}\left(1 - \frac{1}{U_c}\right)\right\}$$

$$+ \phi_{2\bar{r}}\beta_2\left[\frac{E_2}{\bar{R}T_0} \exp\left\{\frac{E_2}{\bar{R}T_0}\left(1 - \frac{1}{U_c}\right)\right\}\right] \tag{30}$$

The conversion of the solid pellet expressed in terms of core radius is given by

$$-\frac{d\xi_c}{dt} = \frac{M_J}{\rho_{J\bar{r}}} k_1(T_0)C_{JO}C_{AO}\frac{\omega_{AC}}{U_c} \exp\left\{\frac{E_1}{\bar{R}T_0}\left(1 - \frac{1}{U_c}\right)\right\}$$

$$+ \frac{M_S}{\rho_{S\bar{r}}} k_2(T_0)C_{SO}C_{AO}\frac{\omega_{AC}}{U_c} \exp\left\{\frac{E_2}{\bar{R}T_0}\left(1 - \frac{1}{U_c}\right)\right\} \tag{31}$$

Let $$\tau_1 = \frac{\rho_{J\bar{r}}}{M_J k_1(T_0)C_{JO}C_{AO}}, \tag{32}$$

$$\tau_2 = \frac{\rho_{S\bar{r}}}{M_S k_2(T_0)C_{SO}C_{AO}}, \tag{33}$$

and

$$\theta_1 = t/\tau_1 \tag{34}$$

Substituting Eqs. 32, 33, and 34 into 31, we get:

$$-\frac{d\xi_c}{d\theta_1} = \frac{\omega_{AC}}{U_c}\left[\exp\left\{\frac{E_1}{\bar{R}T_0}\left(1 - \frac{1}{U_c}\right)\right\} + \frac{\tau_1}{\tau_2} \exp\left\{\frac{E_2}{\bar{R}T_0}\left(1 - \frac{1}{U_c}\right)\right\}\right] \tag{35}$$

On the basis of Eqs. 19 and 35, the rate of change of overall particle size is given by

$$-\frac{d\xi_s}{d\theta_1} = (1 - Z)\frac{\xi_c^2}{\xi_s^2}\frac{\omega_{AC}}{U_c}\left[\exp\left\{\frac{E_1}{\bar{R}T_0}\left(1 - \frac{1}{U_c}\right)\right\}\right.$$

$$\left. + \frac{\tau_1}{\tau_2} \exp\left\{\frac{E_2}{\bar{R}T_0}\left(1 - \frac{1}{U_c}\right)\right\}\right] \tag{36}$$

The above equations will be employed in the mathematical modeling of fluidized bed presented below. When two solid reactants (char and limestone) are present, we shall use primed (limestone) and unprimed (char) symbols to distinguish between them.

Mathematical Model for Fluidized-Bed Combustion Process

The development of mathematical models to describe the thermochemical process occurring in a fluidized bed involves setting up the material and energy balance equations. The total process is represented in terms of a set of independent equations which are solved simultaneously to obtain such quantities as combustion efficiency, sulfur retention, oxygen utilization, oxygen and sulfur dioxide concentration profiles in the bed, etc.

The relationship between various streams, flow rates and particle sizes will be derived following the method of Kunii and Levenspiel (1). First, the relations are derived for char, whose particles generally shrink as they react with oxygen. The overall mass balance for char particles of the system is given by:

$$F_1 - F_3 - F_4 = \left\{ \begin{array}{c} \text{mass of carbon and sulfur} \\ \text{consumed by chemical reaction} \end{array} \right\} \tag{37}$$

In order to evaluate the right side of Eq. 37, we will calculate the mass loss for a single pellet due to reaction and sum up such losses for all particles present in the fluidized bed. Upon combustion, char leaves behind a layer of ash having a different density than that of coke. Thus, the mass of a single char particle, w_i, of size ξ_s in the bed is given by:

$$w_i = \frac{4}{3} \pi r^3 \rho_Q \left[\frac{\rho_a}{\rho_Q} \left(\xi_s^3 - \xi_c^3 \right) + \xi_c^3 \right] \tag{38}$$

Therefore, the rate of change of mass of a single particle size ξ_s is,

$$\frac{dw_i}{dt} = 4 \pi r^3 \rho_Q \left[\alpha_1 \xi_s^2 \frac{d\xi_s}{dt} + (1 - \alpha_1) \xi_c^2 \frac{d\xi_c}{dt} \right] \tag{39}$$

where

$$\alpha_1 = \frac{\rho_a}{\rho_Q} \tag{40}$$

The volume, dV, of the fluidized bed of cross-sectional area A_o and elemental height dH is $A_o dH$. Let f_Q be the fraction of char particles in the bed voidage ε. The volume of char particles of size ξ_s in the elemental volume dV is $f_Q(1 - \varepsilon)A_o P_2(\xi_s)d\xi_s dH$. The number of particles of size ξ_s in this elemental volume is

$$dN^* = \frac{f_Q(1 - \varepsilon)A_o P_2(\xi_s)d\xi_s dH}{(4/3) \, r^3 \, \xi_s^3} \tag{41}$$

Therefore, the mass depletion rate of char particles of size ξ_s in dV due to reaction is $(dw_1/dt)dN*$. Substituting from Eqs. 41 and 39 into this relation we get

$$\frac{dw_1}{dt} dN* = 3f_Q(1-\varepsilon)A_oP_2(\xi_s)\rho_Q \left\{ \frac{\alpha_1}{\xi_s} \frac{d\xi_s}{dt} + \frac{(1-\alpha_1)}{\xi_s^3} \xi_c^2 \frac{d\xi_c}{dt} \right\} d\xi_s dH \quad (42)$$

Thus, the total mass of carbon and sulfur consumed by chemical reaction, needed to evaluate the right side of Eq. 37, can be obtained by integrating Eq. 42 for all ξ_s, ξ_o, and for the entire height of the bed, H_o. The overall mass balance of Eq. 37 can, therefore, be written as

$$F_1 - F_3 - F_4 = \int_o^{H_o} \int_{\xi_{s,min}}^{\xi_{s,max}} 3f_Q(1 - \varepsilon)A_oP_2(\xi_s)\rho_Q$$

$$\left\{ \frac{\alpha_1}{\xi_s} d\xi_s + \frac{(1 - \alpha_1)}{\xi_s^3} \xi_c^2 \frac{d\xi_c}{dt} \right\} d\xi_s dH \quad (43)$$

The feed rate of char F_1, the overflow rate F_3, and the carryover rate F_4 are given in terms of their corresponding volumetric flow rates as follows.

$$F_1 = V_1(1 - \varepsilon_1)\rho_Q \quad (44)$$

$$F_3 = \int_{\xi_{s,min}}^{\xi_{s,max}} V_3(1 - \varepsilon_3)P_3(\xi_s) \rho_Q \left\{ \alpha_1 + (1 - \alpha_1) \frac{\xi_c^3}{\xi_s^3} \right\} d\xi_s \quad (45)$$

$$F_4 = \int_{\xi_{s,min}}^{\xi_{s,max}} V_4(1 - \varepsilon_4)P_4(\xi_s) \rho_Q \left\{ \alpha_1 + (1 - \alpha_1) \frac{\xi_c^3}{\xi_s^3} \right\} d\xi_s \quad (46)$$

The strategy of the calculations involves the manipulation of Eqs. 45 and 46 so that F_3 and F_4 could be determined in terms of the only unknown f_Q. Equation 43 is then employed to establish the value of f_Q. In the following we develop the mathematical relations expressing F_3 and F_4 in terms of various quantities and f_0.

Next we consider the mass balance at the steady state for char particles of size between ξ_s and $\xi_s + \Delta\xi_s$ for the entire system at a particular instant as shown in Figure 3. The corresponding relation for a system of shrinking particles is:
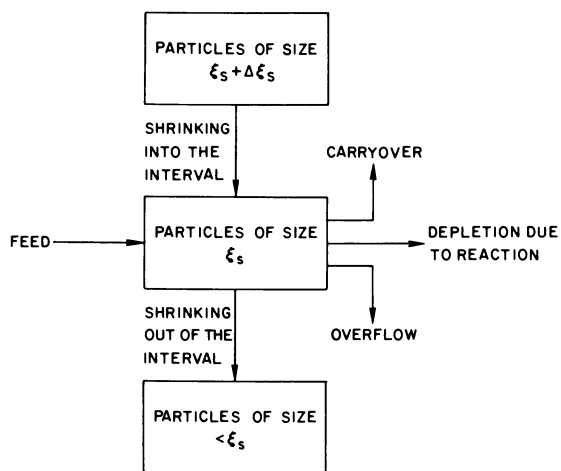
Figure 3.   Mass balance for shrinking char particles of size ξ_s

$$F_1 P_1(\xi_s)\Delta\xi_s - F_3 P_3(\xi_s)\Delta\xi_s - F_4 P_4(\xi_s)\Delta\xi_s$$

$$+ W_Q P_2(\xi_s)\left.\frac{d\xi_s}{dt}\right|_{\xi_s + \Delta\xi_s} - W_Q P_2(\xi_s)\left.\frac{d\xi_s}{dt}\right|_{\xi_s}$$

$$+ \left[\int_0^{H_o} 3f_Q(1-\epsilon)A_o\rho_Q P_2(\xi_s)\left\{\frac{\alpha_1}{\xi_s}\frac{d\xi_s}{dt} + \frac{(1-\alpha_1)}{\xi_s^3}\xi_c^2\frac{d\xi_c}{dt}\right\}dH\right]\Delta\xi_s = 0 \tag{47}$$

Similarly for a system consisting of growing particles

$$F_1 P_1(\xi_s)\Delta\xi_s - F_3 P_3(\xi_s)\Delta\xi_s - F_4 P_4(\xi_s)\Delta\xi_s + W_Q P_2(\xi_s)\left.\frac{d\xi_s}{dt}\right|_{\xi_s}$$

$$- W_Q P_2(\xi_s)\left.\frac{d\xi_s}{dt}\right|_{\xi_s + \Delta\xi_s} + \left[\int_0^{H_o} 3f_Q(1-\epsilon)A_o\rho_Q P_2(\xi_s)\right.$$

$$\left.\left\{\frac{\alpha_1}{\xi_s}\frac{d\xi_s}{dt} + \frac{(1-\alpha_1)}{\xi_s^3}\xi_c^2\frac{d\xi_c}{dt}\right\}dH\right]\Delta\xi_s = 0 \tag{48}$$

For simplicity we define

$$X_1 = \alpha_1 + (1-\alpha_1)(\xi_c^3/\xi_s^3) \tag{49}$$

Dividing Eq. 47 by $\Delta\xi_s$, taking limits as $\Delta\xi_s \to 0$ and substituting for F_1, F_3, F_4, and W_Q we get:

$$V_1(1-\epsilon_1)\rho_Q P_1(\xi_s) - V_3(1-\epsilon_3)\rho_Q X_1 P_3(\xi_s) - V_4(1-\epsilon_4)$$

$$\rho_Q X_1 P_4(\xi_s) + \int_0^{H_o} f_Q(1-\epsilon)A_o\rho_0\frac{d}{d\xi_s}\left(X_1 P_2(\xi_s)\frac{d\xi_s}{dt}\right)dH$$

$$+ \int_0^{H_o} 3f_Q(1-\epsilon)A_o\rho_0 P_2(\xi_s)\left\{\frac{\alpha_1}{\xi_s}\frac{d\xi_s}{dt} + \frac{(1-\alpha_1)}{\xi_s^3}\xi_c^2\frac{d\xi_c}{dt}\right\}dH = 0 \tag{50}$$

Similarly on dividing Eq. 48 by $\Delta\xi_s$, taking limits as $\Delta\xi_s \to 0$ and substituting for F_1, F_3, F_4, and W_Q we get:

$$V_1(1-\epsilon_1)\rho_Q P_1(\xi_s) - V_3(1-\epsilon_3)\rho_Q X_1 P_3(\xi_s) - V_4(1-\epsilon_4)$$

$$\rho_Q X_1 P_4(\xi_s) - \int_0^{H_o} f_Q(1-\epsilon)A_o\rho_Q\frac{d}{d\xi_s}\left(X_1 P_2(\xi_s)\frac{d\xi_s}{dt}\right)dH$$

$$+ \int_0^{H_o} 3f_Q(1-\epsilon)A_o\rho_Q P_2(\xi_s)\left\{\frac{\alpha_1}{\xi_s}\frac{d\xi_s}{dt} + \frac{(1-\alpha_1)}{\xi_s^3}\xi_c^2\frac{d\xi_c}{dt}\right\}dH = 0 \tag{51}$$

It may be noted that for growing particles $(d\xi_s/dt) > 0$ and for shrinking particles $(d\xi_s/dt) < 0$. Comparing Eqs. 50 and 51, which represent the mass balances for particles of size ξ_s for shrinking and growing particles respectively, it is seen that they both differ from each other only in the sign for the fourth term. In order to represent both of them by a single equation, we may substitute the absolute value of $d\xi_s/dt$ in Eq. 51, so that

$$V_1(1 - \epsilon_1)\rho_Q P_1(\xi_s) - V_3(1 - \epsilon_3)\rho_Q X_1 P_3(\xi_s) - V_4(1 - \epsilon_4)$$

$$\rho_Q X_1 P_4(\xi_s) - \int_0^{H_0} f_Q(1 - \epsilon) A_0 \rho_Q \frac{d}{d\xi_s} \left(X_1 P_2(\xi_s)\right) \left|\frac{d\xi_s}{dt}\right| dH$$

$$\hspace{8cm} (52)$$

$$+ \int_0^{H_0} 3 f_Q(1 - \epsilon) A_0 \rho_Q P_2(\xi_s) \left\{\frac{\alpha_1}{\xi_s}\frac{d\xi_s}{dt} + \frac{(1 - \alpha_1)}{\xi_s^3}\xi_c^2 \frac{d\xi_c}{dt}\right\} dH = 0$$

Simplification of Eq. 52 gives

$$V_1(1-\epsilon)P_1(\xi_s) - V_3(1-\epsilon_3)X_1 P_3(\xi_s) - V_4(1-\epsilon_4)X_1 P_4(\xi_s) - \int_0^{H_0} f_Q(1-\epsilon)A_0$$

$$\left[X_1 P_2(\xi_s) \frac{d}{d\xi_s}\left|\frac{d\xi_s}{dt}\right| + X_1 \left|\frac{d\xi_s}{dt}\right| \frac{dP_2(\xi_s)}{d\xi_s} - P_2(\xi_s) \cdot \right.$$

$$\left.\left|\frac{d\xi_s}{dt}\right| \left(\frac{3(\alpha_1 - 1)\xi_0^3 z}{(1 - z)\xi_s^4}\right)\right] dH + \int_0^{H_0} 3 f_Q(1 - \epsilon)A_0 P_2(\xi_s)$$

$$\left\{\frac{\alpha_1}{\xi_s}\frac{d\xi_s}{dt} + \frac{(1 - \alpha_1)\xi_c^2}{\xi_s^3}\frac{d\xi_c}{dt}\right\} dH = 0 \hspace{3cm} (53)$$

Equation 53 consists of three unknown quantities, _viz._, $P_2(\xi_s)$, $P_3(\xi_s)$, and $P_4(\xi_s)$. Fortunately, for fluidized bed operations these quantities are inter-related and this simplifies the calculation procedure. The relationships between these quantities are discussed below.

The solids in the bed are assumed to be backmixed and, therefore,

$$P_2(\xi_s) = P_3(\xi_s) \hspace{6cm} (54)$$

The elutriation constant for char particles is:

$$\kappa_Q(\xi_s) = \frac{V_4(1 - \epsilon_4)P_4(\xi_s)}{f_Q(1 - \epsilon)A_0 H_0 P_2(\xi_s)} \hspace{4cm} (55)$$

Therefore,

$$P_4(\xi_s) = \frac{f_Q(1 - \epsilon)A_o H_o \kappa_Q(\xi_s) P_2(\xi_s)}{V_4(1 - \epsilon_4)} \tag{56}$$

Substituting Eqs. 54 and 56 in Eq. 53 we get on simplification and rearrangement:

$$-f_Q(1-\epsilon)A_o X_1 \frac{dP_3(\xi_s)}{d\xi_s} \int_o^{H_o} \left| \frac{d\xi_s}{dt} \right| dH = -V_1(1 - \epsilon_1)P_1(\xi_s) + \left\{ V_3(1-\epsilon_3) \right.$$

$$\left. +f_Q(1-\epsilon)A_o H_o \kappa_Q(\xi_s) \right\} X_1 P_3(\xi_s) + f_Q(1 - \epsilon)A_o X_1 P_3(\xi_s) \int_o^{H_o} \frac{d}{d\xi_s} \left| \frac{d\xi_s}{dt} \right| dH$$

$$-f_Q(1-\epsilon)A_o \frac{3(\alpha_1-1)\xi_o^{3}Z}{(1-Z)\xi_s^4} P_3(\xi_s) \int_o^{H_o} \left| \frac{d\xi_s}{dt} \right| dH - 3f_Q(1-\epsilon)A_o P_3(\xi_s) \int_o^{H_o}$$

$$\left\{ \frac{\alpha_1}{\xi_s} \frac{d\xi_s}{dt} + \frac{(1-\alpha_1)\xi_c^2}{\xi_s^3} \frac{d\xi_c}{dt} \right\} dH \tag{57}$$

This analysis for particles of size between ξ_s and $\xi_s + d\xi_s$ can be easily extended to the feed with wide size distribution. The feed with wide size distribution can be looked upon as the sum of narrow cuts of solids and it will be reasonable to expect the outflow stream to be the sum of outflow streams from these narrow cuts. To achieve this we shall first examine the system using a single size feed.

Consider a feed of size $R_o(\xi_o)$. The particles change size as the reaction proceeds. Thus, for the entire system all particles will be less than or equal to ξ_o for shrinking particles, and equal to or greater than ξ_o for the growing particles. The above analysis will be performed for this feed for particles in the size range ξ_s and $\xi_s + \Delta\xi_s$ (not including ξ_o). Equation 57 can be applied directly as the feed size is constant and not included in the above size range we have,

$$F_1 P_1(\xi_s)\Delta\xi_s = 0 \tag{58}$$

Therefore, from Eq. 57 we can write as follows:

$$\frac{dP_3^*(\xi_s)}{P_3^*(\xi_s)} = \frac{-\left\{\frac{V_3(1-\varepsilon_3)}{f_Q(1-\varepsilon)A_o} + H_o\kappa Q(\xi_s)\right\}}{\int_o^{H_o}\left|\frac{d\xi_s}{dt}\right|dH} \, d\xi_s \; - \; \frac{\int_o^{H_o}\frac{d}{d\xi_s}\left|\frac{d\xi_s}{dt}\right|dH}{\int_o^{H_{max}}\left|\frac{d\xi_s}{dt}\right|dH} \, d\xi_s$$

$$+ \frac{1}{X_1}\left(\frac{3(\alpha_1-1)\xi_o^3 z}{(1-Z)\xi_s^4}\right) d\xi_s + \frac{3\alpha_1 d\xi_s}{X_1\xi_s^3} + \frac{3(1-\alpha_1)\xi_c^2}{X_1\xi_s^3}\left(\int_o^{H_o}\frac{d\xi_c}{dt}\,dH\right) \Bigg/$$

$$\left(\int_o^{H_o}\left|\frac{d\xi_s}{dt}\right|dH\right) d\xi_s \tag{59}$$

$P_3^*(\xi_s)$ is the size distribution of the particles in the bed and overflow stream for a feed of fixed particle size ξ_o. The relation connecting ξ_s, ξ_c, ξ_o and Z is,

$$\xi_s^3 = Z\xi_o^3 + (1-Z)\xi_c^3 \tag{60}$$

Therefore

$$\left(\frac{d\xi_c}{dt}\right)\Bigg/\left(\frac{d\xi_s}{dt}\right) = \frac{\xi_s^2}{(1-Z)\xi_c^2} \tag{61}$$

Substituting Eqs. 49, 60, and 61 into Eq. 59 we finally get,

$$\frac{dP_3^*(\xi_s)}{P_3^*(\xi_s)} = \frac{-\left\{\frac{V_3(1-\varepsilon_3)}{f_Q(1-\varepsilon)A_o} + H_o\kappa Q(\xi_s)\right\}}{\int_o^{H_o}\left|\frac{d\xi_s}{dt}\right|dH} \, d\xi_s \; - \; \frac{\int_o^{H_o}\frac{d}{d\xi_s}\left|\frac{d\xi_s}{dt}\right|dH}{\int_o^{H_o}\left|\frac{d\xi_s}{dt}\right|dH} \, d\xi_s$$

$$+ \frac{3(\alpha_1-1)\xi_o^3 z}{X_1(1-Z)\xi_s^4} \, d\xi_s + \frac{3(1-\alpha_1 Z)}{X_1(1-Z)\xi_s} \tag{62}$$

where $X_1 = \alpha_1 + (1-\alpha_1)(\xi_s^3 - Z\xi_o^3)/(1-Z)\xi_s^3$ \hfill (63)

Integration with respect to ξ_s leads to the following:

$$\ln \frac{P_3^*(\xi_s)}{P_3^*(\xi_o)} = - \int_{\xi_o}^{\xi_s} \frac{\left\{ \frac{V_3(1-\epsilon_3)}{f_0(1-\epsilon)A_0} + H_0 \kappa_0(\xi_s) \right\}}{\int_0^{H_0} \left| \frac{d\xi_s}{dt} \right| dH} d\xi_s - \ln \frac{\int_0^{H_0} \left| \frac{d\xi_s}{dt} \right| dH}{\int_0^{H_0} \left| \frac{d\xi_s}{dt} \right| dH \Big|_{\xi_s = \xi_o}}$$

$$+ \ln \frac{\xi_s^3}{\xi_o^3} \tag{64}$$

The above expression gives $P_3^*(\xi_s)$ if we could evaluate $P_3^*(\xi_o)$ which comes out to be

$$P_3^*(\xi_o) = \frac{V_1(1-\epsilon_1)}{f_0(1-\epsilon)A_0 \int_0^{H_0} \left| \frac{d\xi_s}{dt} \right| dH} \tag{65}$$

Substituting Eq. 65 into Eq. 64 we get,

$$P_3^*(\xi_s) = \frac{V_1(1-\epsilon)\xi_s^3 I(\xi_s,\xi_o)}{f_0(1-\epsilon)A_0\xi_o^3 \int_0^{H_0} \left| \frac{d\xi_s}{dt} \right| dH} \tag{66}$$

where

$$I(\xi_s,\xi_o) = \exp\left[-\int_{\xi_o}^{\xi_s} \frac{\left\{ \frac{V_3(1-\epsilon_3)}{f_0(1-\epsilon)A_0} + H_0\kappa_0(\xi_s) \right\}}{\int_0^{H} \left| \frac{d\xi_s}{dt} \right| dH} d\xi_s \right] \tag{67}$$

The above results apply to a single size feed. For a wide distribution

$$P_3(\xi_s)\Delta\xi_s = \sum_{\xi_{o,min}}^{\xi_{o,max}} P_3^*(\xi_s)\Delta\xi_s P_1(\xi_o)\Delta\xi_o \tag{68}$$

where $\xi_{o,max}$ and $\xi_{o,min}$ are the largest and the smallest size particles in the feed.

The output distribution function $P_3^*(\xi_s)$ for constant input size ξ_o is already derived and is given by Eq. 66, dividing Eq. 68 by $\Delta\xi_s$ and taking limits as $\Delta\xi_s \to 0$, we get

$$P_3(\xi_s) = \int_{\xi_{o,min}}^{\xi_{o,max}} P_3(\xi_s) \, P_1(\xi_o) d\xi_o \qquad (69)$$

Substituting Eq. 66 into Eq. 69 we get

$$P_3(\xi_s) = \frac{V_1(1-\varepsilon_1)}{f_Q(1-\varepsilon)A_o} \xi_s^3 \int_{\xi_{o,min}}^{\xi_{o,max}} \frac{P_1(\xi_o) I(\xi_s,\xi_o) d\xi_o}{H \; \xi_o^3 \int_o \left| \dfrac{d\xi_s}{dt} \right| dH} \qquad (70)$$

Equation 72 defines $P_3(\xi_s)$ in which there are two unknowns viz., V_3 and f_Q. One of them can be eliminated by utilizing the normal-ization condition for $P_3(\xi_s)$. Integration of Eq. 70 for all sizes of particles in the bed ($\xi_{s,min}$ to $\xi_{s,max}$) yields

$$\frac{f_Q(1-\varepsilon)A_o}{V_1(1-\varepsilon_1)} = \int_{\xi_{s,min}}^{\xi_{s,max}} \int_{\xi_{o,min}}^{\xi_{o,max}} \frac{\xi_s^3 P_1(\xi_o) I(\xi_s,\xi_o)}{H \; \xi_o^3 \int_o \left| \dfrac{d\xi_s}{dt} \right| dH} \, d\xi_o d\xi_s \qquad (71)$$

It may be noted that $\xi_{s,max} = \xi_{o,max}$ for shrinking particles. If H is nondimensionalized such that: $\eta = (H/H_o)$. The resulting equations are then utilized to compute F_3 from Eq. 45 as a function of f_Q. Next we proceed to establish a mathematical framework in a somewhat analogous fashion for calculating F_4 as a function of f_Q.

Combining Eqs. 54 and 56 and substituting for $P_3(\xi_s)$ from Eq. 70 we get,

$$P_4(\xi_s) = \kappa_Q(\xi_s) \frac{V_1(1-\varepsilon_1)}{V_4(1-\varepsilon_4)} \xi_s^3 \int_{\xi_{o,min}}^{\xi_{o,max}} \frac{P_1(\xi_o) I(\xi_s,\xi_o)}{1 \; \xi_o^3 \int_o \left| \dfrac{d\xi_s}{dt} \right| d\eta} \, d\xi_o \qquad (72)$$

The normalization of the size distribution function $P_4(\xi_s)$ finally yields

$$\frac{V_4(1-\epsilon_4)}{V_1(1-\epsilon_1)} = \int_{\xi_{s,min}}^{\xi_{s,max}} \int_{\xi_{o,min}}^{\xi_{o,max}} \frac{\xi_s^3 \kappa_0(\xi_s)P_1(\xi_o)I(\xi_s,\xi_o)}{\xi_o^3 \int_0^1 \left|\frac{d\xi_s}{dt}\right| d\eta} \tag{73}$$

Equations 72, 73 and 71 can be solved simultaneously to obtain $P_4(\xi_s)$ and V_4 as a function of f_0. These relations are then utilized in Eq. 46 to obtain F_4 as a function of f_0 only.

The mathematical development presented so far enables us to employ the mass balance of Eq. 43 to determine uniquely the fraction of char present in the bed for a given set of feed and operating conditions.

A similar set of equations can be derived for the various streams of limestone. For the general case when the size of the particle changes as it reacts with oxygen and sulfur dioxide, the following equations apply. The overall mass balance is given by the following relation which is analogous to Eq. 43 developed above for char particles:

$$F_1' - F_3' - F_4' = \int_{\xi_{s,min}'}^{\xi_{s,max}'} \int_0^1 3f_N(1-\epsilon)A_oH_oP_3'(\xi_s')\rho_N$$

$$\left\{\frac{\alpha_2}{\xi_s'} \frac{d\xi_s'}{dt} + \frac{(1-\alpha_2)\xi_c'^2}{\xi_s'^3} \frac{d\xi_c'}{dt}\right\} d\eta \ d\xi_s' \tag{74}$$

where the feed rate of limestone F_1', the overflow rate F_3', and the carryover rate F_4', may be expressed in terms of the corresponding volumetric flow rates.

Adopting the approach developed above for the char particles combustion, the size distribution function of limestone particles as a result of sulfation reaction in the overflow stream which is the same as in the bed is given by,

$$P_3'(\xi_s') = \frac{V_1'(1-\epsilon_1')}{f_N(1-\epsilon)A_oH_o}\xi_s'^3 \int_{\xi_{o,min}'}^{\xi_{o,max}'} \frac{P_1'(\xi_o')I'(\xi_s',\xi_o')d\xi_o'}{\xi_o'^3 \int_0^1 \left|\frac{d\xi_s'}{dt}\right| d\eta} \tag{75}$$

The normalization property of $P_3'(\xi_s')$ leeds to the following relationship between V_1' and V_3':

$$\frac{f_N(1-\epsilon)A_oH_o}{V_1'(1-\epsilon_1')} = \int_{\xi_{s,min}'}^{\xi_{s,max}'} \int_{\xi_{o,min}'}^{\xi_{o,max}'} \frac{\xi_s'^3 P_1'(\xi_o')I'(\xi_s',\xi_o')d\xi_o'd\xi_s'}{\xi_o'^3 \int_0^1 \left|\frac{d\xi_s'}{dt}\right| d\eta} \tag{76}$$

Here

$$I(\xi_s',\xi_o') = \exp\left[-\int_{\xi_o'}^{\xi_s'}\frac{\left\{\dfrac{V_3'(1-\varepsilon_3)}{f_N(1-\varepsilon)A_oH_o} + \kappa_N(\xi_s')\right\} d\xi_s'}{\displaystyle\int_0^1\left|\frac{d\xi_s'}{dt}\right| d\eta}\right] \tag{77}$$

and

$$\kappa_N(\xi_s') = \frac{V_4'(1-\varepsilon_4)P_4'(\xi_s')}{A_oH_o(1-\varepsilon)f_NP_2'(\xi_s')} \tag{78}$$

The size distribution of limestone in the elutriated stream, $P_4'(\xi_s')$, is obtained from Eq. 78 in which $P_2'(\xi_s')$ is replaced with $P_3'(\xi_s')$ (backmix approximation) as defined by Eqs. 75 and 77.

In the present formulation the size of the fluidized bed is kept constant by the presence of an overflow pipe, Figure 1, and consequently A_o and H_o are constant. The fraction of dolomite in the bed, f_N, is related to the fraction of char in the bed such that

$$f_N = 1 - f_Q \tag{79}$$

f_Q has already been determined and hence it may be assumed that f_N is known.

In case the size and density of the limestone particles remain the same as a result of chemical reaction, the above relations are simplified.

We next develop the mass balance equations for the gaseous reactant (oxygen) and the product (sulfur dioxide). The gas flow in the reactor is assumed to be in plug flow and hence the concentration of these gases will depend only on the height H, in the bed above the distributor plate. The rate of consumption of oxygen by reactions 1, 2 and 3 can be obtained from Eqs. 43 and 80 and the stoichiometry of these reactions. We will first examine Eq. 43 which may be rewritten as follows after appropriate substitutions.

$$\text{RHS of Eq. 43} = \frac{3V_1(1-\varepsilon_1)\rho_0(1-\alpha_1)Z}{\tau_1}\int_{\xi_{s,min}}^{\xi_{s,max}}\int_{\xi_{o,min}}^{\xi_{o,max}}\int_0^1 \frac{\omega AC}{U_c}$$

$$\frac{I(\xi_s,\xi_o)P_1(\xi_o)\exp\left\{\dfrac{E_1}{RT_o}\left(1-\dfrac{1}{U_c}\right)\right\}}{\displaystyle\int_0^1\left|\frac{d\xi_s}{dt}\right| d\eta} d\eta d\xi_o d\xi_s$$

$$+ \frac{3V_1(1-\varepsilon_1)\rho_Q(1-\alpha_1 Z)}{\tau_2} \int_{\xi_{s,min}}^{\xi_{s,max}} \int_{\xi_{o,min}}^{\xi_{s,max}} \int_{0}^{1} \frac{\omega_{AC}}{U_c}$$

$$\frac{I(\xi_s,\xi_o)P_1(\xi_o) \exp\left\{\frac{E_2}{RT_o}\left(1-\frac{1}{U_c}\right)\right\}}{\int_{0}^{1} \left|\frac{d\xi_s}{dt}\right| d\eta} d\eta d\xi_o d\xi_s \qquad (80)$$

The first term of Eq. 80 represents the mass loss of char particles due to carbon combustion and the second term represents the mass loss of char particles due to sulfur reaction with oxygen. Using the stoichiometry of reactions 1 and 2, we can obtain the moles of oxygen used up in these respective reactions for any arbitrary height η as,

$$\begin{bmatrix}\text{Moles of oxygen} \\ \text{used upto bed} \\ \text{height } \eta \text{ due to} \\ \text{reaction 1}\end{bmatrix} = \frac{3V_1(1-\varepsilon_1)\rho_Q(1-\alpha_1 Z)}{M_J \tau_1} \int_{\xi_{s,min}}^{\xi_{s,max}} \int_{\xi_{o,min}}^{\xi_{o,max}} \int_{0}^{\eta} \frac{\omega_{AC}}{U_c}$$

$$\frac{I(\xi_s,\xi_o)P_1(\xi_o) \exp\left\{\frac{E_1}{RT_o}\left(1-\frac{1}{U_c}\right)\right\}}{\int_{0}^{1} \left|\frac{d\xi_s}{dt}\right| d\eta} \qquad (81)$$

$$\begin{bmatrix}\text{Moles of oxygen} \\ \text{used upto bed} \\ \text{height } \eta \text{ due to} \\ \text{reaction 2}\end{bmatrix} = \frac{3V_1(1-\varepsilon_1)\rho_Q(1-\alpha_1 Z)}{M_S \tau_2} \int_{\xi_{s,min}}^{\xi_{s,max}} \int_{\xi_{o,min}}^{\xi_{o,max}} \int_{0}^{\eta} \frac{\omega_{AC}}{U_c}$$

$$\frac{I(\xi_s,\xi_o)P_1(\xi_o) \exp\left\{\frac{E_2}{RT_o}\left(1-\frac{1}{U_c}\right)\right\}}{\int_{0}^{1} \left|\frac{d\xi_s}{dt}\right| d\eta} d\eta d\xi_o d\xi_s \qquad (82)$$

[Moles of oxygen consumed upto bed height η due to reaction 3] $= \dfrac{3V_1'(1-\varepsilon_1')\rho_N(1-\alpha_2 Z')}{2M_S\,\tau_3} \displaystyle\int_{\xi_s',min}^{\xi_s',max} \int_{\xi_o',min}^{\xi_o',max} \int_o^{\eta} \dfrac{\omega_{BC}}{U_C'}$

$$\dfrac{I'(\xi_s',\xi_o')P_1'(\xi_o)\ \exp\left\{\dfrac{E_3}{RT_o}\left(1-\dfrac{1}{U_c'}\right)\right\}}{\displaystyle\int_o^{1}\left|\dfrac{d\xi_s}{dt}\right|\ d\eta} d\eta\, d\xi_o'\, d\xi_s' \qquad (83)$$

Since there is only a small change in the total moles of gases in the fluidized bed combustor as a result of chemical reactions, we can assume that the gas flow remains unchanged. Let this flow be Y. Also the bulk temperature of the fluidized bed remains constant, total gas concentration remains constant throughout the reactor and hence

$$\omega_{AH} = C_{AH}/C_{AO} \qquad (84)$$

The rate of change of oxygen concentration with height in the fluidized bed is given by the following relation.

$$YC_{AO}\,\dfrac{d\omega_{AH}}{d\eta} = -\dfrac{3V_1(1-\varepsilon_1)\rho_O(1-\alpha_1 Z)}{M_J\,\tau_1}\displaystyle\int_{\xi_s,min}^{\xi_s,max}\int_{\xi_o,min}^{\xi_o,max}\dfrac{\omega_{AC}}{U_c}$$

$$\dfrac{I(\xi_s,\xi_o)P_1(\xi_o)\ \exp\left\{\dfrac{E_1}{RT_o}\left(1-\dfrac{1}{U_c}\right)\right\}}{\displaystyle\int_o^{1}\left|\dfrac{d\xi_s}{dt}\right|\ d\eta}\ d\xi_o\,d\xi_s$$

$$\dfrac{-3V_1(1-\varepsilon_1)\rho_O(1-\alpha_1 Z)}{\tau_2\,M_S}\displaystyle\int_{\xi_s,min}^{\xi_s,max}\int_{\xi_o,min}^{\xi_o,max}\dfrac{\omega_{AC}}{U_c}$$

$$\dfrac{I(\xi_s,\xi_o)P_1(\xi_o)\ \exp\left\{\dfrac{E_2}{RT_o}\left(1-\dfrac{1}{U_c}\right)\right\}}{\displaystyle\int_o^{1}\left|\dfrac{d\xi_s}{dt}\right|\ d\eta}\ d\xi_o\,d\xi_s$$

$$- \frac{3V_1'(1-\varepsilon_1')\rho_N(1-\alpha_2 Z')}{2M_S\,\tau_3} \int\limits_{\xi_s',min}^{\xi_s',max} \int\limits_{\xi_o',min}^{\xi_o',max} \frac{\omega_{BC}}{U_c'}$$

$$\frac{I'(\xi_s',\xi_o')P_1'(\xi_o')\,\exp\left\{\dfrac{E_3}{\overline{RT}_o}\left(1-\dfrac{1}{U_c'}\right)\right\}}{\displaystyle\int\limits_o^1 \left|\dfrac{d\xi_s'}{dt}\right|\,d\eta}\,d\xi_o'd\xi_s' \tag{85}$$

The boundary condition for Eq. 85 is

$$\omega_{AH} = 1 \text{ at } \eta = 0 \tag{86}$$

The solution of Eqs. 85 with 86 will yield the oxygen concentration profile along the fluidized bed combustor.

Similarly the mass balance equation for sulfur dioxide is

$$YC_{AO}\frac{d\omega_{BH}}{d\eta} = \frac{3V_1(1-\varepsilon_1)\rho_0(1-\alpha_1 Z)}{\tau_2\,M_S} \int\limits_{\xi_s,min}^{\xi_s,max}\int\limits_{\xi_o,min}^{\xi_o,max}\frac{\omega_{AC}}{U_c}$$

$$\frac{I(\xi_s,\xi_o)P_1(\xi_o)\,\exp\left\{\dfrac{E_2}{\overline{RT}_o}\left(1-\dfrac{1}{U_c}\right)\right\}}{\displaystyle\int\limits_o^1\left|\dfrac{d\xi_s}{dt}\right|\,d\eta}\,d\xi_o d\xi_s$$

$$-\frac{3V_1'(1-\varepsilon_1')\rho_N(1-\alpha_2 Z')}{\tau_3\,M_S}\int\limits_{\xi_o',max}^{\xi_s',max}\int\limits_{\xi_o',min}^{\xi_o',max}\frac{\omega_{BC}}{U_c'}$$

$$\frac{I'(\xi_s',\xi_o')P_1'(\xi_o')\,\exp\left\{\dfrac{E_3}{\overline{RT}_o}\left(1-\dfrac{1}{U_c'}\right)\right\}}{\displaystyle\int\limits_o^1\dfrac{d\xi_s'}{dt}\,d\eta}\,d\xi_o'd\xi_s' \tag{87}$$

The boundary condition for Eq. 87 is given by

$$\omega_{BH} = 0 \text{ at } \eta = 0 \tag{88}$$

The solution of Eq. 87 with Eq. 88 will establish the sulfur dioxide concentration profile along the fluidized bed combustor.

There are two more quantities that must be defined to complete the description of the fluidized bed combustor viz., the carbon combustion efficiency, η_{CCE}, and sulfur absorption efficiency, η_{SAE}. These are:

$$F_1 f_c \eta_{CCE} = \frac{3V_1(1-\epsilon_1)\rho_0(1-\alpha_1 Z)}{\tau_1} \int_{\xi_{s,min}}^{\xi_{s,max}} \int_{\xi_{0,min}}^{\xi_{0,max}} \int_0^1$$

$$\frac{\omega_{AC}}{U_c} \frac{I(\xi_s,\xi_0)P_1(\xi_0) \exp\left\{\frac{E_1}{RT_0}\left(1 - \frac{1}{U_c}\right)\right\}}{\int_0^1 \left|\frac{d\xi_s}{dt}\right| d\eta} d\eta d\xi_0 d\xi_s \tag{89}$$

and

$$\eta_{SAE} = 1 - \frac{C_{Ao}M_S\omega_{BH}(\eta=1)}{F_1 f_s \eta_{CCE}} \tag{90}$$

The sulfur adsorption efficiency, η_{SAE}, is defined as the ratio of moles of sulfur dioxide consumed by the sulfation reaction to the moles of sulfur dioxide produced due to char combustion. The above equations will be utilized to analyze the parametric sensitivity of the fluidized-bed combustion operation.

Numerical Calculations: Parametric Investigations

The mathematical model for char combustion described in the previous two sections is applicable to a bed of constant volume, i.e., to a fluidized bed of fixed height, H_0, and having a constant cross-sectional area, A_0. The constant bed height is maintained by an overflow pipe. For this type of combustor operating for a given feed rate of char and limestone particles of known size distributions, the model presented here can predict the following:
(1) the fraction of char particles in the bed, f_0;
(2) the fraction of limestone particles in the bed, f_N;
(3) the size distribution of char particles in the bed or in the overflow, $P_3(\xi_s)$;

(4) the size distribution of char particles in the bed or
    in the overflow, $P_3'(\xi_s')$;
(5) the overflow rate of char particles, F_3;
(6) the overflow rate of limestone particles, F_3';
(7) the flow rate of char particles in the carryover
    stream, F_4;
(8) the particle size distribution in the carryover stream,
    $P_4(\xi_s)$;
(9) the flow rate of limestone particles in the carryover
    stream, F_4';
(10) the particle size distribution of limestone particles
    in the carryover stream, $P_4'(\xi_s')$;
(11) the concentration profile of oxygen along the fluidized
    bed, ω_{AH};
(12) the concentration profile of sulfur dioxide along the
    fluidized bed, ω_{BH};
(13) the carbon conversion efficiency, η_{CCE}; and
(14) the sulfur absorption efficiency, η_{SAE}.

The above calculation is quite tedious and gets complicated
by the fact that the properties which ultimately control the
magnitude of these fourteen unknown quantities further depend on
the physical and chemical parameters of the system such as
reaction rate constants, initial size distribution of the feed,
bed temperature, elutriation constants, heat and mass transfer
coefficients, particle growth factors for char and limestone
particles, flow rates of solid and gaseous reactants. In a
complete analysis of a fluidized bed combustor with sulfur
absorption by limestone, the influence of all the above parameters
must be evaluated to enable us to optimize the system. In the
present report we have limited the scope of our calculations by
considering only the initial size of the limestone particles and
the reaction rate constant for the sulfation reaction.

Further, it is not necessary to carry out excessive calcu-
lations to investigate the parametric sensitivity of the combustor
operation. The same goal can be accomplished by assuming some of
the fourteen unknowns and determining the remaining by the
solution of the above mentioned equations. This procedure is
adopted here. We assume a form for the oxygen profile, values of
the carbon combustion and sulfur absorption efficiencies, char
feed rate, and the various constants of the system and then the
framework of mathematical model is employed to evaluate the
amount of dolomite, F_1', needed to obtain such an operation. In
general, the functional form for oxygen profile in a combustor is
as follows:

$$\omega_{AH} = a^* + (1 - a^*)e^{-b^*\eta} \tag{91}$$

Here the constants a^* and b^* are to be specified. The constant
a^* is generally related to the excess oxygen in the flue gas
whereas b^* establishes the slope of the profile. A larger value

of b* signifies that a major degree of combustion reactions take
place near the bottom of the reactor.

The fluidized-bed coal combustion calculations described
below according to the mathematical model developed here will
employ the parameter values given in Table 1. The analysis is
confined to a fixed temperature of 1225 K for the bed. Figure 4
gives the normalized particle size distribution for char and
dolomite feeds for a particular case when $\bar{r} = \bar{r}' = 0.04$ cm. The
particle size distribution for char in the feed is held constant,
whereas for dolomite it is changed such that $\bar{r}'$ varies from 0.02
to 0.08 cm. The reaction rate between sulfur dioxide and dolomite
is changed by varying the reaction rate constant, $k_3(T_o)$, from
380 to 960 $cm^4/mol \cdot s$. The changes in the dolomite size and
reaction rate constant reflect in τ_3 and $\phi_{\bar{3}}$ as seen from Table
1. The variation in the heat and mass transfer coefficients due
to change in particle size within the range considered here is
found to be negligible ($\pm 5\%$) and, therefore, is ignored in the
present calculations. In one of our test runs the sulfur
absorption efficiency is kept constant at 0.99 while the carbon
combustion efficiency is varied from 0.7 to 0.995. In all of the
remaining runs, the carbon combustion efficiency is held constant
at 0.995 while the sulfur absorption efficiency is varied from
0.7 to 0.99. It may be pointed out that the dolomite feed rate
is directly proportional to the rate of change of size of the
dolomite particle, Eq. 73, and consequently the dolomite require-
ment is strongly dependent upon the factors influencing the rate
of change of the dolomite particle. Let us examine the effect of
changing oxygen profile on the dolomite requirement.

If the values of η_{CCE} and η_{SAE} are fixed, the parameter a*
of Eq. 91 has a definite value. The oxygen concentration
profiles are then changed by altering the value of the parameter
b*. By assuming b* as 2.5, 4.5 and 6.5, the computed oxygen
distribution in the bed is obtained as shown in Figure 5. The
effect of these profiles is examined for two values of $k_3(T_o)$,
480 and 960 $cm^4/mol \cdot s$, and two values of $\bar{r}'$ (0.04 and 0.08 cm) on
limestone requirement. The results are shown in Figures 6 and 7
for two values of η_{SAE}, viz., 0.8 and 0.99. It is seen that for
the change in oxygen profile considered here, the variation in
limestone requirements, F_1', is within 10%. The trend in the
change of the dolomite requirement with the change in the value
of b* is always the same, regardless of the value of $k_3(T_o)$, $\bar{r}'$
and η_{SAE}. It is, therefore, appropriate to fix a value of
b* while investigating the parametric sensitivity of the proposed
mathematical model.

The concentration profile of oxygen in the bed is fixed by
establishing apriori a value for b* as 4.5 and that of a* as
obtained from the assumed values of carbon conversion and sulfur
absorption efficiencies. For a given oxygen profile the reaction
rate constant, $k_3(T_o)$, and the size of the dolomite feed are
varied. The changes in both of these parameters affect the value
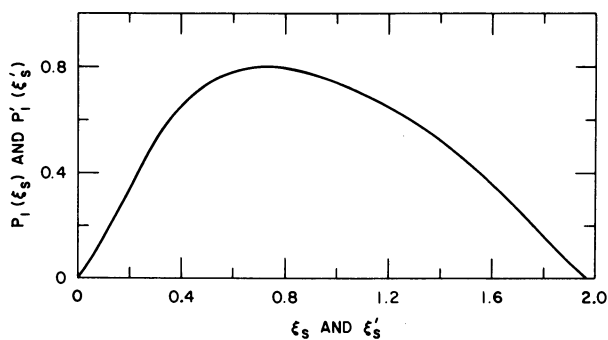
Figure 4. *Particle size distribution of char, $P_1(\xi_s)$, and limestone, $P_1'(\xi_s')$, feeds: $\bar{r} = \bar{r}' = 0.04$ cm*
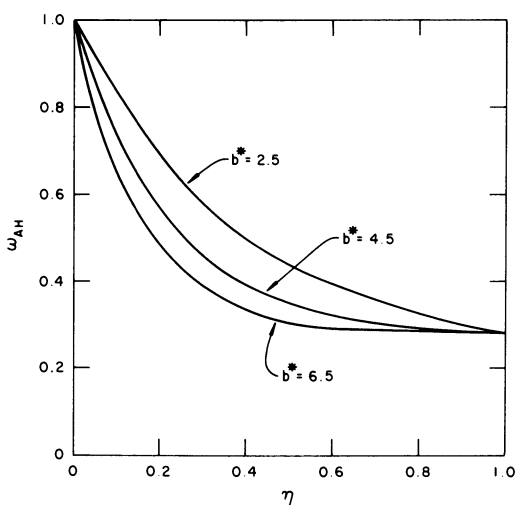

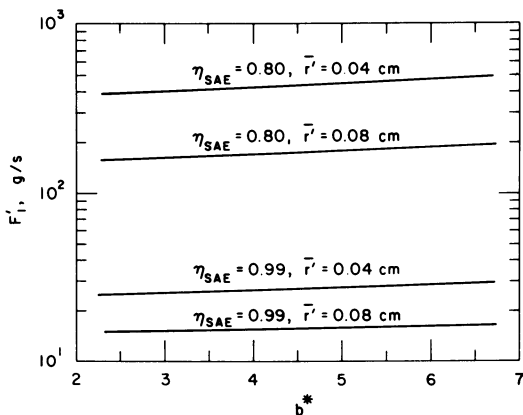Figure 5. *Oxygen profiles in the fluidized-bed combustor corresponding to $\eta_{CCE} = 0.995$ and $\eta_{SAE} = 0.99$*

Figure 6.   Effect of oxygen concentration profile on limestone requirement for different assumed η_{SAE} and $\bar{r}'$
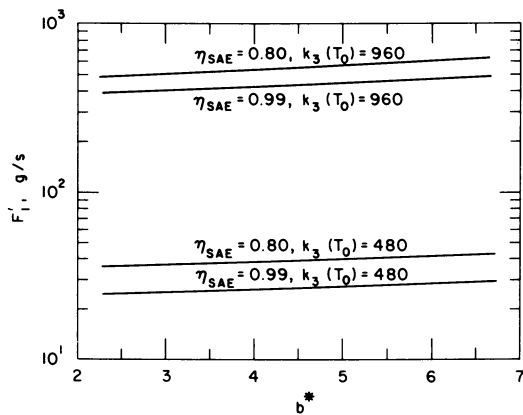

Figure 7.   Effect of oxygen concentration profile on limestone requirement for different assumed η_{SAE} and $k_3(T_o)$

Table 1. Constants Used in Coal Combustion Model Calculations:

$Z = 0.05$, $Z' = 1.25$, $K_1 = 1.0$, $K_3 = 0.4$, $K_4 = 0.2$, $\tau_1 = 7.6$ s,
$\tau_2 = 7.6$ s, $E_1/\bar{R}T_0 = 13.8$, $E_2/\bar{R}T_0 = 12.3$, $E_3/\bar{R}T_0 = 5.9$,
$\beta_1 = 0.0057$, $\beta_2 = 0.0068$, $\beta_3 = 0.0086$, $\phi_{1\bar{r}} = 4.9$, $\phi_{2\bar{r}} = 0.21$,
$F_1 = 52$ g/s, $\varepsilon = 0.50$, $\varepsilon_1 = \varepsilon_1' = \varepsilon_3 = \varepsilon_4 = 0.45$, $u = 76.2$ cm/s,
$H_0 = 140$ cm, $\alpha_1 = 2.1$, $\alpha_2 = 1.36$, $\rho_0 = 1.0$ g/cm^3, $\rho_N = 2.45$ g/cm^3,
$\rho_S = 0.035$ g/cm^3, $M_J = 12$ g/gmole, $M_N = 100$ g/gmole,
$M_S = 32$ g/gmole, $Y = 4.25 \times 10^5$ cm^3/s, $C_{AO} = 1.2 \times 10^{-4}$ mole/cm^3,
$\kappa_0(\xi_s) = 1.6 \times 10^{-5} u^4/\xi_s^3$, $\kappa_N(\xi_s') = 1.6 \times 10^{-5} u^4/\xi_s'^3$, $f_c = 0.82$, and
$\bar{r} = 0.04$ cm.

$\bar{r}'$ cm	$k_3(T_0)$ cm^4/s·mol	$\phi_{3\bar{r}}$ (-)	τ_3 s	η_{CCE} (-)	η_{SAE} (-)
0.04	380	1.29	8.6	0.995	0.7-0.99
0.04	480	1.63	6.8	0.995	0.7-0.99
0.04	580	1.97	5.8	0.995	0.7-0.99
0.04	960	3.26	3.4	0.995	0.7-0.99
0.02	480	0.79	3.3	0.995	0.7-0.99
0.06	480	2.36	9.9	0.995	0.7-0.99
0.08	480	3.14	13.2	0.995	0.7-0.99
0.04	480	1.63	6.8	0.7-0.995	0.99

of $d\xi_s'/dt$ according to Eq. 20. The value of $d\xi_s'/dt$ is directly proportional to $k_3(T_0)$ and also to the dolomite feed size, $\bar{r}'$. Furthermore, the dolomite requirement is directly proportional to $d\xi_s'/dt$. Consequently, F_1' is altered in magnitude which is directly proportional to the changes made in $k_3(T_0)$ and $\bar{r}'$. The changes in the limestone requirement are also related to the residence time of the limestone in the bed. If the rate of reaction $k_3(T_0)$ is increased, less reaction time is needed to achieve the same degree of sulfur retention. Shorter residence times are obtained by increasing the limestone feed rate for the same bed volume. Thus, F_1' will increase with an increase and $d\xi_s'/dt$. Alternately, if for the same volumetric feed rate $d\xi_s'/dt$ is increased, an improved sulfur retention will result.

Figure 8 represents the variation in limestone requirement as a function of sulfur absorption efficiency for various values of $k_3(T_0)$. The results emphasize that for a given value of $k_3(T_0)$, if the lmestone feed rate is increased which for a bed of fixed size implies a reduction in residence time, the sulfur absorption efficiency is correspondingly decreased. The implication of this result for an actual operating plant is important. It is implicit in these plots that if the limestone feed rate is held constant, η_{SAE}, increases with an increase in $k_3(T_0)$.
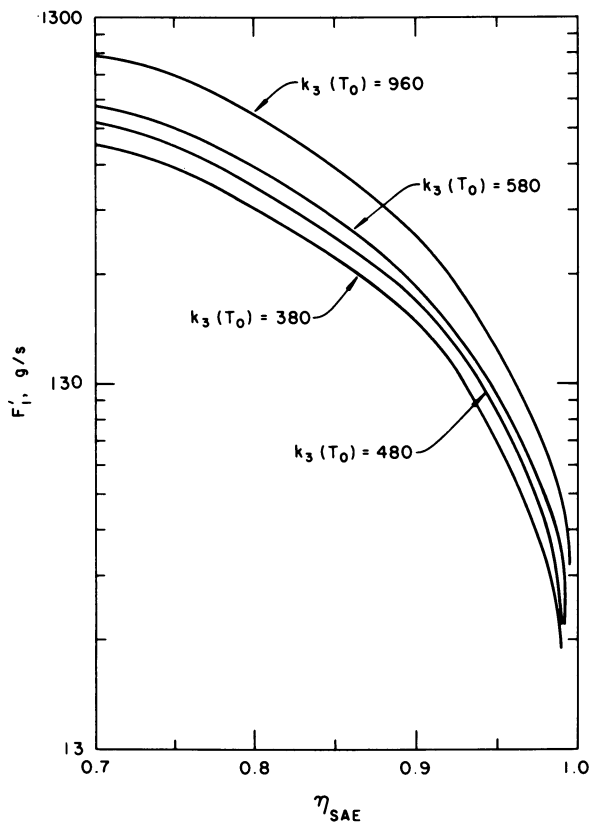
Figure 8.   Limestone requirement, F_1', as a function of η_{SAE} and $k_3(T_o)$ in $cm^4/$ mol · s corresponding to $\bar{r} = \bar{r}' = 0.04$ cm and $\eta_{CCE} = 0.995$
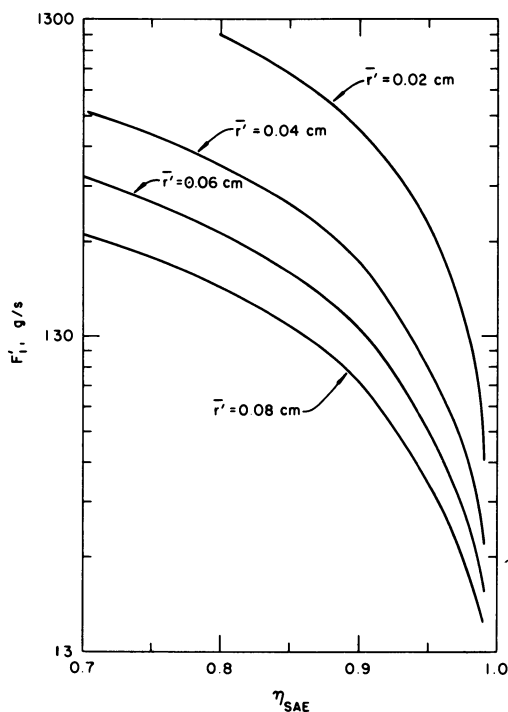
Figure 9. Limestone requirement, F_1', as a function of η_{SAE} and $\overline{r'}$ corresponding to $\overline{r} = 0.04$ cm, $\eta_{CCE} = 0.995$ and $k_s(T_o) = 480$ cm^4/mol · s

Figure 9 illustrates the effect of changing limestone average size, $\bar{r}'$, in the feed stream on the dependence of limestone feed rate, F_1', and on sulfur absorption efficiency, η_{SAE}. All the plots refer to a constant value of $k_3(T_o)$. These results suggest that if the feed size of limestone is kept fixed, an increase in the limestone feed rate will result in the reduction of sulfur absorption efficiency. These results also emphasize that if the same sulfur retention is to be obtained when the size of the limestone particles is decreased the feed rate must be increased. However, for the same feed rate of limestone, a decrease in the size of limestone particles results in an increased sulfur retention. This may be explained on the basis of an increase in the overall surface area per unit volume of the bed when the average diameter of the particles decreases. It may be noted from Figure 9 that regardless of the limestone particle size, if sufficient residence time is allowed for limestone particles in the bed, it is possible to obtain sufficiently high sulfur retention.

The influence of carbon conversion efficiency on the requirement of limestone for a fixed value of sulfur absorption efficiency is also computed. The generation of sulfur dioxide is found to be directly related to the amount of carbon combusted. The generation rate of sulfur dioxide reduces with the decrease in carbon conversion efficiency and hence the limestone requirement also decreases. A reduction in the carbon conversion efficiency from 99.5 to 70.0% causes a reduction in dolomite requirement from 27.5 to 18.9 g/s for a 99% sulfur absorption efficiency.

In Figure 10 the dependence of oxygen profile, ω_{AH}, and sulfur dioxide profile, ω_{BH}, on the dimensionless bed height, η, for the case of 99.5% sulfur absorption efficiency is presented. The particle size distributions in the bed and in the elutriated stream for char and limestone are also computed but for the sake of brevity, these are not presented here. A more detailed discussion of these results are available elsewhere (26).

Acknowledgments

Nomenclature

A_o = cross sectional area of reactor, m^2
a^* = constant in oxygen concentration profile, eq. 91, dimensionless
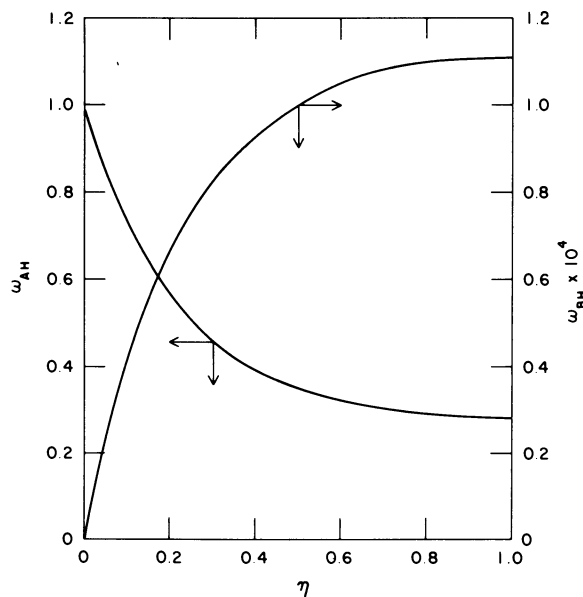
Figure 10.   Concentration profiles of oxygen, ω_{AH}, and sulfur dioxide, ω_{BH}, in the bed corresponding to $\eta_{CCE} = 0.995$, $\eta_{SAE} = 0.99$, $\overline{r} = \overline{r}' = 0.04$ cm and $k_3(T_o) = 480$ cm^4/mol · s

b^* = constant in oxygen concentration profile, eq. 91, dimensionless

c = total concentration of gases, mol/m^3

c_A, c_B = concentrations of the gas components A and B, mol/m^3

c_{AO} = initial concentration of gas component A, mol/m^3

c_{AC}, c_{AS} = concentration of A at the core and surface of char particles, mol/m^3

c_{Ae}, c_{Be} = concentrations of A and B in the off-gas, mol/m^3

c_{AH}, c_{BH} = concentrations of A and B in the bulk gas at height H in the fluidized bed, mol/m^3

c_{BC}, c_{BS} = concentration of B at the core and surface of limestone particle, mol/m^3

c_{JO}, c_{SO}, c_{NO} = initial concentration of solid reactant J and S in the char particle, and N in the limestone particle

D_A, D_B = molecular diffusiviy of the components A and B in the bulk gas phase, m^2/s

D_{eA}, D_{eB} = effective diffusivity of the component A in the ash layer, and of the component B in the layer of solid product E, m^2/s

E_1, E_2, E_3 = activation energy of reactions given by Eqs. 1, 2, and 3, J/mol

F_1, F_1' = feed rate of char and limestone, kg/s

F_3, F_3' = overflow rate of char and limestone from the fluidized bed, kg/s

F_4, F_4' = carryover rate of char and limestone from the fluidized bed, kg/s

f_c, f^* = fraction and weight fraction of carbon in char particles in the fluidized bed, dimensionless

f_Q, f_N = volume fraction of char and limestone particles in the fluidized bed, dimensionless

h, h' = overall convective and radiative heat transfer coefficient for char and limestone particles W/m^2K

H = distance along the bed, m

H_o = height of the fluidized bed, m

$\Delta H_1, \Delta H_2, \Delta H_3$ = heat of reaction per mole of reactant for reaction 1, 2, and 3, J/mol

k = thermal conductivity of the bulk gas, W/mK

k_e, k_e' = effective thermal conductivity of ash layer and solid product, W/mK

k_{mA}, k_{mB} = mass transfer coefficient for the components A and B across the gas film, m/s

k_1, k_2, k_3 = reaction rate constants for Eqs. 1, 2, and 3, $m^4/mol \cdot s$

M_J, M_N, M_S = molecular weight of the solid reactants, J, N, and S

N^* = number of particles of size ξ_s in the fluidized bed

N_{Nu}, N'_{Nu} = Nusselt Number for char and limestone particles, $2Rh/k$, $2R'h'/k$, dimensionless

$N_{Nu\bar{r}}, N'_{Nu\bar{r}}$ = $N_{Nu}(\bar{r}/2R)(k/k_e)$, $N'_{Nu}(\bar{r}/2R')(k/k_e')$, dimensionless

N_{Sh}, N'_{Sh} = Sherwood number for char and limestone particles, $2Rk_{mA}/D_A$, $2R'k_{mB}/D_B$, dimensionless

$N_{Sh\bar{r}}, N'_{Sh\bar{r}}$ = $N_{Sh}(\bar{r}/2R)(D_A/D_{eA})$, $N'_{Sh}(\bar{r}/2R')(D_e/D_{eB})$, dimensionless

$P_1(\xi_s), P'_1(\xi'_s)$ = size frequency distribution of char and limestone feed, 1/m

$P_2(\xi_s), P'_2(\xi'_s)$ = size frequency distribution of char and limestone in the fluidized-bed, 1/m

$P_3(\xi_s), P'_3(\xi'_s)$ = size frequency distribution of char and limestone in the overflow, 1/m

$P_3^*(\xi_s)$ = value of $P_3(\xi_s)$ corresponding to particle of size ξ_o in the feed, 1/m

$P_4(\xi_s), P'_4(\xi'_s)$ = size frequency distribution of char and limestone in the carryover, 1/m

Q = char, --

r = radial position in the limestone particle, m

r' = radial position in the limestone particle, m

$\bar{r}, \bar{r}'$ = average radius general, limestone defined by Eq. 5, m

r_i = radius of the ith size fraction of feed, m

r_B = rate of formation of gas product B, mol/m$^2\cdot$s mol of solid reactant

r_c, r'_c = radius of the unreated core of the char and limestone particles, m

r_D = rate of formation of gas product D, mol/m$^2\cdot$s mol of solid reactant

R, R' = instantaneous radius of char and limestone particles, m

$R_{o,max}(R_{o,min})$ = radius of the largest (smallest) char particle in the feed, m

$R_{s,max}(R_{s,min})$ = radius of the largest (smallest) char particle after complete reaction, m

$R'_{o,max}(R'_{o,min})$ = radius of the largest (smallest) limestone particle in the feed, m

$R'_{s,max}(R'_{s,min})$ = radius of the largest (smallest) limestone particle after complete reaction, m

$\bar{R}$ = gas constant, J/mol K

R_o, R'_o = initial radius of the char and limestone particles in the feed, m

t = time, s

T, T' = temperature of the char particle at radius r, limestone particle at r', K

T_o = temperature of the fluidized bed, K

T_c, T'_c = temperature of the unreacted core surface of char and limestone, K

T_s, T'_s = temperature of the outer surface of the char and limestone particles, K

U, U'	= reduced temperature of the char and limestone particles, T/T_0, dimensionless
U_c	= reduced core temperature of the char and limestone particles, T_c/T_0, dimensionless
U_s	= reduced surface temperature of the char and limestone particles, T_s/T_0, T_s'/T_0, dimensionless
u	= superficial velocity, m/s
V	= volume of the fluidized bed, m^3
V_1, V_3, V_4	= volumetric feed, overflow and carryover rates of char, m^3/s
V_1', V_3', V_4'	= volumetric feed, overflow and carryover rates of limestone, m^3/s
w_i'	= weight fraction of particles in the feed of radius, r_i, dimensionless
W_Q, W_N	= weight of char and limestone particles in the fluidized-bed, kg
x_A, x_B	= mole fraction of components A and B, dimensionless
x_{AC}, x_{AO}, x_{AS}	= value of x_A at the unreacted core surface, bottom of the bed and outer surface of the char particle, dimensionless
x_{AH}	= value of x_A at a height H in the fluidized bed, dimensionless
x_{BC}, x_{BS}, x_{BH}	= value of x_B at the unreacted core surface, outer surface of limestone particle and at height H in the bed, dimensionless
Y	= average rate of gas flow through the reactor bed, m^3/s
Z, Z'	= parameter defining particle growth or shrinkage of char and limestone defined by Eq. 4, dimensionless

Greek Letters

$\varepsilon, \varepsilon_1, \varepsilon_3, \varepsilon_4$	= average void fraction of the bed, char feed, overflow and carryover, dimensionless
ε_1'	= average void fraction of limestone feed, dimensionless
ξ, ξ'	= any reduced distance for char and limestone particles, $r_0/\bar{r}$ and r_0'/r, dimensionless
ξ_c, ξ_c'	= reduced unreacted core radius of char and limestone particles, $r/\bar{r}$ and $r'/\bar{r}$, dimensionless
ξ_s, ξ_s'	= reduced radius of the char and limestone particles, $R/\bar{r}$ and $R'/\bar{r}$, dimensionless
$\xi_{o,max}(\xi_{o,min})$	= reduced radius of the largest (smallest) particle in the char feed, dimensionless
$\xi_{s,max}(\xi_{s,min})$	= reduced radius of the largest (smallest) char particle after complete reaction, dimensionless
$\xi_{o,max}'(\xi_{o,min}')$	= reduced radius of the largest (smallest) limestone particle in the feed, dimensionless

$\xi'_{s,max}(\xi'_{s,min})$ = reduced radius of the largest (smallest) lime-stone particle after complete reaction, dimensionless

ξ_o, ξ'_o = reduced value of R_o and R'_o, $R_o/\bar{r}$ and $R'_o/\bar{r}$, dimensionless

ρ_a, ρ_E = density of the solid product ash and calcium sulfate, kg/m^3

ρ_J, ρ_N = density of the solid reactant J, and limestone N, kg/m^3

ρ_Q, ρ_S = density of char and solid reactant S, kg/m^3

$\phi_{1\bar{r}}$ = a parameter to characterize the rates of intra-particle diffusion resistance to the reaction residence for reaction 1 = $\bar{r}k_1(T_o)C_{JO}/D_{eA}(T_o)$, dimensionless

$\phi_{2\bar{r}}$ = a parameter to characterize the rates of intra-particle diffusion resistance to the reaction residence for reaction 2 = $\bar{r}k_2(T_o)C_{SO}/D_{eA}(T_o)$, dimensionless

$\phi_{3\bar{r}}$ = a parameter to characterize the rates of intra-particle diffusion resistance to the reaction residence for reaction 3 = $\bar{r}k_3(T_o)C_{NO}/D_{eA}(T_o)$, dimensionless

$\omega_A, \omega_{AC}, \omega_{AH}$ = reduced values of x_A, x_{AS}, x_{AH}, x_A/x_{AO}, x_{AC}/x_{AO}, x_{AH}/x_{AO}, dimensionless

ω_{AS}, ω_B = reduced value of x_{AS} and x_B, x_{AS}/x_{AO}, x_{BC}/x_{AO}, dimensionless

$\omega_{BC}, \omega_{BH}, \omega_{BS}$ = reduced value of x_{BC}, x_{BH}, and x_{BS}, x_{BC}/x_{AO}, x_{BH}/x_{AO}, x_{BS}/x_{AO}, dimensionless

$\kappa_Q(\xi_s)$ = elutriation constant for char particles of size ξ_s, $1/s$

$\kappa_N(\xi'_s)$ = elutriation constant for limestone particles of size ξ'_s, $1/s$

η = reduced bed height, H/H_o, dimensionless

η_{CCE} = carbon conversion efficiency defined by Eq. 89, dimensionless

η_{SAE} = sulfur absorption efficiency defined by Eq. 90, dimensionless

Literature Cited

1. Kunii, D.; Levenspiel, O. "Fluidization Engineering"; John Wiley: New York, 1969.
2. Chen, T. P.; Saxena, S. C. AIChE Sym. Series 1968, No. 176, 74, 149-161.
3. Chen, T. P.; Saxena, S. C. Fuel, 1977, 56, 401-413.

4. Saxena, S. C.; Chen, T. P.; Jonke, A. A. "A Slug Flow Model
    for Coal Combustion with Sulfur Emission Control by Limestone
    or Dolomite"; Presented at the 70th Annual AIChE Meeting,
    New York City, 1977, Paper No. 104d.
5. Rengarajan, P.; Krishnan, R; Wen, C. Y. "Simulation of
    Fluidized Bed Coal Combustors"; Report No. NASA CR-159529,
    February 1979, 199 pp.
6. Becker, H. A.; Beer, J. M.; Gibbs, B. M. "A Model for
    Fluidized-Bed Combustion of Coal"; Inst. of Fuel Symposium
    Series No. 1, Proc. Fluidized Combustion Conference 1, Paper
    No. AI, 1975, A1·1-A1·10.
7. Horio, M; Mori, S.; Muchi, I. "A Model Study for the Develop-
    ment of Low NO$_x$ Fluidized-Bed Coal Combustors"; Proc. 5th
    Intern. Conf. on Fluidized-Bed Combustion, Vol. II, 1977,
    605-624.
8. Davidson, J. F.; Harrison, D. "Fluidized Particles";
    Cambridge University Press: New York, 1963.
9. Rehmat, A.; Saxena, S. C. "Single Nonisothermal Noncatalytic
    Gas-Solid Reaction. Effect of Changing Particle Size";
    Ind. Eng. Chem. Process Des. Dev. 1975, 16, 343-350.
10. Rehmat, A.; Saxena, S. C. "Multiple Nonisothermal Noncata-
    lytic Gas-Solid Reaction. Effect of Changing Particle
    Size"; Ind. Eng. Chem. Process Des. Dev. 1977, 16, 502-510.
11. Rehmat, A.; Saxena, S. C.; Land, R. H.; Jonke, A. A. "Non-
    catalytic Gas-Solid Reaction with Changing Particle Size:
    Unsteady State Heat Transfer"; Canadian J. Chem. Eng. 1978,
    56, 316-322.
12. Yagi, S.; Kunii, D. "Studies on Combuston of Carbon
    Particles in Flames and Fulidized Beds"; 5th Symposium
    (Int'l) on Combustion, 1955, 231-244.
13. Burovoi, I. A.; Eliashberg, V. M.; D'yachko, A. G.; Bryukvin,
    V. A. "Mathematical Models for Thermochemical Processes
    Occurring in Fluidized Beds"; Int. Chem. Eng. 1962, 2,
    262-258.
14. Strel'tsov, V. V. "Approximate Relationships for Calculating
    the Kinetics of Reactions of a Solid Phase in a Fluidized
    Bed"; Int. Chem. Eng. 1969, 9, 511-513.
15. Bethell, F. B.; Gill, D. W.; Morgan, B. B. "Mathematical
    Modelling of the Limestone-Sulfur Dioxide Reaction in a
    Fluidized-Bed Combustor"; Fuel 1973, 52, 121-127.
16. Koppel, L. "A Model for Predicting the Extent of Reaction of
    Limestone and Sulfur Dioxide During Fluidized-Bed Combustion
    of Coal"; Appendix C, pp. 60-77, in Jonke, A. A. "Reduction
    of Atmospheric Pollution by the Application of Fluidized Bed
    Combustion"; Argonne National Laboratory Annual Report,
    ANL/ES-CEN-1002, July 1969-June 1970.
17. Avedesian, M. M.; Davidson, J. F. "Combustion of Carbon
    Particles in a Fluidized Bed"; Trans. Inst. Chem. Engrs.
    1973, 51, 121-131.

18. Evans, J. W.; Song, S. "Application of a Porous Pellet Model to Fixed, Moving, and Fluidized Bed Gas-Solid Reactors"; <u>Ind. Eng. Chem. Process Des. Dev.</u> 1974, <u>13</u>, 146-152.

19. Campbell, E. K.; Davidson, J. F. "The Combustion of Coal in Fluidized Beds"; Inst. of Fuel Sym. Series No. 1, Proc. Fluidized Combustion Conference <u>1</u>, Paper No. A2, 1975, A2·1-A2·9.

20. Gibbs, B. M.; "A Mechanistic Model for Predicting the Performance of a Fluidized Bed Coal Combustor"; Inst. of Fuel Sym. Series No. 1, Proc. Fluidized Combustion Conference <u>1</u>, Paper No. A5, 1975, A5·1-A5·10.

21. Beer, J. M.; "The Fluidized Combustion of Coal"; XVIth Sym. (Int'l) on Combustion, 1976, 439-460.

22. Hovmand, S.; Davidson, J. F. Chapter 5 in "Fluidization"; Editors J. F. Davidson and D. Harrison; Academic Press: London, 1971.

23. Horio, M.; Wen, C. Y. "Simulation of Fluidized Bed Combustors: Part I. Combustion Efficiency and Temperature Profile"; <u>AIChE Symp. Series</u> 1978, No. 176, Vol. 74, 101-111.

24. Mori, S.; Wen, C. Y. "Estimation of Bubble Diameter in Gaseous Fluidized Beds"; <u>AIChE J</u> 1975, <u>21</u>, 109-115.

25. Gibbs, B. M.; Pereira, F. J.; Beer, J. M. "Coal Combustion and NO Formation in an Experimental Fluidized Bed"; Institute of Fuel Symp. Series No. 1, Proc. Fluidized Combustion Conference 1, Paper No. D6, 1975, D6·1-D6·13.

26. Rehmat, A.; Saxena, S. C.; Land, R. H. "Application of Noncatalytic Gas-Solid Reactoins for a Single Pellet of Changing Size to the Modeling of Fluidized-Bed Combustion of Coal Char Containing Sulfur"; Argonne National Laboratory Report, ANL/CEN/FE-80-13, September 1980, 86 pp.

Computer Modeling of Fluidized Bed Coal Gasification Reactors

T. R. BLAKE[1] and P. J. CHEN

Fossil Energy Program, Systems, Science and Software, P.O. Box 1620, La Jolla, CA 92038

The application of large scale computer simulations in modeling fluidized bed coal gasifiers is discussed. In particular, we examine a model wherein multidimensional predictions of the internal gas dynamics, solid particle motion and chemical rate processes are possible.

A computer model has been developed to provide numerical simulations of fluidized bed coal gasification reactors and to yield detailed descriptions, in space and time, of the coupled chemistry, particle dynamics and gas flows within the reactor vessels. Time histories and spatial distributions of the important process variables are explicitly described by the model. With this simulation one is able to predict the formation and rise of gas bubbles, the transient and quasi-steady temperature and gas composition, and the conversion of carbon throughout the reactor.

The effects of gas and coal/char feeds and reactor geometries upon these internal processes and, hence, upon the performance of the reactor, can be simulated with this numerical model. The model incorporates representations of particle-particle and particle-gas interactions which account for finite rate heterogeneous and homogeneous chemistry as well as the hydrodynamical processes associated with particle collisions and drag between the particles and the gas flow. The important influences of multicomponent gas phase properties as well as solid particle properties, such as shape and size, are included in the representations.

[1]Current address: Consultant, also Professor, Mechanical Engineering Department, University of Massachusetts, Amherst.

Nature of The Finite Difference Model

It is useful and appropriate to compare some of the specific capabilities of the present model with other representations of reactors. We note that existing models of fluidized beds are typified by the two-phase models of fluidization (e.g., 1-4) which are of great utility, but which do not predict the gas dynamics and solid particle transport in the reactor. Rather, these models require input prescriptions for such transport and provide, in general, one-dimensional axial representations of temperature, carbon consumption and gas composition. The present fluidized bed computer model provides a transient multi-dimensional field description of these process variables and also provides predictions of the gas dynamics and solid particle motion. Within this context, we note that there have been analogous multi-dimensional field descriptions and numerical models for the study of related processes, such as those associated with nuclear reactor safety (e.g., 5, 6, 7) and entrained flow combustion and gasification (e.g., 8, 9, 10). However, physical and chemical mechanisms in such models are rather different from fluidized bed coal gasification reactors and consequently the capabilities of the respective numerical representations are also different. For example, the particle-particle and particle-gas forces dominate the fluidized bed flows. The numerical representations of these physical phenomena, together with the particle-gas mass and energy exchange produced by the heterogeneous combustion and gasification reactions, require the Eulerian-Lagrangian and finite difference implicit capabilities which have been specifically developed for and incorporated into the present fluidized bed coal gasifier computer model.

The computer model is based upon a continuum description of fluidization in coal gasification reactors. In general, fluidized flows are dominated by specific physicochemical processes and, hence, require particular theoretical representations. For example, in the heavily loaded gas-particle regime appropriate to fluidization, the solid particles dominate the transport of momentum and energy. This aspect of fluidization is reflected in the mathematical descriptions which have been used in the fluidized bed model.

These mathematical representations are complex and it is necessary to use numerical techniques for the solution of the initial-boundary value problems associated with the descriptions of fluidized bed gasification. The numerical model is based on finite difference techniques. A detailed description of this model is presented in (11-14). With this model there is a degree of flexibility in the representation of geometric surfaces and hence the code can be used to model rather arbitrary reactor geometries appropriate to the systems of interest. [The model includes both two-dimensional planar and

axisymmetric geometries.] That is, the use of finite difference computational zones permits the numerical "construction" of a wide variety of reactor geometries because the walls, orifices, etc., are resolved incrementally into computational zones. Consequently, the code is not restricted to a specific reactor; rather, it is designed to model classes of reactor flows through the specific nature of the gas dynamic, solid particle and thermochemistry representations which are incorporated into the numerical analogs of the differential equations. This specificity of the conservation equations is based upon the theoretical considerations for fluidized bed flows and upon the incorporation of physicochemical data into the models to define constitutive equations and interaction functions in the theoretical representations.

Within the context of these code applications, simulations of both local flow regimes and flows on the scale of the entire reactor are possible. It is to be noted that these computer codes are designed to provide a resolution of the gas dynamics, solid particle motion and the major coupling of the chemistry and the flow field on time scales which measure the gas residence time in the reactor, but are not, at the present, envisioned to provide a detailed inventory of process variables and gas composition within the gasifier on time scales of hours.

To illustrate this point, one may consider the detailed mass and energy balance calculations that are an integral part of fluidization gasification modeling. For example, Weil and his co-workers, at the Institute of Gas Technology (15), are interpreting PDU and pilot plant data related to high pressure fluidized bed steam-oxygen, steam-air and hydrogasification. An important parameter, in their semi-empirical interpretation of the mass and energy balance in these fluidized beds, is the bubble size. The present fluidized beds model can be used to predict the bubble size in the high pressure and high temperature regime of the experiments and such bubble size predictions can be used in and thereby complement the detailed kinetics studies of Weil.

In this paper we will discuss some numerical calculations related to the IGT bench scale data and also examine some numerical calculations of the Westinghouse Agglomerating Combustor/Gasifier. The emphasis in both of these studies is upon the hydrodynamic mixing processes and the coupling of that hydrodynamic mixing to the chemical reactions. For example, flow visualization experiments performed at Westinghouse are used to verify some of the model predictions.

It is to such applications that the numerical model studies are directed. That is, the predictions of the model are compared with bench scale and pilot plant data and with flow visualization experiments. Such comparisons serve to validate the model and to provide guidance for the experimental trials. It is likely that modifications of the physicochemical aspects

of the model will be required to predict specific reactor environments. When the model has been verified and, if necessary, modified through such comparative studies, then it can be used to predict reactor performance and, in particular, examine questions such as reactor scaleup.

Fluidized Bed Gasifier Theory and Numerical Model

We now discuss the theory and some of the numerical aspects of the model. Again, this model is based upon the theoretical formulation presented in (12, 13, 14). The theoretical formulation, including differential equations and appropriate initial and boundary conditions, defines a complicated initial value problem which, in general, must be solved with numerical methods. A finite difference computer model has been developed to provide such a solution. The mathematical character of the system of equations is of the mixed hyperbolic-parabolic type; consequently, we have used a numerical technique based upon an iterative, implicit, finite difference scheme. While there is an extensive literature related to such techniques and further documentation exists in text books (e.g., 16), the development of an iterative, implicit method for this coupled solids-gas system of equations is unique to the present investigation.

Differential Equations for Fluidized Bed Gasifier Model.
In a hydrodynamical sense, the processes in fluidized bed gasifiers involve the interaction of a system of particles with flowing gas. The motion of these particles and gas is, at least in principle, completely described by the Navier-Stokes equations for the gas and by the Newtonian equations of motion for the particles. Solution of these equations together with appropriate boundary and initial conditions would determine the mechanics of the fluidized bed gasifier. However, such fluidized bed gasifiers contain a large number of closely spaced particles; consequently, such systems are far too complex to permit direct solution. For practical purposes, it is therefore necessary to simplify the governing equations so that the gas-particle system is described by a smaller number of differential equations.

Such a simplification is possible through the introduction of a continuum mathematical description of the gas-solid flow processes where this continuum description is based upon spatial averaging techniques. With this methodology, point variables, describing thermohydrodynamic processes on the scale of the particle size, are replaced by averaged variables which describe these processes on a scale large compared to the particle size but small compared to the size of the reactor. There is an extensive literature of such derivations of continuum equations for multiphase systems (17, 18, 19). In the present study, we have developed (12, 13, 14) a system of equations for

compressible gas flow in a fluidized bed, based upon the method of Anderson and Jackson (18) and we have used laboratory data to define interaction functions and constitutive equations.

These equations have further been coupled to the kinetics and transport relationships associated with the heterogeneous and homogeneous reactions of coal gasification. This coupled system of equations provides the theoretical basis of our computer model of coal gasification reactors.

The derivation of these equations (cf., 14) involves the important assumptions that the gas phase inertia is negligible compared with that of the solid, the temperatures of the solid and gas phases have the same local values and the kinetic energy of the system is small compared with the thermal energy.

Closure of such differential equations requires the definitions of both constitutive relations for hydrodynamical functions and also kinetic relations for the chemistry. These functions are specified by recourse both to theoretical considerations and to rheological measurements of fluidization. We introduce the ideal gas approximation to specify the gas phase pressure and a caloric equation-of-state to relate the gas phase internal energy to both the temperature and the gas phase composition. It is assumed that the gas and solid phases are in local thermodynamic equilibrium so that they have the same local temperature.

A solid phase internal energy is related, again through a caloric equation-of-state, to the temperature. The solid phase pressure is defined as a function of the solid volume fraction where the functional relationship (cf., 14) is based upon the fluidized bed stability measurements of Rietma and his coworkers (20).

The gas phase viscosity is defined by the temperature and the gas composition through a semi-empirical function. For the solid phase shear viscosity, we (cf., 14) use semi-empirical relations based upon the viscometric measurements of Schugerl (21). The solid phase bulk viscosity is, at present, inaccessible to measurement; consequently, we define it to be a multiple of the shear viscosity.

One of the most important functions in the description of fluidization is the drag function which measures the ratio of pressure gradient to gas volume flux. The definition of this drag function is discussed in (14) through recourse to the correlation of Richardson (22).

A thermal conductivity of the gas-solid particle mixture is determined (cf., 14) by the correlation of Gelperin and Einstein (23). We use a law of mixtures to define a radiation diffusion coefficient and, for the present, we consider only the limits of (1) opaque·gas and opaque particles and (2) transparent gas and opaque particles.

Chemistry of Combustion and Gasification. The present model is designed to examine the combustion and gasification regions associated with steam-oxygen gasification in the fluidized bed. Consequently, we consider that the solid phase is composed of char particles. That is, any devolatilization is assumed to occur upon feeding of the coal into the bed and this devolatilization is instantaneous, relative to the hydrodynamic time scales of interest in the present model. The overall mass balance, associated with the evolution of coal to char through devolatilization, can be easily accounted for by a stoichiometric analysis similar to that suggested in (11), viz., the coal feed is simulated by a feed of char and gas with the gas composition representing the volatile yield.

For the present, the following reactions are assumed to occur between the carbon in the char and the gaseous reactants:

$$\gamma C(s) + O_2(g) \to (2-\gamma) \, CO_2(g) + 2(\gamma-1) \, CO(g) \qquad (R1)$$

$$C(s) + H_2O(g) \to CO(g) + H_2(g) \qquad (R2)$$

$$C(s) + CO_2(g) \to 2CO(g) \qquad (R3)$$

$$C(s) + 2H_2(g) \to CH_4(g) \; . \qquad (R4)$$
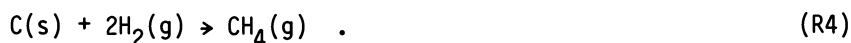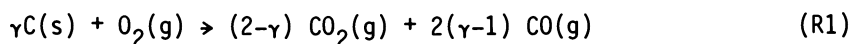
The first of these reactions is the combustion reaction, where γ is a parameter determining the distribution of carbon dioxide and carbon monoxide in the overall combustion process (24). To some extent, it reflects an uncertainty in defining the respective roles of heterogeneous and homogeneous oxidation processes. Naturally, we expect that the heterogeneous reaction involves the production of carbon monoxide at the temperatures of interest (25, 26, 27). However, the extent of mixing and oxidation of this carbon monoxide in the gas phase can certainly occur anywhere from the particle surface ($\gamma=1$) to the ambient gas flow ($\gamma=2$). We do not include any additional homogeneous reaction of carbon monoxide and oxygen in the gas phase, so this latter limit corresponds to no oxidation of the CO. The above statement is, thereby, a parametric expression which measures the extent of carbon monoxide oxidation in the gas phase at the particle surface.

The remaining three heterogeneous reactions involve gasification of carbon by steam, carbon dioxide and hydrogen (28-35).

The homogeneous reaction is that of water gas shift:

$$CO + H_2O \gtrless CO_2 + H_2 \; . \qquad (R5)$$

Again, the homogeneous reaction of carbon monoxide and oxygen is implicitly included in the parameter, γ, of Equation (R1). Further, we neglect the gas phase oxidation of hydrogen

and methane; briefly, with the possible exception of the Westinghouse gasifier, we do not expect significant quantities of these species to be present in that region of the reactor where there is significant oxygen (35).

The water gas shift reaction is considered to be in equilibrium. However, the heterogeneous reactions are influenced by both chemical kinetics and diffusive transport of reactants. Further, in the case of the carbon–steam reaction, the inhibition by both carbon monoxide and hydrogen is also included.

The nature of carbon mass loss is, in general, a complicated function of intra- and extra-particle reactant transport and chemical kinetics (26). While the numerical structure incorporated into the fluidized bed gasifier computer model can include a broad range of particle mass loss configurations. We, for the calculations herein, used an equivalent unreacted shrinking core particle configuration for both combustion and gassification reactions. Thus, the heterogeneous reaction rate, where R_i is the rate of carbn mass loss per unit surface area due to reaction i, is

$$\dot{R}_i = \frac{f_i}{\dfrac{1}{k_i} + \dfrac{1}{k_0} + \dfrac{1}{k_{0E}}}$$

where k_i, k_0 and k_{0E} represent the velocity coefficients associated with kinetics, extra-particle diffusion and intra-particle ash layer diffusion (36), and f_i is a function of the partial pressures of the reactants in the gas phase.

With the equation for R_i we obtain the source terms representing heterogeneous chemistry equations for the solid and gas phase species. Those source terms are discussed briefly in (13).

Numerical Formulation. Let us now consider the general character of the numerical solution of the equations. The model involves a combined Eulerian-Lagrangian formulation which permits calculation of large displacements while at the same time maintaining sharp interfaces. As shown in Figure 1, the x-y plane is divided into a number of rectangular zones of size Δx by Δy. This Eulerian grid is fixed in space. Upon this grid, a large collection of Lagrangian marker particles is superimposed. These marker particles, each of which actually describes the average behavior of a large number of physical particles, move through the Eulerian grid with the local instantaneous solid velocity as the calculation proceeds. Each such particle has assigned to it an amount of mass, horizontal momentum, vertical momentum, and energy, all of which change
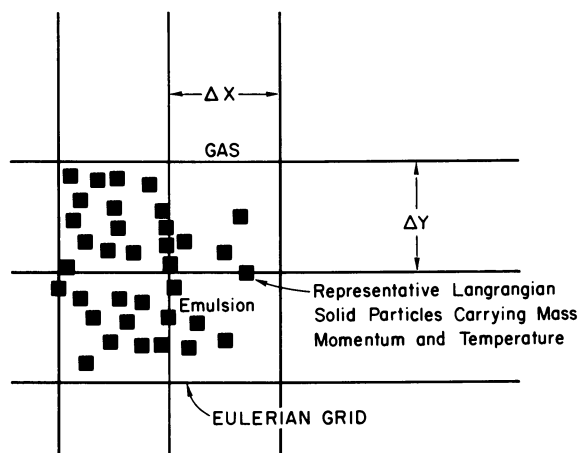
Figure 1. *Eulerian/Langrangian formulation of solid–gas motion*

with time. Thus, the motion of these particles automatically takes into account all solid advection effects.

For a particular time step, the positions of the solid particles are first changed by an amount $(\vec{u} \cdot \Delta t)$, and the field variables assigned to the Eulerian grid are altered to reflect the new particle distribution. Then, the additional terms in the field equations for mass, momentum and energy conservation (viscous stresses, pressure forces, heat conduction, etc.) are taken into account using the Eulerian grid. Finally, the field variable quantities assigned to the representative particles are changed to reflect the effect of these latter terms. This general procedure (or "time cycle") may be repeated as many times as desired, with each such repetition advancing the solution further in time. The use of a superposed Lagrangian representative particles to treat advective effects avoids the computational "smearing" of field variables which often occurs in purely Eulerian computations.

Applications of Fluidized Bed Computer Model

A major factor in fluidized bed behavior is the interaction between the gas flow from individual orifices and the particle and gas mixture within the bed. The jet penetration and the subsequent bubble formation have an important influence upon solids and gas mixing and, ultimately, upon the usefulness of the bed for reactor purposes. While flow visualization data are available at ambient pressures and temperatures, the natures of jet penetration and bubble development at high pressures and temperatures are not easily measured. Typical data on bubble size and bubble velocity at ambient conditions are shown, represented by the small size symbols, in Figure 2. It is well known that bubble volume can be correlated as a function of gas volumetric flow rate (37) and that bubble velocity is related to the size of the bubble radius (38). Such semi-empirical correlations are indicated as solid lines in that figure.

A quantitative comparison between the numerical model and experimental data can be made using those measurements of bubble volume and bubble rise velocity. The calculated values of bubble volume and bubble rise velocity for both ambient and high pressure conditions and also for some complex geometries such as the Westinghouse Cold Flow 30 cm diameter semi-circular model, are shown as large symbols in Figure 2. The specific geometries and flow conditions for the calculations are listed in Table I.

We find that the numerical fluidized bed model predicts bubble size and velocity, at ambient pressure and temperature, which agrees with the data. Further in that figure we show the results of three calculations at high pressure (40 atm) and room temperature ($293°K$) which, when correlated in the same fashion, yield predictions of bubble size and velocity which also agree with the ambient pressure data. This agreement between high

a

b
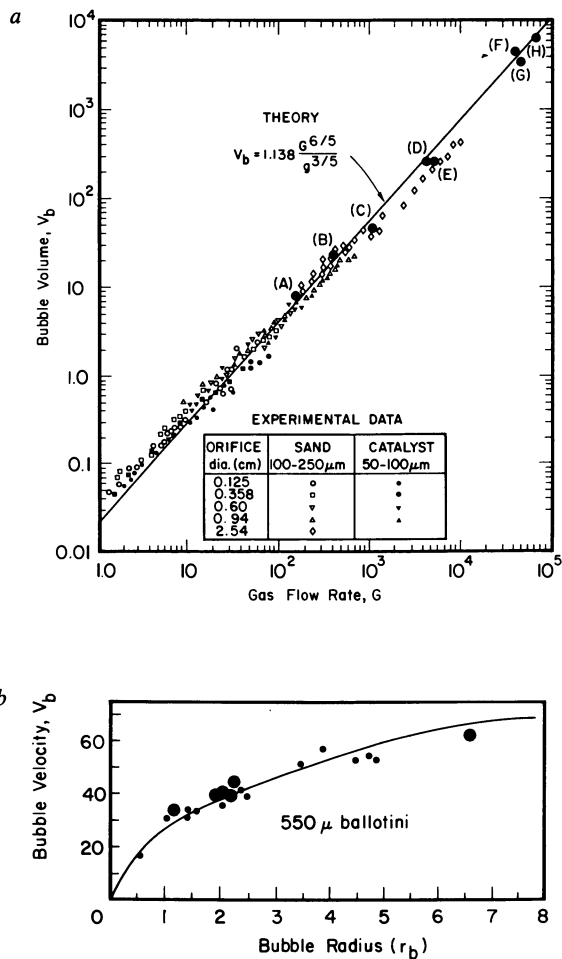
Figure 2.   a, Bubble volume—comparison between numerical model and experiment (37): (●) numerical calculations; b, Bubble velocity as function of equivalent spherical radius—comparison between numerical model and experiment (38): (●) numerical calculations

TABLE I

FLUIDIZATION PARAMETERS FOR CALCULATIONS WITH FLUIDIZED BED COAL GASIFIER MODEL OF BUBBLE VOLUME AND BUBBLE RISE VELOCITY IN FIGURE 2

CALCULATION	A	B	C	D	E	F	G	H
DESCRIPTION	Single Jet in Cylindrical Annulus					Westinghouse Geometry		
Pressure (Atm)	40	40	40	40	32	1	1	1
Gasification Chemistry	No	No	No	Yes	Yes	No	No	No
Particle Diameter (?m)	250	250	750	750	400	2800	2800	2800
Particle Density (gm/cm^3)	1.5	1.5	1.5	1.5	1.5	0.2	0.2	0.2
Maximum Temperature (K)	293	293	293	1200	1200	293	293	293
Mass Flow-Jet (gm/sec)	1.21	3.25	8.26	15.33	35.4	18.3	8.88	30.05
Mass Flow-Annulus (gm/sec)	1.60	1.60	7.07	-	-	12.3	9.66	9.66
Mass Flow-Cone (gm/sec)	-	-	-	-	-	0.22	16.22	16.22

pressure calculations and low pressure data can be explained: first, the influences of pressure and temperature upon the relationship between bubble size and gas flow are implicitly normalized when one correlates the bubble volume with the gas volumetric flow rate through the orifice. Second, in the comparison between high pressure predictions of bubble velocity and the low pressure data there is good agreement because bubble velocity is relatively insensitive to gas density.

The use of the numerical model at high pressures and the comparison of the high pressure calculations with the data suggests scaling relationships between bubble size and velocity, which should be useful in applying such a low pressure data to the reactor environment. Finally, the agreement between bubble size predictions for the complex geometry of the Westinghouse Cold Flow 30 cm Diameter Semi-Circular Model and the data suggests the application of the data to a wide range of conditions. Of course, there are limitations such as suggested in (37), but the broad agreement between calculation and data tends to verify the model.

Simulation of Institute of Gas Technology Six-Inch Diameter Bench Scale Reactor. This model has also been used in preliminary calculations of the Institute of Gas Technology (IGT) six-inch diameter bench scale experiments (39) on steam-oxygen gasification of char. In this reactor the steam, oxygen and nitrogen are injected at the base of the column through a six-cone feed gas distributor and, in the case of nitrogen, also around the distributor to maintain the state of fluidization.

In the numerical calculation of that experiment we use the axisymmetric version of the fluidized bed computer model to reproduce the cylindrical geometry of the reactor. The gas feed is simulated by a fully mixed stream of oxygen, steam and nitrogen which is injected at the base of the reactor within a radius of two-inches, corresponding to the radius through the centers of the injection cones in the actual six-cone feed gas distributor.

A time sequence of bubbling from such a calculation of the IGT six-inch EGO-33 run is shown in Figure 3. The sequence is that of a stationary or quasi-steady pattern of bubble evolution subsequent to the start-up transient. In each individual "frame" of the time sequence a reactor section, bounded by the centerline axis on the left and the reactor radius on the right, is shown. The representative particles are indicated by the black dots while the bubbles and the voids are white. The time corresponding to discrete frames is indicated on the base of the figure and the rise of the bubbles, together with the solids mixing, can be discerned in that sequence of frames. This calculation suggests that a relatively small number of large
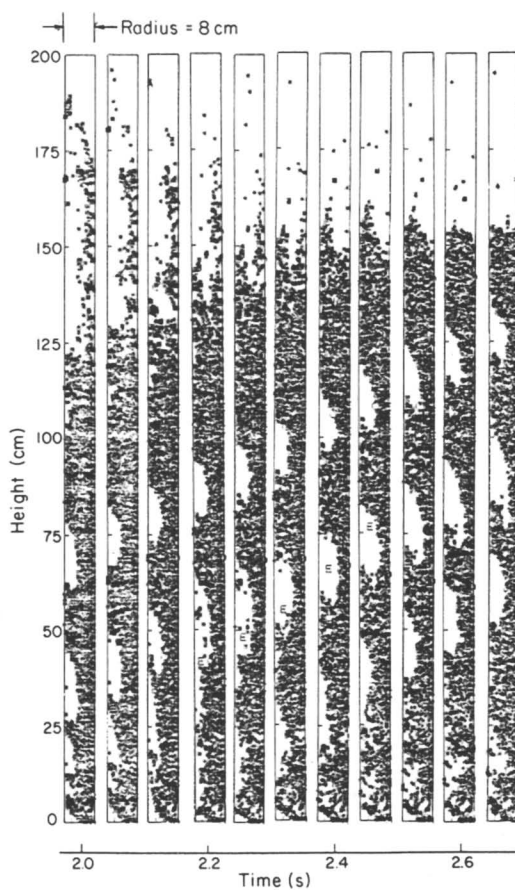
Figure 3. Time sequence of bubble evolution during steam oxygen gasification in IGT 6-in. diameter bench scale reactor

bubbles, in a sequential train, rise through the bed and produce solids and gas mixing. The bubbles are large because of bubble coalescence at the base of the reactor.

We find that while the gas composition in the bubble is quite different from that in the mix of gas and solid particles surrounding the bubbles; near the base of the reactor these respective gas compositions are almost identical by the time that bubbles approach the top of the bed. There is significant exchange of gas between the bubbles and the surrounding emulsion which causes a good mixing of the reactants and products of combustion and gasification. Some particles are entrained into the bubble through the wake.

Preliminary comparisons between the calculated exit gas composition and that measured in the IGT experiments have been made. For example, in the case of IGT Run EGO-33, we find very good agreement between the model and the data for CO, CH_4, H_2 and N_2 but predict less H_2O and more CO_2 in the exit gas than is indicated by our interpretation of the experimental measurements. For example, in the nitrogen-free product gas, including steam, a comparison between our evaluation of the data and a one-dimensional simulation of the reactor process gives the composition mass flows in Table II.

TABLE II
COMPARISON OF PRODUCT AND GAS COMPOSITION IN EXPERIMENT
AND CALCULATION

Species	Mass Flow (lb/hr)	
	IGT	Calculation
CO	38.9	38.5
CO_2	62.1	83.0
H_2	3.9	4.7
CH_4	3.2	3.7
H_2O	93.1	79.0

where the approach factors expressed in N_2-free mol percent X are:

$$\frac{X_{CO_2} \, X_{H_2}}{X_{CO} \, X_{H_2O}} = 0.377, \ 0.730$$

for the IGT and present cases respectively. There is approximately a 20 percent discrepancy between the IGT data and the present simulation with regard to CO_2 and H_2O but there is excellent agreement on the other species. We also note that the total oxides of carbon are within 20 percent agreement. The reason for the difference in steam consumption between calculation and experiment is not clear. We note, however that

the approach factor in the IGT experiments (specifically our interpretation of that data), if indicative of equilibrium, would suggest a temperature of approximately 2230°F which is about 300°F higher than the largest temperature measured.

Simulation of Westinghouse Agglomerating Combustor/ Gasifier. The design of the Westinghouse Agglomerating Combustor/Gasifier includes a nozzle introducing a jet of oxidant to create locally high temperatures for ash sintering and agglomeration. The agglomerates are subsequently removed by falling countercurrently through a cylindrical annulus surrounding the oxidizing jet.

There is relatively little data obtained in the hot reactor environment. Typical measurements include wall temperature records and bed densities. However, there is a continuing cold flow visualization test program at Westinghouse (40). Data from that test program can be used to validate the hydrodynamic aspects of the present model. Then, with that validation the limited hot flow measurements can often provide sufficient information about the validity of hot flow hydrodynamic predictions. Indeed, in the work at Westinghouse some limited hot flow data (40) was used to verify a jet penetration correlation which had been developed from cold flow visualization experiments. Such engineering judgements also apply to the numerical "experiments" which comprise our simulation studies. The advantage of these numerical "experiments" is that they are more cost effective and provide more detailed information than the actual hot flow hydrodynamic experiments.

In the following paragraphs we shall examine some cold and hot flow calculations related to the hydrodynamics of the Westinghouse Agglomerating Combustor/Gasifier.

In Figure 4 we show the cross-section of the Westinghouse cold flow geometry and the corresponding geometry of the computational grid in the numerical simulation. These are both axisymmetric configurations where the axes of symmetry are to the left of the respective figures. Typical cold flow reactor conditions for an experiment and a calculation are shown in Table III.

TABLE III
EXPERIMENTAL AND NUMERICAL COLD FLOW IN
WESTINGHOUSE REACTOR

Particle Diameter (μm)	2800
Particle Density (gm/cm^3)	0.21
Mass Flow, Air Tube (gm/sec)	18.3
Mass Flow, Annulus (gm/sec)	12.3
Mass Flow, Cone (gm/sec)	0.22
Reactor Pressure (atm)	1.0
Reactor Temperature (°K)	293

Figure 4. Schematic of Westinghouse cold flow 30-cm diameter semicircular model and finite difference grid for numerical calculations
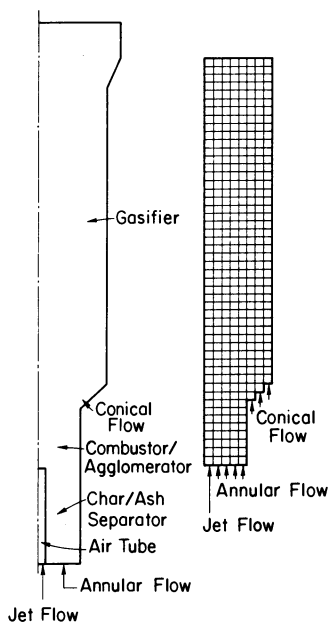
The numerical simulation of the cold flow experiment is in the form of an initial value problem. The computational grid is initially filled with particles and air, at atmospheric pressure and ambient temperature. A flow field is established by gas injections through the air tube, annulus and conical distributors. Subsequently in the calculation a time varying jet is established at the air tube, and the interaction of this jet with the mass flows through the annulus and conical distributors produces particle mixing within the reactor. We find that good agreement exists between this numerical simulation and the Westinghouse cold flow studies (40).

A time sequence of the calculated particle motion is shown in Figure 5 where the centerline of the reactor is the lefthand side and the outer radius of the reactor is the righthand side of each frame in the sequence. The jet penetration is observed qualitatively from the evolution of that flow region where there are no particles. This jet is quite diffused in character and is clearly a transient phenomenon. We define the jet length as the voidage from the jet inlet. Thus, the bubble, before it detaches from the jet, will be considered as part of the jet. The calculation and experiment are in agreement with regard to the bounds of jet penetration into the mix of particles and gas surrounding the air tube. Further, as shown in Figure 6 the mean jet penetrations in the calculation and in the experimental observations are in good agreement.

Associated with the time dependent particle displacement and transient jet is a gas velocity field. In Figure 7 the time average of the gas velocity profiles, normalized by the inlet jet velocity, as a function of the radial distance, normalized by the air tube radius, in the calculation are shown as the solid symbols centered on the axis of the air tube. The calculated jet initially decays in magnitude and disperses radially; but, at larger normalized axial distance $y/r_0 > 10$, this decay decreases. To some extent this behavior reflects a transition in the jet from a flow dominated by gas flow alone for $y/r_0 < 10$ to a flow dominated by solid particle motion for $y/r_0 > 10$. The particles tend to drag the gas with them and, since these particles are large, they maintain their momentum and prevent the jet from decaying. In addition, this jet is confined by the annulus in which the air tube is positioned (c.f., Figure 4). This confinement also limits the dispersion of the jet. There are not comparable measurements of gas velocity in the experiments reported in (40). However, some recent jet gas velocity measurements have been obtained in (41). In these latter experiments the air tube was positioned in the wide part of the cold flow rig, above the conical grid. The velocities were larger than in the present calculation, by a factor of 3 or more, and the bed was composed of denser particles (0.9 gm/cm^3). The measured velocity profiles, normalized and shown in Figure 7 as open symbols, reflect the
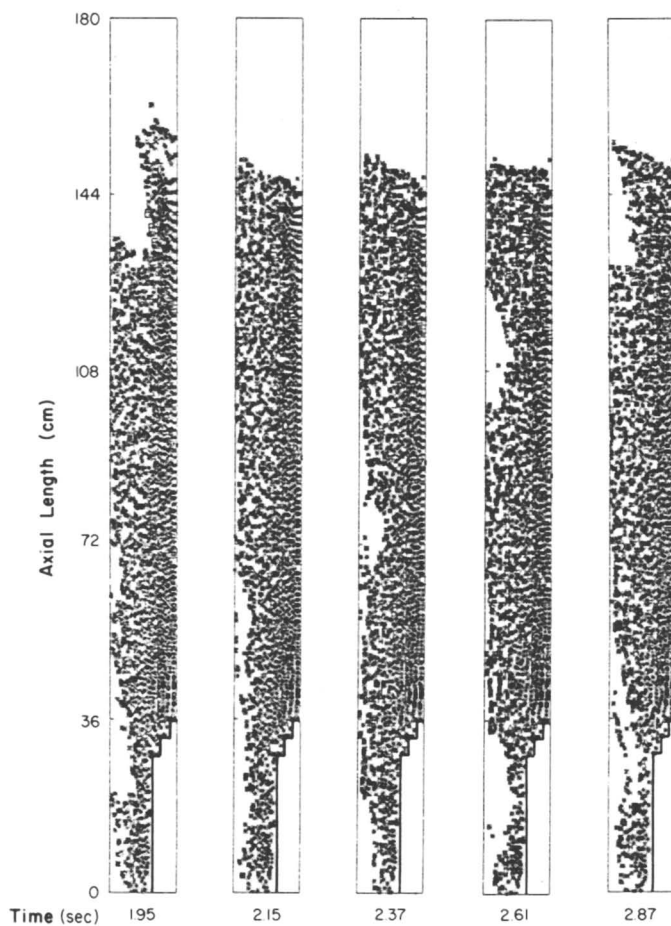
Figure 5.   Time sequence in numerical prediction of cold flow jet penetration and particle mixing in Westinghouse reactor

Air Tube Size, cm	Distance to Conical Grid, cm
• 3.8	0
▼ 3.8	15.2
▲ 3.8	30.5
■ 3.8	45.7
✚ 3.8	30.5 with simulated thermocouple in air tube
○ 5.4	0
▽ 5.4	15.2
△ 5.4	30.5

$$\frac{L}{d_0} = 6.5 \, Fr$$

$$Fr = \left(\frac{\rho_f}{\rho_p - \rho_f} \cdot \frac{V_o^2}{g \, d_0} \right)^{0.5}$$
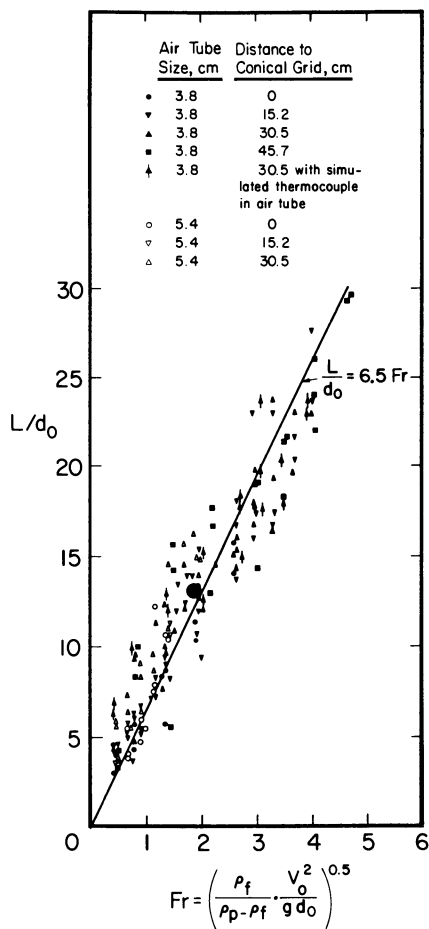
Figure 6. Comparison of the Westinghouse experimental data with (●) calculation, L/d_o = mean jet penetration/air tube diameter, ρ_f = gas density, ρ_p = particle density
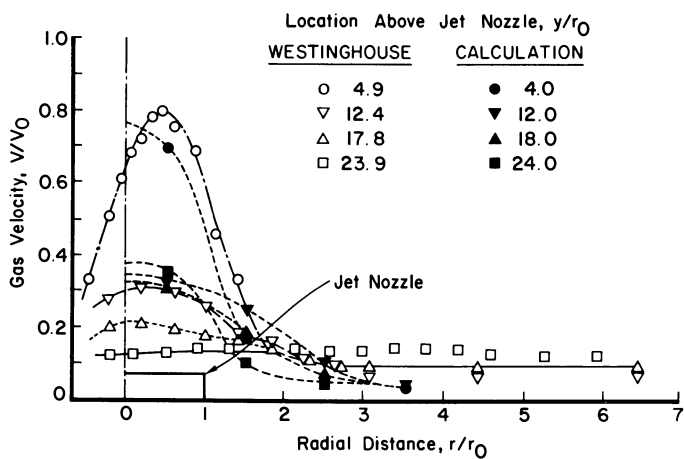
Figure 7.   Comparison between Westinghouse experimental data and numerical calculation of gas phase velocity in jet

similarities and the differences between the latter experiment and the numerical calculation of the jet. The dispersion of the experimental jet is enhanced by the positioning of the jet in the wider section of the reactor. However, despite such differences the normalized calculational and experimental velocity profiles in Figure 7 do show remarkable similarities with regard to both the initially rapid dispersion of the jet between $y/r_0 = 4$ and $y/r_0 = 12$ and to the radial extent of the jet velocity field at most axial (y/r_0) locations above the air tube. Such comparisons tend to validate the hydrodynamic mixing predictions of the numerical model.

This numerical model has also been used to predict the hydrodynamic mixing in a hot reactive environment. The objective of the calculation is to demonstrate the influence of coupled chemistry and hydrodynamics upon the hydrodynamic mixing processes.

In this latter calculation, we use the same geometry as in the previous cold flow calculation (c.f., Figure 4) but change the reactor operating and feed conditions. While there are geometrical differences between the Westinghouse cold and hot flow rigs we, for this present hot flow calculation, keep the geometries the same. The conditions for the hot flow calculation are shown in Table IV where because of the higher nominal gas density in the reactor we increase, relative to the cold flow conditions, the mass flow through the air tube, annulus and conical distributors, thereby maintaining the same nominal superficial velocity in the reactor. Further, we load the reactor with char particles having a particle density of 1 gm/cm^3 (in the present calculation the injection of coal was not included in the simulation).

TABLE IV
REACTOR AND FEED CONDITIONS FOR NUMERICAL SIMULATION OF HOT,
REACTING FLOW IN WESTINGHOUSE REACTOR

Particle Diameter (μm)	2800
Particle Density (gm/cm^3)	1.0
Mass Flow, Air Tube (air, gm/sec)	68.5
Mass Flow, Annulus (H_2O, gm/sec)	6.5
(CO_2, gm/sec)	46.2
Mass Flow, Cone (H_2O, gm/sec)	2.13
Reactor Pressure (atm)	15.0
Reactor Temperature ($^\circ K$)	1290.0

Thus the basic concept of scaling between cold and hot flows which is used herein and implied by the choice of mass flows and gas to particle density ratios in Tables III and IV is that related to the gas density ratio between the hot and cold flows. This scaling criterion, previously used by Westinghouse (40) is, according to our present numerical calculations, a good

one. This can be seen in Figure 8, where we show the numerical prediction of the jet penetration. The mean jet penetrations in the hot and cold flow cases are in agreement and both agree with the Westinghouse data on jet penetration. Further, in that Figure 8, we indicate a single hot flow measurement by Westinghouse (40) which coincides with their cold flow data and by implication suggests that the hot flow numerical calculation is valid.

In addition, the numerical calculation can provide descriptions of the temperature, gas composition, and particle conversion within the reactor. In Figure 9 we show a time sequence of temperature distribution in the gasifier. The oxygen is injected through the air tube and is rapidly consumed by reaction with the char. This oxygen enters the reactor at a temperature of 840°K and, through the combustion which occurs where oxygen and carbon meet, the products of reaction are heated to provide the initial high temperature in the vicinity of the air tube. Subsequent mixing and the endothermic gasification reactions moderate the temperature to provide a fairly uniform temperature distribution in the gasifier.

Concluding Remarks

The fluidized bed coal gasifier computer model is designed to provide a description of the hydrodynamic mixing and coupled chemistry within the reactor. This model should permit a designer to predict:

bubble size,
gas composition and temperature,
stagnant particle regimes,
elutriation,
jet penetration,
and solids mixing.

It is basically a hydrodynamic model, including particle scale effects, which can, therefore, be used to study scale-up and optimization of fluidized bed gasifiers. The hydrodynamic component of the model has been validated through comparison with cold flow visualization data and limited hot flow measurements.

The chemistry component of the model is, in most aspects, identical to the chemistry of the classical models of fluidized bed gasification. A major difference between the classical reactor models and the present fluidized bed coal gasifier computer model is that the classical models require specification of the bed hydrodynamics, such as bubble size. The present model can predict bubble size and the associated solids mixing. Again it is expected that the two types of models are complimentary. The present model can be used to define the hydrodynamics in the hot reactive environment and these hydrodynamics (e.g., bubble size) can then be used as
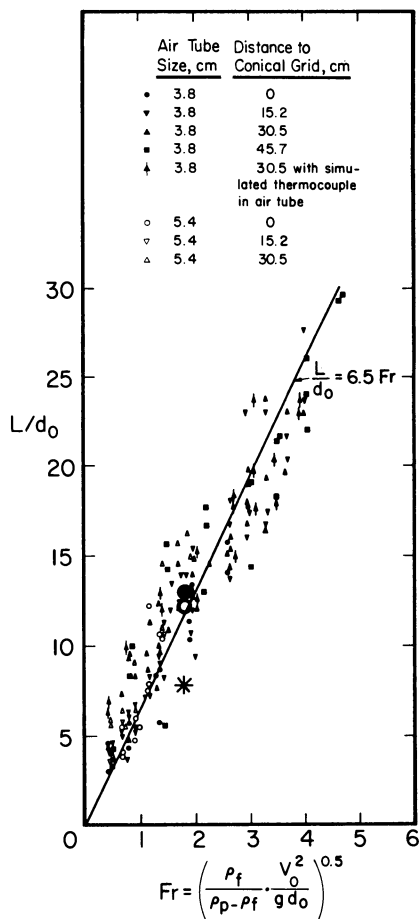
Figure 8. Comparison of the Westinghouse experimental data with (●) cold and (○) hot calculations: Westinghouse cold flow data are indicated by small symbols; Westinghouse hot flow data are indicated by ∗
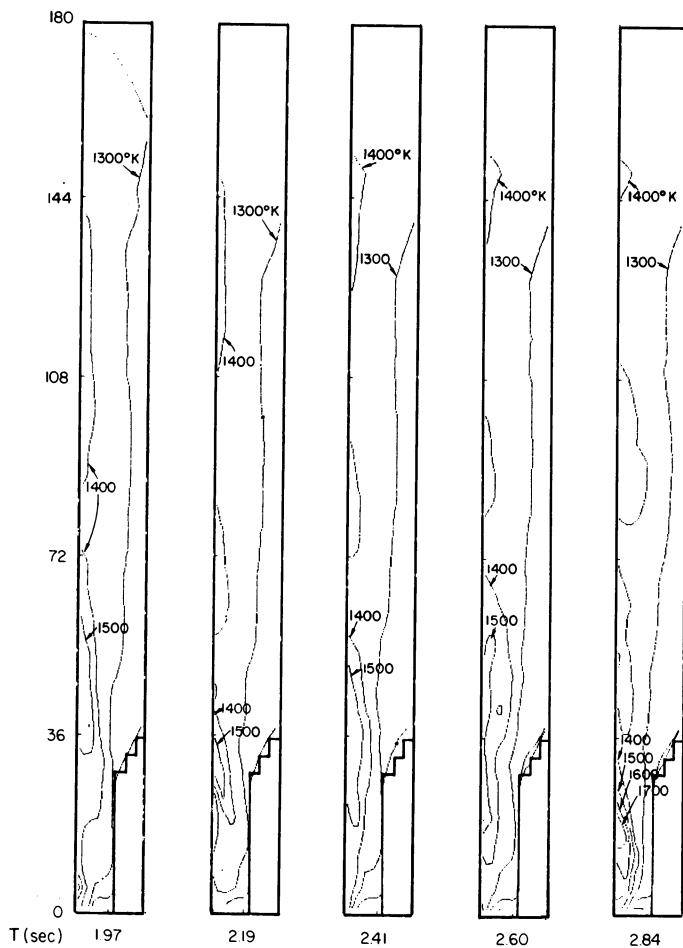
Figure 9.   Numerical calculation of temperature distribution in hot, high pressure, Westinghouse reactor

input to the classical models for a detailed engineering calculation of, say, mass and energy balances for the reactor.

Legend Of Symbols

d_0	=	air tube diameter (cm)
f_i	=	function of partial pressures of reactants in reaction i.
F_r	=	Froude number
G	=	gas volume flow rate (ml/sec)
g	=	acceleration of gravity
k_i	=	kinetic rate coefficient for heterogeneous reaction i (gm/dyne sec)
k_o	=	intra-particle diffusion coefficient (gm/dyne sec)
k_{oE}	=	extra-particle diffusion coefficient, i.e., ash layer of particle (gm/dyne sec)
L	=	mean jet penetration length — the mean of the maximum and minimum jet lengths
$\dot{R}_i$	=	rate of carbon mass loss per unit surface area in i^{th} reaction
r	=	radial distance (cm)
r_0	=	air tube radius (cm)
r_b	=	bubble radius (cm)
V_0	=	air tube gas velocity (cm/sec)
$\vec{U}$	=	velocity vector of a solid particle (cm/sec)
V	=	gas velocity
ν_b	=	bubble volume (ml)
V_b	=	bubble velocity (cm/sec)
X	=	mol percent (N_2 free)
x	=	spatial variable in horizontal or radial direction (cm)
y	=	spatial variable in vertical direction (cm)
γ	=	mole ratio of carbn to oxygen involved in reaction
Δt	=	time increment
$\Delta x, \Delta y$	=	spatial increment in x and y, respectively
ρ_f, ρ_p	=	mass densities of gas and solid phases (gm/cm^3)

Acknowledgements

Literature Cited

1. Toomey, R. D.; Johnston, H. F.; <u>Chem. Eng. Progr.</u>, 1952, <u>48</u>, p. 220

2. Davidson, J. F.; Harrison, D.; "Fluidized Particles," Cambridge University Press, 1963.

3. Kunii, P.; Levenspiel, O.; Ind. Eng. Chem. Fund., 1968, 7, p. 446.

4. Kato, K.; Wen, C. Y.; Chem. Eng. Sci., 1969, 24, p. 1351.

5. Harlow, F. H.; Amsden, A. A.; J. Comp. Phys., 1974, 61, p.1.

6. Gidaspow, D.; Solbrig, C. W.; Presented at AIChE 81st National Meeting, Kansas City, April 11-14, 1976.

7. Sha, W. T.; Soo, S. L.; "Multidomain Multiphase Mechanics," Argonne National Laboratory Technical Memo, ANL-CT-77-3, 1977.

8. Blake, T. R.; Brownell, D. H., Jr.; Schneyer, G. P.; "A Numerical Simulation Model for Entrained Flow Coal Gasification, I. The Hydrodynamical Model," Proceedings, Miami International Conference on Alternative Energy Sources, 1978.

9. Smith, P. J.; Fletcher, T. H.; Smoot, L. D.; Eighteenth Symposium on Combustion, the Combustion Institute, Pittsburgh, 1980.

10. Chan, R. K.-C.,; Dietrich, D. E.; Goldman, S. R.; Levine, H. B.; Meister, C. A.; Scharff, M. F.; Ubhayakar, S. K.; "A Computer Model for the BI-GAS Gasifier," Jaycor Report J510-80-008A-2183, 1980.

11. Blake, T. R.; Garg, S. K.; Levine, H. B.; Pritchett, J. W.; "Computer Modeling of Coal Gasification Reactors," Annual Report June 1975 - June 1976, U.S. Energy Research and Development Administration Report FE-1770-15, 1976.

12. Blake, T. R.; Brownell, D. H., Jr.; Garg, S. K.; Henline, W. D.; Pritchett, J. W.; Schneyer, G. P.; "Computer Modeling of Coal Gasification Reactors - Year 2," 1977, Department of Energy Report FE-1770-32.

13. Blake, T. R.; Brownell, D. H., Jr.,; Chen, P. J.; Cook. J. L.; Garg, S. K.; Henline, W. D.; Pritchett, J. W.; Schneyer, G. P.; "Computer Modeling of Coal Gasification Reactors, Year 3,: Vol. I," 1979, Department of Energy Report FE-1770-49.

14. Pritchett, J. W.; Blake, T. R.; and Garg, S. K.; AIChE Progress Symposium Series, 1978, 176, (4), p. 134.

15. Weil, S., Private communication, 1977.

16. Richtmyer, R. D.; Morton, K. W.; "Difference Methods for Initial Value Problems," 2nd ed., Interscience, New York, 1967.

17. Murray, J. D.; J. Fluid Mech., 1965, 21, Part 2, pp465-493.

18. Anderson, T. B.; Jackson, R.; Ind. Eng. Chem. Fund., 1967, 6. p. 527.

19. Garg, S. K.; Pritchett, J. W.; J. of Appl. Physics, 1975, 46, p. 4493.

20. Rietema, K.; Chem. Eng. Sci., 1973, 28, pp. 1493-1497.

21. Schugerl, K.; in "Fluidization," eds. J. F. Davidson and D. Harrison, Academic Press, London, 1971, pp. 261-292.

22. Richardson, J. F.; in "Fluidization," eds., J. F. Davidson and D. Harrison, Academic Press, London and New York, 1971, pp. 26-64.
23. Gelperin, N. I.; Einstein, V. G.; in "Fluidization,: eds. J. F. Davidson and D. Harrison, Academic Press, London, 1971, pp. 471-540.
24. Yoon, H.; Wei, J.; Denn, M. M.; AIChE Journal, 1978, 24, p. 885.
25. Field, M. A.; Gill, D. W.; Morgan, B. B.; Hawksley, P. B.; "Combustion of Pulverized Coal," BCURA, Leatherhead, 1967.
26. Gray, D.; Cogoli, J. G.; Essenhigh, R. H.; Adv. in Chemistry, 131, ACS., 1974, p. 72-91.
27. Libby, P. A.; Blake, T. R.; Comb. and Flame, 1979, 36, p. 139.
28. Batchelder, H. R.; Busche, R. M.; Armstrong, W. P.; I EC, 1953, 45, No. 9, p. 1856.
29. Blackwood, J. D.; McGrory, R.; Australia Journal of Chem., 1958, 11, p. 16.
30. Blackwood, J. D.; Ingeme, A. H.; Australia Journal of Chem., 1960, 13, p. 194.
31. von Fredersdorf, C. F.; Elliott, M. A.; "Chemistry of Coal Utilization," Supplement Volume, H. H. Lowry, Editors, John Wiley, New York, 1963, pp. 892-1022.
32. Johnson, J. L.; Advances in Chemistry, 1974, 131, p. 145.
33. Dobner, S.; "Modelling of Entrained Bed Gasification: The Issues," EPRI Internal Report, 1976.
34. Wen, C. Y.; Dutta, S.; "Solid-Gas Reactions in Coal Conversion Processes," unpublished report, Department of Chemical Engineering, University of West Virginia, 1976.
35. Wen, C. Y.; Chaung, T. Z.; "Entrained-Bed Coal Gasification Modeling," 71st Annual AIChE Meeting, Miami, 1978.
36. Essenhigh, R. M.; Froberg, R.; Howard, J. B.; Ind. Eng. Chem., 1965, 57 p. 33.
37. Davidson, J.F.; Harrison, D.; Guedes de Carvalho, J.R.F.; in Annual Review of Fluid Mechanics, 1977, 9, p. 55-86.
38. Rowe, P. N.; in "Fluidization," eds. Davidson and Harrison, Academic Press, New York, 1971, p. 121a.
39. Anonymous; "HYGAS; 1964-1972, Pipeline Gas from Coal-Hydrogenation (IGT Hydrogasification Process)" Final Report OCR Contract 14-01-0001-381, 1975, 1-4.
40. Salvador, L. A.; Keairns, D. L.; "Advanced Coal Gasification System for Electric Power Generation Research and Development" Quarterly Progress Report: October-December, 1976; April-June 1977, (ERDA Reports 1514-61; 1514-69), 1977.
41. Yang, W. C.; Keairns, D. L.; "Momentum Dissipation of and Gas Entrainment into a Gas Jet in a Fluidized Bed," 72nd AIChE Annual Meeting, Nov., 1979, San Francisco, 1979.

Study of the Behavior of Heat and Mass Transfer Coefficients in Gas–Solid Fluidized Bed Systems at Low Reynolds Numbers

J. RAMÍREZ, M. AYORA, and M. VIZCARRA

Departamento de Ingeniería Química, División de Estudios de Posgrado, Facultad de Química, Universidad Nacional Autónoma de México

Correlations to estimate heat and mass transfer coefficients in gas-solid fluidized beds operating in the controversial low Reynolds numbers zone are proposed.The correlations incorporate the influence of particle diameter to bed length and particle diameter to bed diameter ratios and gas flowrate. Also, the experimental data are used to analyse the models proposed by Kato and Wen , and Nelson and Galloway in order to explain the behaviour of fluid bed systems operating at low Reynolds numbers.

In spite of the amount of research effort directed towards the determination of the fluid to particle heat and mass transfer coefficients in fluidized beds of fine particles,there is a wide spread in the correlations proposed to estimate them.

A close look at the available experimental data on heat and mass transfer coefficients (1),shows that in the low Reynolds numbers zone exists the peculiar fact that both,the heat and mass transfer coefficients fall well below the value predicted by Ranz (2)for a single sphere submerged in a fluid in laminar flow(Sh=2). In this zone,the numerical results from the different studies also show major disagreement. In general, this is not the case in the high Reynolds numbers zone.

Literature correlations to estimate heat and mass transfer coefficients are generally of the form: $Sh=a\ Re^m$ (3).In general, they do not take into account the scale factors dp/D and dp/L which should be important, especially in the case of fluidized beds, given the complex hydrodynamics of these systems.

From studies on the behaviour of fluidized beds it is already known that bubbles are of great importance if one seeks to describe these systems . Mori and Wen(4)have shown an influence of the ratio dp/D on the growth of bubbles, and it is well known that bubbles grow when they rise through the bed. Clearly,it

should be important to include the factors dp/D and dp/L in the correlations to estimate fluid to particle mass and heat transfer coefficients in fluidized beds.

Kato and Wen (5) found, for the case of packed beds, that there was a dependency of the Sherwood and Nusselt numbers with the ratio dp/L. They proposed that the fall of the heat and mass transfer coefficients at low Reynolds numbers is due to an overlapping of the boundary layers surrounding the particles which produces a reduction of the available effective area for transfer of mass and heat. Nelson and Galloway (6) proposed a new model in terms of the Frossling number, to explain the fall of the heat and mass transfer coefficients in the zone of low Reynolds numbers. The model was developed to show that if the proper boundary conditions are used, one should not expect at low Reynolds numbers that the Nusselt and Sherwood numbers approach the limiting value of two, which is valid for a sphere in an infinite static medium. Since the particles are members of an assemblage, they assume in their model that there is a concentric spherical shell of radius $R > r_o$, on which the radial derivative of temperature or concentration is zero. This change in the boundary condition has a profound effect on the character of the transfer process, especially at low Reynolds numbers. In this case, the dependence of Sherwood number on Reynolds number becomes linear at low enough flowrates, and the limiting zero flow value of the Sherwood number is zero.

The model proposed by Nelson and Galloway can be stated as follows:

$$\mathcal{D} \frac{1}{r^2} \frac{\partial}{\partial r} \left(r^2 \frac{\partial c}{\partial r} \right) = \frac{\partial c}{\partial t}$$

$$c(r,0) = C_o$$

$$c(r_o,t) = C_o'$$

$$\frac{\partial c(R,t)}{\partial r} = 0$$

which for the limit of interest when Re → 0 gives:

$$\lim_{Re \to 0} Sh = \frac{1}{(1-\varepsilon)^{1/3}} \left[\frac{1}{(1-\varepsilon)^{1/3}} - 1 \right] \frac{\alpha^2}{2} Re \ Sc^{2/3}$$

Nelson and Galloway (6) propose a value of $\alpha = 0.6$ as an aproximation to compare experimental data. Clearly, the proposals of Kato and Wen (5) and Nelson and Galloway (6) are the most interesting ones.

In the present work, fluidized bed studies of simultaneous

heat and mass transfer are performed and analyzed in an effort to
add some light into the zone of low Reynolds numbers.

To this end, experimental heat and mass transfer coefficients
were determined in a fluidized bed. Nusselt and Sherwood numbers
were obtained in terms of Reynolds number and aspect ratios dp/L
and dp/D. The results are also analyzed in terms of the Kato and
Wen(5) and Nelson and Galloway(6) models.

Experimental Work

Figure 1 depicts the experimental apparatus used in the
determination of heat and mass transfer coefficients.A compressor
(A) feeds the air to a tank (B), to minimize pulse fluctuations
in flowrate. The air is dried as it passes trough a bed of silica
gel (C). Air flowrate is measured with a rotameter and in addition
with a calibrated capillary meter(E). The inlet air moisture
content is measured by means of a dry and wet bulb thermometer
system (D) prior to its entrance to a coil submerged in a constant
temperature bath (F). From here, the air enters the bottom of the
fluidized bed (G) where its temperature is measured.The fluidized
bed consisted of an insulated QVF glass tube 2 inches in diameter
and 12 inches in length. A system for the collection of fines(I)
was installed after the bed to evaluate entrainment, although at
all experimental conditions used in this work entrainment was
absent. A thermometer placed on top of the bed of solids was used
to measure the temperature of the bed exit.Air moisture content
was also determined at the outlet of the fluidized bed by means
of a hygrometer and a wet and dry bulb temperature system(J).

At time intervals, a sample of solid was taken out of the
bed for moisture content analysis. This was determined by weight
using an analytical scale.

The data used for the calculation of heat and mass transfer
coefficients were taken only from the constant rate drying period.
It was assumed that during this time the solid surface was well
saturated with moisture.

The solid used in this work was silica gel of two different
mean particle diameters. The fine silica gel ranged between 0.0058
to 0.0304 cm., and the coarser between 0.020 to 0.050 cm. in
particle diameters. The mean particle diameters were 0.0125 cm.
and 0.035 cm. respectively. Minimum fluidization velocities were
0.4113 cm/sec. and 1.67 cm/sec. respectively for the small and big
particle diameters.Solid particle density was 1.25 g/cm^3.

In order to obtain uniform moisture content in the solid,
this was humidified in the same fluidized bed. The time interval
for data recording was normally 15 min.

The fluid bed distributor was an aluminium perforated disc
whose holes were 0.5 mm. in diameter arranged in one centimeter
square pitch. A stainless steel 325 mesh screen was fixed at the
entrance side of the perforated disc. The thermometers used for
temperature measuring had 0.1 degree centigrade divisions.In order
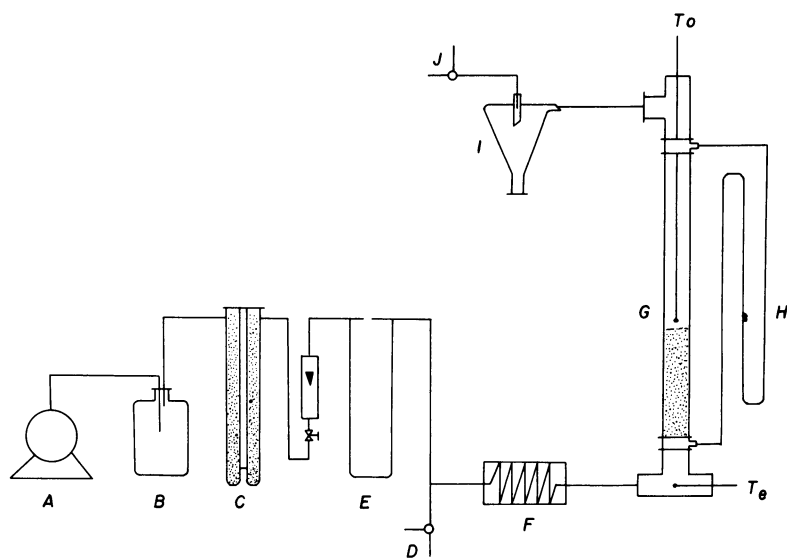
Figure 1.   Experimental apparatus: A, air compressor; B, tank; C, silica gel trap; D, dry and wet bulb thermometer system; E, capillary meter; F, constant temperature bath; G, fluidized bed; I, fines collector; J, dry and wet bulb thermometer system; T_e, entrance temperature thermometer; H, U tube manometer; T_o, outlet temperature thermometer

to avoid condensation problems and to maintain uniform operating temperatures, all lines after the constant temperatures, all lines after the constant temperature bath as well as the fluidized bed were well insulated with glass fibre and asbestos tape.

At time intervals, air and solid moisture content was determined in order to construct the drying curves. A typical set of drying curves is presented in Figure 2.

By carrying out mass and heat balances over the constant rate drying period, mass and heat transfer coefficientes can be obtainded:

$$-\rho_s \frac{dH}{d\Theta} = km\ A\ (X_{bh} - X)_{LM}\ \rho_a \qquad\qquad 1$$

from this equation; the mass transfer coefficient can be readily obtained if one knows the slope of the graph of solid moisture content versus time and the humidities of the air:

$$km = \frac{\rho_s\ (-\frac{dH}{d\Theta})}{A\ (X_{bh} - X)_{LM}\ \rho_a} \qquad\qquad 2$$

Similarly, the heat balance equation is:

$$-\rho_s\ (\frac{dH}{d\Theta}) = \frac{hA}{\lambda}\ (T - T_{bh})_{LM}$$

accordingly the heat transfer coefficient will be expressed as:

$$h = \frac{\rho_s\ (-\frac{dH}{d\Theta})\ \lambda}{A\ (T - T_{bh})_{LM}} \qquad\qquad 3$$

Experimental Results and Conclusiones

During the experimental runs, the air flowrate was varied over the range 5.3 to 20.29 1/min. (Re=0.28 to Re=3.0), the bed height was also varied between 2 and 8 cm. Also, two different particle diameters were used. This gave a variation of the dp/L ratio from 0.0016 to 0.0152 and the dp/D ratio from 0.025 to 0.007 that is an order of magnitud in both ratios.

From the experimental data, taken at time intervals and equations 2 and 3, experimental heat and mass transfer coefficients were obtained. Tables I and II show the values of the experimental heat and mass transfer coefficients.

Figures 3 to 5 show the effect of introducing the scale factors dp/L, dp/D into the correlations to predict heat and mass transfer coefficients.

It comes up clearly from these figures that one way not to correlate heat and mass transfer coefficients, at least in fluidized bed systems, at low Reynolds is a correlation of the
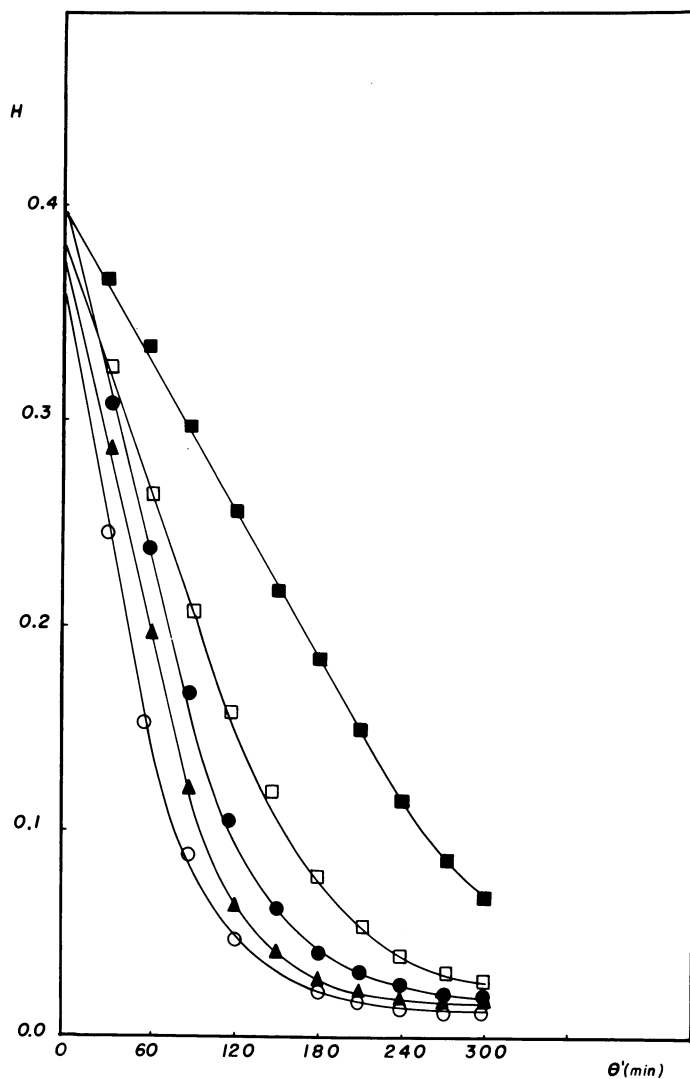
Figure 2.   Typical drying curves; L = 4; D = 5.08; dp = 0.0125: *(■)* Re = 0.285; *(□)* Re = 0.462; *(●)* Re = 0.663; *(▲)* Re = 0.85; *(○)* Re = 0.94

Table I. Calculated values of the mass transfer coefficient at the different operating conditions.

	dp=0.035 cm. km' (m/hr)				dp=0.0125 cm. km' (m/hr)		
Re	L/D=0.39	L/D=0.76	L/D=1.49	Re	L/D=0.39	L/D=0.76	L/D=1.49
3.05	35.55	19.62	19.14	1.06	48.06		
2.48		18.64		0.94	37.52	31.34	10.42
2.20	25.36		16.90	0.85		17.31	7.33
1.74	17.18	11.25	7.93	0.66	23.75	16.19	6.64
1.40	13.08	7.76		0.46	15.79	11.47	5.87
1.22			4.58	0.28	13.34	6.58	4.48

Table II. Calculated values of the heat transfer coefficient at the different operating conditions.

	dp=0.035 cm. km' (m/hr)				dp=0.0125 cm. km' (m/hr)		
Re	L/D=0.39	L/D=0.76	L/D=1.49	Re	L/D=0.39	L/D=0.76	L/D=1.49
3.05	8.09	4.92	5.37	1.060	11.97		
2.48		3.92		0.941	8.56	7.72	2.39
2.20	6.10		3.64	0.850		4.48	1.89
1.74	3.99	2.52	1.68	0.663	5.12	3.84	1.68
1.40	3.09	1.82		0.462	3.36	2.90	1.38
1.22			1.09	0.285	3.08	1.60	1.08
0.826		1.03					
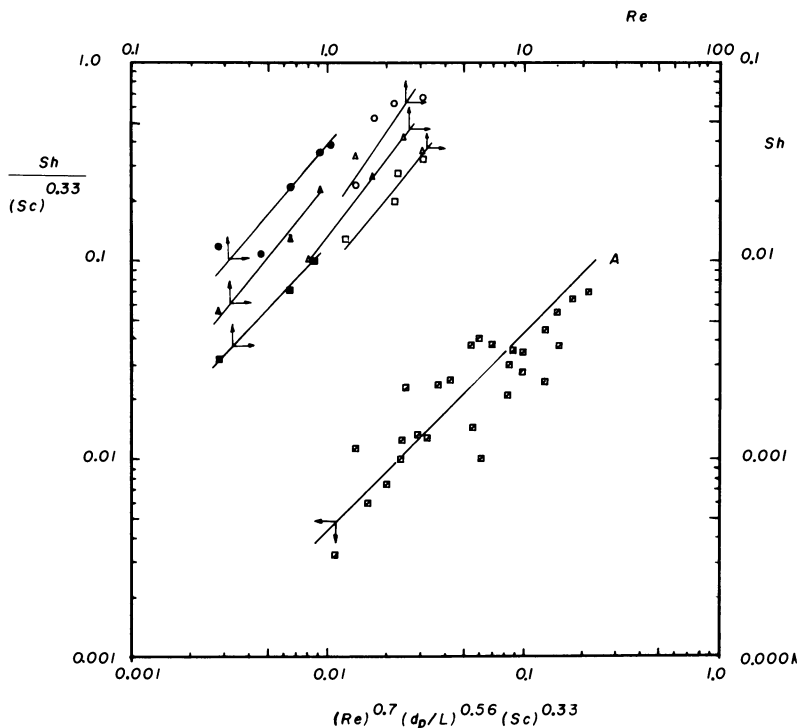
Figure 3.   Effect of the dp/L *ratio on the estimation of Sherwood numbers: (●)* L/D = 0.39, dp = 0.0125; *(▲)* L/D = 0.76, dp = 0.125; *(■)* L/D = 1.49, dp = 0.0125; *(○)* L/D = 0.39, dp = 0.035; *(△)* L/D = 0.76, dp = 0.035; *(□)* L/D = 1.49, dp = 0.035. *The crossed squares (▨) encompass all the experimental data and line A shows the fit to the correlation:* $Sh = 0.4329 (Re)^{0.7}$ $(dp/L)^{0.56} (Sc)^{0.33}$
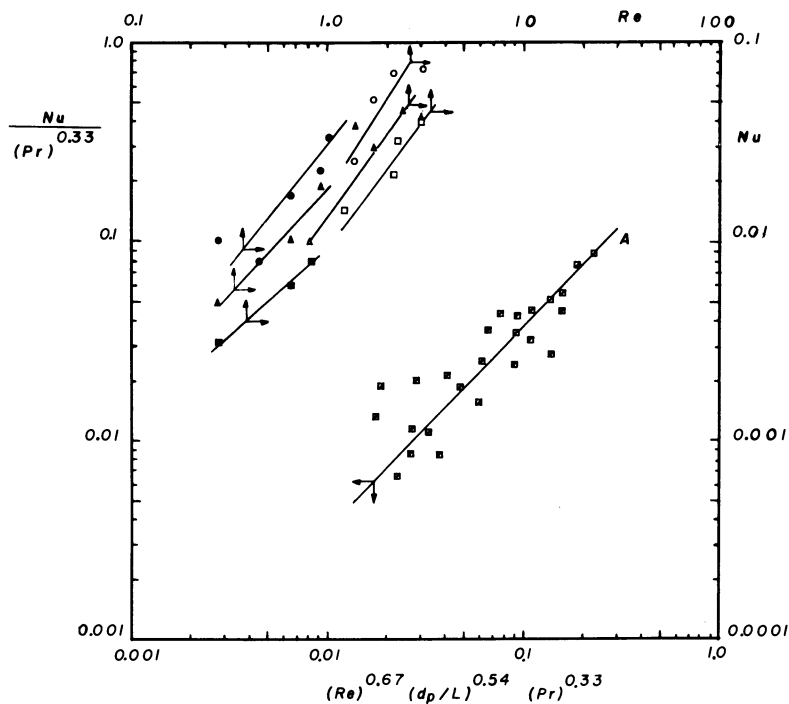
Figure 4. Effect of the d_p/L *ratio on the estimation of Nusselt numbers:* (●) $L/D = 0.39$, $dp = 0.0125$; (▲) $L/D = 0.76$, $dp = 0.0125$; (■) $L/D = 1.49$, $dp = 0.0125$; (○) $L/D = 0.39$, $dp = 0.035$; (△) $L/D = 0.76$, $dp = 0.035$; (□) $L/D = 1.49$, $dp = 0.035$. *The crossed squares* (⊠) *encompass all the experimental data and line A shows the fit to the correlation:* $Nu = 0.3726 \, (Re)^{0.67} \, (dp/L)^{0.54} \, (Pr)^{0.33}$
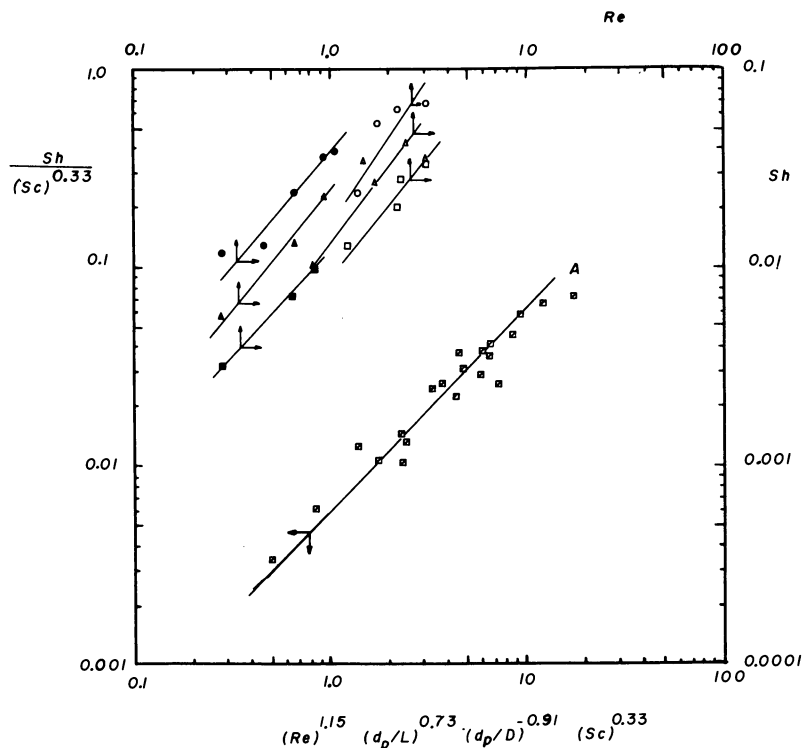
*Figure 5.   Effect of introducing both aspect ratios dp/L and dp/D on the correla-
tion to estimate the Sherwood number: (●) L/D = 0.39, dp = 0.0125; (▲) L/D
= 0.76, dp = 0.0125; (■) L/D = 1.49, dp = 0.0125; (○) L/D = 0.39, dp =
0.036; (△) L/D = 0.76, dp = 0.035; (□) L/D = 1.49, dp = 0.035. The crossed
squares (⊠) encompass all the experimental data and line A shows the fit to the
correlation: Sh = 0.00632 (Re)$^{1.15}$ (dp/L)$^{0.73}$ (dp/D)$^{-0.91}$ (Sc)$^{0.33}$*

form $Sh = a Re^n$ or $Nu = a Re^n$. Unfortunately, this is the way in which the data are presented in the literature.

Exclusion of the dp/L and dp/D ratios from the correlations lead to gross errors up to 200% in the prediction of heat and mass transfer coefficients. Correlations of this form will be too particular to be useful for design.

The final correlations obtained which encompass all the experimental data in this work are:

$$Sh = 0.00632 \ (Re)^{1.15}(dp/L)^{0.73}(dp/D)^{-0.91}(Sc)^{0.33}$$

$$Nu = 0.004948 \ (Re)^{1.14}(dp/L)^{0.71}(dp/D)^{-0.94}(Pr)^{0.33}$$

One can see from the values of the exponents in the aspect ratios dp/D and dp/L, that both parameters are important and their influence cannot be neglected.

As for the Nelson and Galloway model, Figures 7 and 8 show that the proposed model predictions get closer to the experimental results as long as one uses a different value of the parameter α. The value of $\alpha = 0.6$ proposed by Nelson and Galloway predicts too high values of the mass transfer coefficients. If one uses a value of $\alpha = 0.3$, the model predictions get closer to the experimental results of this work.

In other works(7,8) , Galloway and Sage state that the Frossling number (α) varies in the turbulent regimes(900≤Re≤75000) from 0.5 to 1.6. Given the low Reynolds numbers in this work it is quite possible that α should have a value lower than 0.5. This is in agreement to the value of 0.3 which makes the model predict in the range of our experimental values.

Finally, Kato and Wen(5) have proposed that the drastic fall observed for heat and mass transfer coefficients in the zone of low Reynolds numbers is due to an overlapping of the boundary layers surrounding the solid.

This overlapping will in fact reduce the available area for heat and mass transfer. During the present work , some boundary layer thicknesses were estimated for the experimental conditions of this work. As a result , the boundary layers only overlap for Reynolds numbers below 0.826. For the case of Reynolds numbers of 1.74 and 3.05 using the particle diameter of 0.035 cm. , the boundary layers do not overlap. Table III shows some of the values obtained. Clearly, this effect cannot explain completely the low heat and mass transfer coefficients at low Reynolds numbers.

Summing up, for design purposes one should continue using empirical correlations and from this, the ones which include the effect of the scale factors dp/L, dp/D, as the ones proposed in this work , especially at low Reynolds numbers.

As for the theoretical explanation of lower heat and mass transfer coefficients:

The Kato and Wen proposal does not seems to explain all the experimental findings, and the Nelson and Galloway model seems
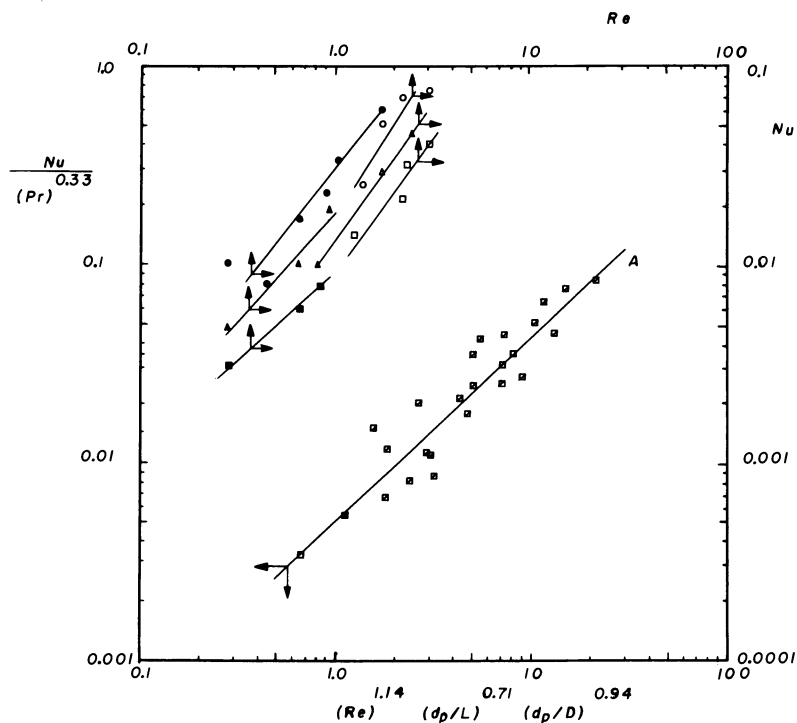
Figure 6. Effect of introducing both aspect ratios dp/L and dp/D on the correlation to estimate the Nusselt number: (●) L/D = 0.39, dp = 0.0125; (▲) L/D = 0.76, dp = 0.0125; (■) L/D = 1.49, dp = 0.0125; (○) L/D = 0.39, dp = 0.035; (△) L/D = 0.76, dp = 0.035; (□) L/D = 1.49, dp = 0.035. The crossed squares (⧄) encompass all the experimental data and line A shows the fit to the correlation: $Nu = 0.004948 \, (Re)^{1.14} \, (dp/L)^{0.71} \, (dp/D)^{-0.94} \, (Pr)^{0.33}$
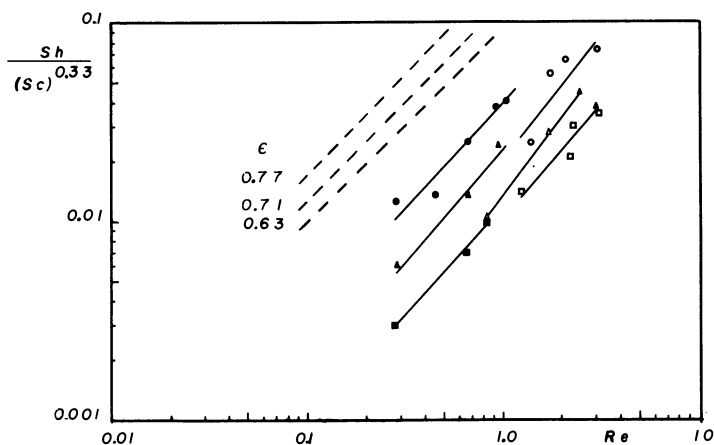
Figure 7. Experimental and predicted values of the Sherwood number using Nelson and Galloway model with $\alpha = 0.6$: ($\bullet$) L/D = 0.39, dp = 0.0125, $\epsilon = 0.77$; ($\blacktriangle$) L/D = 0.76, dp = 0.0125, $\epsilon = 0.74$; ($\blacksquare$) L/D = 1.49, dp = 0.0125, $\epsilon = 0.71$; ($\bigcirc$) L/D = 0.39, dp = 0.035, $\epsilon = 0.69$; ($\triangle$) L/D = 0.76, dp = 0.035, $\epsilon = 0.66$; ($\square$) L/D = 1.49, dp = 0.035, $\epsilon = 0.63$. The broken lines show the model predictions.
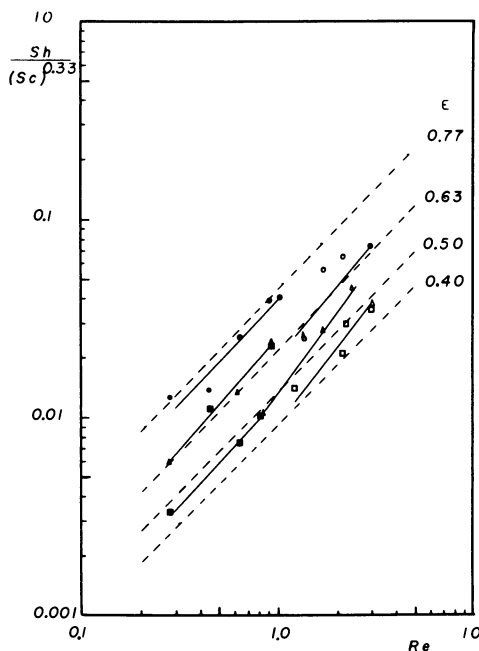
Figure 8.   Experimental and predicted values of the Sherwood number using Nelson and Galloway model with α = 0.3: (●) L/D = 0.39, dp = 0.0125, ε = 0.77; (▲) L/D = 0.76, dp = 0.0125, ε = 0.74; (■) L/D = 1.49, dp = 0.0125, ε = 0.71; (○) L/D = 0.39, dp = 0.035, ε = 0.69; (△) L/D = 0.76, dp = 0.035, ε = 0.66; (□) L/D = 1.49, dp = 0.035, ε = 0.63.   The broken lines show the model predictions.

Table III. Momentum (S) and mass (Sm) boundary layer thinckness calculated at the different operating conditions.

	dp=0.035 cm			dp=0.0125 cm.	
Re	S(cm)	Sm(cm)	Re	S(cm)	Sm(cm)
0.2845	0.0147	0.0154	0.100	0.1600	0.1800
0.2845	0.0144	0.0151	0.826	0.0287	0.0301
0.2845	0.0138	0.0145	0.826	0.0274	0.0287
0.4616	0.0096	0.0101	0.826	0.0262	0.0274
0.4616	0.0094	0.0098	1.74	0.0136	0.0142
0.4616	0.0090	0.0094	1.74	0.0130	0.0136
1.06	0.0076	0.0080	1.74	0.0124	0.0130
1.06	0.0075	0.0079	·3.05	0.0078	0.0082
1.06	0.0072	0.0075	3.05	0.0074	0.0078
3.5	0.0038	0.0040	3.05	0.0071	0.0074
3.5	0.0037	0.0039			
3.5	0.0037	0.0038			

to point in the right direction. More study about the value of the Frossling numbre (α) with Reynolds number will be necessary before one takes up this model.

The dependence of heat and mass transfer coefficientes on the scale factors dp/L and dp/D can also be rationalized in terms of gas bypassing through the bed in the form of bubbles. Since bubbles coalesce and grow as the rise from the distributor, a longer bed, big L/D values, will operate with larger bubbles in its upper part. This will lead to smaller values of the Sherwood and Nusselt numbers since the interchange coefficient between bubble and emulsion phase varies inversely with bubble diameter.

It seems clear that a two phase model will be able to predict low values of the heat and mass transfer coefficients as Kunii has done (1). The trouble with this approach will be an accurate estimate of the equivalent bubble bed diameter. Thus, improved empirical correlations are still useful for design purposes, when one looks for estimates of gas-solid heat and mass transfer coefficients.

Notation

A   area per unir volume, cm^2/cm^3
c   concentration, gm/cm^3
C_o initial concentration, gm/cm^3
D   bed diameter,cm.
dp   particle diameter, cm.
h   heat transfer coefficient $cal/sec-cm^2-°C$
h'   heat transfer coefficient $Kcal/hr-m^2 - °C$
H   solid moisture content, $gm\ H_2O/gm.$ dry solid
km   mass transfer coefficient cm/sec.
km'   mass transfer coefficient m/hr,
L   bed length, cm.
r   radial coordinate, cm.
r_o particle radius, cm.
S   momentum boundary layer thickness, cm.
Sm   mass boundary layer thickness, cm.
T   fluid temperature °C
T_{bh} wet bulb temperature °C
X air moisture content gm. $H_2O/gm.$ dry solid
y   logarithmic mean fraction of inert nondiffusing component
P_r Prandtl number $c_p\ \mu/\ k$
R_e Reynolds number $dp\ \rho_a\ v/\mu$
Sc   Schmidt number $\mu/\rho_a \mathcal{D}$
Sh   Sherwood number $km\ dp\ y/\mathcal{D}$
α Frossling number, $(Sh-2)/Re^{0.5}\ Sc^{0.33}$
$\mathcal{D}$ Diffusion coefficient, $cm^2/sec.$
ε bed porosity
θ time, sec
ρ_a air density, gm/cm^3
ρ_s solid density, gm/cm^3
λ heat of vaporization, cal/gm

Literature Cited

1. Kunii, D.; Levenspiel, O., "Fludization Engineering",Wiley, New York 1969, 199,215.
2. Ranz W.E. Chem.Eng.Progr. 1952, 48, 247.
3. Ayora, M.; "Determinación Experimental de parámetros de diseño para secadores de lecho fluidizado sólido-gas" Tesis de Maestría, Fac.de Química, UNAM, México 1978.
4. Mori, S.; Wen, C.Y. AIChE J. 1975, 21, 190.
5. Kato, K.; Wen, C.Y. Chem. Eng. Prog. Symp. Ser.1970,66,100.
6. Nelson, P.; Galloway, T. Chem. Eng.Sci. 1975,30, 1-6.
7. Galloway, T.; Sage,B.H. Chem. Eng. Sci. 1970,25 ,495.
8. Galloway,T.; Sage,B.H. AIChE, J. 1967, 13 , 563.

Bubble Column

An Overview

YATISH T. SHAH

Chemical and Petroleum Engineering Department, University of Pittsburgh,
Pittsburgh, PA 15261

Bubble columns have been widely used in chemical
and petroleum industries. This paper presents a
brief overview on the present state of art of ver-
tically sparged bubble columns. Hydrodynamics,
mixing and transport characteristics of the bubble
column are briefly evaluated. Recommendations for
the future experimental work are also made.

Bubble column is a term used to describe a vertical column
wherein gas is bubbled through either a moving or stagnant pool
of liquid or liquid-solid slurry. The name is rather loosely
used because the gas is not retained in the column in the form
of bubbles at high gas velocity. The column need not be verti-
cal either; it can be horizontal or even coil shaped. This brief
overview examines the present state of art of the vertically
sparged bubble columns. The discussion is restricted to gas-
liquid systems only.

The important variables that affect the bubble dynamics and
flow regime in a bubble column are gas velocity, fluid properties
(e.g. viscosity, surface tension etc.), nature of the gas distri-
butor, and column diameter. Generally, at low superficial gas
velocities (approximately less than 5 cm/sec) bubbles will be
small and uniform though their nature will depend on the proper-
ties of the liquid. The size and uniformity of bubbles also de-
pends on the nature of the gas distributor and the column dia-
meter. Bubble coalescence rate along the column is small, so
that if the gas is distributed uniformly at the column inlet, a
homogeneous bubble column will be obtained.

At high superficial gas velocities (greater than approxi-
mately 5 cm/sec), the bubble coalescence rate increases signifi-
cantly, the gas-liquid flow becomes non-homogeneous (see Figure I)
and the bubble column contains a mixture of large and small
bubbles. The fraction of gas occupied by large bubbles increases
with the gas velocity. The size of the large bubbles depends on
the nature of the gas distributor, column diameter and physical

Homogeneous   Heterogeneous

(Bubbly flow)   Churn-Turbulent   Slug flow
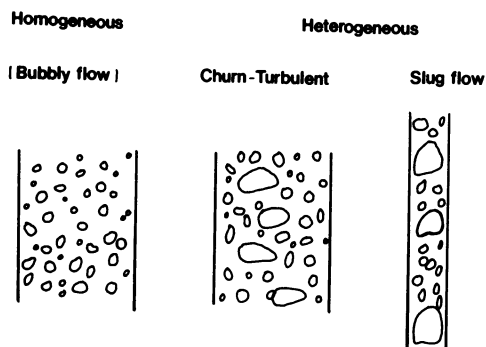
Figure 1.   Different flow regimes in a bubble column
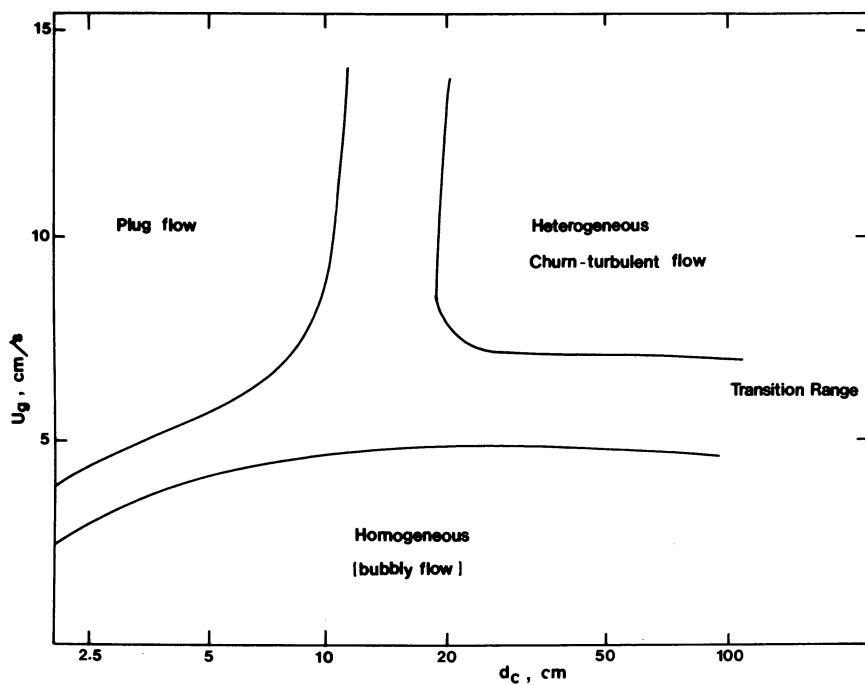
Figure 2.   Flow regime plot for the bubble column

properties of the liquid. The hydrodynamic, mixing and transport properties of a non-homogeneous bubble column should be considerably different from that of a homogeneous column.

A bubble column can be divided into three regions. In the first region near the bottom (i.e. entrance region), the behavior and the properties of the bubbles are determined by the sparger design and the gas flow rate. The second region, above the first, occupies a large fraction of column volume. In this region, bubble properties are determined by the liquid flow pattern and the liquid properties. In the third region, close to the top, bubble coalescence occurs. The position of the regions are affected by superficial gas velocity. As the velocity increases, the coalescence occurs at earlier stage.

A plot of the flow regime prevailing in the major part (i.e., second region in the above classification) of the column in terms of gas velocity and column diameter is described in Figure II. Future work should clearly illustrate the effects of fluid properties and the nature of the gas distributor on the flow regime. From the practical point of view, both homogeneous and non-homogeneous flow regimes are important. The present state of art on hydrodynamics, mixing and transport characteristics of a bubble column in these flow regimes are separately outlined below.

Homogeneous Flow

The hydrodynamic, transport and mixing characteristics in this flow regime are reasonably well understood.

For small liquid velocities, gas holdup is essentially independent of liquid velocity. Provided the ratio of the column to bubble diameter is large, say > 40, the column diameter does not significantly affect the holdup. Usually a column diameter of 10 cm is sufficient to yield holdup values which are close to the ones obtained in larger diameter columns under the same conditions. Dependence of gas holdup on the gas velocity is generally of the form

$$\varepsilon_G \propto u_g^n \tag{1}$$

where in values from 0.7 to 1.2 are reported (1-11). The drift flux theory (12) would give n = 1. The holdup also depends on the fluids employed and trace impurities. The effects of fluid properties such as density, viscosity and surface tension on the gas holdup have been empirically correlated (1-11,13,14). Liquids that have been examined are organic liquids (mostly alcohols and halogenated hydrocarbons), aqueous solutions of glycol, glycerol, ethanol, NaCl, Na_2SO_3, synthetic fermentation media and a variety of electrolytes. The holdup may depend on the liquid phase composition.

Future work should concentrate on large diameter (both short and tall) bubble columns. The applicability of the existing correlation should be examined for these columns for a variety of organic liquids and electrolytes and different types of gas distributors. Very little is known about the bubble dynamics and the gas holdup in a bubble column containing highly viscous polymeric solution and water soluble polymer solutions. This area should be explored.

The gas-liquid interfacial area has been measured by both physical and chemical methods. The accuracy of these measurements is generally very poor (15). The interfacial area has been related to the energy input per unit volume and the gas holdup by the expression (6-19)

$$a \propto (\frac{E}{V_R})^{0.4} (1 - \varepsilon_G)^n \qquad (2)$$

If physico-chemical properties of the system are changed, the above relation may not be completely valid (13). Future efforts should be concentrated in examining the validity of the existing correlations for large diameter (tall and short) bubble columns operated with a variety of gas spargers.

The dependence of the volumetric gas-liquid mass transfer coefficient on gas velocity can be expressed as (26)

$$K_L a = b u_g^n \qquad (3)$$

For water and electrolyte solutions, n = 0.82. The constant b largely depends on the nature of distributor and the liquid media (26). For the coalescing media and if strong absorption takes place, $K_L a$ would be the largest near the gas distributor and would decrease along the length. In industry, porous plates are usually not used even though they provide high mass transfer rates. The gas is either sparged by two-phase nozzles of injector, ejector and slot types (1,16,18-22) or by single and multiorifice distributors. Two phase nozzles with liquid recirculation (jet and slot injectors) provide intimate mixing and high interfacial areas, and hence high mass transfer rates (1,18,19,20). The performance charcteristics and design principles of various gas spargers are treated in the literature (16,18,20-25). For single and multi-orifice spargers, the correlation of Akita and Yoshida (6) is recommended for oxygen in water and aqueous solutions. $K_L a$ data for aqueous solutions of alcohols and glucose, with and without the presence of inorganic electrolytes, are given by Schugerl et al. (1) and for CMC solutions by Buchholz et al. (27), Deckwer et al. (28), Schumpe and Deckwer (29) and Nakanoh and Yoshida (30). $K_L a$ data for large diameter bubble columns, for non-aqueous organic media like alcohols, ketones, esters and

hydrocarbons and for gases such as hydrogen, chlorine etc., are
needed.

In the homogeneous bubble flow regime, the gas phase is
generally assumed to move in plug flow and the liquid phase axial
mixing is characterized by the axial dispersion coefficient. The
axial dispersion coefficient is dependent upon gas velocity and
column diameter according to (26,41,42)

$$E_L \; \alpha \; u_g^{1/3} \; d_c^{4/3} \tag{4}$$

The dispersion coefficient is essentially independent of liquid
velocity. The effect of liquid properties on the dispersion co-
efficient has been found to be very mild and correlated by Cova
(31) and Hikita and Kikukawa (32) as

$$E_L \; \alpha \; \rho_L^{0.07} \; (1/\mu_L)^{0.12} \tag{5}$$

The dispersion coefficient was found to be essentially indepen-
dent of liquid surface tension. The effects of liquid properties
on the dispersion coefficient were also examined by Kato and
Nishiwaki (33), Akita (34), and Ulbrecht and Sema Baykara (35).
A number of hydrodynamics and mixing models have been reported in
the literature and are reviewed by Joshi and Shah (36). Future
work should include the testing of these models for large columns.

The heat transfer in a bubble column is very high. Numerous
data reported in the literature are reviewed and analyzed by
Joshi et al. (37). Further work should be carried out in large
diameter columns only.

Non-Homogeneous Flow

As mentioned earlier, for superficial gas velocities larger
than approximately 5 cm/sec, flow in a bubble column generally
becomes non-homogeneous. This flow regime prevails in most in-
dustrial bubble columns. The flow becomes unstable and coales-
cence occurs. Large bubbles with high rise velocities coexist in
the presence of small bubbles. The large bubbles are no longer
spherical but take the form of spherical caps of varying form
with a very mobile and flexible interface. These large bubbles
can grow up to diameters of about 10 cm. In small diameter
columns, large bubbles can be stabilized by the column wall which
leads to the formation of slugs. In tall columns slugs can be
observed for column diameters as large as 15 cm. The rising
bubbles cause liquid to flow downwards resulting in a circulation
of liquid within the column. The non-homogeneous flow is, there-
fore, sometimes called recirculating flow (38).

In non-homogeneous flow, the knowledge of gas holdup is not very meaningful unless it is divided into two parts: (a) holdup occupied by large bubbles and (b) holdup occupied by small bubbles. The large bubbles will collapse much more rapidly than small bubbles as the gas flow is turned off. Figure IIIa shows the experimental data of Beinhauer (39,40) in a bubble column of 10 cm diameter using water as the liquid phase. At large gas velocities, a large fraction of the column is occupied by large bubbles. As shown in Figure IIIb, large bubbles move faster than smaller bubbles. A proper hydrodynamic characterization of the bubble column under non-homogeneous flow conditions require the holdups occupied by both size bubbles. The literature shows a very low value of n in Equation (1) in non-homogeneous flow regime.

Just as with the gas holdup, gas-liquid interfacial area should also be divided into two parts. The literature, however, gives a unified correlation. The same is true for volumetric gas-liquid mass transfer coefficients and mixing parameters for both gas and liquid phases. The fundamental mechanism for inter-phase mass transfer and mixing for large bubbles is expected to be different from the one for small bubbles. Future work should develop a two phase model for the bubble column analogous to the two phase model for fluidized beds.

General Remarks

The literature on bubble columns is abundant (42,43,44). Future experimental work should be concentrated on large diameter, tall bubble columns. Organic and non-newtonian fluids should be examined. High pressure, high temperature operations need to be emphasized. Theoretical work needs to be concentrated on non-homogeneous flow regime. Solutions to various scale-up problems would be facilitated with a better fundamental understanding of the non-homogeneous flow regime.

Nomenclature

a	gas-liquid interfacial area
b	a constant in Equation (3)
d_c	column diameter
E/V_R	energy per unit volume
E_L	liquid phase axial dispersion coefficient
$K_L a$	volumetric gas-liquid mass transfer coefficient
n	coefficients in Equations (1) and (3)
u_g	superficial gas velocity
u_g^*	bubble rise velocity
ε_G	gas holdup
ρ_L	liquid density
μ_L	liquid viscosity
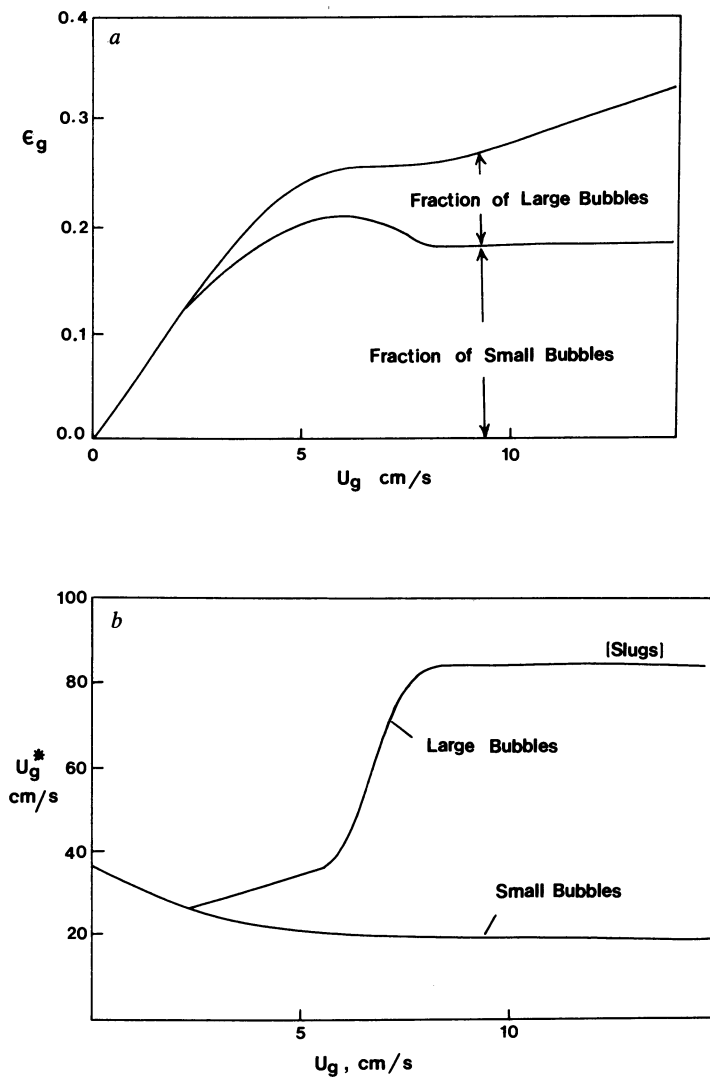
Figure 3.   a, Fractional gas holdup of large and small bubbles (39); b, rise velocity of large and small bubbles (39)

References

1. Schugerl, K.; Lucke, J,; Oels, U. Adv. Biochem. Engng. Ed. by Ghose, T.K.; Fiechter, A.; Balkeborogh, N. 1977, 7, 1.
2. Hammer, H.; Rahse, W. Chem.-Ing.-Tech. 1973, 45, 968.
3. Zlokarnik, M. Chem.-Ing. Tech. 1971, 43, 329.
4. Deckwer, W. D.; Louisi, Y.; Zaidi, A.; Ralek, M. I&EC Process Des. Dev. 1980, 19, 699.
5. Reith, T.; Renken, S.; Israel, B. A. Chem. Eng. Sci. 1968, 23, 619.
6. Akita, K.; Yoshida, F. I&EC Proc. Des. Dev. 1973, 12, 76.
7. Botton, R.; Cosserat, D.; Charpentier, J. C. Chem. Eng. J. 1978, 16, 107.
8. Mersmann, A. Ger. Chem. Eng. 1978, 1, 1.
9. Bach, H. F., Dr.-Ing. Thesis, TU Munich 1977.
10. Bach, H. F.; Pilhofer, T. Ger. Chem. Eng. 1978, 1, 270.
11. Sharma, M. M.; Mashelkar, R. A. Instn Chem. Engrs. Sympos. Ser. 1968, 28, 10.
12. Wallis, G. "One-Dimensonal Two-Phase Flow"; McGraw-Hill: New York, NY, 1969.
13. Oels, U.; Lucke, J.; Buchholz, R.; Schugerl, K. Germ. Chem. Eng. 1978, 1, 115.
14. Hikita, H.; Asai, S.; Tanigawa, K.; Segawa, K. paper presented at CHISA'78, Prague 1978.
15. Schumpe, A.; Deckwer, W.-D. Chem. Eng. Sci. 1980, 35, 1275.
16. Nagel, O.; Kurten, H.; Hegner, B. Chem.-Ing.-Tech. 1973, 45, 913.
17. Nagel, O.; Kurten, H. Chem.-Ing.-Tech. 1976, 48, 513.
18. Nagel, O.; Hegner, B.; Kurten, H. Chem.-Ing.-Tech. 1978, 50, 934.
19. Nagel, O.; Kurten, H.; Hegner, B. in "Two-Phase Momentum, Heat, and Mass Transfer in Chemical Process, and Engineering Systems," ed. by Durst, F.; Tsiklauri, G. V.; Afgan, N. H. Hemisphere Publ. Corp.: Washington, DC 1979, 2, 835.
20. Zlokarnik, M. Chem. Eng. Sci. 1979, 34, 1265.
21. Zlokarnik, M., Verfahrenstechn. (Mainz) 1979, 13, 601.
22. Witte, J.H., Brit. Chem. Eng. 1965, 10, 602.
23. Fair, J. R. Chem. Eng. 1967, 67.
24. Litz, W. J. Chem. Eng. 1972, 162.
25. Bhavaraju, S. M.; Russel, T. W. F.; Blanch, H. W. AIChE J. 1978, 24, 454.
26. Deckwer, W.-D.; Burckhart, R.; Zoll, G. Chem. Eng. Sci. 1974 29, 2177.
27. Buchholz, H.; Buchholz, R.; Lucke, J.; Schugerl, K. Chem. Eng. Sci. 1978, 33, 1061.
28. Deckwer, W.-D.; Schumpe, A.; Nguyen-Tien, K. Biotechn. Bioeng. to be published 1981.
29. Schumpe, A.; Deckwer W.-D. paper presented at ACS Meeting, Atlanta, March 30-April 3, 1981.

30. Nakanoh, M.; Yoshida, F. I&EC Process Des. & Develop. 1980, 19, 190.
31. Cova, D.R. I&EC Process Des. & Develop. 1974, 13, 392.
32. Hikita, H.; Kikukawa, H. Chem. Eng. J. 1974, 8, 191.
33. Kato, Y.; Nishiwaki, A. Int. Chem. Eng. 1972, 12, 182.
34. Akita, K., Dr.-Ing. Dissertation, Kyoto University, zitiert in /26/, 1973.
35. Ulbrecht, J. J.; Baykara, Z. Sema "Liquid Phase Mixing in Bubble Columns with Dilute Polymer Solutions," paper presented at ACS Las Vegas Meeting, August 1980.
36. Joshi, J. B.; Shah, Y. T. "Hydrodynamic and Mixing Models for Bubble Column Reactors," paper presented at ACS Las Vegas Meeting, August 1980.
37. Joshi, J. B.; Shah, Y. T.; Sharma, M. M. "A New Model for Heat Transfer in Bubble Column," paper presented at ACS Las Vegas Meeting, August 1980.
38. Ueyama, K.; Miyauchi, T. AIChE J. 1979, 25, 258.
39. Beinhauer, R., Dr.-Ing. Thesis, TU Berlin 1971.
40. Kolbel, H.; Beinhauer, R.; Langemann, H. Chem.-Ing.-Tech. 1972, 44, 697.
41. Baird, M. H. I.; Rice, R. G. Chem. Eng. J. 1975, 9, 17.
42. Shah, Y. T.; Stiegel, G. J.; Sharma, M. M. AIChE J. 1978, 24, 369.
43. Shah, Y. T.; Deckwer, W.-D. a chapter on "Fluid-Fluid Reactors" in "Scaleup in the Chemical Process Industries" ED. Bisio, A; Kabel, R. J. Wiley & Sons: New York, NY to be published.
44. Shah, Y. T.; Kelkar, B. G.; Godbole, S.; Deckwer, W.-D. "Bubble column Reactors" submitted to AIChE J. 1981.

Access of Hydrodynamic Parameters Required in the Design and Scale-Up of Bubble Column Reactors

WOLF-DIETER DECKWER

Institut für Technische Chemie, Universität Hannover, Callinstrasse 3,
D-3000 Hannover, Federal Republic of Germany

The general difficulties in design and
scale-up of bubble column reactors concern
reaction specific data, such as solubili-
ties and kinetic parameters as well as hy-
drodynamic properties. The paper critically
reviews correlations and new results which
are applicable in estimation of hydrody-
namic parameters of two-phase and three-
phase (slurry) bubble column reactors.

Bubble column reactors (BCR) are widely used in chemical
process industries to carry out gas-liquid and gas-
-liquid-solid reactions, the solid suspended in the liq-
uid phase being most frequently a finely divided cata-
lyst (slurry reactor). The main advantages of BCR are
their simple construction, the absence of any moving
parts, ease of maintenance, good mass transfer and ex-
cellent heat transfer properties. These favorable prop-
erties have lead to their application in various fields:
production of various chemical intermediates, petroleum
engineering, Fischer-Tropsch synthesis, fermentations
and waste water treatment.

Owing mainly to their simple construction and the
absence of moving parts and installments (which usually
provide for a somewhat settled flow pattern) the hydro-
dynamic behavior of BCR is rather complex and changes
considerably with variations in physico-chemical proper-
ties and operational conditions. This causes difficulties
in the design and scale-up of BCR and leads to errors
and unreliabilities which, in turn, often result in over-
dimensioning of the reactors.

Flow Regimes

If a gas is distributed in a liquid by means of a certain sparger the bubbles are uniform in size and uniformly distributed provided the gas velocity is low, say less than 5 cm/s. There is no or little interaction between the bubbles, and this regime is called bubbly or homogeneous flow, see Fig. 1. The bubble size distribution is narrow, and the rise velocities of the bubbles in the swarm lie between 20 and 30 cm/s.

At higher gas velocities with an increasing number of bubbles, the pseudohomogeneous bubble-in-liquid dispersion can no longer be maintained. The flow becomes unstable and coalescence sets in leading to larger diameter bubbles. This flow regime where large bubbles with high rise velocities coexist with small bubbles is called heterogeneous or, owing to the movement of the large bubbles, churn-turbulent flow regime. The large bubbles are nonspherical and of varying form with very mobile and flexible surfaces, for instance, spherical caps. These large bubbles can have diameters of about 8 to 10 cm. Though small in number the large bubbles carry the bulk of the gas through the columns as their rise velocity is large ($\geqslant 1$ m/s).

A peculiar situation occurs in small diameter columns. At high gas flow rates, the larger bubbles are stabilized by the column wall leading to the formation of bubble slugs. In tall columns bubble slugs can be observed for column diameters as large as 20 cm.

A rough indication of the prevailing flow regime for a known column diameter and gas velocity, which are thought to be the major variables, can be taken from Fig. 2. However, other parameters, such as the sparger design, physico-chemical properties and the liquid velocity can effect the transition from one flow regime to the other. For instance, it is well known that in highly viscous solutions, with Newtonian as well as non-Newtonian behavior, large bubbles occur at gas velocities considerably less than 5 cm/s. The type of gas sparger also decisively influences the flow regimes and the transition range between them. Porous spargers with mean pore sizes less than 150 μm commonly lead to bubbly flow up to gas velocities of about 5 to 8 cm/s. On the other hand, if perforated plates, single or multi-nozzle distributors with orifice diameters larger than 1 mm are used homogeneous flow can only be realized at very low gas velocities. At larger orifice diameters

homogeneous   heterogeneous

(bubbly flow)   churn-tur-   slug flow

                     bulent
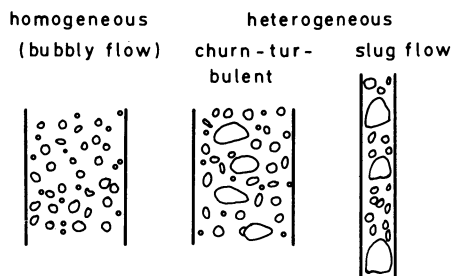
Figure 1.   Flow regimes in BCR
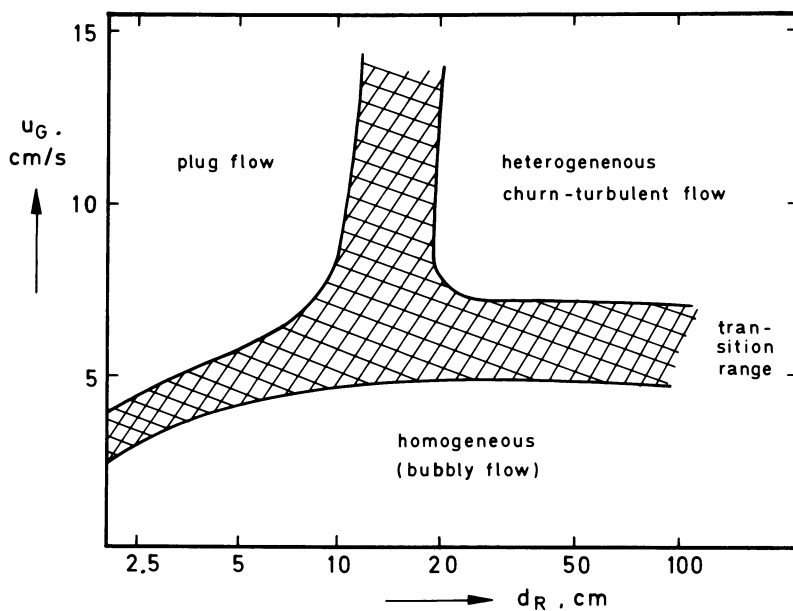
Figure 2.   Dependence of flow regime on gas velocity and column diameter (qualitatively for low viscosity liquids)

bubbly flow may not occur at all if pure liquids are
aerated. For mixtures the situation may change again.
Therefore, the boundaries between the different flow
regimes are not fixed.

The rising bubbles transport liquid on their rear
from the bottom to the top of the column. Therefore, for
continuity, liquid must flow downwards. This results in
a circulation of liquid within the column which leads
to pronounced liquid velocity profiles. The liquid cir-
culation causes a nonuniformity of the gas holdup at any
cross-section. The voidage is usually very large in the
center of the column. It is clear that the circulation
velocity increases with increasing gas throughput.
Therefore, the heterogeneous flow is also called recir-
culating flow regime.

Parameters Involved in BCR Design

In general, the procedure for designing a bubble
column reactor (BCR) (1) should start with an exact de-
finition of the requirements, i.e. the required produc-
tion level, the yields and selectivities. These quan-
tities and the special type of reaction under consider-
ation permits a first choice of the so-called adjustable
operational conditions which include phase velocities,
temperature, pressure, direction of the flows, i.e. co-
current or countercurrent operation, etc. In addition,
process data are needed. They comprise physical proper-
ties of the reaction mixture and its components (den-
sities, viscosities, heat and mass diffusivities, sur-
face tension), phase equilibrium data (above all solu-
bilities) as well as the chemical parameters. The latter
are particularly important, as they include all the ki-
netic and thermodynamic (heat of reaction) information.
It is understood that these first level quantities (see
Fig. 3) are interrelated in various ways.

For the case of single phase reactors the informa-
tion given in this first level would be sufficient to
design the reactor from first principles provided addi-
tional knowledge on the residence time distribution is
available. In multiphase reactor design hydrodynamic
properties constitute another group of important para-
meters. These are more or less "nonadjustable" or self-
adjusting" quantities dependent on the chosen reactor
geometry, the adjustable operational conditions as well
as the process data. Under this notion we summarize the
phase holdups, the interfacial areas, the heat and mass
transfer properties and the dispersion coefficients. All

these quantities, i.e. the geometry, the process data,
the adjustable and nonadjustable parameters, are then
introduced in the reactor model equations derived on the
basis of the physical and chemical phenomena which are
suspected to take place within the reactor. Usually the
model equations have to be solved numerically as they
contain strong nonlinearities (temperature dependency
of reaction rates and solubilities, phase flow varia-
tion). It is understood that the general scheme outlined
in Fig. 3 must be run through several times since the
desired optimal reactor design cannot be obtained ex-
plicitly and is commonly subjected to various economic
choices. The complete design model consisting of the
model equations and the outlined scheme is usually em-
bedded in effective optimization procedures. Such op-
timization techniques can lead to different choices de-
pending on the specific objectives and the conditions
to which the chemical process may be subjected.

The use of models and model simulations are ex-
tremely useful in all design and scale-up considera-
tions. Mathematical methods to solve model equations of
any degree of complexity are available now, and fast
numerical techniques have been developed. In addition,
almost everywhere abundant computer facilities are at
hand. Therefore, a reliable design and scale-up should
use mathematical models formulated on the basis of
first principles, even if these models are very sophis-
ticated. Such models and simulations based on them pre-
sent the most efficient and probably the cheapest way
in today's design works.

The use of models and particularly those of a so-
phisticated nature is, however, seriously restricted
by the limitations of the parameters involved in the
model equations. It is actually the determination of
certain parameters which becomes the crucial point in
designing. The major uncertainties originate from two
sources. Firstly, the process data, i.e. estimation of
phase equilibria (solubilities), diffusivities and es-
pecially kinetic rate data, involves inaccuracies. The
second major source of large uncertainties is the re-
liability of the nonadjustable hydrodynamic quantities.

Correlations for Fluiddynamic Properties

In the following sections, some correlations for
the important hydrodynamic parameters involved in BCR
design are presented and critically discussed. The brief
review includes recent data of the author as well as va-
rious other investigators.
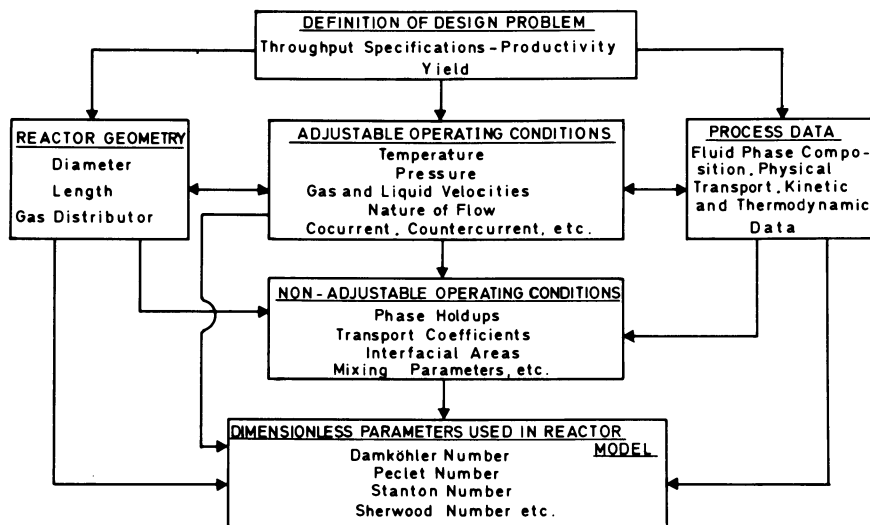
Figure 3.   General procedure to design and scale-up BCR
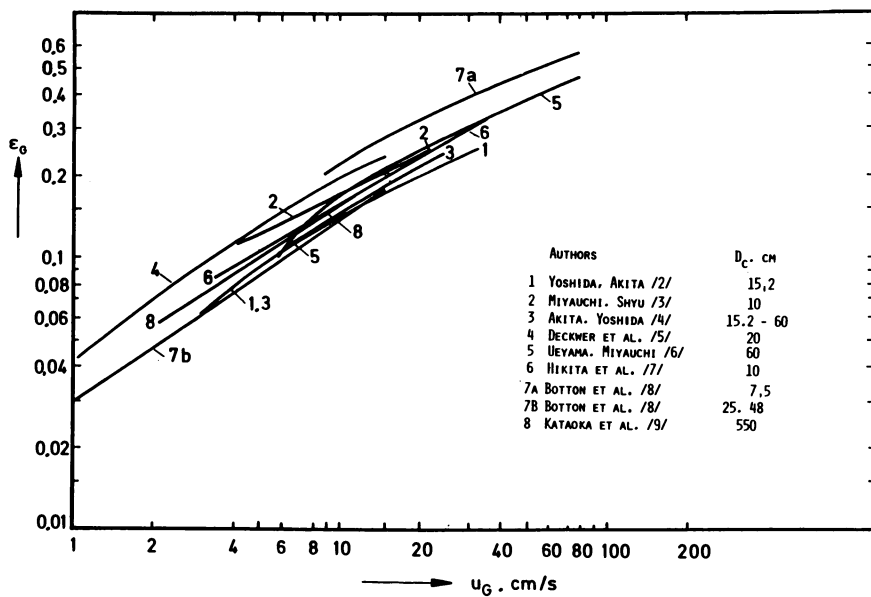
Figure 4.   Measured gas holdup in water for single and multinozzle spargers

In general, little arbitrary and independent variation of the hydrodynamic parameters is possible for a certain reaction system. These properties are determined by complex relationships and interactions of all the quantities given in the first level of parameters in Fig. 3. For estimating the nonadjustable hydrodynamic parameters numerous empirical correlations have been proposed in the literature. Only those correlations are reported here which, at least under certain conditions, seem to be of broader applicability and yield rather reliable results. Particular emphasis is placed on those correlations which are based on sound theoretical concepts.

Gas Holdup

An important parameter to characterize gas-in-liquid dispersions is the gas holdup, ε_G. It depends mainly on the gas throughput and, to a small extent, on the sparger and physico-chemical properties. The column diameter has no influence on ε_G provided the ratio of column to bubble diameter is large, say ≥ 40. This condition is usually fulfilled for column diameters larger than 10 cm.

The dependency of ε_G on the gas velocity u_G can be expressed by

$$\varepsilon_G \alpha u_G^n \ , \tag{1}$$

the value of the exponent, n, depends on the flow regime. In homogeneous bubbly flow n varies from 0.7 to 1.2, while for churn-turbulent flow n is in the range from 0.4 to 0.7. Fig. 4 presents some data for single and multinozzle spargers ($d_n \geq 1$ mm), for water and aqueous systems. The flow is heterogeneous for these conditions and the exponent in Eqn. (1) is about 0.6.

From the numerous correlations for ε_G reported in the literature only two will be given here. Akita and Yoshida (4) correlated their data for water and aqueous solution of glycol, glycerol, methanol, NaCl and Na_2SO_3 by

$$\frac{\varepsilon_G}{(1-\varepsilon_G)^4} = 0.2 \ \left(\frac{gd_c^2 \rho_L}{\sigma}\right)^{1/8} \ \left(\frac{gd_c^3}{\nu_L^2}\right)^{1/12} \ \left(\frac{u_G}{\sqrt{gd_c}}\right) \tag{2}$$

The column diameter d_c in Eqn. (2) is only included to make the various terms dimensionless. Generally, the correlation of Akita and Yoshida gives a conservative estimate.

Bach and Pilhofer /10/ proposed the following relation

$$\frac{\varepsilon_G}{1-\varepsilon_G} = 0.115 \ (\frac{u_G^3}{v_L g \Delta \rho/\rho_L})^{0.23} = 0.115 \ (ReFr)^{0.23} \qquad (3)$$

which describes holdup data for water and various pure organic liquids.

In many practical applications the above correlations as well as others often fail (11-13). This is particularly the case with liquid mixtures and porous spargers. As the holdup can easily be measured it is recommendable to carry out some measurements in labscale equipment with a column diameter of 10 cm or larger.

Interfacial Area

Like the gas holdup the gas-liquid interfacial area, a, represents an important quantity. If the reaction takes place in the fast reaction regime of diffusion-reaction theory, the interfacial area is the main design criterion. Gas holdup and interfacial area are related by

$$a = \frac{6 \ \varepsilon_G}{d_s} \qquad (4)$$

where d_s is the Sauter (volume-to-surface mean) bubble diameter defined by

$$d_s = \frac{\sum N_i d_{bi}^3}{\sum N_i d_{bi}^2} \qquad (5)$$

Values of d_s usually vary between 2 and 6 mm. For water and electrolyte solutions Deckwer et al. (14) recommend a value of d_s = 2.9 mm which was obtained from a lot of data in various bubble columns. For jet spargers in aqueous solutions of organic substances lower values of d_s (1 mm or even less) are also found. Correlations for d_s and the interfacial area are reported by Akita and Yoshida (15).

Various physical and chemical methods can be applied to determine interfacial areas. Unfortunately, the different methods yield largely differing results. The methods used most often are photography and sulfite oxidation. Schumpe and Deckwer (16) recently showed that in the bubble flow regime, i.e. at $u_G \leqslant 5$ cm/s, the photographic area and that obtained from sulfite oxidation are related by

$$a_{photo} = 1.35\ a_{chem} \tag{6}$$

though the measurements were carried out in equal columns. In churn-turbulent flow, the difference between the two methods is about 100 % and maybe even larger, in agreement with the findings of other authors (17,18).

Different chemical methods do not lead to equal interfacial areas either. This is demonstrated in Fig. 5 where areas found with sulfite oxidation and CO_2 absorption in alkali in equal or similar equipment are plotted against u_G. The data considered in Fig. 5 and an explanation of these discrepancies is given in detail elsewhere (19). The main reasons are nonlinear dependency of conversion on a and nonuniformity of bubble sizes and their rise velocities. The results presented in Fig. 5 and also comparison of various physical methods lead to the conclusion that the interfacial area in gas-in-liquid dispersions has serious errors and only rough estimates are available. However, Schumpe and Deckwer (19) presented some reasonable guidelines for efficient experimentation and recommended the use of sulfite oxidation. The sulfite oxidation method may be particularly useful to compare the efficiency of different chemical reactors. Indeed, sulfite oxidation was extensively used by Nagel and coworkers (20-24) to determine interfacial areas in various gas-liquid contactors. On the basis of Kolmogoroff's theory of isotropic turbulence Nagel et al. (22, 24) derived an expression for a as a function of the energy dissipation rate per unit volume of the reactor (E/V_R). Fig. 6 presents their results as a plot of a vs. (E/V_R). In various articles (21-24) Nagel et al. demonstrated the usefulness of their findings for design and scale-up considerations of gas-liquid reactors. It should, however, be pointed out that Fig. 6 refers solely to interfacial areas obtained from the sulfite oxidation system. The picture may be changed considerably if other liquid systems are taken into consideration (25).
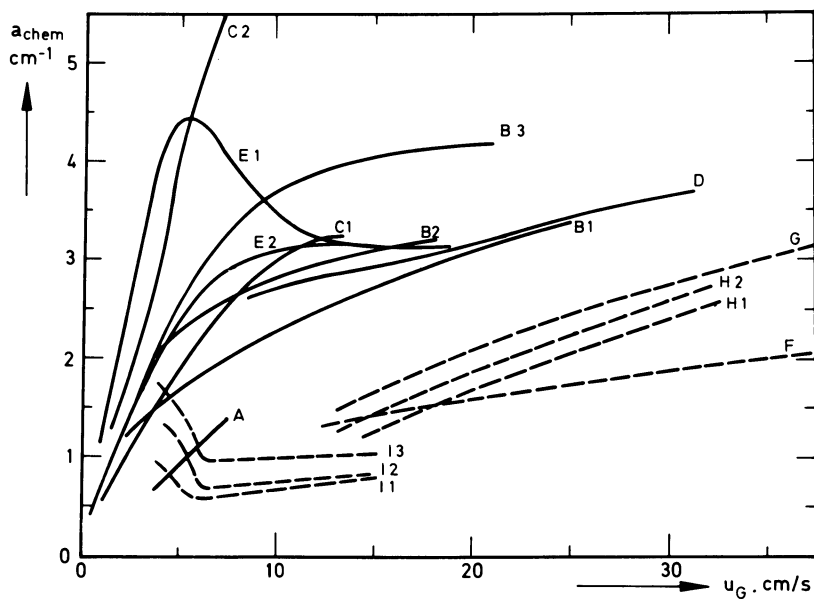
Figure 5.   Interfacial areas from (———) sulfite oxidation and (– – –) CO₂ absorption in alkali
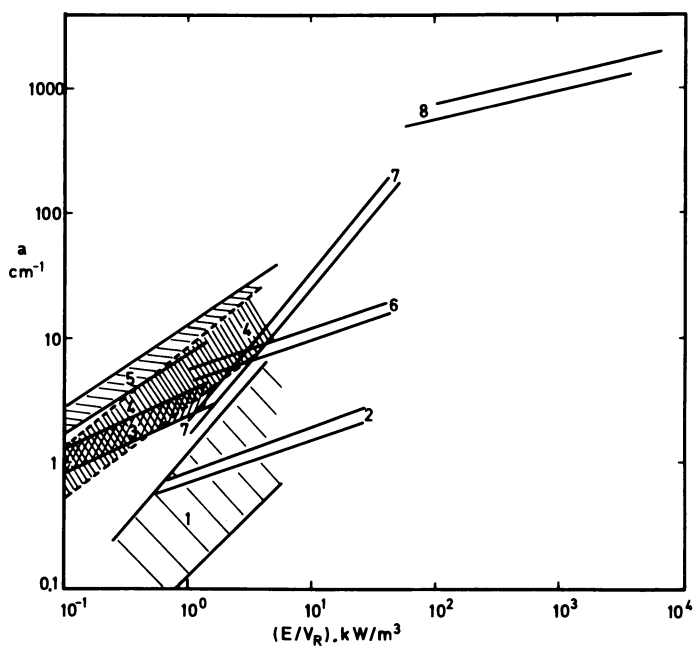
Figure 6. *Interfacial area vs. energy dissipation rate (23): 1, dual-flow column; 2, pipe flow; 3, bubble column; 4, stirred tank; 5, bubble column with 2-phase nozzle; 6, co-current packed bed; 7, jet tube washer (2-phase nozzle); 8, tube reactor with 2-phase nozzle*

Volumetric Mass Transfer Coefficients

The determination of volumetric mass transfer co-
efficients, $k_L a$, usually requires additional knowledge
on the residence time distribution of the phases. Only
in large diameter columns the assumption is justified
that both phases are completely mixed. In tall and
smaller diameter bubble columns the determination of
$k_L a$ should be based on concentration profiles measured
along the length of the column and evaluated with the
axial dispersed plug flow model (5, 12).

Since gas flow strongly influences a it also main-
ly affects $k_L a$. Fig. 7 shows a log-log plot of $k_L a$ vs.
the mean gas velocity, u_G, for oxygen mass transfer in
water. The data refers to different column sizes, gas
spargers and operational conditions. The $k_L a$ values are
not influenced by column geometry, direction of flow,
i.e. cocurrent or countercurrent flow, and mass trans-
fer, i.e. absorption or desorption. But the nature of
the gas sparger obviously exerts a major influence
though the columns are tall. The data for sintered plate
spargers and nozzles can be well described by straight
lines in Fig. 7. The least square fit gives

$$k_L a = b\, u_G^{0.82} \tag{7}$$

where b is 0.0107 for nozzle spargers and 0.0296 for
sintered plates. The exponent of u_G in Eqn. (7) is in
full agreement with a theoretical relation derived by
Kastanek (26) on the basis of Higbie's penetration
theory and Kolmogoroff's theory of isotropic turbulence.
The value of b in Eqn. (7) is influenced not only by the
sparger but also by the physico-chemical properties of
the fluid phases. The $k_L a$ values are independent of the
liquid velocity except at unusually high liquid flow
rates (27).

For the case of the less effective single and mul-
tinozzle spargers Akita and Yoshida (4) proposed the
following correlation

$$k_L a\, \frac{d_c^2}{D_L} = 0.6\, \varepsilon_G^{1.1} \left(\frac{\nu_L}{D_L}\right)^{0.5} \left(\frac{g d_c^2 \rho_L}{\sigma}\right)^{0.62} \left(\frac{g d_c^3}{\nu_L^2}\right)^{0.31} \tag{8}$$

Sparger	d_c,cm	L,cm	Flow	Key
Cross of	20	250	↑↑	x
nozzles,1mm	20	723	↑↑	o
	20	723	↑↑	□
Sintered	10	250	↑↑	●
plate,150 μm	15	440	↑↑	△
	15	440	↑↓	◇
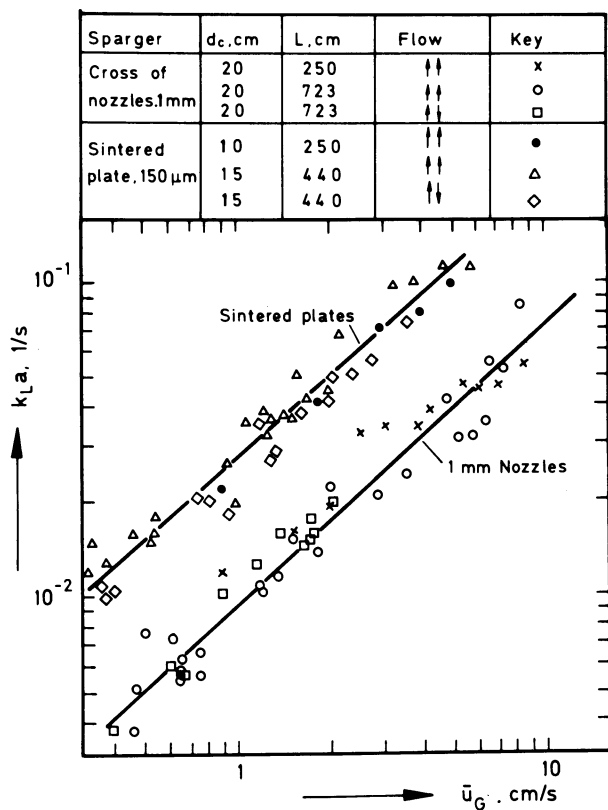
Figure 7. *Volumetric mass transfer coefficients vs. gas velocity in various BCR*

Fig. 8 demonstrates that this empirical correla-
tion describes fairly well the oxygen mass transfer
data of various authors and for large-scale equipment.
Therefore the equation of Akita and Yoshida can be re-
commended for low mass transfer rates, i.e. the mass
transfer of slightly soluble gases. It usually gives
a conservative estimate of $k_L a$.

$k_L a$ data for oxygen mass transfer in aqueous solu-
tions of alcohols and glucose in the presence and ab-
sence of inorganic electrolytes (simulated fermentation
media) in bubble columns equipped with various sparg-
ers are presented by Schügerl et al. (12,25,28). The
somewhat surprising results cannot be correlated by
simple equations but the experimental findings can be
explained qualitatively by means of coalescence pro-
moting and hindering properties of the liquid media.
The studies give some reasonable guidelines for esti-
mating the relative influence of various substances on
$k_L a$ (12,25,28) which are in general agreement with the
findings of Zlokarnik in aerated stirred vessels (29,30)
and larger diameter bubble columns (31). $k_L a$ data for
oxygen transfer in highly viscous and non-Newtonian
media can be found in refs. (32-34).

Special effects can be observed at high mass trans-
fer rates, i.e. with gases of high solubilities, e.g.
CO_2 in water and aqueous solutions. In such cases the
evaluation of mass transfer data from measured profiles
requires the use of sophisticated models (14,15). Due
to variations in gas velocity and gas holdup along the
column the volumetric mass transfer coefficient is not
constant (14,35). The situation becomes even more com-
plex if mass transfer of two gases takes place simul-
taneously (36).

Volumetric mass transfer data for nonaqueous media
such as alcohols, ketones, esters and hydrocarbons
(which are widely used solvents in the chemical process
industry) are scarce. Recently, $k_L a$ values for CO mass
transfer in molten higher paraffins were reported. This
data refers to conditions prevailing in the Fischer-
-Tropsch slurry process (37).

Liquid Side Mass Transfer Coefficient

For mass transfer processes accompanied by slow
chemical reaction it is not required to separate the
volumetric mass transfer coefficient into its individ-
ual quantities, i.e. k_L and a. If the reaction in the

$$\frac{D_L}{d_c^2}\left(\frac{\nu_L}{D_L}\right)^{1/2}\left(\frac{g\,d_c^2\,\rho_L}{\sigma}\right)^{0.62}\left(\frac{g\,d_c^3}{\nu_L^2}\right)^{0.31}\varepsilon_G^{1.1}$$
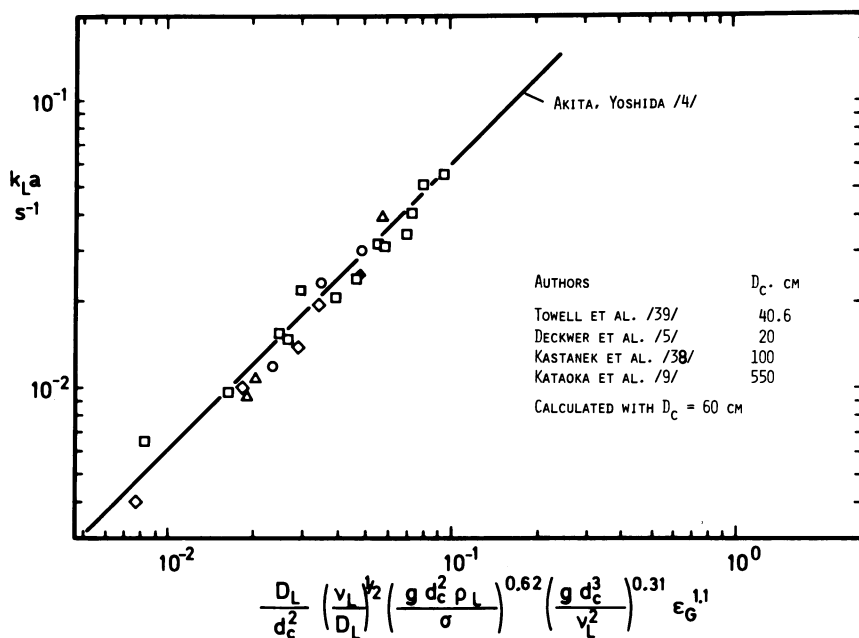
Figure 8.   Check of correlation of Akita and Yoshida (water–air system)

liquid is fast and instantaneous the locale of the re-
action is within the liquid film and knowledge of k_L is
required to calculate the enhancement factors.

A number of empirical and theoretical equations
for evaluating k_L, is available in the literature (12,
15, 40-44). However, the predictions of the various cor-
relations scatter considerably. The correlation proposed
by Akita and Yoshida (15) seems to give rather low val-
ues. The empirical equations developed by Hughmark (42)
and by Calderbank and Moo-Young (41) are widely used
and their application can be recommended. For instance,
the data reported by Zaidi et al. (37) for CO transfer
in molten paraffin at 260 to 290 ^{o}C is in sufficient
agreement with both correlations. As a rule of thumb
it can generally be assumed that for gas-in-liquid dis-
persions k_L varies from 0.01 to 0.03 cm/s.

Mixing

A useful description of mixing in bubble columns
is provided by the dispersion model. The global mixing
effects are generally characterized by the dispersion
coefficients E_L and E_G of the two phases which are de-
fined in analogy to Fick's law for diffusive transport.
Dispersion in bubble columns has been the subject of
many investigations which have recently been reviewed
by Shah et al. (45). Particularly, plenty of data are
available for liquid-phase dispersion.

The dispersion coefficients of the liquid phase
are dependent on the gas velocity and on the column
diameter. The liquid flow, the type of gas sparger and
physico-chemical properties like viscosity do not in-
fluence the dispersion coefficient, E_L, or, at best,
these parameters are of very minor importnace. For in-
stance, Hikita and Kikukawa (46) found only a slight
viscosity influence, i.e. $E_L \alpha u^{-0.12}$.

Baird and Rice (47) derived a theoretical equation
for E_L on the basis of Kolmogoroff's theory of isotrop-
ic turbulence. Their expression is

$$E_L = A \, d_c^{4/3} \, (u_G g)^{1/3} \tag{9}$$

where A is a constant. The exponents of d_c and u_G are
in striking agreement with the experimental results (5).
By introducing dimensionless groups

$$Pe_L = \frac{u_G d_c}{E_L} \qquad (10)$$

and

$$Fr = \frac{u_G^2}{g d_c} \qquad (11)$$

eqn. (9) can be written as

$$Pe_L = c\, Fr^{1/3} \qquad (12)$$

A plot of Pe_L vs Fr based on the data of various authors (5,46,48–54) is shown in Fig. 9. A least square fit of all the data gives

$$Pe_L = 2.83\, Fr^{0.34} \qquad (13)$$

which is indeed in excellent agreement with the theoretical prediction. Empirical equations in terms of Pe_L and Fr were also proposed by Kato and Nishiwaki (51) and by Akita (55), see Fig. 9. Another theoretical approach to calculate the liquid dispersion coefficient is based on the circulation velocity in bubble columns which can be obtained from an overall energy balance (56,57).

Data on gas phase dispersion are rather scarce, and in general they reveal considerable scatter. Towell and Ackerman (52) proposed the following empirical equation

$$E_G = 0.2\, d_c^2 u_G \qquad (14)$$

which includes the data provided by Kölbel et al. (58) and Carleton et al. (59). On the basis of comprehensive experiments with various liquids (water, propanol, glycerol) Mangartz and Pilhofer (60) concluded that the bubble rise velocity in the swarm ($u_G = u_G/\varepsilon_G$) is a characteristic variable which mainly influences the gas dispersion. Mangartz and Pilhofer correlated their results by

$$E_G = 5 \times 10^{-4}\, u_G^3\, d_c^{1.5} \quad . \qquad (15)$$
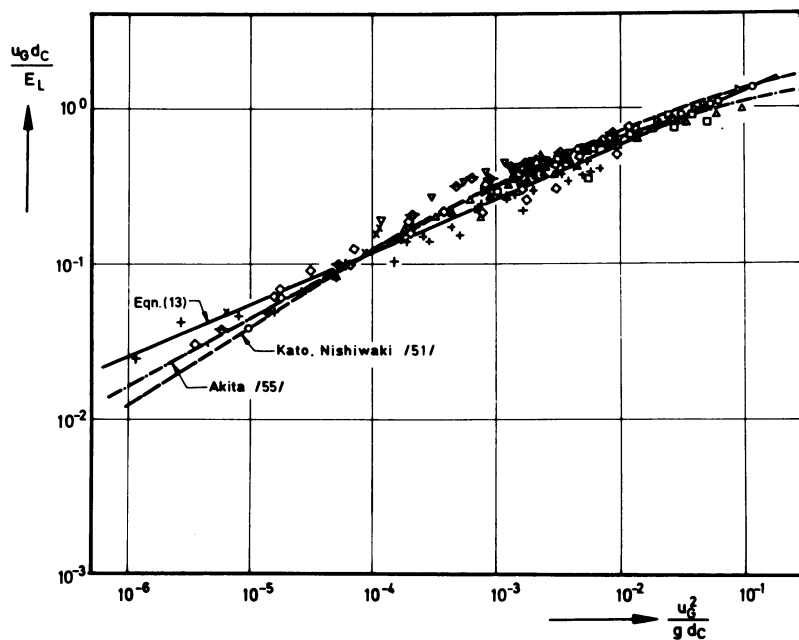
Figure 9.   Correlation of liquid phase dispersion coefficients

   Though the gas phase dispersion coefficients are
large and often larger than those of the liquid phase
the influence of the gas phase dispersion on conversion
should not be overestimated. One has to consider that
it is not the dispersion coefficient itself but the
Peclet number which is the governing parameter in the
model equations. The Peclet number has to be formulated
under consideration of the fractional gas holdup

$$Pe_G = \frac{u_G L}{\varepsilon_G E_G} \cdot \qquad (16)$$

   As ε_G is usually small the detrimental effect of
gas phase dispersion on the performance of bubble col-
umns can be neglected in columns less than 20 cm in
diameter (61). For illustrating the influence of gas
phase dispersion some computed conversions are pre-
sented in Fig. 10 (1). The simulations refer to CO_2 ab-
sorption in carbonate buffer in a column 5 m in length.
E_G was calculated from eqn. (15). The liquid phase dis-
persion does not affect the conversion in the present
case as the process takes place in the diffusional re-
gime of mass transfer theory. As shown in Fig. 10, the
decrease in conversion due to gas phase dispersion in-
creases with increasing diameter and gas velocity. How-
ever, in the favorable bubbly flow regime and in small
diameter columns the effect is less pronounced.

Heat transfer

   BCR are particularly useful to carry out high exo-
thermic gas-liquid reactions like oxygenations, hydro-
genations, and chlorinations. One reason for applying
BCR certainly are their favorable heat transfer proper-
ties, i.e. the large heat capacity of the liquid phase
and high wall-to-dispersion heat transfer coefficients
which are commonly larger by about one order of mag-
nitude than for single phase flow (62). Deckwer (63)
proposed a theoretical heat transfer model by combining
Higbie's penetration model with Kolmogoroff's theory of
isotropic turbulence. The final result can be expressed
in dimensionless form by

$$St = 0.1 \ (ReFrPr^2)^{-1/4} \qquad (17)$$

where

$$St = \frac{h}{\rho c_p u_G} \qquad (18)$$
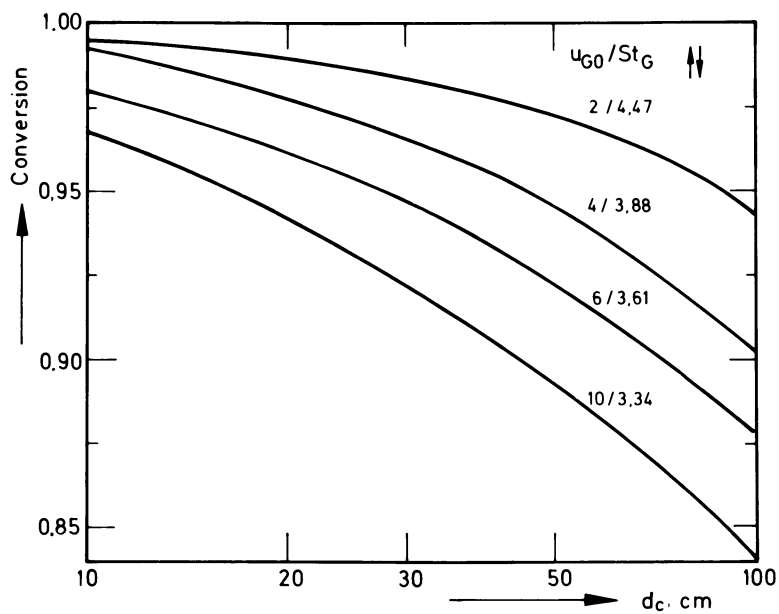
Figure 10.   Effect of gas phase dispersion on conversion by increasing BCR diameter and gas flow rate

$$ReFr = \frac{u_G^3}{\nu g} \tag{19}$$

$$Pr = \frac{\nu \rho c_p}{k} \tag{20}$$

Fig. 11 shows that eqn. (17) describes measured data of various authors (62,64-66) with surprising agreement for a large range of Prandtl numbers.

Effect of Solids

Bubble columns are convenient for catalytic slurry reactions also (67). It is therefore important to know how the hydrodynamic properties of the gas-in-liquid dispersion is influenced by the presence of suspended solid particles. In the slurry reactor absorption enhancement due to chemical reaction cannot be expected. However, if particle sizes are very small, say less than 5 μm, and if, in addition, the catalytic reaction rate is high a small absorption enhancement can occur (68). Usually the reaction is in the slow reaction regime of mass transfer theory. Hence, it is sufficient to know the volumetric mass transfer coefficient, $k_L a$, and there is no need to separate $k_L a$ into the individual values.

In typical slurry reactions like hydrogenations and oxidations the particle sizes are usually smaller than 200 μm and their concentration is less than 10 wt. percent. Under such conditions, the variations in $k_L a$ due to the presence of solids reported (31,69-72) do not commonly exceed 10 to 20 %. If the particles are small ($\leqslant$ 50 μm) the suspended solid and the liquid behave as a pseudohomogeneous phase. This can be concluded from a study on the CO conversion reaction on a catalyst suspended in molten paraffin where no significant effect on ε_G and $k_L a$ could be observed (13,37).

The above result is correct as far as slurries of non-porous particles are concerned. If particles of small size and high porosity are suspended a significant increase in $k_L a$ over that for the gas-liquid system can be observed (68,73,74). Kars et al. (74) and Alper et al (68) studied physical absorption in the presence of suspended activated carbon and found increased k_L values. Alper et al. (68) explained their findings with the absorption capacity of charcoal which leads to in-

creased absorption if the particles enter the boundary
layer at the gas-liquid interface.

Heat transfer in bubble column slurry reactors was
studied by Kölbel and coworkers (75-77) and Deckwer et
al. (13). The addition of solids increases the wall-to-
-suspension heat transfer coefficient. However, this
increase is only due to changes in the physico-chemical
properties and represents no independent contribution
of the particles. Therefore, the heat transfer model,
i.e. eqn. (17), developed by Deckwer (63) for two-phase
BCR also applies to slurry reactors as was proved for
particle sizes up to 120 μm. This confirms that solids
and liquid in the slurry can be regarded as a pseudo-
homogeneous phase provided the gas velocity is large
enough to provide for complete fluidization of the par-
ticles.

Due to density differences the particles have the
tendency to settle. Thus, solid concentration profiles
result which can be described on the basis of the sedi-
mentation-dispersion model (78,79,80). This model in-
volves two parameters, namely, the solids dispersion
coefficient, E_S, and the mean settling velocity, u_S,
of the particles in the swarm. Among others Kato et al.
(81) determined E_S and u_S in bubble columns for glass
beads 75 and 163 μm in diameter. The authors propose
correlations for both parameters, E_S and u_S. The equa-
tion for E_S almost completely agrees with the correla-
tion of Kato and Nishiwaki (51) for the liquid phase
dispersion coefficient.

In catalytic slurry reactors the locale of the re-
action is the catalyst surface. Hence, in addition to
the mass transfer resistance at the gas-liquid inter-
face a further transport resistance may occur at the
boundary layer around the catalyst particle. This is
characterized by the solid-liquid mass transfer coef-
ficient, k_s, which has been the subject of many theoret-
ical and experimental studies. Brief reviews are given
by Shah (82). In general, the liquid-solid mass trans-
fer coefficient is correlated by expressions like

$$\frac{k_s d_p}{D} = 2 + \alpha \left(\frac{\nu}{D} \right)^n \left(\frac{u_s d_p}{\nu} \right)^m \tag{21}$$

or

$$Sh = 2 + \alpha \, Sc^n Re_p^m . \tag{22}$$

As the slip velocity, u_s, of the particles is difficult to estimate it is now common to compute the Reynolds number on the basis of Kolmogoroff's theory which leads to

$$Re_p = C \; (\frac{\epsilon d_p^4}{\nu^3})^p \tag{23}$$

where the value of exponent p depends on the ratio of the particle size to the scale of the microeddies. ϵ is the energy dissipation rate per unit mass which in the case of BCR can simply be calculated from

$$\epsilon = u_G g \tag{24}$$

While many studies on k_s in the two-phase liquid-solid system have been carried out only few have been reported for three-phase bubble columns (83,84). Most recently, Deckwer and Sänger (85) investigated liquid-solid mass transfer on suspended ionic resin beads in a bubble column, the range of the Schmidt number was varied from 137 to 5×10^4 by using aqueous solutions of polyethylene glycol. The findings were correlated by

$$Sh = 2 + 0.545 \; Sc^{1/3} \; (\frac{\epsilon d_p}{\nu^3})^{0.264} \tag{25}$$

Fig. 12 shows that the description of the measured data is fairly good. This is one more example which demonstrates the usefulness of Kolmogoroff's turbulence theory to correlate hydrodynamic parameters in BCR. Eqn. (25) is in reasonable agreement with the results of Sano et al. (84), and compares also well with correlations established for two-phase systems, i.e. stirred liquid-solid suspensions (1).

Summary

The hydrodynamic parameters involved in BCR design and scale-up are mainly dependent on adjustable operational conditions, physico-chemical properties and geometrical sizes. In general, little arbitrary variations are possible with respect to changes in chemical processes. Though a large amount of data has been reported the parameters which characterize the gas-liquid mass transfer properties are still subject to considerable error and unreliabilities. Only for aqueous systems
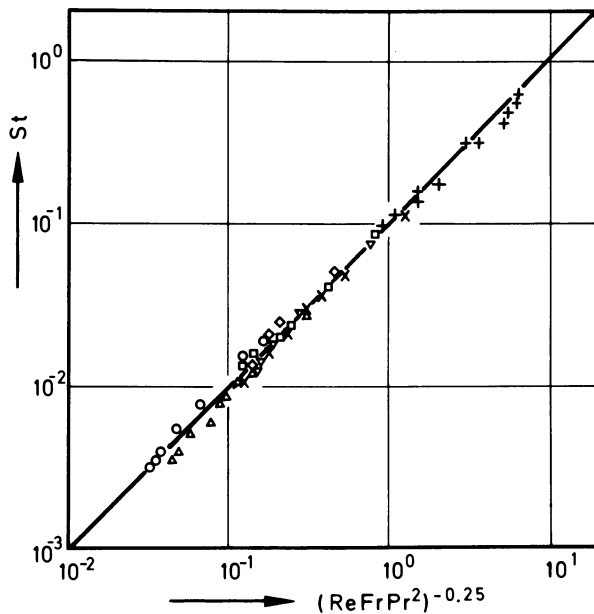
Figure 11.   Correlation of heat transfer data by Equation 17
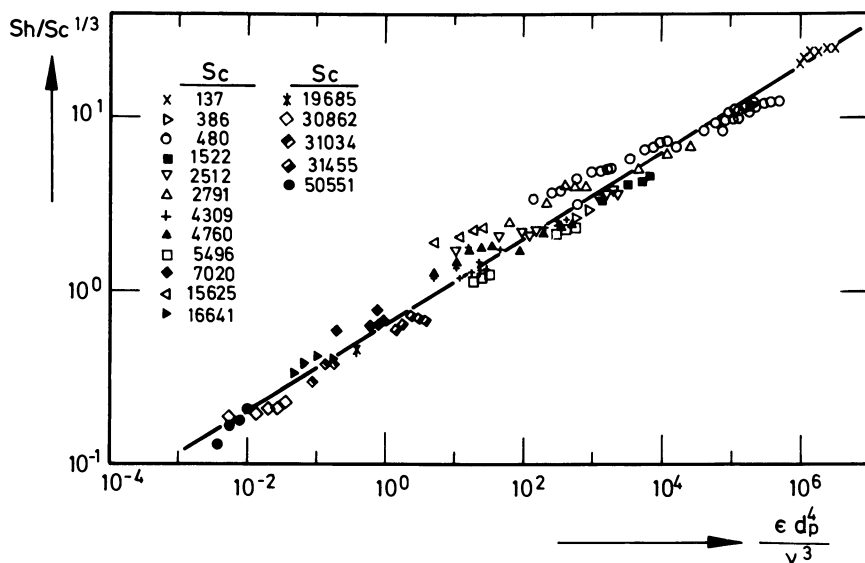
Figure 12.   Correlation of liquid–solid mass transfer coefficients, Equation 25

do the correlations give rather accurate estimates. Contrary to gas-liquid mass transfer parameters the dispersion coefficients of both phases and the wall-to-dispersion heat transfer coefficients can be predicted reliably from theoretical models which have been validated experimentally. Also the influence of solids on the hydrodynamic parameters in three-phase systems is predictable provided the particle sizes are less than about 200 μm and the solids concentration is lower than 10 wt.%. Special effects can only be observed in powdered microporous suspensions.

Legend of Symbols

a	specific gas-liquid interfacial area
c_p	heat capacity
d_c	column diameter
d_{bi}	bubble diameter (of class i)
d_p	particle diameter
d_s	Sauter bubble diameter
D	diffusivity
E	dispersion coefficient
E/V_R	energy dissipation rate per volume
Fr	Froude number, eqn. (11)
g	gravitational acceleration
h	heat transfer coefficient
k	thermal conductivity
k_L	liquid side mass transfer coefficient
k_s	liquid-solid mass transfer coefficient
L	column length
N_i	number of bubbles of diameter class i
Pe_G	gas phase Peclet number, defined by eqn. (16)
Pe_L	Peclet number, defined by eqn. (10)
Pr	Prandtl number, defined by eqn. (20)
Re	Reynolds number, $u_G d/$
Re_p	particle Reynolds number, see eqs. (21) to (23)
Sc	Schmidt number, V /D
Sh	Sherwood number, $k_s d_p/D$

St   Stanton number, defined by eqn. (18)

St_G gas phase Stanton number, $k_L a$ $(L/u_{GO})(RT/H)$

u_G linear gas velocity

u_S slip velocity

u_G rise velocity of bubbles in swarm, u_G/ε_G

ε fractional holdup

ϵ energy dissipation rate per unit mass, see eq.(24)

ν kinematic viscosity

ρ density

σ surface tension

Indices

o   refers to inlet

G   refers to gas phase

L   refers to liquid phase

Acknowledgment

Literature Cited

1.   Shah, Y.T.; Deckwer, W.-D. In: "Scale-up in the
     Chemical Process Industries". Ed. by R. Kabel and
     A. Bisio, John Wiley & Sons, New York, to be pub-
     lished
2.   Yoshida, F.; Akita, K. AIChE-J. 1965, 11, 9
3.   Miyauchi, T.,; Shyu, C.N. Kagaku Kogaku 1970, 34,
     958
4.   Akita, K.; Yoshida, F. Ind. Eng. Chem. Proc. Des.
     Dev. 1973, 12, 76
5.   Deckwer, W.-D.; Burckhart, R.; Zoll, G. Chem. Eng.
     Sci. 1974, 29, 2177
6.   Ueyama, K.; Miyauchi, T. Kagaku Kogaku Ronbunshu,
     1977, 3, 19
7.   Hikita, H.; Asai, S.; Tanigawa, K.; Segawa, K.
     Paper presented at CHISA '78, Prague 1978
8.   Botton, R.; Cosserat, D.; Charpentier, J.C. Chem.
     Eng. J., 1978, 16, 107

9.   Kataoka, H.; Takuchi, H.; Nakao, K.; Yagi, H.;
      Tadaki, T.; Otake, T.; Miyauchi, T.; Washimi, K.;
      Watanabe, K.; Yoshida, F. J. Chem. Eng. Japan 1979,
      12, 105
10. Bach, H.F.; Pilhofer, T. Ger. Chem. Eng. 1978, 1,
      270
11. Hammer, H.; Rähse, W. Chem.-Ing.-Tech. 1973, 45,
      968
12. Schügerl, K.; Lücke, J.; Oels, U. Adv. Biochem.
      Engng. 1977, 7, 1
13. Deckwer, W.-D.; Louisi, Y.; Zaidi, A.; Ralek, M.
      Ind. Eng. Chem. Proc. Des. Dev. 1980, 10, 699
14. Deckwer, W.-D.; Adler, I.; Zaidi, A. Can. J. Chem.
      Eng. 1978, 56, 43
15. Akita, K.; Yoshida, F. Ind. Eng. Chem. Process Des.
      Dev. 1974, 13 84
16. Schumpe, A.; Deckwer, W.-D. Chem.-Ing.-Tech. 1980,
      52, 468
17. Voyer, R.D.; Miller, A.I. Can. J. Chem. Eng. 1968,
      46, 335
18. Weisweiler, W.; Rösch, S. Ger. Chem. Eng. 1978, 1,
      212
19. Schumpe, A.; Deckwer, W.-D. Chem. Eng. Sci. 1980,
      35, 2221
20. Nagel, O.; Kürten, H.; Sinn, R. Chem.-Ing.-Tech.
      1972, 44, 367,399
21. Nagel, O.; Kürten, H.; Hegner, B. Chem.-Ing.-Tech.
      1973, 45 913
22. Nagel, O.; Kürten, H. Chem.-Ing.-Tech. 1976, 48,
      513
23. Nagel, O.; Hegner, B.; Kürten, H. Chem.-Ing.-Tech.
      1978, 50, 934
24. Nagel, O.; Kürten, H.; Hegner, B. In: "Two-Phase
      Momentum, Heat, and Mass Transfer in Chemical Pro-
      cess and Engineering Systems". Ed. by F. Durst,
      G.V. Tsiklauri and H.H. Afgan, Vol. 2, p. 835,
      Hemisphere Publ. Corp., Washington DC, 1979
25. Oels, U.; Lücke, J.; Buchholz, R.; Schügerl, K.
      Ger. Chem. Eng. 1978, 1, 115
26. Kastanek, F. Coll. Czechoslov. Chem. Commun. 1977,
      42, 2491
27. Alvarez-Cuenca, M.; Baker, C.G.J.; Bergeougnou, M.
      A. Chem. Eng. Sci. 1980, 35, 1121
28. Voigt, J.; Schügerl, K. Chem. Eng. Sci. 1979, 34,
      1221
29. Zlokarnik, M. Chem.-Ing.-Techn. 1975, 47, 281
30. Zlokarnik, M. Adv. Biochem. Engng. 1978, 8, 133
31. Zlokarnik, M. Chem. Eng. Sci. 1979, 34, 1265
32. Buchholz, H.; Buchholz, R.; Lücke, J.; Schügerl, K.
      Chem. Eng. Sci. 1978, 33, 1061

33. Buchholz, H.; Buchholz, R.; Niebelschütz, H.; Schügerl, K. Eur. J. Appl. Microbiol. Biotechnol. 1978, 6, 115

34. Nakanoh, M.; Yoshida, F. Ind. Eng. Chem. Proc. Des. Dev. 1980, 19, 190

35. Deckwer, W.-D.; Hallensleben, J.; Popovic, M. Can. J. Chem. Eng. 1980, 58, 190

36. Hallensleben, J. Dr. thesis, Universität Hannover, 1980

37. Zaidi, A.; Louisi, Y.; Ralek, M.; Deckwer, W.-D. Ger. Chem. Eng. 1979, 2, 94

38. Kastanek, F.; Kratochvil, J.; Rylek, M. Coll. Czechoslov. Chem. Commun. 1977, 42, 3549

39. Towell, G.D.; Strand, C.P.; Ackerman, G.H. Preprints AIChE-Instn. Chem. Engrs. Joint Meeting, London, June 1965, Chem. Eng. Symp. Series 10 (1965), 97

40. Ranz, W.E.; Marshall, W.F. Chem. Eng. Progr. 1952, 48, 141

41. Calderbank, P.H.; Moo-Young, M.B. Chem. Eng. Sci. 1961, 16, 39

42. Hughmark, G.A. Ind. Eng. Chem. Proc. Des. Dev. 1967, 6, 218

43. Reuß, M. Dr.-Ing. thesis, TU Berlin, 1970

44. Gestrich, W.; Esenwein, H.; Krauss, W. Chem.-Ing.-Tech. 1976, 48, 399

45. Shah, Y.T.; Stiegel, G.J.; Sharma, M.M. AIChE-J. 1978, 24, 369

46. Hikita, H.; Kikukawa, H. Chem. Eng. J. 1974, 8, 191

47. Baird, M.H.I.; Rice, R.G. Chem. Eng. J. 1975, 9, 17

48. Reith, T.; Renken, S.; Israel, B.A. Chem. Eng. Sci. 1968, 23, 619

49. Aoyama, Y.; Ogushi, K.; Koide, K.; Kubota, H. J. Chem. Eng. Japan 1968, 1, 158

50. Ohki, Y.; Inoue, H. Chem. Eng. Sci. 1970, 25, 1

51. Kato, Y.; Nishiwaki, A. Int. Chem. Eng. 1972, 12, 182

52. Towell, G.D.; Ackerman, G.H. Proc. 2nd Int. Symp. Chem. React. Engng. B 3-1, Amsterdam, 1982

53. Deckwer, W.-D.; Graeser, U.; Langemann, H.; Serpemen, Y. Chem. Eng. Sci. 1973, 28, 1223

54. Badura, R.; Deckwer, W.-D.; Warnecke, H.J.; Langemann, H. Chem.-Ing.-Tech. 1974, 46, 399

55. Akita, K. Dr. thesis, Kyoto University, 1973

56. Joshi, J.B.; Sharma, M.M. Trans. Instn. Chem. Engrs. 1979, 57, 244

57. Joshi, J.B. Trans. Instn. Chem. Engrs., to be published

58. Kölbel, H.; Langemann, H.; Platz, J. Dechema-Monogr. 1962, 41, 225

59. Carleton, A.J.; Flain, R.J.; Rennie, J.; Valentin, F.H.H. Chem. Eng. Sci. 1967, 22, 1839

60. Mangartz, K.-H.; Pilhofer, Th. Verfahrenstechn. (Mainz) 1980, 14, 40
61. Deckwer, W.-D. Chem. Eng. Sci. 1978, 31, 309
62. Kast, W. Int. J. Heat Mass Transf. 1962, 5 329
63. Deckwer, W.-D. Chem. Eng. Sci. 1980, 35, 1341
64. Perner, D. Diplom-Arbeit, TU Berlin, 1960
65. Müller, D. Dr.-Ing. thesis, TU Berlin, 1962
66. Burkel, W. Dr.-Ing. thesis, TU Munich, 1974
67. Deckwer, W.-D.; Alper, E. Chem.-Ing.-Tech. 1980, 52, 219
68. Alper, E.; Wichtendahl, B.; Deckwer, W.-D. Chem. Eng. Sci. 1980, 35, 217
69. Sharma, M.M.; Mashelkar, R.A. Proc. Sym. Mass Transfer with Chemical Reaction 1968, No. 28, 10
70. Kato, Y.; Nishiwaki, A.; Kago, T.; Fikuda, T.; Tanaka, S. Int. Chem. Eng. 1973, 13, 582
71. Sittig, W. Verfahrenstechn. (Mainz) 1977, 11, 730
72. Joosten, G.E.H.; Schilder, J.G.M.; Janssen, J.J. Chem. Eng. Sci. 1977, 32, 563
73. Chandrasekaran, K.; Sharma, M.M. Chem. Eng. Sci. 1974, 29, 2130, 1977, 32, 669
74. Kars, R.L.; Best, R.J.; Drinkenburg, A.A. Chem. Eng. J. 1979, 17, 201
75. Kölbel, H.; Siemes, W.; Maas, R.; Müller, K. Chem.-Ing.-Tech. 1958, 30, 400
76. Kölbel, H.; Borchers, E.; Müller, K. Chem.-Ing.-Tech. 1958, 30, 792
77. Kölbel, H.; Borchers, E.; Martins, J. Chem.-Ing.-Tech. 1960, 32, 84
78. Cova, D.R. Ind. Eng. Chem. Proc. Des. Dev. 1966, 5, 21
79. Suganuma, T.; Yamanishi, T. Kakagu Kogaku 1966, 30, 1136
80. Imafuku, K.; Wang, T.-Y.; Koide, K.; Kubota, H. J. Chem. Eng. Japan 1968, 1, 153
81. Kato, Y.; Nishiwaki, A.; Fukuda, T.; Tanaka, S. J. Chem. Eng. Japan 1972, 5, 112
82. Shah, Y.T. Gas-Liquid-Solid Reactor Design. McGraw-Hill, New York, 1979
83. Kamawura, K.; Sasona, T. Kagaku Kokagu 1965, 29, 693
84. Sano, Y.; Yamaguchi, N: Adachi, T. J. Chem. Eng. Japan 1974, 7, 255
85. Sänger, P.; Deckwer, W.-D. to be published in Chem. Eng. J. 1981

A New Model for Heat Transfer Coefficients in Bubble Columns

YATISH T. SHAH, J. B. JOSHI[1], and M. M. SHARMA[1]

Chemical and Petroleum Engineering Department, University of Pittsburgh, Pittsburgh, PA 15261

In many multiphase (gas-liquid, gas-solid, liquid-liquid and gas-liquid-solid) contactors, a large degree of circulation of both discrete and continuous phases occurs. This circulation causes a good degree of mixing and enhances heat and mass transfer between fluid and walls. The degree of circulation depends on a number of parameters such as the size of equipment, the nature of the phases involved, velocities of various phases, nature of the internals within the equipment and many others. The importance of circulation in bubble columns, gas-solid fluidized beds and agitated contactors has been extensively examined in the literature. In this paper we present a generalized procedure for the calculation of bed-wall heat transfer coefficient in bubble columns on the basis of their hydrodynamic behavior. It has been shown that the high values of heat transfer coefficient obtained in bubble columns, as compared to the single phase pipe flow, can be explained on the basis of the enhanced local liquid velocities in the presence of gas phase. A comparison between the predicted and experimental values of heat transfer coefficient is presented over a wide range of design and operating variables.

There are several industrially important multiphase reactors in which the chemical reaction is accompanied by large heat effects (Table I). Heat is either supplied or removed depending upon whether the reaction is endothermic or exothermic. For the heat to be transferred an area is provided in the form of either coils or vertical or horizontal bundle of tubes or the column

[1] Current address: Department of Chemical Technology, University of Bombay, Bombay, India.

TABLE I

THE REACTIONS OF INDUSTRIAL IMPORTANCE WHICH ARE
CARRIED OUT IN BUBBLE COLUMNS AND SLURRY REACTORS
AND ARE ACCOMPANIED BY LARGE HEAT EFFECTS

   (i)   Oxidation of organic compounds such as toluene, cumene,
         o-xylene, ethylene, acetaldehyde, butane, sec-butyl
         benzene.
  (ii)   Chlorination of benzene, toluene, phenol, ethylene,
         ethanol, acetic acid, and paraffin wax.
 (iii)   Hydrogenation of benzene, nitrobenzene, acetone, adiponi-
         trile, butynediol and "oxo" aldehydes.
  (iv)   Hydration of olefins to alcohols.
   (v)   Fischer-Tropsch synthesis.
  (vi)   Manufacture of organic chemicals by alkylation such as
         cumeme and sec-butyl benzene.

wall. In the last two decades, several investigators have re-
ported the experimental values of heat transfer coefficients in
the multiphase or bubble columns and proposed correlations to ex-
plain their data. Table II gives a summary of the heat transfer
studies made in bubble columns. The experimental observations
may be summarized as follows:
     (i) The heat transfer coefficient at the wall (h_w) is in-
dependent of the column diameter.
     (ii) The values of h_w are 20 to 100 times larger than the
single phase pipe flow and are comparable to those obtained from
mechanically agitated contactors.
     (iii) The values of h_w are practically independent of the
sparger design.
     (iv) The heat transfer coefficient does not increase inde-
finitely with the superficial gas velocity (V_G). The value of h_w
levels off at some value of V_G depending upon the column diameter
and the other physical properties of the gas-liquid system.
     In the past, there have been two major approaches to analyze
the problem of heat and mass transfer across the liquid-solid
interface. The first approach can be broadly classified as "Ana-
logies." This method essentially consists of (von Karman (1) and
Wasan and Wilke (2)): (i) development of velocity profile near
the interface, (ii) suitable assumption for the variation of eddy
diffusivity with respect to the distance from the interface, and
(iii) solution of the Reynolds modification of the Navier-Stokes
equation for the turbulent flow.
     For the case of single phase pipe flow, von Karman (1)
selected the universal velocity profile. The value of eddy vis-
cosity was obtained from the slope of the velocity profile.
Further, it was assumed that the numerical values of eddy vis-
cosity and the eddy diffusivity are the same. The following
equation was obtained:

TABLE II

EXPERIMENTAL DETAILS OF HEAT TRANSFER STUDIES
IN BUBBLE COLUMNS

Symbols in Figures 1 and 4	Tank Dia. T, m	$\dfrac{c_p\mu}{k}$	System	Investigator
○ ⊕	0.46 ⎱ 1.06 ⎰	7.6	air-water	Fair et al. (10)
△	0.099	3.0	-do-	Hart (11)
▽	0.099	36.5	air-ethylene glycol	
□	---	6.0	air-water	Permer (12)
■	---	8.0	air-ethylene -alcohol	
⊖	0.19	6.0	air-water	Burkel (13)
–○–	0.09 ⎱ 0.19 ⎰ 0.29	6.0	air-water	Muller (14)
+	0.1	4.0	air-xylene	Louisi (15)
⊕	0.1	6.1	air-kogasene	
✕	0.1	10.2	air-decalin	

$$\frac{1}{St} = \frac{2}{f} + \frac{2}{f} \cdot f\ (Pr) \tag{1}$$

where f is the fanning fraction factor and its value is obtained
from a suitable correlation. There are several other analogies
available in the published literature. The equations widely used
for the calculation of heat transfer coefficient are the dimen-
sionless correlations which find their basis in analogies. For
instance, Sieder and Tate (3) have proposed the following cor-
relations:

$$\frac{h_w T}{k} = 0.027 \cdot \left\{\frac{TV_a\rho}{\mu}\right\}^{0.8} \left(\frac{c_p\mu}{k}\right)^{1/3} \left(\frac{\mu}{\mu_w}\right)^{0.14} \tag{2}$$

A theoretical approach to analyze the problem of heat trans-
fer is to develop some form of surface renewal model. The rate
of surface renewal is found from the knowledge of energy input
per unit mass. Recently Deckwer (4) has analyzed the problem of
heat transfer in bubble columns on the basis of surface renewal
model. The present study uses the earlier approach.

Mathematical Model

     The enhancement in the bed-wall heat transfer coefficients
in bubble columns as well as the two- and three-phase contactors
as compared to the single phase pipe flow is likely because of
the strong circulation flow pattern in the continuous phase.
Joshi (5) has shown that the average continuous phase circulation
velocities in multiphase contactors are 1 to 2 orders of magni-
tude larger than the net superficial continuous velocities.
Joshi (5) has proposed the following equations:
     The average liquid circulation velocity is given by the fol-
lowing equation.

$$V_c = 1.31' \{gT \ (V_G - \varepsilon V_{b\infty})\}^{1/3} \tag{3}$$

     The average axial and radial components of the liquid velo-
city are given by the following equations:

$$V_a = 1.18' \{gT \ (V_G - \varepsilon V_{b\infty})\}^{1/3} \tag{4}$$

$$V_r = 0.42' \{gT \ (V_G - \varepsilon V_{b\infty})\}^{1/3} \tag{5}$$

     The values of V_a predicted by Equation (4) as well as the
predicted velocity profile agree with the experimental values
reported by several investigators within 15 percent.
     Since the velocity profile in bubble columns is known, the
procedure for the calculation of heat transfer coefficient can be
developed on a more rational basis. Substitution of Equation (4)
in (1) gives:

$$\frac{h_w T}{k} = 0.031' \left\{ \frac{T^{1.33} g^{1/3} (V_G - \varepsilon V_{b\infty})^{1/3} \rho}{\mu} \right\}^{0.8} \left(\frac{c_p \mu}{k}\right)^{1/3} \left(\frac{\mu}{\mu_w}\right)^{0.14} \tag{6}$$

     From Equation (6) it can be seen that h_w is practically in-
dependent of the column diameter ($T^{0.066}$) which agrees with the
experimental observation. However, the values of h_w calculated
from Equation (6) are about 25 to 35 percent of the experimental
values. This may be because of the presence of radial component
of the liquid velocity in bubble columns as against its absence
in the pipe flow.
     In the case of helical coils it is known that the enhance-
ment in h_w occurs because of the presence of radial flow. The
enhancement factor is given by the following equation (Perry and
Chilton (6)):

$$E_c = 1 + 3.5 \, d/D_H \tag{7}$$

where,

$$d/D_H = Re_c/De \tag{8}$$

$$Re_c = \frac{dV_a\rho}{\mu} \tag{9}$$

$$De = \frac{dV_r\rho}{\mu} \tag{10}$$

and

$$\frac{d}{D_H} = \frac{V_r^2}{V_a^2} \tag{11}$$

The above analysis can be applied for the case of bubble columns. From Figure I it can be seen that, near the wall the axial component of the liquid velocity is downwards, whereas the radial component of the liquid velocity is towards the wall in the top half of the circulation cell and away from the wall in the lower half of the circulation cell. As a result, for one circulation cell the enhancement factor is given by the following equation:

$$E_c = 1 + \left(\frac{2V_r}{V_a}\right)^2 \tag{12}$$

Substitution of Equations (4) and (5) in (12) gives:

$$E_c = 2.8 \tag{13}$$

Equation (12), therefore, takes the following form:

$$\frac{h_w T}{k} = 0.087' \left\{ \frac{T^{1.33} g^{1/3} (V_G - \epsilon_G V_{b\infty})^{1/3} \rho^{0.8}}{\mu} \right\} \left(\frac{c_p \mu}{k}\right)^{1/3} \left(\frac{\mu}{\mu_w}\right)^{0.14} \tag{14}$$

From Figure II it can be seen that the predicted and experimental values are within 30 percent.
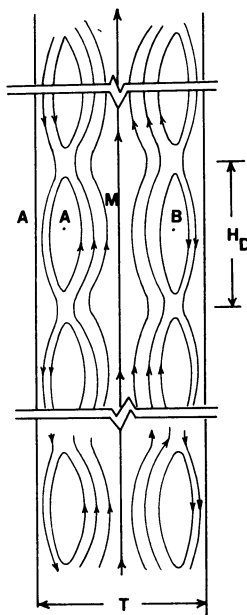
Figure 1. Liquid flow pattern in a bubble column
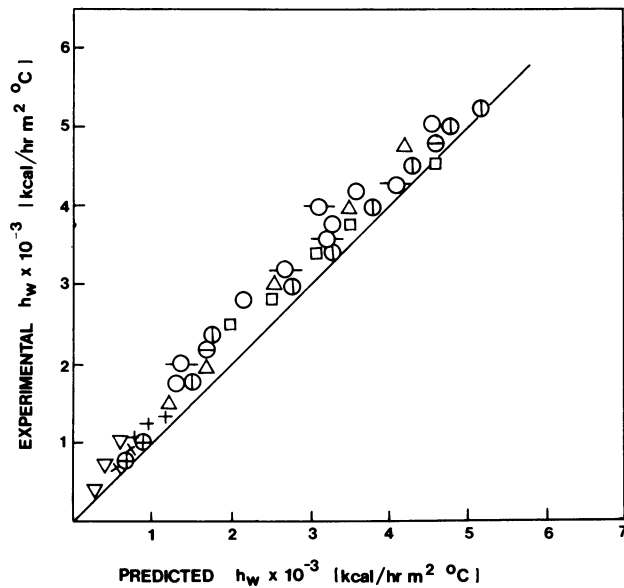
Figure 2. Comparison between experimental and predicted (Equation 24) heat transfer coefficients: bubble column (analogy with pipe flow); for symbol key, see Table II

Comparison with Mechanically Agitated Contactors. The heat transfer coefficient at the wall of mechanically agitated contactors is given by the following equation (Perry and Chilton (6)):

$$\frac{h_w T}{k} = C \left(\frac{ND^2 \rho}{\mu}\right)^{2/3} \left(\frac{c_p \mu}{k}\right)^{1/3} \left(\frac{\mu}{\mu_w}\right)^{0.14} \qquad (15)$$

for

$$40 < \frac{ND^2 \rho}{\mu} < 3 \times 10^5$$

where N and D are the impeller speed and the impeller diameter, respectively. The value of C in Equation (15) is 0.6 for the case of six-bladed disk (Rushton) turbine.

The values of h_w for bubble columns can probably be calculated from the above correlation if the comparison between bubble columns and mechanically agitated contactors is based on the same value of average liquid circulation velocity, V_c.

The value of average liquid circulation velocity in the case of mechanically agitated contactors can be calculated from the data on mixing time. The flow pattern generated by a Rushton disk turbine is shown in Figure III. It can be seen from Figure III that four circulation cells (in a plane, two donut cells in three dimensions) are developed due to the impeller action. The average length of the path for a fluid element leaving the impeller and returning back to the impeller, for any circulation cell, depends on the vessel diameter, the liquid height and the impeller speed. The following value is selected for the central location of the impeller (H = 2h'), where h' is the distance between the impeller and the liquid surface:

$$L = T + H \qquad (16)$$

The circulation time, therefore, is given by the following equation:

$$t_c = \frac{L}{V_c} \qquad (17)$$

Holmes et al. (7) and Norwood and Metzner (8) have shown that the mixing time is about four to five times the circulation time or (say):

$$\theta_{mix} = 4t_c \qquad (18)$$

The value of V_c can be calculated from correlations reported for the mixing time. Thus for instance, Holmes et al. (7) have reported the following equation:
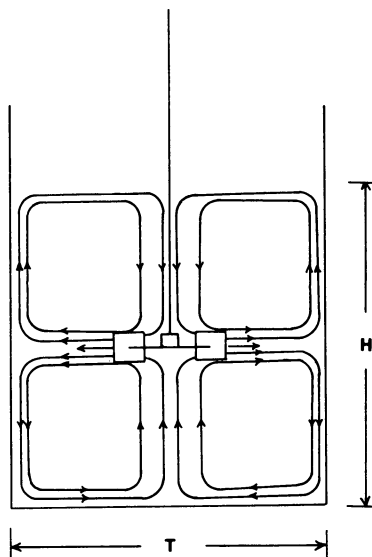
Figure 3.   Liquid flow pattern generated by disk turbine
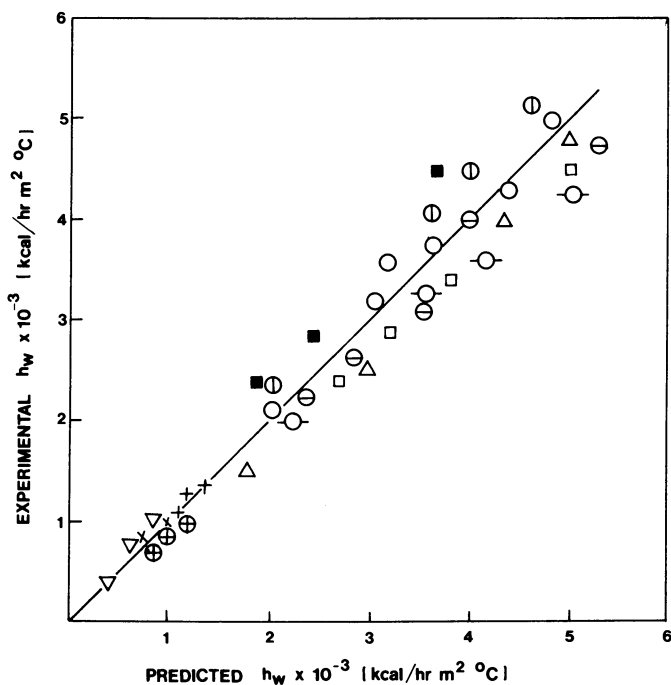
Figure 4.   Comparison between experimental and predicted heat transfer coefficients in bubble columns (Equation 24) (analogy with mechanically agitated contactors); for symbol key, see Table II

$$\theta_{mix} = \frac{4.3(T/D)^2}{N} \qquad (19)$$

Substitution of Equations (16), (17) and (18) in (19) gives:

$$V_c = \frac{(H+T)N}{1.075(T/D)^2} \qquad (20)$$

$$= \frac{1.86ND^2}{T} \text{ for } T = H \text{ and } H = 2h' \qquad (21)$$

Since, $\theta_{mix} \propto L$, and for $T \neq 2h'$

$$V_c = 3.72 \ ND^2/(1+2h'/T)T \qquad (22)$$

Substitution of Equation (21) in (15) gives:

$$\frac{h_w T}{k} = 0.4 \ (\frac{TV_c\rho}{\mu})^{2/3} (\frac{c_p\mu}{k})^{1/3} (\frac{\mu}{\mu_w})^{0.14} \qquad (23)$$

Equation (23) will be applicable for bubble columns if an appropriate value of V_c is incorporated. Substitution of Equation (3) in (23) gives:

$$\frac{h_w T}{k} = 0.48' \{\frac{T^{1.33}g^{0.33}(V_G-\epsilon V_{b\infty})^{1/3}\rho^{0.66}}{\mu}\} (\frac{c_p\mu}{k})^{1/3} (\frac{\mu}{\mu_w})^{0.14} \qquad (24)$$

Figure IV shows a comparison between the experimental (Table II) values of h_w and those predicted by Equation (24). It can be seen that the agreement is within 15 percent. Further, from Equation (24) it can be seen that h_w varies as $T^{-0.11}$. Because of low power on T, the value of h_w are found to be practically independent of T (the variation of column diameter from 1 m to 0.1 m gives only 22 percent reduction). Some more details on this comparison and the application of the present model to other multiphase contactors are recently outlined by Joshi et al. (9).

Nomenclature

c_p	specific heat of the liquid, kcal/kg^{o}C
D	impeller diameter, m
De	Dean's number, $dV_r\rho/\mu$

D_H	helix diameter of a coil, m
d	tube diameter, m
d_B	average bubble diameter, m
E_b	enhancement factor for heat transfer coefficient due to the presence of radial component of the liquid velocity: bubble column
E_c	enhancement factor for heat transfer coefficient due to the presence of radial component of the liquid velocity: helical coil
Fr	Froude number, V_G^2/gd_B
f	fanning friction factor
g	acceleration due to gravity, m/s^2
H	liquid height in mechanically agitated contactors
h	heat transfer coefficient, $kcal/hr\ m^2\ ^\circ C$
h_w	bed-wall heat transfer coefficient, $kcal/hr\ m^2\ ^\circ C$
k	thermal conductivity of the continuous phase, $kcal/hr\ m\ ^\circ C$
k_1, k_2	constants in Equations (30) and (32), respectively
L	length of the path in a circulation cell, m
N	impeller speed, revolutions/s
Pr	Prandtl number, $c_p\mu/k$
Re	Reynold's number for bubble (Equation (3))
Re_c	Reynold's number for coil (Equation (15))
St	Stanton number, $h_w/\rho c_p V_a$
T	column diameter or vessel diameter, m
V_a	average axial component of the continuous phase velocity, m/s
$V_{b\infty}$	terminal rise velocity of bubbles, m/s
V_c	average continuous phase circulation velocity, m/s
V_G	superficial gas velocity, m/s
V_{mf}	minimum velocity for fluidication, m/s
V_0	average rise velocity of bubbles, m/s
V_r	radial component of the continuous phase velocity
t_c	circulation time, s
ρ	density of the liquid, g/cc
ε	fractional gas holdup, dimensionless
μ	viscosity of the continuous phase, cp
θ_{mix}	mixing time, s

Literature Cited

1. von Karman, Th. Trans. ASME 1939, 61, 705.
2. Wasan, D. T.; Wilke, C. R. Int. J. Heat and Mass Transfer 1964, 7, 87.
3. Sieder, E. N.; Tate, G. E. Ind. Eng. Chem. 1936, 28, 1429
4. Deckwer, W. D. Chem. Eng. Sci. 1980, 35, 1341.
5. Joshi, J. B. Trans. Instn. Chem. Engr. 1980, 58, 155.
6. Perry, R. H.; Chilton, C. H. "Chemical Engineers Handbook," 5th ed.; McGraw-Hill: New York, NY, 1973.
7. Holmes, D. B.; Voncken, R. M.; Dekker, J. A. Chem. Eng. Sci 1964, 19, 201.

8. Norwood, K. W.; Metzner, A. B. AIChE J. 1960, 6, 432.
9. Joshi, J. B.; Sharma, M. M.; Shah, Y. T.; Singh, C. P. P.; Ally, M.; Klinzing, G. E. "Heat Transfer in Multiphase Contactors," Chem. Eng. Communication 1981 (in press).
10. Fair, J. R.; Lambright, A. J.; Anderson, J. M. I&EC Proc. Des. and Develop. 1962, 1, 33.
11. Hart, W. F. I&EC Proc. Des. and Develop. 1976, 15, 109.
12. Permer, D. Dipl. Arbeit, TU Berlin, 1960.
13. Burkel, W. Dr. Ing. Thesis, TU Munchen, 1974.
14. Muller, D. Dr. Ing. Thesis, TU Berlin, 1962.
15. Louisi, Y. Dr. Ing. Thesis, TU Berlin, 1979.

Dispersion and Hold-Up in Bubble Columns

RICHARD G. RICE

Department of Chemical Engineering, Louisiana State University, Baton Rouge, LA 70803

JORMA M. I. TUPPERAINEN and ROBYN M. HEDGE

Department of Chemical Engineering, University of Queensland,
St. Lucia, Queensland, Australia

The performance of a new type rubber-sheet sparger is
compared with the rigid perforated plate gas distributor
Impulse response tests were analyzed using the weighted-
moments method to determine voidage and dispersion coefficients
in a countercurrent bubble column of 9.5 cm diameter. The
flexible rubber sheet sparger produced more uniform emulsions,
smaller bubbles and larger voidages than perforated plates,
while dispersion coefficients were reduced for a range of
superficial gas velocities. The mixing results are contrasted
with predictions based on Taylor, entrainment and energy dissi-
pation models.

Bubble columns are a cheap, simple gas-liquid contractor
in which gas is bubbled co-currently or counter-currently
through a liquid. Bubble columns have been used in the process
industries for over twenty years for carrying out gas-liquid
reactions. They are likely to find increasing use in the
future as tower fermenters in the production of liquid fuels
from biological materials. Furthermore, it has been shown that
bubble columns are prime candidates for fine-particle flotation.
Flotation columns can increase the number of effective stages
relative to the same volume in a cell device, and moreover,
gangue carry-over is reduced because tailings and froth are
widely separated. One can foresee a significant increase in
the use of bubble-column contactors in the future, but the
fundamentals of the technology are only thinly developed.
    In the present research, we study two fundamental proper-
ties of bubble columns: liquid hold-up and mixing. Both of
these properties depend on the flow rates of the gas and liquid
phases. These two properties may be considered response vari-
ables in the sense that their values depend on the way bubbles
are formed. We present results for two types of bubble gener-
ating devices (or, for short, spargers) i.e. perforated rigid
plates and perforated rubber sheets. An advantage of the
rubber-sheet sparger is the self-cleaning feature. This is

because during operation the rubber sheet oscillates and
deforms, thus preventing mud build-up on the spargers in
practical applications such as mineral flotation. Moreover,
the rubber sparger is self regulating in the sense the holes
expand to accomodate high flow rates.

Axial mixing refers to the mechanism by which a phase can
move or disperse against the direction of its main flow. In
counter-current bubble columns, which are the most common
physical configuration, liquid phase axial mixing is induced
mainly by the rising gas bubbles dragging the liquid against
its net downward flow. The bulk circulation pattern thus set
up leads to a "spreading out" of solute or reactant and thus
enhances mixing in the longitudinal direction. To a lesser
extent, the trajectory, coalescence rate and deformations of a
bubble also affect the mixing process. The overall effect of
increasing the axial mixing in a contacting process is to
reduce the number of theoretical stages available in the column
as compared with simple plug flow.

One can visualize in the design of bubble columns that
there must exist an optimization problem at hand. Thus, ef-
forts to reduce bubble size should increase interfacial mass
transfer rates. This of course means shorter columns. At the
same time, smaller bubbles may tend to increase axial mixing,
and this effect serves to increase column design length. In
addition, column diameter seems to have an even more important
effect on the magnitude of axial mixing as shown by Baird and
Rice (1). It is well known that the general liquid flow pat-
tern is that of upflow at the center and downflow near the
walls. This circulation pattern induces the large axial mixing
effect, and in fact it has been shown (2) that center-counted
baffles can significantly reduce dispersion coefficient.

Flow Regimes

In characterizing upward movement of bubble swarms, Wallis
(3) suggests there exists three separate flow regimes. These
regimes occur in order of increasing gas rates as follows:

    (i)   Bubbly Flow is characterized by a constant
              bubble size, bubble velocity and gas hold-up
              throughout the column.

    (ii)   Churn-Turbulent Flow exhibits an unsteady flow
              pattern with channeling due to bubbles following
              in each other's wakes. The bubble sizes and
              velocities vary throughout the column. One
              might tend to model the system dynamics as an
              equilibrium between rate of bubble coalescence
              and rate of breakage.

    (iii)   Slug Flow is characterized by a series of indi-
              vidual large bubbles which almost fill the
              column cross-section.

Of the above regimes, Bach and Pilhofer ($\underline{4}$) suggest the churn-turbulent "heterogeneous" regime is the one commonly encountered in industrial scale bubble columns. Transition effects have been reported by Anderson and Quinn ($\underline{5}$) in the presence of minute amounts of trace contaminants in tap water. It is now well known that small amounts of surface active agents have a very strong effect on the flow regime and the bubble size distrubution. For example, Lockett and Kirkpatrick ($\underline{6}$), under special conditions, have demonstrated ideal bubbly flow at gas hold-ups up to 66%.

Gas-liquid systems are classified as coalescing or non-coalescing, depending on the behavor exhibited by the bubbles. Water is classed as coalescing by Konig ($\underline{7}$). Examples of systems exhibiting lower coalescence rates are 0.5% propanol solutions, dilute solutions of surfactants and many of the media used in fermentation reactions.

The degree of coalscence plays an important part in determining the bubble size distribution. Otake et al. ($\underline{8}$) showed that the interaction between the wake of a leading bubble and a trailing bubble could lead to either coalescence of the two bubbles, or alternately to the breakup of the trailing bubble. The net balance between rates of coalescence and rates of breakage must determine the ultimate bubble size distribution, and this in turn determines the properties such as liquid hold-up, interfacial area, swarm velocity and finally, axial mixing. On a small scale, bubble columns are inherently non-linear and unsteady in behavior. This suggests a non-linear analysis to uncover the multiple steady-states would be a productive avenue to follow.

Characterization of Liquid Holdup or Voidage

In this section, we give a brief overview and the important developments relating to the characterization of liquid hold-up (or gas voidage) in bubble columns.

Wallis ($\underline{3}$) introduced the concept of "drift-flux" analysis as a means to relate phase flow rates, voidage and certain physical properties. The slip velocity for counter-current flow is defined as:

$$(1) \quad v_s = \frac{u_{og}}{\varepsilon} + \frac{u_{ol}}{1-\varepsilon}$$

where ε is the gas voidage. Wallis defines the drift-flux as simply the product of slip velocity times the respective hold-ups, so that

$$(2) \quad j_D = v_s(1-\varepsilon)\varepsilon = u_{og}(1-\varepsilon) + u_{ol}\varepsilon$$

To complete the drift-flux model, the phenomenological theory of Lapidus and Elgin (9) is used, wherein it was suggested for dispersed flow systems that the slip velocity depends directly on terminal bubble rise velocity, U_∞, so that

(3) $v_s = U_\infty \phi(\varepsilon)$.

Combining this with equation (2), the drift-flux becomes

(4) $j_D = U_\infty \varepsilon(1-\varepsilon) \phi (\varepsilon)$

and we see that

(5) $U_\infty \varepsilon(1-\varepsilon) \phi (\varepsilon) = u_{og}(1-\varepsilon) + u_{ol}(\varepsilon)$.

The usefulness of the drift-flux structure resides in the simplicity afforded in obtaining a graphical solution. Thus, one sees that the RHS of equation (5) is linear in ε, while the LHS is (usually) non-linear. Given the structure of $\phi (\varepsilon)$, along with the phase flow rates, one determines ε by finding the intersection of the linear RHS with the non-linear LHS. An example of this construction is shown in Figure 3.

   Forms for $\phi(\varepsilon)$ proposed in the literature are summarized by Lockett and Kirkpatrick (6). These relationships vary significantly, but with voidages less than 0.2 they are quite close to one another. Lockett and Kirkpatrick (6) give the following list of slip functions:

Turner $\phi(\varepsilon) = 1$

Davidson and Harrison $\phi(\varepsilon) = 1/(1-\varepsilon)$

Wallis $\phi(\varepsilon) = (1-\varepsilon)^{n-1}$

                                where: n = 2 for small bubbles
                                       n = 0 for larger bubbles

Richardson and Zaki $\phi(\varepsilon) = (1-\varepsilon)^{1.39}$

Marrucci $\phi(\varepsilon) = (1-\varepsilon)/(1-\varepsilon^{5/3})$

In the presence of a surfactant (Terpineol), Rice et al. (2) obtained a very good fit between theory and experiment using $\phi(\varepsilon) = (1-\varepsilon)$ which is the Wallis model with n = 2. In the work cited, average bubble size was around 1 mm diameter. This particular structure shows, according to equation (3), that the slip velocity approaches terminal rise velocity as voidage becomes small, as one expects.

   A different approach, first proposed by Towell et al. (10) and later confirmed by Reith et al. (11), suggests that slip velocity is apparently independent of voidage:

(6) $v_s = U_\infty + 2\ u_{og}$.

This equation has been tested at superficial gas velocities up to 45 cm/sec and superficial liquid velocities up to 2 cm/sec. If one compares equation (6) with equation (3), we see that

(7) $\phi = 1 + 2\ (\dfrac{u_{og}}{U_\infty})$.

Bubbles moving along straight trajectories in an otherwise quiescent liquid obey the mass balance:

(8) $\dfrac{u_{og}}{U_\infty} \cong \varepsilon$

which shows that, approximately, Towell's (10) slip velocity expression requires:

(9) $\phi \cong 1 + 2\ \varepsilon$

which is quite different from the structure of the researchers listed above. However, all the proposed functions $\phi(\varepsilon)$ have the property:

(10) $\lim\limits_{\varepsilon \to 0} \phi(\varepsilon) \to 1.0$

which imples that slip velocity approaches the terminal rise velocity of a single bubble at low voidages.

Axial Mixing

When a steady stream of liquid enters a bubble column, the effect of axial mixing is to cause elements of the liquid, which enter the column together, to leave at times which differ from the mean residence time.

Two main types of models are in common use for describing axial mixing in bubble columns. The most commonly used model is the Dispersion Model. Here, a diffusion-like process is superimposed on piston or plug flow. The stirred tanks-in-series model has also been used to describe flow of liquids in bubble columns. Levenspiel (12) presents a number of models incorporating various combinations of mixed tanks to model stagnant regions and backflow.

In the present research, we use a dispersion-type model. Techniques for estimating dispersion coefficients are classed as non-steady or steady state. Steady-state methods usually incorporate the continuous addition of a fixed tracer concentration into the liquid stream followed by the measurement of the steady-state concentration profile along the column length.

This method has been used by Ohki and Inoue (13), Smith et al. (14) and Reith et al. (11)

Unsteady-state methods are experimentally easier to do, whereby a shot of tracer is added followed by the measurement downstream of the time variation of tracer concentration. This technique was used in bubble columns by Seher and Schumacher (15) and Rice et al. (2). Some researchers carried out studies using both methods as a double-check on parameters, cf. Konig et al. (7), Deckwer et al. (16) and Rice et al. (2)

Taking the liquid velocity profile to be uniform, the dispersion equation is represented by

$$(11) \quad \frac{\partial C}{\partial t} + v \frac{\partial C}{\partial z} = E \frac{\partial^2 C}{\partial z^2}$$

where C is the liquid composition, v is the liquid interstitial velocity, and E is the liquid interstitial dispersion coefficient. Special note should be taken of the fact that E is based on available liquid area, not on total column cross-sectional area. Wen and Fan (17) suggest the application of a dispersion-type model to bubble columns is not always satisfactory. However, it has been our experience (2) that the dispersion model can give a very satisfactory fit of response data, especially when bubble size is maintained small by the addition of surfactant. The fit is not as good when coalescence occurs, such as operation in the churn-turbulent regime. A poor fit to the dispersion equation also results for very low gas rates such that chain bubbling occurs, and the bubble swarm is not uniformly distributed across the column cross-section. Under such conditions, dead-water or unmixed pockets may occur. The pockets exchange mass with the bulk flow mainly by the slow process of molecular diffusion. Dead-water pockets are always present, even under uniform bubbly flow conditions. For example, the liquid entrapped in the region following the wake of bubbles causes the appearance of spreading of tracer in impluse response tests. One sees there are good reasons for treating the liquid phase as comprised of two parts: bulk flowing liquid and dead-water.

Suppose we denote the liquid in dead-water regions as having compositon C_D, and liquid within the main bulk flow to have composition C_B. The liquid hold-up in the two regions would in general be different, but the sum of the two would be taken to be equal to the hydrostatically measured holdup. Thus, a two-region dispersion model can be represented by, firstly an overall mass balance:

$$(12) \quad \varepsilon_D \frac{\partial C_D}{\partial t} + \varepsilon_B \frac{\partial C_B}{\partial t} + \varepsilon_B v \frac{\partial C_B}{\partial z} = \varepsilon_B E \frac{\partial^2 C_B}{\partial z^2}$$

and secondly a mass balance on the dead-water phase, assuming the deadpockets are fixed in space:

(13) $\varepsilon_D \dfrac{\partial C_D}{\partial t} = q_E (C_B - C_D)$

The liquid holdups, ε_D and ε_B, are for deadwater and bulk liquid, respectively. Here, one would surmise that the exchange coefficient, q_E, is proportional to molecular diffusion. This model may have advantages in characterizing bubble column behavior, and may explain the long-tail response which often occurs in experimental response curves. However, the parameter estimation problem is unwieldy, reqiring the determination of four parameters (ε_D, ε_B, E, q_E) instead of the simple plug flow dispersion model which has only two parameters (ε, E).

In the present work, we use the weighted-moments method to estimate parameters by fitting the theoretical Laplace domain moments to the experimentally generated moments for the impulse response. Thus, for the model without deadwater (equation 11), the Laplace transform for the response variable at the exit is (2):

(14) $\overline{C}(s,L) = Q \exp \left[\tfrac{1}{2} \text{Pe} \left(1 - \sqrt{1 + \dfrac{4s\tau}{\text{Pe}}} \right) \right]$

where

$\quad$ Q $\quad = \quad$ strength of the impulse stimulus
$\quad$ Pe $\quad = \quad$ Peclet number, vL/E
$\quad$ τ $\quad = \quad$ liquid phase residence time, L/v

The deadwater model comprised of equation (12) and (13) is similar in many respects to the equations describing adsorption in packed columns. When equations (14) and (13) are expressed with dimensionless independent variables, we have

(15) $R \dfrac{\partial C_D}{\partial \theta} + \dfrac{\partial C_B}{\partial \theta} + \dfrac{\partial C_B}{\partial \zeta} = \dfrac{1}{\text{Pe}} \dfrac{\partial^2 C_B}{\partial \zeta^2}$

(16) $\dfrac{\partial C_D}{\partial \theta} = \beta (C_B - C_D)$

where

$\quad$ R $\quad = \quad$ $\varepsilon_D/\varepsilon_B$
$\quad$ θ $\quad = \quad$ t v/L, dimensionless time
$\quad$ ζ $\quad = \quad$ z/L, dimensionless distance
$\quad$ Pe $\quad = \quad$ vL/E, Peclet number
$\quad$ β $\quad = \quad$ q_E L/vε_D, dimensionless exchange coefficient

The Laplace solution for exit composition following an impulse at the inlet, written in terms of a "dimensional s" (as in equation 14), can easily be seen to be:

$$(17) \quad \bar{C}_B(s) = Q \exp \left[\tfrac{1}{2}Pe \left(1 - \sqrt{1 + \frac{4}{Pe} \left(\frac{R\beta}{s\tau+\beta} + s\tau \right)} \right) \right]$$

which of course reproduces the simple dispersion model when R or $\beta \to 0$. The unknown parameters usually would be taken to be τ, Pe, R, and β. In addition, an optimum weighting factor "s" must be found (2). One can use independently determined static hold-up measurements to check consistency,

$$(18) \quad \varepsilon_{static} = \varepsilon_D + \varepsilon_B$$

and to apportion the relative hold-ups. However, this does not reduce the complexity of the moments analysis, since four unknown parameters still exist. This analysis requires at least four experimental moments.

Another model worth considering is to assume all the deadwater resides in the stagnant pockets in bubble wakes. Here, a moving coordinate system would be used, taking the bubble swarm velocity to be U_∞. For this model, equation (13) is replaced by the distributed parameter equation:

$$(19) \quad \varepsilon_D \frac{\partial C_D}{\partial t} + \varepsilon_D U_\infty \frac{\partial C_D}{\partial z} = q_E (C_B - C_D)$$

The parameter estimation problem remains essentially the same as before, since U_∞ could be determined separately from hold-up measurements.

Correlations and Theories for Axial Mixing in Bubble Columns

Workers in the field have reached several generalizations regarding the behavior of axial dispersion coefficients. Firstly, there are indications that E depends strongly on superficial gas velocity. Secondly, an even stronger dependence of E on column diameter has been observed. The scale-up problem is thus quite sensitive to column diameter.

There is much discrepancy in the reported literature regarding the dependence of E on the two key variables, d, (column diameter) and u_{og} (superficial gas velocity). Thus, Reith et al. (11) observed, following a large number of experiments, an approximately constant value for a Peclet number:

$$(20) \quad \frac{v_s d}{E} \sim 3$$

A short time later, Ohki and Inoue (13) produced the following dimensional correlation based on a large number of experiments

$$(21) \quad E = 0.3 \, d^2 \, u_{og}^{1.2} + 170 \, \delta$$

where

δ = sparger hole diameter (cm)

d = column diameter (cm)

u_{og} = superficial gas velocity (cm/sec)

E = dispersion coefficient (cm^2/sec)

Since sparger hole diameter in some sense relates to bubble diameter, this correlation suggests mixing increases with increased bubble diameter. These workers also suggest that dispersion coefficient for the coalescent bubble-slug flow conditions follows:

$$(22) \quad E = 14d/(1-\varepsilon)^2$$

More recently, Deckwer et al. ([16]) have tested a correlation originally proposed by Towell et al. to give the dimensional correlation

$$(23) \quad E = 2.7d^{1.4}u_{og}^{0.3} \quad \text{(units are cm, sec)}$$

This relationship shows quite different exponents compared to that of Ohki and Inoue, especially the exponent on u_{og}.

Using the isotropic turbulence theory of Kolmogoroff, Baird and Rice ([1]) deduced the following expression with a single arbitrary constant to describe mixing in large diameter bubble columns

$$(24) \quad E = K \, d^{4/3}(u_{og}g)^{1/3}$$

Analysis of a broad range of published data produced a value of K, which is dimensionless, equal to 0.35. Later, Smith et al. ([14]) found their experiments exceeded by a factor of two the predictions of the isotropic turbulence model.

The exponents in the isotropic turbulence model (equation 24) are very close to those found in the comprehensive work by Deckwer et al. (equation 23). The isotropic turbulence model is also attractive owing to dimensional consistency, since any set of consistent units can be used to correlate dispersion data. While the diameter dependence of the varous researchers is not too wide afield (ranging from d to d^2), the dependence on gas velocity varies widely (ranging from $u_{og}^{.3}$ to $u_{og}^{1.2}$). While a comprehensive theory is not yet available, these authors suspect mixing follows the flow regime according to

(i) chain bubbling $\quad E \propto u_{og}^2$

(ii) bubbly flow $\quad E \propto u_{og}^{1/2}$ to u_{og}^1

(iii)   churn-turbulence $E \propto u_{og}^{1/3}$ to $u_{og}^{1/2}$

(iv)   slug flow $E \propto u_{og}^{o}$

This leads one to conclude that maxima in E with respect to u_{og} should exist, and this phenomenon has been reported in the recent literature (Smith et al. (14)). In experiments conducted at the University of Queensland, we observed a sharp maxima to exist when surfactant (terpineol) was present; presently we show an apparent maxima also exists for "clean" systems.

The behavior of E depends of course on the method of determining this parameter. None of the methods used to date have included the possibility of deadwater. The growth and decay of deadwater pockets clearly must affect the value deduced for E. Thus one has the expectation that deadwater is large at small gas rates, smaller at intermediate gas rates, but then becomes larger again at high (slugging) gas rates. The presence of deadwater manifests itself as a spreading of the Impulse Response Curve, hence this dispersive force gives an appearance of being caused by axial mixing. If deadwater is significant, one suspects there should be a difference between values of E obtained by unsteady-state and steady-state methods. Deckwer et al. (16) used both methods and there seemed to be no significant difference in mixing coefficients. However, the experiments may have been conducted in the flow region of small deadwater. It is not possible to quantify this any further at this time. It should be possible to measure deadwater effects in the various flow regimes and thereby deduce if a dispersion coefficient maxima is real or simply a consequence of the force-fitting of an incorrect model. Recently, Tuppurainen (18) found that a tanks-in-series model including backmix could be fitted to response curves with a smaller IAE than the dispersion model. However, three parameters (rather than two in the dispersion model) were required to be fitted. It would seem the loss of physical reality in using a tanks-in-series model is too high a price to pay.

Some Preliminary Experiments

Dispersion coefficients were determined using salt tracer response curves along with the weighted moments method of analysis applied to equation (14) (details in Appendix I). The circular column was 9.5 cm in diameter and 182.2 cm long.

Liquid hold-up was measured by simultaneously closing the liquid inlet and outlet valves and measuring the height of the collapsed column. As a check, manometer measurements along the column length were taken to deduce hold-up. Superficial liquid velocity was held relatively constant (.36 cm/sec ± 10%) for all experiments.

Three different spargers were used in the experiments. Details are given in Table I. The experimental arrangement and sparger details are shown in Figures 1 and 2, respectively.

Table I

Details of Spargers

Material & Designation	Thickness (mm)	Hole			
		Number	Diameter(mm)	Arrangement	Holes /cm²
Polyethylene (PE)	12.5	68	2	6mm,sq.pitch	2.8
Rubber (R1)	1.4	300	2*	random	7.5
Rubber (R2)	1.4	120	2.8*	random	3.0

*This hole diameter refers to the size of nail used to pierce the vulcanized rubber sheet.

The drift flux curves for the three spargers are shown in Figure 3 for the 9.5 cm diameter column. The solid curves represents j_D versus ε, with U_∞ as a fitted parameter. Note the function $\phi(\varepsilon)$ used here was orginally suggested by Wallis (taking n = 2). The experimental points are generated, according to equation (5), as follows. Taking the left hand ordinate scale as $j_D = u_{og}$ (where $\varepsilon = 0$) and the right hand ordinate scale as $j_D = u_{o1}$ (where $\varepsilon = 1$), one simply draws a straight line between experimental values of u_{og} and u_{o1}, marking along this line the measured voidage (abcissa). The drift flux, $j_D(\varepsilon)$, is fitted to the first four points, which also gives a fitted value for U_∞.

When the data abruptly departs from the drift flux curve, a change in the flow regime is assumed to occur; flooding, according to Wallis (3). It was visually observed that increased coalescence and slugging occurred when the experimental data diverged from the drift flux curve.

We take note of the fact that the flexible rubber spargers produced uniform bubbly-flow up to a gas voidage of around 0.2. The perforated plate sparger (PE), however, sustained bubbly flow only up to a voidage 0.1. The points of departure from the drift flux curve highlights this transition. The gas velocity at the transition points were 2.8 cm/sec and 3.7 cm/sec for the perforated plate and flexible rubber spargers, respectively. The rubber spargers therefore sustain significantly higher gas rates and voidages before flooding occurs. Bubble size from the rubber sparger appeared to be about half that resulting from the perforated plate.
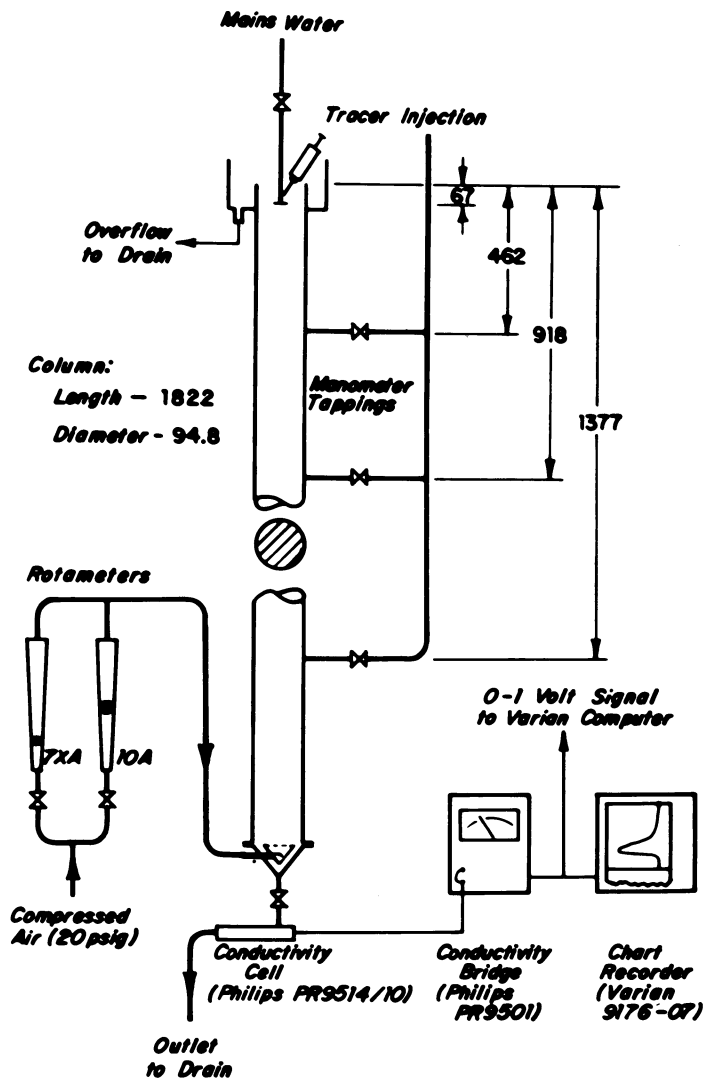
Figure 1. Schematic of typical equipment arrangement; all lengths given in milli-meters

Figure 2. Sparger design

Curves Drawn of the Form
$$j_D = u_\infty \epsilon (1-\epsilon)^2$$
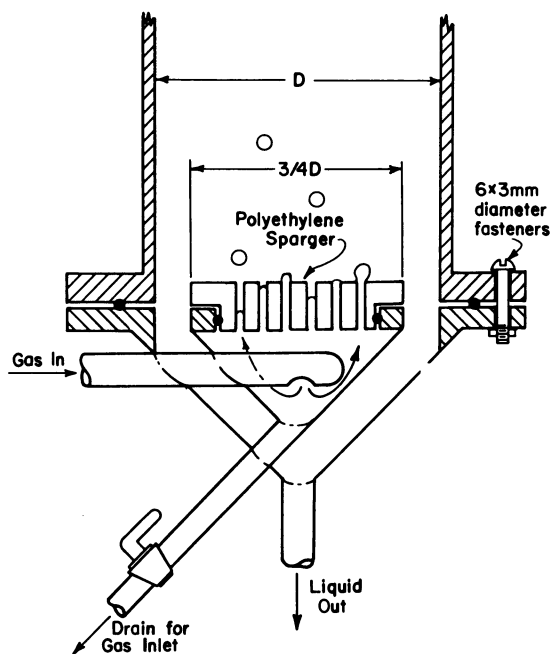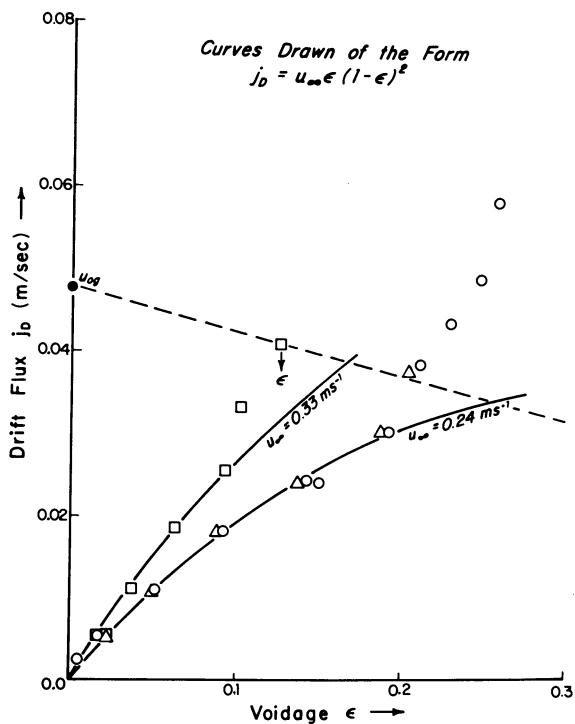
Figure 3. Drift–flux curves for 9.5-cm diameter column: (□) PE spargers, (○) R1 sparger, (△) R2 sparger; (– – –) placement of experimental point (u_{og} = LH ordinate; u_{ol} = RH ordinate; ϵ = abscissa)

Figure 4 shows how the hold-up data (d = 9.5 cm) compares with the limits of literature values (4).   In Figure 5, we treat the data from the two types of spargers according to the slip velocity model of Towell et al (10).   The slip velocity for the rubber spargers behaves rather curiously, sustaining a minimum when superficial gas velocity if ~ 3 cm/sec.

A detailed comparison of axial mixing coefficents in the 9.5 cm column for the two types of spargers is given in Figure 6.   One would expect the smaller bubbles from the rubber sparger to produce increased axial mixing.   This did no appear to happen; mixing coefficients from the perforated plate sparger were always larger than the flexible rubber sparger. None of the dispersion data seemed to follow the trends suggested by literature correlation.   The data suggests that a maxima in E may occur around u_{og} ~ 1 cm/sec.

Discussion of Results

The dispersion coefficients are surprisingly lower than reported elsewhere (see Figure 6), especially those obtained using the flexible rubber sheet sparger.   Apparently the energy dissipated in mixing is significantly less than the input energy.   Thus, the Baird-Rice (1) model suggests

$$(25) \quad E = K \, \ell^{4/3} \, (P_m)^{1/3}$$

where

ℓ = turbulent mixing length (taken as column diameter by Baird and Rice)

P_m = specific energy dissipation rate per unit mass of liquid

The specific energy dissipation rate for mixing was equated to the input energy rate so that Baird and Rice (1) used

$$(26) \quad P_m = \frac{(u_{og} \, A)(\rho_L g \, L(1-\varepsilon))}{\rho_L \, (A \, L)(1-\varepsilon)} = u_{og} \, g$$

which is simply the power input per unit mass liquid.   Field and Davidson (19) argue that the actual rate of energy dissipation which is available for mixing under true bubbly flow conditions (no radial variation in voidage) is given by

$$(27) \quad P_m = [\, g \, (\, u_{og} - \varepsilon \, v_s \pm \frac{\varepsilon}{1-\varepsilon} \, u_{ol})]$$

where the ± is positive for counter-current, negative for co-current flow.   This contrasts with the result of Joshi and
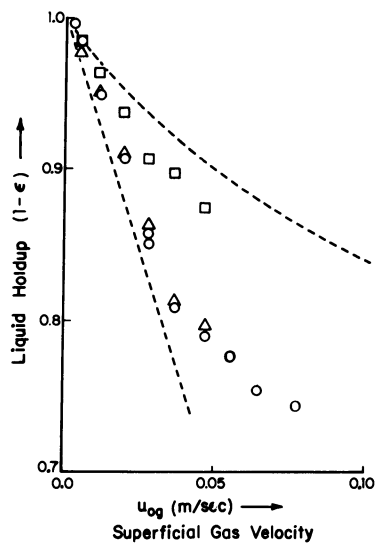
Figure 4. Comparison of liquid hold-up with literature (9.5-cm diameter column): (□) PE sparger, (○) R1 sparger, (△) R2 sparger; (---) reported limits (4)
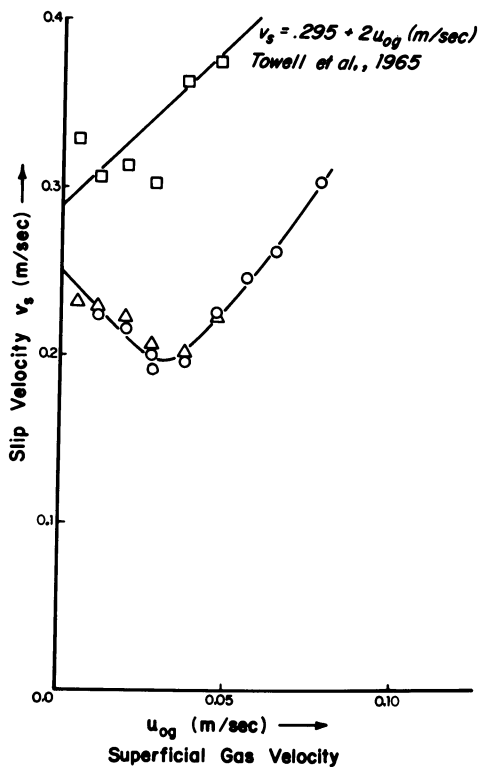
Figure 5. Comparative slip velocities for 9.5-cm diameter column: (□) PE sparger, (○) R1 sparger, (△) R2 sparger
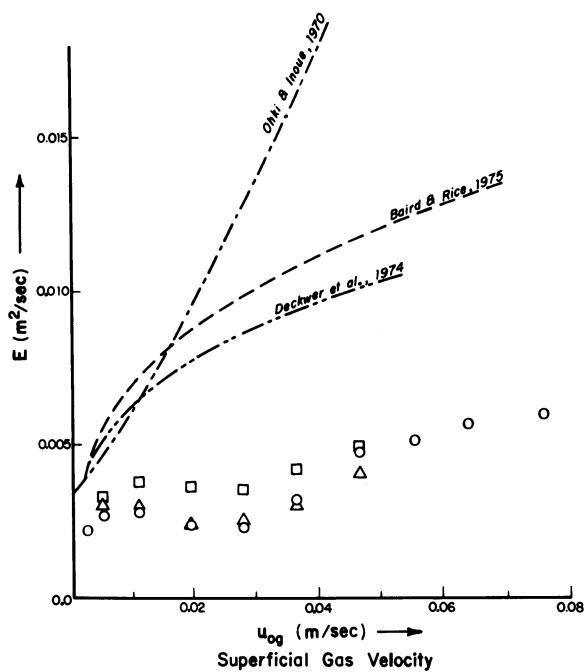
Figure 6. Comparative dispersion coefficients for 9.5-cm diameter column: (□) PE sparger, (○) R1 sparger, (△) R2 sparger

Sharma (20) who deduct the energy dissipated in bubble wakes to obtain

$$(28) \quad P_m = [g \, (u_{og} - \varepsilon \, v_s)]$$

Using the definition of slip velocity given by equation (1), it is seen that the Field-Davidson model requires P_m to be identically zero, while the Joshi-Sharma modification suggests the unrealistic result that P_m is negative if the slip velocity definition is obeyed.

Presumably, when very uniform bubbly flow is maintained, the Field-Davidson (19) modification suggests that mixing owing to energy dissipation is expected to be quite small, and this was indeed the observation in the present work. Bubble emulsions were quite uniform, especially when using the rubber sheet sparger. Thus, for very uniform emulsions, mixing occurs mainly by entrainment in wakes (deadwater transfer) and by Taylor dispersion arising from the liquid velocity profile. If the Taylor mechanism is controlling, then one expects

$$(28) \quad E \sim d \, v \, 3.57 \, \sqrt{f}$$

where Taylor has taken the radial eddy diffusion equal to the eddy viscosity and f is the Fanning friction factor. For the present case, the average interstitial velocity varies but little and can be taken as $v \sim .4$ cm/sec, $d \sim 9.5$ cm and $f \sim .04$, from which the effective dispersion coefficient is estimated to be $E \sim 2.8$ cm^2/sec. This is much lower than the observed values of order 25 cm^2/sec. Joshi (21) has suggested a method to calculate the liquid circulation arising from wake entrainment to give:

$$(29) \quad V_c = \frac{\varepsilon}{1-\varepsilon} \, \alpha \, U_\infty$$

where α is the ratio of wake to bubble volume and takes a value around 11/16. For the present work U_∞ varies between 24 and 33 cm/sec (see Figure 6) so that $v_c \sim 2.1$. Taking eddy dispersion to be the product of mixing length and turbulence velocity, and assuming the turbulence velocity is approximated by the circulation arising from wake entrainment (v_c), one obtains

$$(30) \quad E \sim V_c \cdot \ell$$

If we take $\ell \sim d$ and $v_c \sim 2.1$ cm/sec as before, then equation (30) gives $E \sim 20$ cm^2/sec, which is very close to the experimental observations for small superficial gas velocities. We note in passing that the entrainment model suggests $E \propto u_{og}$ since $U_\infty \sim u_{og}/\varepsilon$.

Conclusions

Dispersions coefficients were found to lie somewhere in between predictions based, on the low side, the entrainment model, and on the high side the isotropic turbulence model (energy dissipation). From the previous discussion, one is tempted to propose a two-regime model comprised of entrainment and energy dissipation mechanisms:

Entrainment: $E = d \left(\dfrac{\varepsilon}{1-\varepsilon} \alpha U_\infty \right)$

Energy dissipation: $E = K \, d^{4/3} \, P_m^{1/3}$

The transition between the two mdoels is not yet clear, however it would seem departure from the drift-flux curve may indicate this transition. It remains to be determined the precise form that P_m should take, but for engineering estimates, P_m can be taken $\sim u_{og} g$. Combining the two models gives:

$$(31) \quad E = K_1 \, (u_{og} d) + K_2 \, (u_{og} \cdot g)^{1/3} \, d^{4/3}$$

where K_1, K_2 are dimensionless constants.

Finally, we conclude that the type of bubble generating device has a very significant effect on the flow regime, especially for a low superficial gas velocity less than 5 cm/sec. Apparently, to minimize mixing without using intervals such as baffles, one must use a sparger which produces uniform emulsions at the source. In this respect, the rubber sheet sparger is quite suitable, and moreover, this device is somewhat self-regulating since sparger holes expand as flow increases. Apparently, this work constitutes the first effort to study a thin, flexible perforated rubber sheet as a gas sparger.

Nomenclature

A	=	column cross-sectional area
C	=	tracer composition
d	=	column diameter
E	=	eddy dispersion coefficient
f	=	Fanning friction factor
j_D	=	drift-flux (eqn 2)
$K_k(s)$	=	kth weighted cumulant
L	=	column length
ℓ	=	liquid mixing length
$M_k(s)$	=	kth weighted moment
N	=	number of bubbles
Pe	=	liquid Peclet number (vL/E)
P_m	=	rate of energy dissipation per unit mass of liquid
s	=	Laplace operator, or weighting variable.

t   =   time
U_∞ =   terminal rise velocity
u_{og} =   superficial gas velocity
u_{ol} =   superficial liquid velocity
v_l =   interstitial liquid velocity
v_c =   interstitial liquid circulation velocity
v_s =   slip or relative velocity
z   =   axial position from injection point

<u>Greek</u>

α =   ratio wake to bubble volume
ε =   gas voidage
ζ =   dimensionless axial coordinate (z/L)
τ =   liquid residence time (L/v)
$\phi(\varepsilon)$ =   slip function (eqn 3)
ρ_L =   liquid density

Literature Cited

(1) Baird, M.H.I. and R.G. Rice, <u>Chem. Eng. Journ</u>. 1975, <u>9</u>,
     171-174.
(2) Rice, R.G., Oliver, A.D., Newman, J.P. and R.J. Wiles,
     <u>Powder Tech</u>. 1974, <u>10</u>, 201-210.
(3) Wallis, G.B. "One Dimensional Two-Phase Flow" McGraw-Hill,
     New York (1969), Chap. 9.
(4) Bach, H.F. and T. Pilhofer, <u>Ger. Chem. Eng</u>. <u>1978</u>, <u>1</u>,
     270-275.
(5) Anderson, J.L. and J.A. Quinn, <u>Chem. Eng. Sci</u>. 1970, <u>25</u>,
     373-380.
(6) Lockett, M.J. and R.D. Kirkpatrick, <u>Trans. Inst. Chem.
     Eng</u>. 1975, <u>53</u>, 267-273.
(7) König, B., Bucholz, R., Lücke, J. and K. Schügerl, <u>Ger.
     Chem. Eng</u>. 1978, <u>1</u>, 199-205.
(8) Otake, T., Tone, S., Nakao, K. and Y. Mutsuhashi, <u>Chem.
     Eng. Sci</u>. 1977, <u>32</u>, 377-383.
(9) Lapidus, L. and J.C. Elgin, <u>AIChE Journ</u>. 1957, <u>3</u>, 63-68.
(10) Towell, G.D., Strand, C.P. and G.H. Ackerman, AIChE -
     Inst. Chem. Engrs. Joint Mtg. Series No. 20, p. 97-105,
     1968.
(11) Reith, T., Renken, S. and B.A. Israel, <u>Chem. Eng. Sci</u>.
     1968, <u>23</u>, 619-629.
(12) Levenspiel, O., "Chemical Reaction Engineering" 2nd ed.,
     Wiley and Sons, New York, 1972.
(13) Ohki, Y. and H. Inoue, <u>Chem. Eng. Sci</u>. 1970, <u>25</u>, 1-16.
(14) Smith, E.L., Fidgett, M. and J.S. Salek, BHRA Fluid
     Engineering, 2nd European Conf. on Mixing, Mar. 30-Apr. 1,
     paper G2, 1977.
(15) Seher, A. and V. Schumacher, <u>Ger. Chem. Eng</u>. 1979, <u>2</u>,
     117-122.

(16) Deckwer, W.D., Burckhart, R. and G. Zoll, <u>Chem. Eng. Sci.</u> 1974, <u>29</u>, 2177-2188.

(17) Wen, C.Y. and L.T. Fan, "Models for Flow Systems and Chemical Reactors," Marcel Dekker, Inc., N.Y., 1975.

(18) Tuppurainen, J.M.I., "Liquid Holdup and Axial Dispersion in an Unbaffled bubble Column," B. Eng. Thesis, University of Queensland (Australia), 1979.

(19) Field, R.W. and J.F. Davidson, <u>Trans. I. Chem. E.</u> 1980, <u>58</u>, 228.

(20) Joshi, J.B. and M.M. Sharma, <u>Trans. I. Chem. E.</u> 1979, <u>57</u>, 244.

(21) Joshi, J.B., <u>Trans. I. Chem. E.</u>, (in press, 1981).

APPENDIX I

Building on the Laplace solution given by equation (14), the moments method proceeds as follows; the kth weighted moment is defined:

$$(A1) \quad M_k(s) = \int_0^\infty e^{-st} t^k C(t,L) dt$$

We note that the zeroth weighted moment is exactly the Laplace solution (equation (17)):

$$(A2) \quad M_0(s) = \int_0^\infty e^{-st} C(t,L) dt = \overline{C}(s,L)$$

By successive differentiation, it is easy to prove the recurrence relation

$$(A3) \quad \frac{dM_k(s)}{ds} = -M_{k+1}(s).$$

Applying (A3) to (A2), using equation (17), gives

$$(A4) \quad \frac{M_1(s)}{M_0(s)} = \frac{\tau}{\sqrt{1+4s\tau/Pe}}$$

This does not allow the separation of the two parameters v and E. However, this separation can be made by defining <u>weighted cumulants</u> as follows; define the zeroth cumulant as $\overline{K}_0(s) = \ln M_0(s)$ and noting as before the recurrence relation, there results:

$$(A5) \quad Pe = \frac{2}{\tau} K_1^3/K_2$$

$$(A6) \quad \tau = K_1/\sqrt{1-2s\,K_2/K_1}$$

where the cumulants are determined experimentally from impulse
response curves using (A1) and (A2) along with the definitions:

(A7) $K_1 = M_1/M_o$

(A8) $K_2 = (\dfrac{M_2}{M_1} - M_1{}^2/M_o{}^2).$

RECEIVED June 3, 1981.

Packed Bed Reactors

An Overview

ARVIND VARMA

Department of Chemical Engineering, University of Notre Dame, Notre Dame, IN 46556

Packed-bed reactors are discussed qualitatively,
particularly with respect to their models. Features
of the two basic types of models, the pseudohomogene-
ous and the heterogeneous models, are outlined. Addi-
tional issues -- such as catalyst deactivation; steady
state multiplicity, stability, and complex transients;
and parametric sensitivity -- which assume importance
in specific reaction systems are also briefly discussed.

Packed-bed reactors are commonly used in industrial practice
for conducting solid-catalyzed reactions. Most often, they phys-
ically consist of tube-bundles, which are packed with pellets on
which the active catalyst is deposited. The reactants enter at
one end of the tubes, and the reaction products are withdrawn
from the other end. The reaction(s) proceed over the length of
the tube, and so the species concentrations, as well as the fluid
and solid temperatures, vary as a function of position within the
tube. The tube bundles are stacked in a shell, and because most
industrial reactions are exothermic, cooling medium flows in the
shell to maintain a desired temperature distribution over the
tube length.
At a fixed concentration of reacting species and temperature,
the rate of solid-catalyzed reactions is directly proportional to
the active catalyst surface area. The pellets are normally a
means to support the catalytically active metal or metal oxide,
and maintain it in dispersed form -- thus with a high surface
area. Catalyst preparation is frequently described as an art,
with doses of serendipity; there is, of course, more to it than
that - as Satterfield ($\underline{1}$) has recently described.
Some prominent industrial examples of packed-bed reactors
are in ammonia, methanol or vinyl acetate synthesis, and in ethy-
lene, methanol, naphthalene, xylene or SO_2 oxidation. In recent
years (since the 1975 model year), an important application of
packed-bed reactors has been as catalytic converters for pollu-
tion control from automotive exhausts.

Transport Processes

A variety of gradients in species concentrations and temperature exist within a packed-bed reactor. Since reaction(s) proceed along the tube length, there are obvious gradients in concentration, and fluid and solid temperatures in the axial direction. Because of heat transfer at the tube wall between the reacting mixture and the cooling medium, radial gradients in temperature and species concentrations also exist. At any location within the tube, there are concentration and temperature gradients between the fluid and solid phases. Finally, there are species concentration (but negligible temperature) gradients within each of the individual catalyst pellets, if the active catalyst is distributed throughout the pellet.

A variety of transport processes therefore occur in a packed-bed reactor, simultaneously with chemical reaction(s). Accurate modeling of these processes is essential to predict reactor performance.

Packed-Bed Reactor Models

A relatively large number of models can be written down for a packed-bed reactor, depending on what is accounted for in the model. These models, however, basically fall into two categories: pseudohomogeneous models and heterogeneous models. The various models are described in standard reaction engineering texts -- such as those of Carberry (2), Froment and Bischoff (3), and Smith (4), to cite just a few -- and in review articles (cf., 5-8), and so details of their equations will not be reported here. We will, instead, only make some qualitative remarks about the models.

Pseudohomogeneous Models. The basic assumption that is made in a pseudohomogeneous model is that the reactor can be described as an entity consisting only of a single phase. Since, in reality, two phases are present, the properties used in describing the reactor are so-called "effective" properties which respect the presence of two phases. A comprehensive review of estimating these effective properties has recently been published (9).

The simplest pseudohomogeneous model is the "plug-flow" model, in which the fluid is taken to move as a plug through the reactor tube, and the reaction rate - which depends on local species concentration and temperature - is described as rate of species generation or consumption per unit reactor volume. In the steady state, the model equations are a set of coupled first-order ordinary differential equations - one each for every independent reaction, and one for temperature - with prescribed initial conditions describing the fluid composition and temperature at the reactor inlet. These equations are, in general, nonlinear but can be readily and efficiently integrated numerically with

modern-day digital computers to provide concentration and temper-
ature profiles as a function of axial distance from the reactor
inlet.

The plug-flow model can be augmented by including axial and/
or radial dispersions, for both mass and heat transport. These
dispersions are characterized by so-called Peclet numbers. It
is generally agreed that axial dispersion of mass is not signifi-
cant if the tube length/pellet diameter ratio is $\geq$ 50, while that
for heat is also negligible if the same ratio is $\geq$ 300.

Radial dispersion, on the other hand, is generally more im-
portant than axial dispersion, since the ratio of tube/pellet
diameters is frequently quite modest -- as compared with the tube
length/pellet diameter ratio. The radial Peclet number for mass
transport (ud_p/D_{mr}) is approximately 10, while for heat transport
(ud_p/D_{hr}) it lies between 5-10 ($\underline{2}$). Radial dispersion becomes
negligible if the reactor is adiabatic, because there is then no
driving force for long-range gradients to exist in the radial
direction.

For non-adiabatic reactors, along with radial dispersion,
heat transfer coefficient at the wall between the reaction mixture
and the cooling medium needs to be specified. Correlations for
these are available (cf. $\underline{9}$, $\underline{10}$); however, it is possible to modify
the effective radial thermal conductivity (k_r), by making it a
function of radial position, so that heat transfer at the wall is
accounted for by a smaller k_r value near the tube-wall than at
the tube center ($\underline{11}$).

Inclusion of axial dispersion in the plug-flow model makes
the model equations a boundary-value problem, so that conditions
at both the reactor inlet and outlet need to be specified. The
commonly used boundary conditions are the so-called Danckwerts
type ($\underline{12}$), although their origin goes back to Langmuir ($\underline{13}$).
When radial dispersion is included, even the steady state equa-
tions are partial differential equations -- in the axial and
radial space variables. The dispersion model equations can be
numerically solved by finite-difference schemes, or more effi-
ciently, by orthogonal collocation methods ($\underline{14}$, $\underline{15}$).

The basic plug-flow model, with or without dispersions, is a
"continuous" model because the concentrations and temperature are
described by differential equations. An alternative representa-
tion is by a discrete model - the so-called "cell" model ($\underline{16}$, $\underline{17}$),
in which it is assumed that the reactor can be broken down into
several connected cells. It had long been assumed that the con-
tinuous and discrete models are equivalent ways of representing
a reactor; however, this assumption has recently been questioned
in two different contexts ($\underline{18}$, $\underline{19}$).

Heterogeneous Models. The two-phase character of a packed-bed
is preserved in a heterogeneous model. Thus mass and energy con-
servation equations are written separately for the fluid and solid
phases. These equations are linked together by mass and heat
transport between the phases.

The simplest heterogeneous model is one with plug-flow in the fluid phase, mass and heat transfer between the fluid and solid phases, and surface catalytic reaction on the solid -- if the catalyst is indeed deposited near the pellet external surface. More complex fluid phase behavior can be accommodated by axial and radial dispersion features, among which radial dispersion ones are again the more important -- and those only for a non-adiabatic reactor.

If the catalyst is dispersed throughout the pellet, then internal diffusion of the species within the pores of the pellet, along with simultaneous reaction(s) must be accounted for if the prevailing Thiele modulus $\gtrsim 1$. This aspect gives rise to the "effectiveness factor" problem, to which a significant amount of effort, summarized by Aris (20), has been devoted in the literature. It is important to realize that if the catalyst pellet effectiveness factor is different from unity, then the packed-bed reactor model must be a heterogeneous model; it cannot be a pseudohomogeneous model.

There are theoretically sound correlations available for estimating effective diffusion coefficients in porous catalyst pellets (cf., 21, 22). It has been shown that for most gas-solid catalytic reactions, the pellets are virtually isothermal, so that temperature gradients within them can safely be ignored (23, 24).

There are correlations available for estimating heat and mass transfer coefficients between the phases (2, 3, 4); they are generally cast in form of j-factors, as functions of the fluid Reynolds number. Caution must, however, be exercised in using these since most of the correlations were developed for non-reactive systems -- although successful attempts have been made for relatively simple reactive cases (25). In a specific experimental study in a packed-bed reactor (26), it was recently shown that because of increased convection between the catalyst pellet and the bulk gas, caused by relatively large temperature differences between the two phases when a highly exothermic reaction occurs, the transport coefficients increase considerably -- although their power dependence on Reynolds number, which arises from boundary layer arguments, remains the same as in cases without reaction.

Along with wall heat transfer coefficient in non-adiabatic reactors, another effect frequently added in models is that of thermal conduction in the solid phase (27, 28, 29). One should be particularly careful here, since most of the correlations available in the literature (9, 30, 31, 32) are for effective transport parameters to be used with pseudohomogeneous models, and not for the solid phase alone.

Intrinsic Reaction Kinetics

Either with pseudohomogeneous or with heterogeneous models,

the reaction rate term must always be included in the reactor model. This takes the form of specifying the rate of reaction, as a function of species concentration and catalyst temperature; this information is always obtained experimentally for each reaction system in kinetics experiments. It is crucial that when reaction kinetics are measured, that there be no transport effects present; otherwise the kinetic data would be influenced by such effects. For gas-solid reactions, the most commonly used reactors are the spinning-basket and the recycle reactors (2). Weekman (33), and Doraiswamy and Tajbl (34) have provided recent reviews summarizing advantages and limitations of various reactors used in the laboratory for procurement of intrinsic kinetic data.

Some Other Issues

Under this heading, some issues which assume importance in specific reaction systems, are briefly outlined.

Catalyst Deactivation. Most catalysts suffer from decay in their activity with time, which arises as a consequence, in general, of one among three causes. In "thermal sintering", purely as a result of high temperature, nature of the reactive atmosphere and of the support, smaller crystallites of the active catalyst grow into larger ones with time via various agglomeration processes (35). Thus the active surface area decreases, resulting in a loss of catalytic activity per unit weight of the catalyst. The second cause is "chemical poisoning", normally the result of chemisorption of reactants, reaction products, or impurities in the feedstream, whereby such species permanently occupy sites otherwise available for catalysis. Finally, "fouling" is a term commonly used for physical adsorption of a species upon the catalytic surface, thereby covering or blocking it from future catalytic action -- such as in overcracking of hydrocarbons to produce coke ("coking"), or in lead poisoning of noble metal catalysts in catalytic converters for automotive exhausts. A thorough review of catalyst deactivation is available (36).

With deactivation, the reactor model must immediately become a transient one, to account for change in catalyst activity with time. Among others, two successful instances of packed-bed reactor modeling, in the presence of catalyst deactivation and including comparisons with experiments, are found in the works of Weekman (37, 38) and Butt (39, 40).

Steady State Multiplicity, Stability, and Complex Transients. This subject is too large to do any real justice here. Ever since the pioneering works of Liljenroth (41), van Heerden (42), and Amundson (43) with continuous-flow stirred tank reactors, showing that multiple steady states -- among them, some stable to perturbations, while others unstable -- can arise, this topic has

become one of the major ones in reaction engineering. Over the
years, virtually all types of reactors have shown these features,
in both experimental and modeling studies. These features arise
either as a consequence of interactions between reaction and
transport processes, or purely as a consequence of complex re-
action kinetics; examples in the former category presently far
outnumber those in the latter. An authoritative survey of the
area was given in 1974 by Schmitz (44); more recent reviews are
also available (45, 46, 47). These aspects in the diffusion-
reaction context were treated comprehensively by Aris (20), and
by Luss (48). For stirred tanks and empty tubular reactors,
Varma and Aris (49) may be consulted.

Jensen and Ray (50) have recently tabulated some 25 experi-
mental studies which have demonstrated steady state multiplicity
and instabilities in fixed-bed reactors; many of these (cf., 29,
51, 52) have noted the importance of using a heterogeneous model
in matching experimental results with theoretical predictions.
Using a pseudohomogeneous model, Jensen and Ray (50) also present
a detailed classification of steady state and dynamic behavior
(including bifurcation to periodic solutions) that is possible in
tubular reactors.

A feature related to steady state multiplicity and stability
is that of "pattern formation", which has its origins in the bio-
logical literature. Considering an assemblage of cells contain-
ing one catalyst pellet each, Schmitz (47, 53) has shown how
non-uniform steady states – giving rise to a pattern – can arise,
if communication between the pellets is sufficiently small. This
possibility has obvious implications to packed-bed reactors.

Parametric Sensitivity. One last feature of packed-bed
reactors that is perhaps worth mentioning is the so-called "para-
metric sensitivity" problem. For exothermic gas-solid reactions
occurring in non-adiabatic packed-bed reactors, the temperature
profile in some cases exhibits extreme sensitivity to the opera-
tional conditions. For example, a relatively small increase in
the feed temperature, reactant concentration in the feed, or the
coolant temperature can cause the hot-spot temperature to in-
crease enormously (cf. 54). This sensitivity is a type of insta-
bility, which is important to understand for reactor design and
operation. The problem was first studied by Bilous and Amundson
(55). Various authors (cf. 56, 57) have attempted to provide
estimates of the heat of reaction and heat transfer parameters
defining the parametrically sensitive region; for the plug-flow
pseudohomogeneous model, critical values of these parameters can
now be obtained for any reaction order rather easily (58).

A related phenomenon is the "wrong-way behavior" of packed-
bed reactors, where a sudden reduction in the feed temperature
leads to a transient temperature rise. This has been observed
(52, 59) and satisfactorily analyzed using a plug-flow pseudo-
homogeneous model (60).

Acknowledgements

Literature Cited

1. Satterfield, C. N., "Heterogeneous Catalysis in Practice," McGraw-Hill, New York, 1980.
2. Carberry, J. J., "Chemical and Catalytic Reaction Engineering," McGraw-Hill, New York, 1976.
3. Froment, G. F.; Bischoff, K. B., "Chemical Reactor Analysis and Design," John Wiley, New York, 1979.
4. Smith, J. M., "Chemical Engineering Kinetics," Third Edition, McGraw-Hill, New York, 1980.
5. Amundson, N. R. Ber. Bunsen-Gesellschaft für Phys. Chemie 1970, 74, 90.
6. Froment, G. F. Adv. Chem. 1972, 109, 1.
7. Karanth, N. G.; Hughes, R. Catal. Rev.-Sci. Eng. 1974, 9, 169.
8. Hlaváček, V.; Votruba, J., Chapter 6 in "Chemical Reactor Theory - A Review," L. Lapidus and N. R. Amundson (Editors), Prentice-Hall, Englewood Cliffs, New Jersey, 1977.
9. Kulkarni, B. D.; Doraiswamy, L. K. Catal. Rev.-Sci. Eng. 1980, 22, 325.
10. Li, C.-H.; Finlayson, B. A. Chem. Eng. Sci. 1977, 32, 1055.
11. Ahmed, M.; Fahien, R. W. Chem. Eng. Sci. 1980, 35, 889.
12. Danckwerts, P. V. Chem. Eng. Sci. 1953, 2, 1.
13. Langmuir, I. J. Amer. Chem. Soc. 1908, 30, 1742.
14. Finlayson, B. A., "The Method of Weighted Residuals and Variational Principles," Academic Press, New York, 1972.
15. Villadsen, J.; Michelsen, M. L., "Solution of Differential Equation Models by Polynomial Approximation," Prentice-Hall, Englewood Cliffs, New Jersey, 1978.
16. Deans, H. A.; Lapidus, L. AIChE Jl. 1960, 6, 656.
17. Coste, J.; Rudd, D.; Amundson, N. R. Canad. Jl. Chem. Eng. 1961, 39, 149.
18. Sundaresan, S.; Amundson, N. R.; Aris, R. AIChE Jl. 1980, 26, 529.
19. Varma, A. Ind. Eng. Chem. Fundls. 1980, 19, 316.
20. Aris, R., "The Mathematical Theory of Diffusion and Reaction in Permeable Catalysts," Volumes I and II, Clarendon Press, Oxford, England (1975).
21. Feng, C.; Stewart, W. E. Ind. Eng. Chem. Fundls. 1973, 12, 143.
22. Luss, D., Survey paper on "Interactions between Transport Phenomena and Chemical Rate Processes," at ISCRE4, Heidelberg, Germany; DECHEMA, Frankfurt (1976), 487.
23. Carberry, J. J. Ind. Eng. Chem. Fundls. 1975, 14, 129.
24. Pereira, C. J.; Wang, J. B.; Varma, A. AIChE Jl. 1979, 25, 1036.

25. Sørensen, J. P.; Stewart, W. E. Chem. Eng. Sci. 1974, 29, 833.
26. Paspek, S. C.; Varma, A. Chem. Eng. Sci. 1980, 35, 33.
27. Eigenberger, G. Chem. Eng. Sci. 1972, 27, 1909.
28. Rhee, H.-K.; Foley, D.; Amundson, N.R. Chem. Eng. Sci. 1973, 28, 607.
29. Paspek, S. C.; Varma, A. AIChE Jl. (in press).
30. Yagi, S.; Kunii, D. AIChE Jl. 1957, 3, 373.
31. Kunii, D; Smith, J. M. AIChE Jl. 1960, 6, 71.
32. DeWasch, A.P.; Froment, G. F. Chem. Eng. Sci. 1971, 26, 629.
33. Weekman, V. W., Jr. AIChE Jl. 1974, 20, 833.
34. Doraiswamy, L. K.; Tajbl, D. G. Catal. Rev.-Sci. Eng. 1974, 10, 177.
35. Wanke, S. E; Flynn, P. C. Catal. Rev.-Sci. Eng. 1975, 12, 93.
36. Butt, J. B., Adv. Chem. 1972, 109, 259.
37. Weekman, V. W., Jr. Ind. Eng. Chem. Proc. Des. Dev. 1968, 7, 90.
38. Weekman, V. W., Jr.; Nace, D. M. AIChE Jl. 1970, 16, 397.
39. Weng, H. S.; Eigenberger, G.; Butt, J. B. Chem. Eng. Sci. 1975, 30, 1341.
40. Price, T. H.; Butt, J. B. Chem. Eng. Sci. 1977, 32, 393.
41. Liljenroth, F. G. Chem. Met. Eng. 1918, 19, 287.
42. van Heerden, C. Ind. Eng. Chem. 1953, 45, 1242.
43. Bilous, O.; Amundson, N. R. AIChE Jl. 1955, 1, 513.
44. Schmitz, R. A. Adv. Chem. 1975, 148, 156.
45. Gilles, E. D., Survey paper on "Reactor Models" at ISCRE4, Heidelberg, Germany; DECHEMA, Frankfurt (1976), 459.
46. Ray, W. H., in "Applications of Bifurcation Theory," Academic Press, 1977, 285.
47. Schmitz, R. A. Proc. JACC 1978, Vol. II, 21.
48. Luss, D., Chapter 4 in "Chemical Reactor Theory - A Review," L. Lapidus and N. R. Amundson (Editors), Prentice-Hall, Englewood Cliffs, New Jersey, 1977.
49. Varma, A; Aris, R., Chapter 2 in "Chemical Reactor Theory - A Review," L. Lapidus and N. R. Amundson (Editors), Prentice-Hall, Englewood Cliffs, New Jersey, 1977.
50. Jensen, K. F.; Ray, W. H., Paper presented at the AIChE Annual Meeting, Chicago, November 1980.
51. Hegedus, L. L.; Oh, S. H.; Baron, K. AIChE Jl. 1977, 23, 632.
52. Sharma, C. S.; Hughes, R. Chem. Eng. Sci. 1979, 34, 625.
53. Schmitz, R. A.; Tsotsis, T. T., Paper presented at the AIChE Annual Meeting, San Francisco, November 1979.
54. Emig, G.; Hofmann, H.; Hoffman, U.; Fiand, U. Chem. Eng. Sci. 1980, 35, 249.
55. Bilous, O.; Amundson, N. R. AIChE Jl. 1956, 2, 117.
56. Barkelew, C. H. Chem. Eng. Prog. Symp. Ser. 1959, 25 (55), 37.
57. Van Welsenaere, R. J.; Froment, G. F. Chem. Eng. Sci. 1970, 25, 1503.
58. Morbidelli, M.; Varma, A. AIChE Jl. (in press).
59. Van Doesburg, H.; DeJong, W. A. Chem. Eng. Sci. 1976, 31, 45.
60. Mehta, P. S.; Sams, W. N.; Luss, D. AIChE Jl. 1981, 27, 234.

RECEIVED June 3, 1981.

Solution of Packed Bed Heat-Exchanger Models by Orthogonal Collocation Using Piecewise Cubic Hermite Functions

A. G. DIXON[1]

Mathematics Research Center, 610 Walnut Street, Madison, WI 53706

An orthogonal collocation method for elliptic partial differential equations is presented and used to solve the equations resulting from a two-phase two-dimensional description of a packed bed. Comparisons are made between the computational results and experimental results obtained from earlier work. Some qualitative discrimination between rival correlations for the two-phase model parameters is possible on the basis of these comparisons. The validity of the numerical method is shown by applying it to a one-phase packed-bed model for which an analytical solution is available; problems arising from a discontinuity in the wall boundary condition and from the semi-infinite domain of the differential operator are discussed.

The choice of a model to describe heat transfer in packed beds is one which has often been dictated by the requirement that the resulting model equations should be relatively easy to solve for the bed temperature profile. This consideration has led to the widespread use of the pseudo-homogeneous two-dimensional model, in which the tubular bed is modelled as though it consisted of one phase only. This phase is assumed to move in plug-flow, with superimposed axial and radial effective thermal conductivities, which are usually taken to be independent of the axial and radial spatial coordinates. In non-adiabatic beds, heat transfer from the wall is governed by an apparent wall heat transfer coefficient.

The earliest heat-transfer studies neglected the effective axial conduction term as this was expected to be negligible by comparison with the bulk-flow term in the long beds typically used in industry. Axial dispersion was also neglected in mixing studies, and experiments by Hiby (1) confirmed the absence of axial

[1]Current address: Department of Chemical Engineering, Worcester Polytechnic Institute, Worcester, MA 01609

back-mixing. More recently it has been shown (2-4) that measure-
ments of temperature profiles in non-reacting systems in labora-
tory packed bed heat exchangers can yield statistically meaning-
ful heat transfer parameter estimates only if the measurements
are made at relatively short bed depths, where significant axial
and radial temperature gradients are present. The omission of
axial conduction at such bed depths leads to systematic errors in
the predicted temperature profiles, which cause the model to be
statistically rejected when it is fitted to data taken at several
bed depths. If the model is fitted depth-by-depth, the parameter
estimates are found to have a depth-dependence, as noticed by
De Wasch and Froment (5). In this case, they must be regarded as
length-averaged values rather than point values. Li and Finlay-
son (6) argue that constant asymptotic values should be used, as
obtained from data taken at long bed depths, although this would
give badly-determined estimates.

When a chemical reaction is present, implying larger tempera-
ture gradients, Young and Finlayson (7) have shown that an effec-
tive axial dispersion term should be included, and Mears (8) has
given criteria for the neglect of axial dispersion which show
that increasing fluid velocity reduces axial effects. This is to
be expected, since conduction through the solid, a static effect,
is believed to be the major contributor to axial effects.

The disadvantage of including axial dispersion is that an
exit boundary condition must be specified, and in cases where an
analytical solution is not available, a numerical boundary-value
problem must be solved in the axial direction, rather than an
initial-value problem.

For steady-state heat transfer an elliptic partial differen-
tial equation is the result of using the one-phase model. Pre-
vious studies (7,9) have used the orthogonal collocation method
due to Villadsen and Stewart (10) to determine the coefficients
of trial-function expansions in both spatial coordinates. This
method works well when the temperature gradients are moderate and
few collocation points are required. For steep profiles, however,
such as may be encountered at a "hot-spot" in the reactor, many
collocation points may be required, especially as the generation
of these points as roots of polynomials does not allow them to be
placed in the region of interest. Such a collocation scheme is a
global one, resulting in a collocation matrix which is large and
not usefully sparse, so that the solution of the resulting alge-
braic equations may become costly.

The answer to this difficulty lies in the use of piecewise
approximants, such as cubic splines, which are in general use in
the mathematics literature (11). Carey and Finlayson (12) have
introduced a finite-element collocation method along these lines,
which uses polynomial approximants on sub-intervals of the domain,
and apply continuity conditions at the break-points to smooth the
solution. It would seem more straight-forward, however, to use
piecewise polynomials which do not require explicit continuity

equations; in this paper the use of piecewise cubic Hermite functions is considered, as described by Prenter and Russell (13).

The advantages of piecewise polynomials are firstly that the subintervals may be clustered in regions of interest, so that an improved approximation may be obtained where gradients are steep, and secondly that the collocation matrix is banded, allowing advantage to be taken of this special structure, both in work required for decomposition and in computer storage used. This second advantage was clearly demonstrated in a preliminary study on the one-phase model (14), where the cubic Hermite function method was shown to give an order-of-magnitude improvement in exit temperature profile over the polynomial collocation method even when the subintervals were chosen to be of equal length. A more extensive investigation using the one-phase model as a test case is described in the present work.

The use of two-phase homogeneous continuum models in packed bed modelling has often been avoided due to the computational difficulties. Recently, Paspek and Varma (15) have found a two-phase model to be necessary to describe an adiabatic fixed-bed reactor, while Dixon and Cresswell (16) have shown that the effective parameters of the one-phase model may be interpreted in terms of the more fundamental parameters of a two-phase model, thus demonstrating more clearly their qualitative dependencies on the operating and design characteristics of the bed. When two phases and several species are involved, the computational advantages of the cubic Hermite method may be anticipated to be high.

In this paper the coupled elliptic partial differential equations arising from a two-phase homogeneous continuum model of heat transfer in a packed bed are solved, and some attempt is made to discriminate between rival correlations for those parameters not yet well-established, by means of a comparison with experimental results from a previous study (3,4).

Collocation using piecewise bicubic Hermite functions

The use of piecewise bicubic Hermite functions in collocation schemes for the solution of elliptic partial differential equations has been described by Prenter (13,17); a short outline is presented here.

Consider partitioning the interval [a,b] into subintervals by $a = \xi_1 < \xi_2 < \ldots < \xi_p < \xi_{p+1} = b$. Then the piecewise cubic Hermite functions are defined for $1 \le i \le p+1$ by

$$\phi_i(\xi) = \begin{cases} -2((\xi-\xi_{i-1})/h_{i-1})^3 + 3((\xi-\xi_{i-1})/h_{i-1})^2 & (\xi_{i-1} \le \xi \le \xi_i) \\ 1 + 2((\xi-\xi_i)/h_i)^3 - 3((\xi-\xi_i)/h_i)^2 & (\xi_i \le \xi \le \xi_{i+1}) \\ 0 & \text{otherwise} \end{cases}$$

$$\psi_i(\xi) = \begin{cases} (\xi-\xi_i)((\xi-\xi_{i-1})/h_{i-1})^2 & (\xi_{i-1}\leq\xi\leq\xi_i) \\ (\xi-\xi_i)((\xi_{i+1}-\xi)/h_i)^2 & (\xi_i\leq\xi\leq\xi_{i+1}) \\ 0 & \text{otherwise} \end{cases}$$

The length of subinterval $[\xi_i,\xi_{i+1}]$ is denoted by h_i. The functions ϕ_1, ψ_1 are restricted to the interval $[\xi_1,\xi_2]$ and ϕ_{p+1}, ψ_{p+1} are restricted to the interval $[\xi_p,\xi_{p+1}]$.

If the domain $[a,b] \times [c,d]$ of an elliptic partial differential operator is partitioned into subrectangles by

$$a = y_1 < y_2 < \ldots < y_n < y_{n+1} = b$$

and

$$c = x_1 < x_2 < \ldots < x_m < x_{m+1} = d \; ,$$

then the piecewise bicubic Hermite interpolation polynomial to a function $T(y,x)$ is

$$T(y,x) \doteq s_{n,m}(y,x) \tag{1}$$

$$= \sum_{i=1}^{n+1} \sum_{j=1}^{m+1} \{T(y_i,x_j)\phi_i(y)\phi_j(x) + \frac{\partial T}{\partial y}(y_i,x_j)\psi_i(y)\phi_j(x)$$

$$+ \frac{\partial T}{\partial x}(y_i,x_j)\phi_i(y)\psi_j(x) + \frac{\partial^2 T}{\partial y\partial x}(y_i,x_j)\psi_i(y)\psi_j(x)\} \; .$$

This expression is used as a trial-function expansion for T in much the same way as the Lagrange interpolation polynomial is in the polynomial collocation method of Villadsen and Stewart (10,18). There are four unknown constants associated with each node, giving a total of $4(n+1)(m+1)$ unknowns in the expansion.

The Gaussian points of subinterval $[\xi_i,\xi_{i+1}]$ are

$$\xi_{i1} = \xi_i + (\sqrt{3}-1)h_i/2\sqrt{3} \; , \; \xi_{i2} = \xi_{i+1} - (\sqrt{3}-1)h_i/2\sqrt{3} \; ;$$

combining the two points for each of $[y_i,y_{i+1}]$ and $[x_j,x_{j+1}]$ gives four Gaussian points for the subrectangle $[y_i,y_{i+1}] \times [x_j,x_{j+1}]$. Collocation at these points for each subrectangle yields a total of 4 nm equations. It should be noted that at any collocation point $(y_{ik},x_{j\ell})$ only sixteen bicubic product functions are non-zero, hence each collocation equation involves only sixteen unknowns.

The remaining $4n + 4m + 4$ equations required to determine the expansion coefficients are supplied by the boundary conditions as follows:
   (i)   on the lines $y = 0$ and $y = 1$, the boundary conditions given are differentiated with respect to x. Together

with the original equations this yields two equations on each boundary, which may be applied at each of the m - 1 internal boundary nodes to obtain a total of 4m - 4 conditions. For example, given $\frac{\partial T}{\partial y} = 0$ at y = 0, then $\frac{\partial^2 T}{\partial y \partial x} = 0$ at y = 0 also, and hence

$$\frac{\partial T}{\partial y} \ (0,x_j) = 0$$

$$\frac{\partial^2 T}{\partial y \partial x} \ (0,x_j) = 0 \qquad j = 2,3....m$$

(ii)   a similar procedure may be followed on the lines x = 0, x = 1, to obtain 4n - 4 conditions.

(iii) at each corner both (i) and (ii) above may be applied, to give four conditions. However only three of these will be independent, and one must be eliminated, except when there is a corner discontinuity, when an arbitrary decision must be made.

The 4n + 4m + 4 conditions derived above may be used either to eliminate unknowns and thus reduce the size of the system of equations to be solved, as was done in the original paper (13), or to generate extra equations. The latter procedure is easier to apply when mixed boundary conditions are used, the resulting increase in computer time used being offset by the saving in programming effort.

A proper numbering of the equations and unknowns ensures that the matrix representing the linear part of the differential operator will be a band matrix with bandwidth proportional to the lesser of m and n. Standard methods for decomposing such matrices exist (19), which allow savings in both storage and time.

The application of the above method is facilitated by the definition of suitable notation and the use of some simple subroutines to produce the cubic Hermite functions and their derivatives. These are described in detail elsewhere (20), the approach used imitates that of Villadsen and Stewart (10).

One-phase continuum model

The packed bed heat exchanger considered here is that used in recent experimental studies (2,4) and shown schematically in Figure 1. The long unheated calming section, (a), and the heated test section, (b), are each considered to be semi-infinite and packed with similar solid particles. There is a step change in wall temperature at the plane z = 0, which is represented by the Heaviside step function in equation (6).

The model equations are well-known, and are, in dimensionless form,

$$\frac{\partial \theta}{\partial x} = \frac{1}{Pe_A} \frac{\partial^2 \theta}{\partial x^2} + \frac{1}{Pe_R} \left(\frac{\partial^2 \theta}{\partial y^2} + \frac{1}{y} \frac{\partial \theta}{\partial y}\right) \tag{2}$$

$$\frac{\partial \theta}{\partial y} = 0 \quad \text{at} \quad y = 0 \tag{3}$$

$$\theta \to 0 \quad \text{as} \quad x \to -\infty \tag{4}$$

$$\theta \to 1 \quad \text{as} \quad x \to \infty \tag{5}$$

$$\frac{\partial \theta}{\partial y} + (Bi)\theta = (Bi)H(x) \quad \text{at} \quad y = 1 \tag{6}$$

The downstream axial boundary condition, equation 5, was found to be consistent with experimental data in a previous study (4).

The equations (2) - (6) have an easily-determined analytic series solution in terms of Bessel functions (4); this is therefore a good test case upon which to try out the numerical method.

There are two points of interest associated with the numerical solution of equations (2) - (6): (i) the x-domain is infinite and (ii) there is a step-function in the wall boundary condition.

<u>Transformation of the infinite domain</u>. There are several ways of dealing with an infinite domain. Guertin et al. (21) chose perturbation solutions of the model as basis functions. This approach may be difficult to extend to more complicated equations than the non-linear initial-value problems which they considered; even so, the modeller must do a considerable amount of analytical work with this method.

Birnbaum and Lapidus (22) suggest the use of polynomials which are orthogonal over the infinite domain, obtaining these either by using a weighting function such as e^{-x^2}, which gives Hermite polynomials orthogonal over $(-\infty,\infty)$, or by transforming the infinite domain onto a finite domain, and using conventional polynomials such as shifted Legendre polynomials. The drawback to these methods is that there is no control of the placement of the collocation points, some of which are always included in regions where the profile is essentially flat, and are thus wasted.

The use of standard piecewise polynomials, together with an appropriate transformation of the infinite domain, overcomes these difficulties, provided some care is taken in the transformation.

Verhoff and Fisher (23) used the form $t = \frac{1}{\pi} \tan^{-1}(\frac{x}{\alpha})$ in their solution of the Graetz problem with axial conduction. Somewhat neater equations result from taking $t = \tanh(x/\alpha)$ giving

$$\left(\frac{1-t^2}{\alpha}\right)(1 + \frac{2t}{\alpha Pe_A})\frac{\partial\theta}{\partial t} = \frac{1}{Pe_R}(\frac{\partial^2\theta}{\partial y^2} + \frac{1}{y}\frac{\partial\theta}{\partial y}) + \frac{(1-t^2)^2}{\alpha^2 Pe_A}\frac{\partial^2\theta}{\partial t^2} \qquad (7)$$

$$\frac{\partial\theta}{\partial y} = 0 \quad \text{at} \quad y = 0 \qquad (8)$$

$$\theta = 0 \quad \text{at} \quad t = -1 \qquad (9)$$

$$\theta = 1 \quad \text{at} \quad t = 1 \qquad (10)$$

$$\frac{\partial\theta}{\partial y} + (Bi)\theta = Bi\ H(t) \quad \text{at} \quad y = 0 \qquad (11)$$

Initially it may appear simpler to let $\alpha = 1$, and use $t = \tanh x$. However this results in the region $x > 3$ in the bed being mapped onto a small interval $[0.995,1]$. This is undesirable for two reasons:

1) If subintervals are required in the bed downstream of $x = 3$, it becomes difficult to place the breakpoints in the t-domain
2) If axial gradients are present downstream of $x = 3$, they will become very sharp in the t-domain, since

$$\frac{\partial\theta}{\partial t} = \frac{\alpha}{(1-t^2)}\frac{\partial\theta}{\partial x} \quad \text{so} \quad \frac{\partial\theta}{\partial t} \to \infty \quad \text{as} \quad t \to 1 \ .$$

It can be seen that for a fixed choice of $\{t_i\}$, different choices of α will locate the induced partition $\{x_i\}$ in different physical parts of the bed. Thus α must be chosen so that the collocation points in the t-domain are placed in a way that makes physical sense in the x-domain. The appropriate value is found by trial and error; an empirical rule suggested by experience is to take $\alpha \approx Pe_R$.

The effect of an inappropriate value for α is shown in Figure 2. It should be noted that although Verhoff and Fisher used $\alpha = 1$ throughout, their computations were made for sufficiently short beds to ensure good results; larger values of α would be required for temperature profiles further downstream, which would be of interest in the presence of reaction.

Step-change in wall boundary condition. It was anticipated that the discontinuity in wall temperature at $x = 0$, and the resulting steep local gradients, would lead to a locally poor approximation which might have adverse effects further downstream. It was soon found that mesh refinement in the axial direction improved the results considerably over the use of an equally-spaced mesh, whereas mesh refinement in the radial direction had little effect, and a fairly coarse uniform radial mesh was always found to be adequate.

The mesh refinement was carried out by heuristically search-
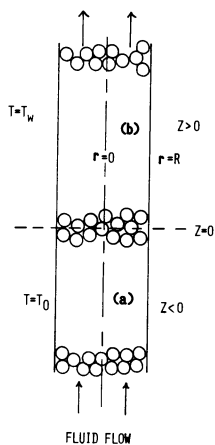
Figure 1.   Schematic of packed bed
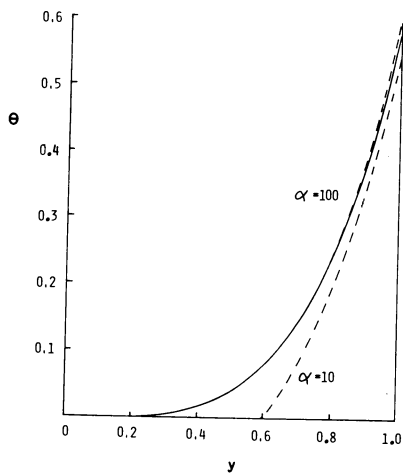
Figure 2.   Effect of choice of scaling factor α: $x = 4.0$, $Pe_A = 4.0$, $Pe_R = 120.0$, $Bi = 5.0$; (———) analytic solution, (– – –) numerical solution

ing for good breakpoint distributions, the final choice (corresponding to m = 10) being $\{t_j\}$ = {-0.1, -0.05, -0.025, 0, 0.025, 0.05, 0.1, 0.2, 0.6}. Any further refinement led to improved values only at extremely short bed depths.

The effect of the wall temperature discontinuity may also be mitigated by an alternative implementation of the wall boundary condition to that described in the previous section. The two equations at each interior boundary node $(1,t_j)$, j = 2,3,...,m, are dropped, together with one equation at each of (1,-1) and (1,1). These 2m equations are replaced by application of the boundary conditions at two points within each subinterval on the line y = 1. The Gaussian points are not necessarily the optimal choice, but were used in the absence of any other guideline.

For the case of a uniform mesh, the Gaussian point implementation was an order-of-magnitude improvement over the breakpoint implementation. When the refined mesh was used, the two methods gave essentially the same results, except at low bed depths near the wall, where the Gaussian point method was slightly better. Consequently it was the method used in the rest of the work.

The reason for the above differences is not clear but appears to lie in the wall temperature specification. No difference between the methods was found when applied to the centre-line condition, and reduction of Bi to lessen effects of the discontinuity also greatly reduced the advantage of the Gaussian point method.

When considering the degree of accuracy to be required from a numerical method, it is necessary to take into account the potential uses of the model equations being solved. It would be inappropriate to require high accuracy in the present study, as bed temperature profiles are seldom accurately measured. Consequently errors of 1°C in comparing numerical and analytical results were considered reasonable.

The comparisons were made at y = 0.1,0.2...1.0 for each of 5 bed depths: x = 1.33,2.67,4.00,5.33,6.67. The parameter ranges covered were $0.25 \leq Pe_A \leq 20.0$, $2.5 \leq Pe_R \leq 120.0$ and $0.5 \leq Bi \leq 8.0$ which are based on a tube-to-particle diameter ratio in the range $5 \leq d_t/d_p \leq 20$, for flow rates corresponding to Reynolds number Re ≥ 50.

The refined mesh given above was used in the axial direction; the radial mesh used n = 3, $\{y_i\}$ = {0.25,0.5,0.75}. It was found possible to use the same mesh throughout in the t-domain, due to the freedom to vary the scaling factor α. This avoided heuristic searching for a new mesh for each new set of parameters. Automatic mesh generation was not felt to be worthwhile, in view of the extra costs involved and the relatively underdeveloped state of the art (24).

The 1°C criterion was met in all cases except for Pe_A = 20 using this method. For that case the centre-line discrepancy rose to approximately 3°C at lower bed depths. Presumably this error could be eliminated by taking higher order approximations. A typical computation time to produce one set of solutions (i.e.,

5 bed depths) was approximately 1.5 sec on a UNIVAC 1110 computer, a reasonable compromise between cost and accuracy.

Two-phase continuum model

Two-phase continuum models, in which the solid particles and their associated stagnant fillets of fluid are regarded as a continuous pseudo-solid phase, are to be preferred to the more traditional cell model of a particle bathed in fluid, which does not allow conduction from particle to particle. In previous studies, such models have been simplified by considering a one-dimensional model only (25). This study considers the full equations, which are, in dimensionless form:

$$\frac{1}{Pe_{RF}} \left(\frac{\partial^2 T_f}{\partial y^2} + \frac{1}{y}\frac{\partial T_f}{\partial y} \right) + \frac{1}{Pe_{AF}}\frac{\partial^2 T_f}{\partial x^2} - \frac{N_f}{Pe_{RF}}(T_f - T_s) = \frac{\partial T_f}{\partial x} \qquad (12)$$

$$\left(\frac{\partial^2 T_s}{\partial y^2} + \frac{1}{y}\frac{\partial T_s}{\partial y} \right) + \frac{\partial^2 T_s}{\partial x^2} + N_s(T_f - T_s) = 0 \qquad (13)$$

$$\frac{\partial T_f}{\partial y} = \frac{\partial T_s}{\partial y} = 0 \quad \text{at} \quad y = 0 \qquad (14)$$

$$\left. \begin{array}{l} \dfrac{\partial T_f}{\partial y} + (Bi_f)T_f = (Bi_f)H(x) \\[2mm] \dfrac{\partial T_s}{\partial y} + (Bi_s)T_s = (Bi_s)H(x) \end{array} \right\} \quad \text{at} \quad y = 1 \qquad (15)$$

$$T_f, T_s \to 0 \quad \text{as} \quad x \to -\infty \qquad (16)$$

$$T_f, T_s \to 1 \quad \text{as} \quad x \to \infty . \qquad (17)$$

A semi-analytical solution to these equations was derived by Dixon and Cresswell (16), who then matched the fluid phase temperature profile to the one-phase model profile to obtain explicit relations between the parameters of the two models.

The numerical solution to the system of equations (12) - (17) parallels that of the one-phase model almost exactly, with longer computation times due to the increased size of the collocation matrix and its bandwidth. Typical computation times to produce fluid and solid temperature profiles at each of five bed-depths were 3 - 4 seconds.

A discussion of the correlations available for prediction of the parameters required in the two-phase model is presented in (16); those chosen in this study were

$$\frac{1}{Pe_{RF}} = \frac{2d_p}{d_t} \left(\frac{1}{Pe_{rf}(\infty)} + \frac{0.67\varepsilon}{(Re)(Pr)} \right) \tag{18}$$

$$\frac{1}{Pe_{AF}} = \frac{2d_p}{d_t} \left(\frac{1/Pe_{af}(\infty)}{1.0 + 9.7\varepsilon/(RePr)} + \frac{0.73\varepsilon}{(RePr)} \right) \tag{19}$$

$$Bi_f = 0.12 \, Pe_{rf}(\infty) \frac{d_t}{d_p} (Pr)^{-0.67} (Re)^{-0.25} \tag{20}$$

$$N_s = \frac{1.5(1-\varepsilon)(d_t/d_p)^2}{(k_{rs}/k_g)(1/Nu_{fs} + 0.1k_g/k_p)} \tag{21}$$

$$N_f = \frac{2d_p}{d_t} \left(\frac{k_{rs}}{k_g} \right) \frac{N_s Pe_{RF}}{(RePr)} \tag{22}$$

$$Nu_{fs} = \frac{0.255}{\varepsilon} (Pr)^{0.33} (Re)^{0.665} \tag{23}$$

As the fluid was air, $Pr = 0.72$; the bed voidage ε was taken as
0.4. The ratios k_{rs}/k_g and k_p/k_g were related using the formulas
of Zehner and Schlünder (27). Preliminary sensitivity tests
showed that the parameter Nu_{fs} had very little effect on the pro-
files; in the presence of reaction this parameter would be more
important. The correlations for the fluid-phase Peclet numbers,
equations (18) and (19), were obtained by analogy from reported
mass transfer work.

It is clear that by adjusting the parameters of this model
by nonlinear regression, an excellent fit to the experimental data
could be obtained. The value of such a procedure is rather dubi-
ous, however, and it is more useful to use the model to obtain
qualitative information about the quantities $Pe_{rf}(\infty)$, $Pe_{af}(\infty)$ and
Bi_s, which are poorly determined in the literature.

The value for the radial fluid-mixing Peclet number, $Pe_{rf}(\infty)$,
is often given in the range 8.0-12.0, as determined by Fahien and
Smith (28) and later workers. The radially-averaged Peclet num-
bers of such workers include mass transfer resistance all the way
to the wall, however, whereas the extra resistance to fluid phase
transport near the wall is covered in the present model by the use
of the parameter Bi_f. Thus the appropriate value for present pur-
poses would be nearer the bed-centre value of $Pe_{rf}(\infty) = 8.0$, also
reported by Fahien and Smith (28).

Recent work of Hsiang and Haynes (29) shows the commonly-
taken value of $Pe_{af}(\infty) = 2.0$ to be questionable in the (d_t/d_p)
range considered here. It was decided to use the relationship
$Pe_{af} \approx Pe_a$, which results from the model matching of (16) when
$Re \geq 20$-30. The values of Pe_a were poorly determined from mea-

surements made at bed exit alone (4), so estimates from data which
included profiles at z = 0 were used (3). These values led to
great improvements in the slopes of the predicted profiles.

Values of Bi_s may lie between the theoretical lower bound de-
rived by Olbrich (26):

$$Bi_s \geq (2.12)(\frac{R}{d_p})$$

and $Bi_s = \infty$, corresponding to no thermal resistance between solid
and wall.

If equation (20) is used to predict Bi_f, then it is necessary
to take $Bi_s = 1000$ for a good fit, as shown in Figure 3 for a ty-
pical case. However, it should be noted that equation (20) under-
estimates the values of $Bi_f(= Bi)$ found in (4). This is probably
due to the unreliable correlation used for Nu_{wf}, as pointed out in
(3). If the experimental estimates of Bi are used instead of
equation (20), then values of Bi_s in the range 10 - 20 are needed.
Some of these results are shown in Figures 4 - 7.

This result indicates that only precise determination of Bi_f
will allow any conclusions to be drawn on Bi_s, since these para-
meters may be mutually varied over fairly large ranges and similar
results obtained.

The computed temperature profiles in Figures 4-7 show good
general agreement with experiment; some deviation is apparent in
the centre of the bed for Re = 73 and 224. Agreement is improved
if lower values of $Pe_{rf}(\infty)$ are used, but there is no justification
for this in the literature.

Conclusions

The orthogonal collocation method using piecewise cubic Her-
mite polynomials has been shown to give reasonably accurate solu-
tions at low computing cost to the elliptic partial differential
equations resulting from the inclusion of axial conduction in
models of heat transfer in packed beds. The method promises to be
effective in solving the nonlinear equations arising when chemical
reactions are considered, because it allows collocation points to
be concentrated where they are most effective.

The fluid-phase temperatures predicted from a two-phase
pseudo-homogeneous model were shown to give reasonable agreement
with experimental measurements, without explicitly adjusting the
model parameters. It was demonstrated that more refined experi-
mental measurements will be needed to determine the parameters of
the model; in particular, the solid and fluid phase wall Biot
numbers were mutually adjustable.
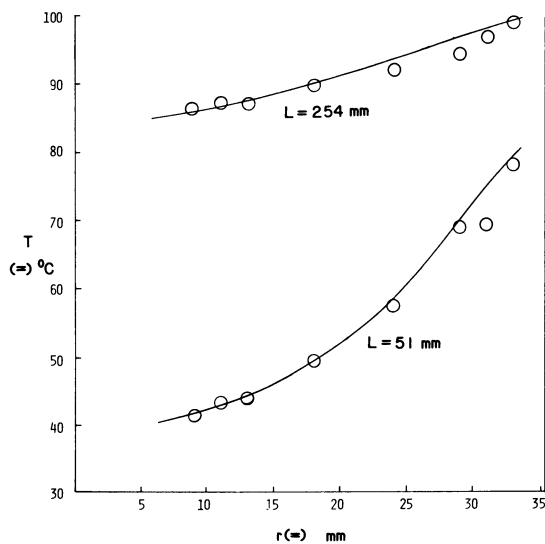
Figure 3. Temperature profiles for 9.5-mm ceramic beads: Re = 120, Pe_rf (∞) = 8.0, Pe_af (∞) = 0.49, Bi_f = 3.35, Bi_s = 1000, (○) experimental points, (——) calculated results
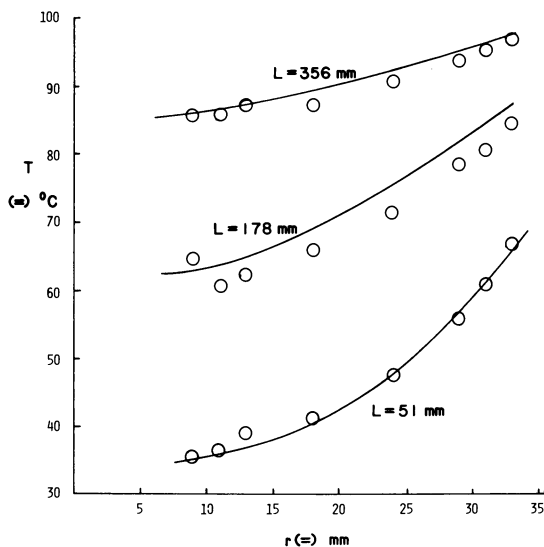
Figure 4. Temperature profiles for 12.7-mm ceramic beads: Re = 430, Pe_{rf} (∞) = 8.0, Pe_{af} (∞) = 0.45 Bi_f = 2.85, Bi_s = 10.0; (○) experimental points, (———) calculated results
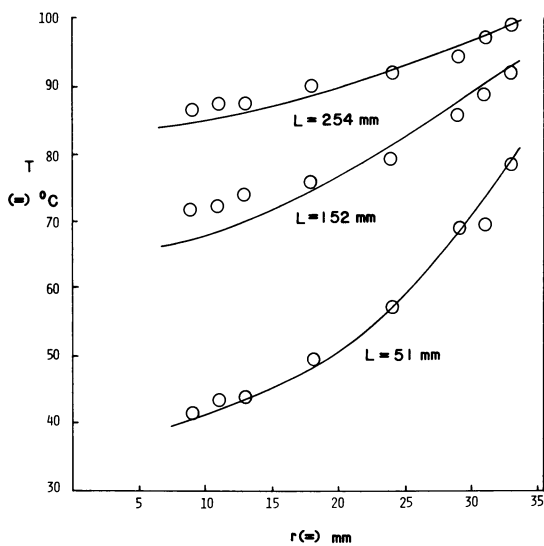
Figure 5. Temperature profiles for 9.5-mm ceramic beads: Re = 120, Pe_{rf} (∞) = 8.0, Pe_{af} (∞) = 0.49, Bi_f = 4.57, Bi_s = 20.0; (○) experimental points, (———) calculated results
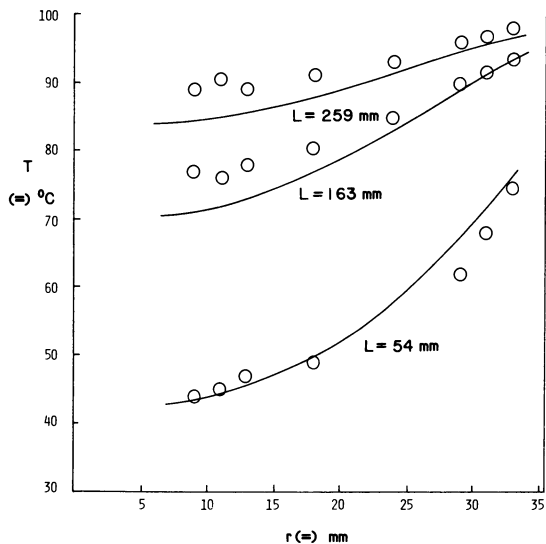
Figure 6. Temperature profiles for 9.5-mm steel balls: $Re = 224$, $Pe_{rf}(\infty) = 8.0$, $Pe_{af}(\infty) = 0.31$, $Bi_f = 3.90$, $Bi_s = 20.0$; ($\bigcirc$) experimental points, (——) calculated results
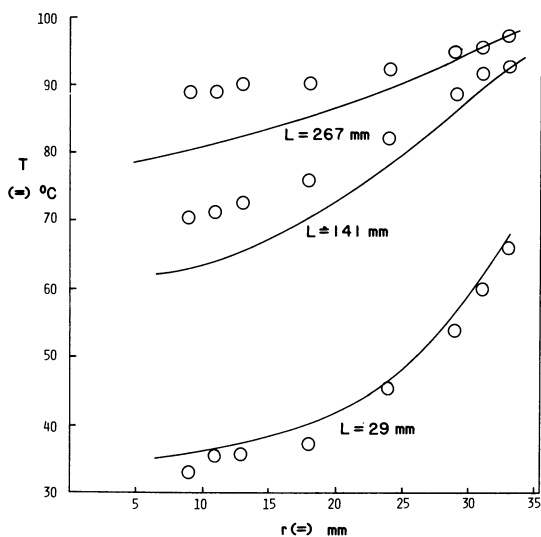
Figure 7. Temperature profiles for 6.4-mm ceramic beads: $Re = 73$, $Pe_{rf}(\infty) = 8.0$, $Pe_{af}(\infty) = 0.14$, $Bi_f = 5.85$, $Bi_s = 20.0$; ($\bigcirc$) experimental points, (——) calculated results

Nomenclature

a	specific interfacial surface area (m^{-1})
c_p	fluid specific heat (kJ/kg°C)
d_p	pellet diameter (m)
d_t	tube diameter (m)
G	superficial mass flow rate $(kg/m^2 s)$
h	apparent interphase heat transfer coefficient $(w/m^2 °C)$
h_w	apparent wall heat transfer coefficient $(w/m^2 °C)$
h_{wf}	wall-fluid heat transfer coefficient $(w/m^2 °C)$
h_{ws}	wall-solid heat transfer coefficient $(w/m^2 °C)$
h_{fs}	fluid-solid heat transfer coefficient $(w/m^2 °C)$
k_a	axial effective conductivity $(w/m°C)$
k_r	radial effective conductivity $(w/m°C)$
k_{af}	axial conductivity of fluid phase $(w/m°C)$
k_{as}	axial conductivity of solid phase $(w/m°C)$
k_{rf}	radial conductivity of fluid phase $(w/m°C)$
k_{rs}	radial conductivity of solid phase $(w/m°C)$
k_g	molecular conductivity of fluid $(w/m°C)$
k_p	pellet conductivity $(w/m°C)$
L	length of packed test section (m)
R	tube radius (m)
r	radial coordinate (m)
T_b	bed temperature, one-phase model (°C)
T_{bf}	fluid phase temperature (°C)
T_{bs}	solid phase temperature (°C)
T_0	temperature of calming section wall (°C)
T_w	temperature of test section wall (°C)
u	superficial fluid velocity (m/s)
z	axial co-ordinate (m)

Dimensionless parameters

Bi	apparent wall Biot number, $h_w R/k_r$
Bi_f	fluid-wall Biot number, $h_{wf} R/k_{rf}$
Bi_s	solid-wall Biot number, $h_{ws} R/k_{rs}$
h_i	subinterval length
m	number of axial subintervals
n	number of radial subintervals
N_F	interphase heat transfer group, $aR^2 h/k_{rf}$
N_S	interphase heat transfer group, $aR^2 h/k_{rs}$
Nu_w	apparent wall Nusselt number, $h_w d_p/k_g$
Nu_{fs}	fluid-solid Nusselt number, $h_{fs} d_p/k_g$
Nu_{wf}	fluid-wall Nusselt number, $h_{wf} d_p/k_g$
Pe_a	effective axial Peclet number, $Gc_p d_p/k_a$
Pe_A	effective axial Peclet number (based on R), $Gc_p R/k_a$
Pe_r	effective radial Peclet number, $Gc_p d_p/k_r$
Pe_R	effective radial Peclet number (based on R), $Gc_p R/k_r$
Pe_{af}	axial fluid Peclet number, $Gc_p d_p/k_{af}$

Pe_{AF} axial fluid Peclet number (based on R), Gc_pR/k_{af}
Pe_{rf} radial fluid Peclet number, Gc_pd_p/k_{rf}
Pe_{RF} radial fluid Peclet number (based on R), Gc_pR/k_{rf}
$Pe_{rf}(\infty)$ asymptotic value of Pe_{rf} as Re $\to \infty$
$Pe_{af}(\infty)$ asymptotic value of Pe_{af} as Re $\to \infty$
Pr Prandtl number, $\mu c_p/k_g$
Re Reynolds number, Gd_p/μ
y normalized radial co-ordinate (r/R)
t transformed axial co-ordinate
T_f dimensionless fluid temperature $(T_{bf}-T_0)/(T_w-T_0)$
T_s dimensionless solid temperature $(T_{bs}-T_0)/(T_w-T_0)$
x normalized axial co-ordinate (z/R)

Greek symbols

α axial scaling factor
ϵ bed voidage
ϕ_i cubic Hermite basis function
ψ_i cubic Hermite basis function
θ dimensionless bed temperature, $(T_b-T_0)/(T_w-T_0)$
μ viscosity of fluid (kg/ms)
ρ density of fluid (kg/m^3)
ξ a general independent variable

Acknowledgments

Literature Cited

1. Hiby, J.W. Inst. Chem. Eng. Symp. Series 1962, 9, 312.
2. Gunn, D.J.; Khalid, M. Chem. Eng. Sci. 1975, 30, 261.
3. Dixon, A.G. Ph.D. Thesis, University of Edinburgh 1978.
4. Dixon, A.G.; Cresswell, D.L.; Paterson, W.R. ACS Symp. Series, 1978, 65, 238.
5. DeWasch, A.P.; Froment, G.F. Chem. Eng. Sci. 1972, 27, 5667.
6. Li, Chi-Hsuing; Finlayson, B.A. Chem. Eng. Sci. 1977, 32, 1055.
7. Young, L.C.; Finlayson, B.A. I.E.C. Fund. 1973, 12, 412.
8. Mears, D.E. I.E.C. Fund. 1976, 15, 20.
9. Stewart, W.E.; Sørensen, J.P. Proceedings 2nd ISCRE, Amsterdam, 1972: (B8) 75-88.
10. Villadsen, J.V.; Stewart, W.E. Chem. Eng. Sci. 1967, 22, 1483; 1968, 23, 1515.

11. de Boor, C. "A Practical Guide to Splines," Springer-Verlag, Berlin, 1978.
12. Carey, G.F.; Finlayson, B.A. Chem. Eng. Sci. 1975, 30, 587.
13. Prenter, P.M.; Russell, R.D. SIAM J. Number. Anal., 1976, 13, 923.
14. Paterson, W.R.; Dixon, A.G.; Cresswell, D.L. paper 3 in "Computers in Chemical Engineering. Recent Developments in Education and Practice." Meeting of Inst. of Chem. Eng. (Scottish Branch), Edinburgh 1977.
15. Paspek, S.C.; Varma, A. Chem. Eng. Sci. 1980, 35, 33.
16. Dixon, A.G.; Cresswell, D.L. AIChE J. 1979, 25, 663
17. Prenter, P.M. "Splines and Variational Methods," Wiley Inter-science, New York, 1975.
18. Villadsen, J.V.; Michelsen, M.L. "Solution of Differential Equation Models by Polynomial Approximation," Prentice-Hall, Englewood Cliffs, 1978.
19. Martin, R.S.; Wilkinson, J.H. Numer. Math. 1967, 9, 279.
20. Dixon, A.G. MRC Technical Summary Report #2116, Mathematics Research Center, University of Wisconsin-Madison, 1980.
21. Guertin, E.W.; Sørensen, J.P.; Stewart, W.E. Comp. Chem. Eng., 1977, 1, 197.
22. Birnbaum, J.; Lapidus, L. Chem. Eng. Sci. 1978, 33, 455.
23. Verhoff, F.H.; Fisher, D.P. Trans. ASME, J. Heat Transfer, 1973, 95, 132.
24. Russell, R.D.; Christiansen, J. SIAM J. Numer. Anal., 1978, 15, 59.
25. Littmann, H.; Barile, R.G.; Pulsifer, A.H. I.E.C. Fund., 1968, 1, 554.
26. Olbrich, W.E. Proc. "CHEMECA" '70 Conf., Melbourne and Sydney, August 19-26, 1970, Butterworth, London, 1971, p.101.
27. Zehner, P.; Schlünder, E.U. Chemie-Ing.-Techn. 1970, 42, 933.
28. Fahien, R.W.; Smith, J.M. AIChE J. 1955, 1, 28
29. Hsiang, T.C.; Haynes, H.W. Jr. Chem. Eng. Sci. 1977, 32, 678.

An Analysis of Radial Flow Packed Bed Reactors

How Are They Different?

HSUEH-CHIA CHANG

Department of Chemical and Nuclear Engineering, University of California, Santa Barbara, CA 93106

JOSEPH M. CALO

Department of Chemical Engineering, Princeton University, Princeton, NJ 08544

An analysis of radial flow, fixed bed reactor (RFBR) is carried out to determine the effects of radial flow maldistribution and flow direction. Analytical criteria for optimum operation is established via a singular perturbation approach. It is shown that at high conversion an ideal flow profile always results in a higher yield irrespective of the reaction mechanism while dependence of conversion on flow direction is second order. The analysis then concentrates on the improvement of radial profile. Asymptotic solutions are obtained for the flow equations. They offer an optimum design method well suited for industrial application. Finally, all asymptotic results are verified by a numerical experience in a more sophisticated heterogeneous, two-dimensional cell model.

The radial flow, fixed bed reactor (RFBR) was originally developed to handle the large gas flow rates in the catalytic synthesis of ammonia. Since then, RFBR's have been used, or considered for catalytic reforming, desulfurization, nitric oxide conversion, catalytic mufflers, and other processes in which fluids must be contacted with solid particles at high space velocity. The four basic types of flow configurations are shown in Figure 1. In all these configurations fluid enters parallel to the reactor axis either through the center pipe or the peripheral annulus, and then flows radially (perpendicular to the reactor axis) into the catalyst bed contained in the annular basket. The relatively large flow area offered by the inner or outer surface of the catalyst basket decreases fluid velocity through the bed, thereby permitting the use of a relatively short bed, which significantly reduces pressure drop.

Work on the fluid mechanics of radial flow reactors can be traced back to the calculations of radial velocity profiles by Soviet investigators (1,2). This analysis was later repeated by
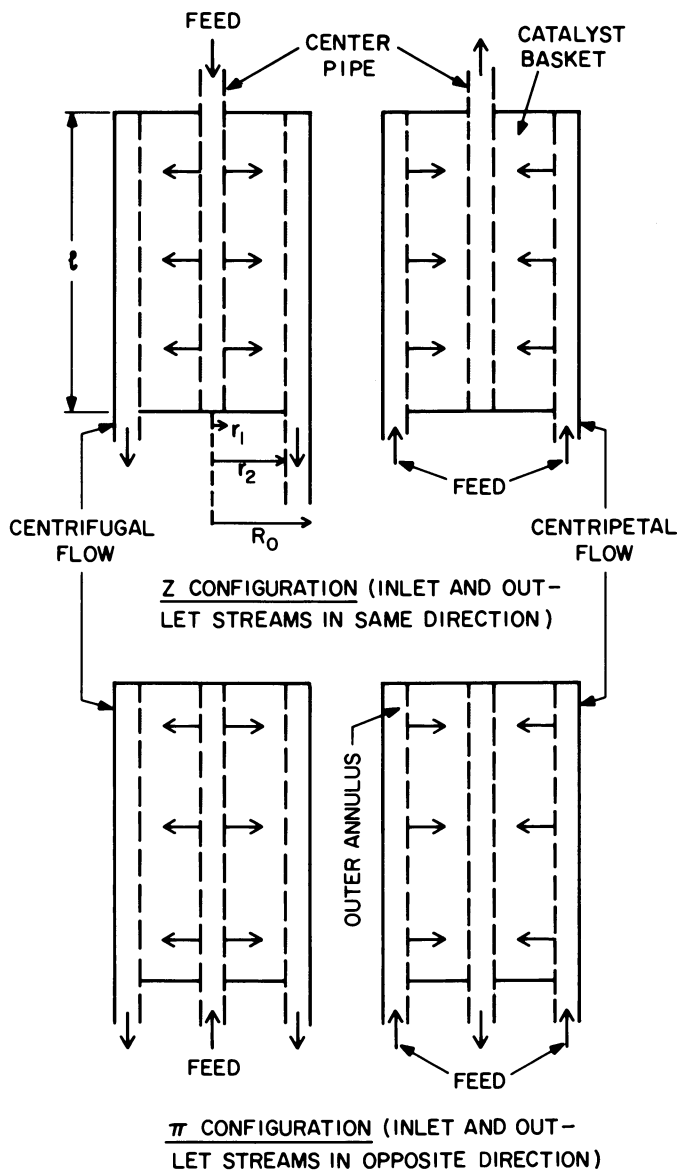
Figure 1.   Schematic of radial flow, fixed bed reactor operation

Kaye (3) who also obtained experimental data on a larger scale radial reactor sector model.

Perhaps the first published analysis of an RFBR was by Raskin et al. (4), who developed a quasicontinuum model for a radial ammonia synthesis reactor and later applied it to carbon monoxide conversion (5).

Hlavacek et al. (6) and Dudukovic et al. (7) have shown that the direction of radial flow has little effect on conversion for isothermal and first order exothermic reactions if one assumes a perfect radial flow profile. No extension to more general kinetics was attempted by these workers. The effect of imperfect radial flow profiles on conversion was more recently investigated by Ponzi and Kaye (8). These authors found, numerically, using assumed flow profiles, that a perfect radial flow profile always yields higher conversion than an imperfect one in the high conversion regime, for the cases they considered. Calo (9) has used a cell model to investigate the stability and steady state multiplicity of the centrifugal (CFRF) and centripetal flow directions (CPRF). However, this study was limited to first order irreversible, exothermic reactions. In a previous paper (10) we extended Calo's approach to a two-dimensional model using flow profiles calculated using the earlier Soviet results (1,2).

The present work generalizes, unifies, and extends that done previously. Limiting analytical results are obtained, allowing generalizations and conclusions which are presently not available from the numerical work of previous investigators. These results can serve as design guidelines as well as tools for analyzing the effects of the physical parameters on total conversion. First, it is shown that the dependence of conversion on total flow direction for perfect distribution and near plug flow conditions is second order. Nevertheless, analytical criteria for the superiority (in the sense of conversion) of the two flow directions is established. Realizing that for perfect distribution, all operating modes are approximately equivalent, the analysis then concentrates on the effects of nonideal radial flow profiles, or fluid maldistribution. It is proven that at high conversion an ideal flow profile always results in a higher yield irrespective of the reaction mechanism. Moreover, the nonuniformity of radial velocity decreases conversion at an infinite rate near maximum conversion for some representative kinetics, thereby rigorously confirming the conjecture that flow maldistribution is the single most important variable in attaining optimal radial flow operation.

Armed with this knowledge, we then set out to examine the fluid mechanics of the reactor. Limiting asymptotic solutions are obtained for some of the flow equations which allow the determination of the optimum flow configuration for actual conditions which approximate those assumed. Outside the domain of validity of the asymptotic solutions, numerical integration must be applied, of course. These results substantiate conclusions arrived at using the asymptotic solutions, even in parametric regions where the

asymptotic solutions are not valid. Finally, numerical experiments with a two-dimensional cell model are carried out to assess the effects of dispersion and interphase heat and mass transport, which are not considered in the analytical approach. Although the cell model represents a more detailed analysis of the problem, the results were found to be in agreement with the simpler models.

Flow Direction Dependence Of Perfect Radial Flow Distribution At Near-Plug Flow Conditions

In order to investigate the dependence of conversion on flow directions (CPRF vs. CFRF), the radial flow profile is assumed to be uniform and a one-dimensional quasicontinuum model is chosen. At high Reynolds numbers, as assumed here, experimental evidence indicates that $D/u d_p$, $k/\rho c_p u d_p$ is constant with respect to Reynolds number (4,5,7). This means that the heat and mass dispersion coefficients are directly proportional to the velocity, u. However, for a perfect radial profile, the continuity equation yields $ur = u_1 r_1 = u_2 r_2 = $ constant. Thus for high Reynolds numbers D and $k/\rho c_p$ are inversely proportional to r. Introducing the following dimensionless variables:

$$c = \frac{c'}{c_o} \quad : \quad \theta = \frac{T}{T_o}; Pe_M = \frac{r_2 u_2}{D}; \quad Pe_H = \frac{\rho c_p r_2 u_2}{k}$$

$$Le = \frac{Pe_H}{Pe_M} \quad ; \quad Da = \frac{k_o r_2 c_o^{n-1}}{u_2} \quad ; \quad B = \frac{(-\Delta H)}{\rho C_p}; \quad \bar{r} = \frac{r}{r_2}; \quad f = \frac{R}{k_o c_o^{n}}$$

The governing equation and boundary conditions can be unified for both flow directions, viz.,

$$Le \; \varepsilon \; \frac{d^2 c}{dy^2} - \left[\frac{dc}{dy} + Da \; h(y) \; f \; (c, \theta) \right] = 0 \tag{1}$$

$$\varepsilon \; \frac{d^2 \theta}{dy^2} - \left[\frac{d\theta}{dy} - Da \; B \; h(y) \; f \; (c, \theta) \right] = 0 \tag{2}$$

$$y = 0 \quad : \quad Le \; \varepsilon \; \frac{dc}{dy} = c - 1 \tag{3}$$

$$\varepsilon \; \frac{d\theta}{dy} = \theta - 1 \tag{4}$$

$$y = 1 - \rho \quad : \quad \frac{dc}{dy} = \frac{d\theta}{dy} = 0 \tag{5}$$

where

$$h(y) = \begin{cases} y + \rho \quad ; \quad \text{CFRF} & \text{(6)} \\ 1 - y \quad ; \quad \text{CPRF} & \text{(7)} \end{cases}$$

and $\varepsilon = 1/Pe_H$ becomes the perturbation parameter when $Pe_H \gg 1$ (i.e., $\varepsilon \ll 1$).

Perturbation Solution for Le = 1. The simplest case of Le = Pe_H/Pe_M = 1 is analyzed here. This assumption yields the adiabatic invariant, $B(1 - c) = \theta - 1$ which can be used to further simplify Eqns. (1)-(5) to

$$\varepsilon \frac{d^2c}{dy^2} - \left[\frac{dc}{dy} + Da\,h(y)\,f(c) \right] = 0 \tag{8}$$

$$y = 0 : \varepsilon \frac{dc}{dy} = c - 1 \tag{9}$$

$$y = (1 - \rho): \frac{dc}{dy} = 0 \tag{10}$$

When $\varepsilon \ll 1$, this becomes a singular perturbation problem.

Outer Solution. Let the outer solution, $\bar{c}$, be expressed as the following power series in ε,

$$c = \sum_{n=o}^{\infty} \varepsilon^n \bar{c}_n \tag{11}$$

Consequently,

$$f = f_o + (\bar{c} - \bar{c}_o)\, f_{\bar{c}_o} + - - - - = f_o + \varepsilon \bar{c}_1\, f_{\bar{c}_o} + - - - - \tag{12}$$

where $\quad f_o = f(\bar{c}_o) \quad$ and $\quad f_{\bar{c}_o} = \left(\frac{\partial f(\bar{c})}{\partial \bar{c}} \right)_{\bar{c}_o} \tag{13}$

ε^o Term. Substituting Eqns. (11), (12) into Eqns. (8)-(10), one obtains, for the zeroth order, the plug-flow equation

$$\frac{d\bar{c}_o}{dy} + Da\,h(y)\,f_o = 0 \tag{14}$$

$$\text{B.C.:} \quad y = o : \bar{c}_o = 1 \tag{15}$$

Eqns. (14) and (15) can be integrated,

$$\int_{1}^{\bar{c}_{oe}} \frac{d\bar{c}_o}{f_o} = - Da \int_{0}^{1-\rho} h(y) \, dy = - \frac{Da(1-\rho^2)}{2} \tag{16}$$

where $\bar{c}_{oe}$ is the value at $y = 1 - \rho$. Since Eqn. (16) is indepen-
dent of flow direction, to the zeroth order (i.e., plug flow),
there is no difference in conversion between the two flow direc-
tions, and any differences that do arise can only be of higher
order. This is an important conclusion of this section.

$$\underline{\varepsilon^1 \text{ Term.}} \quad \frac{d^2\bar{c}_o}{dy^2} - \frac{d\bar{c}_1}{dy} - \bar{c}_1 \, Da \, h(y) \, f_{\bar{c}_o} = 0 \tag{17}$$

$$\text{B.C.:} \quad y = o \; ; \quad \frac{d\bar{c}_o}{dy} = \bar{c}_1$$

Using the integral form of the solution to Eqn. (17),

$$\bar{c}_1 = - Da \, e^{-g(y)} \int_{0}^{y} e^{g(y')} \frac{dhf_o}{dy'} \, dy' - Da \, h(o) f_o(o) e^{-g(y)} \tag{18}$$

$$\text{where} \quad g(y) = \ln \frac{f_o(y=o)}{f_o} \tag{19}$$

Substituting Eqn. (19) into Eqn. (18), one obtains

$$\bar{c}_{1_e} = - Da \, f_o(e) \, h_e + \int_{o}^{e} h \, d\ln f_o \tag{20}$$

where (e) denotes the value at the exit, $y = 1 - \rho$ (e.g. $f_o(e) = f_o(\bar{c}_{oe})$). Higher order terms are more difficult to obtain, but do
not contribute significantly.

   Inner Solution. Rescaling the spatial coordinates at the
boundary layer located at $y = 1 - \rho$, by $z = [y-(1-\rho)]/\varepsilon$, one
obtains

$$\frac{d^2\hat{c}}{dz^2} - \left[\frac{d\hat{c}}{dz} + \varepsilon \, Da \, h \, f \, (\hat{c}) \right] = 0 \tag{21}$$

B.C.: $z = 0$, $\dfrac{d\hat{c}}{dz} = 0$ (22)

where $h = \begin{cases} \varepsilon z + 1 & ; \quad \text{CFRF} \\ \rho - \varepsilon z & ; \quad \text{CPRF} \end{cases}$ (23)

$\underline{\varepsilon^{\circ} \text{ Term}}$.   The zeroth order equation is simply $\hat{c}_o = c_1$, a constant to be determined by matching.

$\underline{\varepsilon^1 \text{ Terms}}$. $\dfrac{d^2\hat{c}_1}{dz^2} - \dfrac{d\hat{c}_1}{dz} - Da\ h(z)\ f_o = 0$ (24)

B.C: $z = 0$, $\dfrac{d\hat{c}_1}{dz} = 0$

Integrating Eqn. (24) and applying the appropriate boundary conditions, one obtains,

$$\hat{c}_1 = Da\ f_o\ (\hat{c}_o)h_e\ \left[e^z - z - 1\right] + \hat{c}_{1e}$$ (25)

$\underline{\text{Matching}}$.   The constants $\hat{c}_o$ and $\hat{c}_{1e}$ must be evaluated by matching with the outer solution:

$\lim\limits_{z \to \infty} \hat{c} = \hat{c}_o - \varepsilon\ Da\ f_o(\hat{c}_o)\ h_e\ (z+1) + \varepsilon\ \hat{c}_{1e} + 0\ (\varepsilon^2)$ (26)

$\lim\limits_{y \to -\rho} \bar{c} = \bar{c}_{oe} - \varepsilon\ Da\ f_o\ (\bar{c}_{oe})\ h_e\ z + \varepsilon\bar{c}_{1e} + 0\ (\varepsilon^2)$ (27)

The composite solution is thus

$c = \bar{c} + \hat{c} - \lim\limits_{\varepsilon \to o} \bar{c}\ (\varepsilon z + 1 - \rho)$

$= \bar{c}_o + \bar{\varepsilon}c_1 + \varepsilon\ Da\ f_o(e)\ h_e\ e^{\frac{y-(1-\rho)}{\varepsilon}} - \dfrac{y-(1-\rho)}{\varepsilon}$ (28)

and the difference in exit concentration for the two flow directions is

$\Delta c_e = c_{e_{CF}} - c_{e_{CP}} = \varepsilon\ \left[\bar{\Delta c}_{1e} + Da\ f_o(e)\ (1-\rho)\right] + 0\ (\varepsilon^2)$ (29)

But from Eqn. (20),

$$\Delta c_e = \varepsilon \left[- Da\, f_o(e)\,(1-\rho) - Da\, f_o \int_o^e (h_{CF} - h_{CP})\, d\ln f_o + Da\, f_o(e)(1-\rho) \right]$$

$$= \varepsilon\, Da\, f_o(e) \int_o^e (h_{CP} - h_{CF})\, d\ln f_o \qquad (30)$$

Eqn. (30) requires a specific relationship between $h(y)$ and f_o in order to be evaluated. Recalling the indefinite version of Eqn. (16), i.e.,

$$\int_1^{\bar{c}_o} \frac{d\bar{c}_o}{f_o} = - Da \int_o^y h(y)\, dy \qquad (31)$$

let

$$- \int_1^{\bar{c}_o} \frac{d\bar{c}_o}{f_o} = \Gamma\, (\bar{c}_o) \qquad (32)$$

since f_o, the reaction expression, is yet to be specified. Then

$$\frac{\Gamma}{Da} = \begin{cases} \dfrac{y^2}{2} + \rho y & ; \quad CFRF \\[2ex] y - \dfrac{y^2}{2} & ; \quad CPRF \end{cases} \qquad (33)$$

and

$$\Delta c_e = \varepsilon\, Da\, f_o(e) \int_1^{\bar{c}_o e} \left[\sqrt{1 - \frac{2\Gamma}{Da}} - \sqrt{\rho^2 + \frac{2\Gamma}{Da}} \right] \frac{d\ln f_o}{d\bar{c}_o}\, d\bar{c}_o \qquad (34)$$

Eqn. (34) determines the difference in exit concentrations for the two flow directions, given the rate expression $f_o(\bar{c}_o)$. The relative effect of flow direction can be determined from the sign of Δc_e; i.e., $\Delta c_e > 0 \to$ CPRF has higher conversion, $\Delta c_e < 0 \to$ CFRF has higher conversion.

An important conclusion can be derived from Eqn. (34). Note that Δc_e is proportional to $f_o(e)$, the rate of reaction at the exit. For irreversible endothermic and isothermal positive order reactions, the rate at the exit is the lowest in the reactor and Δc_e is small. Consequently, if the flow direction is a factor for conversion, the effects should be most pronounced for negative

order or highly exothermic reactions far removed from plug-flow conditions.

Under certain conditions the Lewis number may be close to unity. For these cases one can extend the analysis in the previous section to include the effect of Lewis number by perturbing about Le = 1. The results indicate that the effects of non-unity Le appear only in $O(\delta\varepsilon)$ and higher terms. Consequently, the solution in the previous section represented by Eqn. (34) is also valid here to order $(\delta\varepsilon)$, and since Eqn. (34) is only exact to order ε, it is also appropriate as the solution for non-unity Lewis number.

<u>Isothermal nth Order Irreversible Reaction</u>. Here $f = c^n$ and the zeroth order equation representing the outer solution is

$$\frac{d\bar{c}_o}{dy} = - Da \ h(y) \ \bar{c}_o{}^n \tag{35}$$

<u>n = 0</u>. For this case, f is independent of c and it is obvious, without further analysis, from Eqns. (1)-(5) that $\Delta c_e = 0$.

<u>n = 1</u>. $\Gamma = - \ln \bar{c}_o$ and $\Gamma_e = \dfrac{Da \ (1-\rho^2)}{2}$

Thus, $\Delta c_e = \varepsilon Da \ f_o(e) \displaystyle\int_0^{\Gamma_e} \sqrt{1-\frac{2\Gamma}{Da}} - \sqrt{\rho^2 + \frac{2\Gamma}{Da}} \ d\Gamma = 0 \tag{36}$

<u>n ≠ 1</u>. The zeroth order outer solution is

$$\bar{c}_o = \left[1 - (1-n) \ Da \int_0^y h \ dy\right]^{\frac{1}{1-n}} \tag{37}$$

Note that for n < 1, the argument on the left hand side of Eqn. (37) can be negative which may make the solution meaningless. Thus, we define the restriction

$$2 \int_0^y h \ dy = \rho^2 - 1 > b \tag{38}$$

for orders of reaction less than unity, where b = 2/Da(n-1). Thus, from Eqn. (34),

$$\Delta c_e = - \ \varepsilon \ Da \ f_o(e) n \int_0^\Gamma e \left[\frac{\sqrt{1- \dfrac{2\Gamma}{Da}} - \sqrt{\rho^2 + \dfrac{2\Gamma}{Da}}}{(n-1) \ \Gamma \ + \ 1}\right] d\Gamma \tag{39}$$

The integral in Eqn. (39) cannot be expressed in closed form. However, the sign of the integral can be obtained by making the substitution, $u = \Gamma/\Gamma_e - 1/2$ which yields

$$\Delta c_e = \frac{2n\ f_o(e)}{n-1}\ \varepsilon\ \chi\ (b,\ \rho) \tag{40}$$

where

$$\chi\ (b,\ \rho) = \int_{-\frac{1}{2}}^{\frac{1}{2}} \frac{g\ (u)}{q\ (u)}\ du \qquad q(u) = b + (1-\rho^2)\ (u + \tfrac{1}{2})$$

and

$$g(u) = [u + \tfrac{1}{2} - \rho^2\ u + \rho^2/2]^{\frac{1}{2}} - [-u + \tfrac{1}{2} + \rho^2 u + \rho^2/2]^{\frac{1}{2}}$$

Note that g is asymmetric with respect to u, i.e. $g(u) = -g(u)$. It can then be shown that

$$\chi = \int_{o}^{\frac{1}{2}}\ g(u)\ \rho(u)\ du \tag{41}$$

where

$$\rho(u) = \frac{-2\ (1-\rho^2)u}{b + \tfrac{1}{2}\ (1-\rho^2)\ -\ (1-\rho^2)^2 u^2}$$

Note that also $g(0) = 0$ and the derivative of g with respect to u is positive for u between 0 and 1/2. Thus, $g(u) > 0$ for u in that range. The signs of Δc_e are obtained in the following theorems from the preceding information.

<u>Theorem 1</u>. $n > 1 \rightarrow \Delta c_e < 0$

Proof: $n > 1 \rightarrow b > 0 \rightarrow [b + \tfrac{1}{2}\ (1-\rho^2)]^2 - (1-\rho^2)^2\ u^2 > o$

for $u\ \varepsilon\ (o,\ \tfrac{1}{2})$

$\rightarrow 2\ (b + \frac{1-\rho^2}{2}) \qquad b + \frac{1}{2}\ (1-\rho^2)^2 - (1-\rho^2)^2\ u > 0$

for $u\ \varepsilon\ (o,\ \tfrac{1}{2})$

$\rightarrow \rho(u) < 0 \rightarrow \chi < o \rightarrow \frac{2n}{n-1}\ f_o(e)\ \varepsilon\ \chi < 0 \rightarrow \Delta c_e < 0$ Q.E.D.

<u>Theorem 2</u>. $n < 1$ and $b < \rho^2 - 1 \rightarrow \Delta c_e > 0$

Proof: $b < \rho^2 - 1 \rightarrow b + \frac{1}{2}\ (1-\rho^2) < \frac{\rho^2-1}{2}$

$$\to \quad b + \frac{1}{2}(1-\rho^2)^2 \quad > \quad \frac{\rho^2-1}{2}^2 \quad \text{Since} \quad \frac{\rho^2-1}{2} < 0$$

$$\to \quad p(u) < 0 \qquad \to \quad \chi < 0$$

$$\to \quad \frac{2n}{n-1} f_0 \, \varepsilon \, \chi > 0 \quad \text{since } n-1<0 \qquad \to \Delta c_e > 0 \qquad Q.E.D.$$

Thus, in general, CFRF yields higher conversion for reaction orders greater than unity, while CPRF is the preferred direction for $0 < n < 1$. For zeroth and first order reactions, there is no difference between conversions for the two flow directions to the ε order.

<u>Nonisothermal Conditions</u>.   For   nonisothermal   conditions,

$$f_0 = \bar{c}_0^{\,n} \, e^{-\Upsilon/\theta_0} = \bar{c}_0^{\,n} \, e^{-\Upsilon/(1+B[1-c_0])} \quad \text{and} \quad \Gamma = - \int_1^{\bar{c}_0} \frac{d\bar{c}_0}{f_0} \qquad (42)$$

Eqn. (42) cannot be integrated in closed form. Thus Eqn. (34) will be evaluated numerically. In Figure 2, the locus of $\Delta c_e = 0$ is plotted in the $B-\bar{c}_{oe}$ domain for different reaction orders. Note that at high conversions ($\bar{c}_{oe} \to 0$) CPRF yields a higher conversion for exothermic reactions with reaction order greater than unity. This is the same conclusion arrived at by Calo (<u>9</u>) using a simple cell model for $n = 1$.

It is interesting to note that the underlying cause of the difference in conversion for different flow directions is dispersion or mixing. It is well known that, at isothermal conditions, dispersion reduces conversion for reactions of order greater than unity and increases conversion for negative order reactions, while the first order reaction is completely unaffected (<u>11</u>). In the present context one expects CFRF to exhibit a lower degree of mixing relative to CPRF, since CFRF yields higher conversions for $n > 1$ and less for $n < 1$. However, it would be more appropriate to say that the major amount of dispersion in CPRF is near the exit of the bed. Apparently, the total amount of dispersion is the same for both configurations and it is the <u>distribution</u> of dispersion in the radial direction which is the actual cause of the difference in conversion. For nonisothermal reactors, such generalizations are not possible <u>a priori</u>, as shown by Ray et al. (<u>12</u>), and one must consult Figure 2 for any specific case. In any event, the large flow rates in industrial reactors tend to minimize the effects of dispersion and one should be able to model radial flow reactors adequately with using the plug flow assumption. On the other hand, for laboratory or small scale reactors care should be exercised.
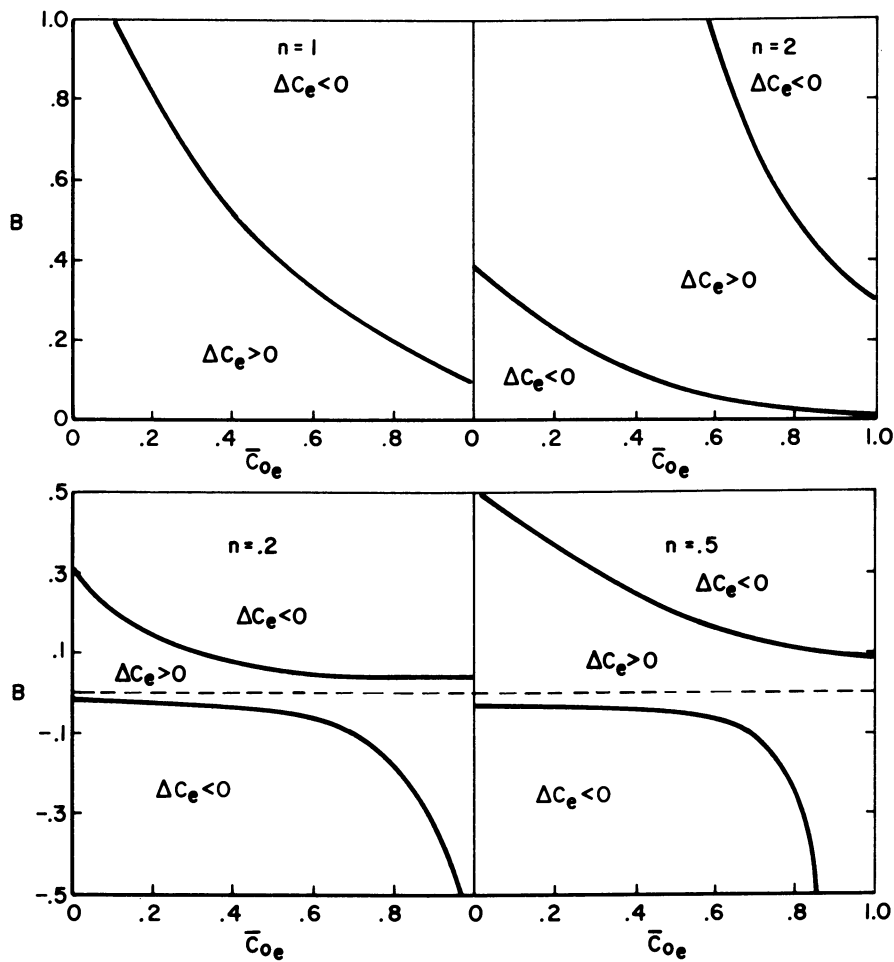
Figure 2.   *The $\Delta c = 0$ locus in $B - \bar{c}_{o_e}$ space for nth order, irreversible, exothermic reaction, $\gamma = 10$, $\rho = 0.2$*

Effects Of Maldistribution On Conversion

In the previous section, it was recognized that for perfect fluid distribution flow direction has only a second order effect on conversion. In this section, the effects of maldistribution are investigated. In order to eliminate the influence of flow direction, a pseudo-homogeneous plug flow model is used with purely radial flow through the catalyst basket. The governing equation is thus Eqn. (14), which in more convenient form is

$$\int_{o}^{x(\bar{v})} \frac{dx}{R(x)} = \frac{\Omega}{\bar{v}} \quad , \tag{43}$$

where $\qquad \Omega = \dfrac{2\ \tau\ 1}{C_o r_1} \qquad \bar{w}_1 = w/w_o; \ \bar{v} = 2v1/r_1; \ z = z'/1$

For perfect fluid distribution, $\bar{v}(z) = 1$ and the conversion x_p, is defined by

$$\int_{o}^{x_p} \frac{dx}{R} = \Omega\ (x_p) \tag{44}$$

The deviation of the total conversion for maldistributed flow from that at perfect distribution is defined by:

$$\Delta = \frac{\int_{o}^{1} x\bar{v}dz}{x_p} \tag{45}$$

Equating total radial flow to inlet axial flow, one obtains the following constraint on $\bar{v}$,

$$\int_{o}^{1} \bar{v}\ dz = 1 \tag{46}$$

The term Δ is expressible in terms of x_p if $\bar{v}(z)$ is known from the flow solutions delineated in Section 4. However, the effects of maldistribution on conversion can be assessed without any information on $\bar{v}(z)$ in the manner outlined below. We shall investigate the behavior of Δ near high conversion and near perfect distribution, which are both limits of practical interest.
Expanding x in a Taylor series of $\bar{v}$ about $\bar{v} = 1$,

$$x(\bar{v}) = x_p + \frac{\partial x}{\partial v}\bigg|_{\bar{v}=1} (\bar{v} - 1) + - - - - \tag{47}$$

where from Eqn. (43),

$$\left(\frac{\partial x}{\partial \bar{v}}\right)_{v=1} = -\left(\frac{\Omega\ R(x)}{\bar{v}^2}\right)_{v=1} = -\Omega\ (x_p)\ R(x_p) \qquad (48)$$

Substituting Eqns. (47) and (48) into Eqn. (45) and invoking constraint (49) one obtains

$$\Delta \sim 1 - \frac{\Omega(x_p)\ R(x_p)}{xp} \left[\int_0^1 \bar{v}^{-2}dz - 1\right] \qquad (49)$$

However, from Eqn. (44),

$$\frac{\partial \Omega}{\partial x_p} = \frac{1}{R(x_p)}$$

Thus, $$\frac{\partial \Delta}{\partial x_p} \sim \frac{[\int_0^1 \bar{v}^{-2}dz-1]}{x_p^2} [x_p\Omega\ \frac{\partial R}{\partial x} + x_p - R\Omega] \qquad (50)$$

At high conversions, $x_p \to x_{eq}$ where x_{eq} is the equilibrium conversion, and

$$\lim_{x_p \to x_{eq}} \frac{\partial \Delta}{\partial x_p} \sim$$

$$-\ \frac{\int_0^1 v^{-2}dz\ -1}{x_{eq}} \left[\Omega(x_p)\ \frac{\partial R}{\partial x}\Bigg|_{x_p = x_{eq}} + 1 - R\Omega\right]_{x_p = x_{eq}} \qquad (51)$$

From Eqns. (49) and (51) it can be seen that the behavior at Δ and $\partial\Delta/\partial x_p$ in the neighborhood of $c_p = 1$ is determined by the following two limits,

$$\lim_{x_p \to x_{eq}} R\Omega \qquad \text{and} \qquad \lim_{x_p \to x_{eq}} \Omega\ \frac{\partial R}{\partial x}$$

For positive order reactions, $R(x_{eq}) = 0$ and $\lim_{x_p \to x_{eq}} \Omega = \infty$. Thus, the evaluation of the limits (51) must be carried out with care. Expanding $R(x)$ about $x = x_e$:

$$R(x) = \left(\frac{d^m R}{d x^m}\right)_{x=x_{eq}} \frac{(x - x_{eq})^m}{m!} + - - - \tag{52}$$

where m is the first nonvanishing derivative of R at x_e, since it is possible that the first few derivatives might vanish at x_e. Then

$$\Omega(x) = \int_0^x \frac{dx}{R} = \frac{-m!}{\dfrac{\partial^m R}{\partial x^m}\bigg|_{x_{eq}}} \left[\frac{1}{(m-1)(x-x_{eq})^{m-1}} - \frac{(-x_{eq})^{m-1}}{m-1}\right] + --- \tag{53}$$

The limits can be evaluated by using Eqns. (52) and (53)

$$\lim_{x \to x_{eq}} R\Omega = 0 \quad \text{for } m \geq 1$$

$$\lim_{x \to x_{eq}} \Omega \frac{\partial R}{\partial x} = \left.\begin{array}{ll} \dfrac{-m}{m-1} & \text{for } m > 1 \\ -\infty & \text{for } m = 1 \end{array}\right\}$$

Thus, $\lim_{x_p \to x_{eq}} \Delta = 1$

and $\lim_{x_p \to x_{eq}} \dfrac{\partial \Delta}{\partial x_p} = +\infty$ for $m = 1$

$$= \frac{1}{m-1} \left[\int_0^1 \bar{v}^{-2} dz - 1\right] > 0 \quad \text{for } m > 1$$

The expression is positive since from constraint (46),

$$\int_0^1 \bar{v}^{-2} dz \geq \int_0^1 \bar{v} dz \int_0^1 v dz = 1$$

Thus, $\lim_{x_p \to x_{eq}} \dfrac{\partial \Delta}{\partial x_p} > 0 \tag{54}$

and Δ decreases with x_p near x_{eq}, sometimes infinitely fast (for the m = 1 case). Thus, the nonuniformity of the radial flow pro-file can cause drastic differences in conversion in the high con-version regime. Results for typical specific reaction kinetics

indicate that for a first order reaction, regardless of whether it is isothermal and irreversible, or nonisothermal and irreversible, or isothermal and reversible; conversion would decrease at an infinitely fast rate upon the slightest deviation from perfect distribution in the high conversion region. (For detailed calculations, see (16).) This effect can also be seen in the results of Ponzi and Kaye (8), reproduced in Figure 3. By assuming that the nonuniform radial profile is the form $v = sy^{s-1}$, the figure shows the predicted infinite slope as x_p approaches x_{eq}. Near x_{eq} (i.e. in the high conversion region), reduction by as much as 50% occurs for a first order exothermic irreversible reaction.

Radial Flow Profile Determination

In the previous section, the importance of the uniformity of the radial flow profile was established. In the present section, the fluid mechanical equations for all four flow configurations in Figure 1 are derived and solved for comparison. The development of equations closely follows the approach of Genkin et al. (1,2). Here we extend their work to include both radial and axial flow in the catalyst bed. Following our derivation in reference (16), the dimensionless equations for the axial velocity in the center-pipe for all four configurations are (the primes denote derivative with respect to the dimensionless axial coordinate),

$$a_1 \bar{w}_1' \bar{w}_1'' + a_2 \bar{w}_1 \bar{w}_1' + a_3 \bar{w}_1^2 = 0 \qquad (55)$$

$$\text{B.C.:} \qquad \bar{w}_1(0) = 0 \qquad \bar{w}(1) = 1 \qquad \text{(CPRF)}$$

$$\bar{w}_1(0) = 1 \qquad \bar{w}(1) = 0 \qquad \text{(CFRF)}$$

$$a_1 \bar{w}_1'' + a_4 \bar{w}_1 \bar{w}_1' + a_5 \bar{w}_1' + a_6 (1-\bar{w}_1)^2 + a_7 \bar{w}_1^2 = 0 \qquad (56)$$

$$\text{B.C.:} \qquad \bar{w}_1(0) = 0 \qquad \bar{w}_1(1) = 1 \qquad \text{(CPRF)}$$

$$\bar{w}(0) = 1 \qquad \bar{w}(1) = 0 \qquad \text{(CFRF)}$$

where

$$a_1 = \frac{1}{\ell^2}\left\{\frac{r_1^4}{4r_2^2\phi_2^2} - \frac{r_1^2}{4\phi_1^2} - \left[\frac{b^*\phi_2^2 r_2^2}{\chi^3}\left(\frac{r_2 - r_1}{r_1 r_2}\right) + \frac{1}{2}\left(1 - \left[\frac{\phi_2 r_2}{\phi_1 r_1}\right]^2\right)\right]2\left(\frac{r_1^2}{2\phi_2 r_2}\right)^2\right\}$$

$$a_2 = a_4 = \frac{3}{2}(\xi^2-1); \quad \xi = \frac{r_1^2}{R_o^2-r_2^2}; \quad a_3 = -\frac{R_o}{R_o^2-r_2^2}\xi^2 + \frac{1}{r_1} f\ell; \quad a_5 = -\frac{3}{5}\xi^2$$

$$a_6 = \frac{R_o}{R_o^2 - r_2^2} f\ell \, \xi^2 \quad ; \quad a_7 = -\frac{f\ell}{r_1}$$

The radial velocities are related to the axial velocities by

$$\pm \frac{r_1}{2\phi_1} \bar{w}_1' = \bar{v}_1 \qquad \begin{cases} + & \text{CPRF} \\ - & \text{CFRF} \end{cases} \qquad (57)$$

$$\pm \frac{R_o^2 - r_2^2}{2r_2\phi_2} \bar{w}_2' = \bar{v}_2 \qquad \begin{cases} + & \begin{array}{l} \text{CPRF} - \Pi \\ \text{CFRF} - Z \end{array} \\ - & \begin{array}{l} \text{DPRF} - Z \\ \text{CFRF} - \Pi \end{array} \end{cases} \qquad (58)$$

Even before carrying out the actual numerical integration, certain qualitative features of the solutions are evident. It should be noted that if $\xi^2 = 1$ and $a_3 = 0$, the flow equation yields the solution for perfect distribution; i.e.,

$$\bar{w}_{1_{ideal}} = \begin{cases} 1 - z & \text{CF} \\ z & \text{CP} \end{cases} \qquad (59)$$

upon inspection. This does not apply to the Z-flow equation which yields nonideal distribution at the same conditions. These conditions correspond to equal center-pipe and outer annulus cross-sectional area, and negligible feed and exit channel flow resistances. Consequently, one expects, a priori, that π-flow reactors will yield better profiles than Z-flow reactors.

The flow distribution superiority of the π-flow configuration has a simple physical interpretation. When frictional losses in the feed channel are low, pressure increases in the flow direction due to momentum loss. In the exit channel, the opposite is true. Thus in Z-flow a large radial pressure drop occurs at the exit end of the reactor, while a much smaller one occurs at the entrance end. This relatively large gradient in radial pressure drop is essentially what causes the flow maldistribution. In π-flow, however, due to the opposite flow of feed and product streams, pressure increases in the same direction in both channels and results in a more uniform pressure drop, and consequently, fluid distribution.

The effects of flow direction can be diagnosed likewise. Since the superiority of π-flow has already been established, we will only investigate the effects of flow direction for π-flow reactors. At near ideal distribution $a_2/a_1 \sim a_3/a_1 \to 0$. Thus, we can rewrite Eqn. (55) as

$$\bar{w}_1' \bar{w}_1'' + \varepsilon \, \bar{w}_1 \bar{w}_1' \pm \delta \, \bar{w}_1^2 = 0 \qquad (60)$$
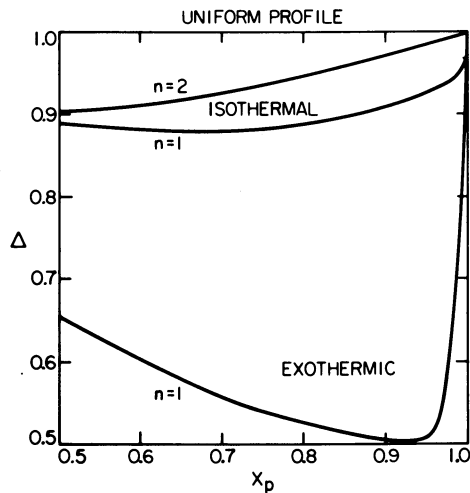
Figure 3.   Results of Ponzi and Kaye (8) for Δ vs. x_p assuming the radial profile is in the form of $\bar{v} = sy^{s-1}$ for first- and second-order isothermal reactions and first-order exothermic reaction (s = 2, γ = 2.4, β = 1)
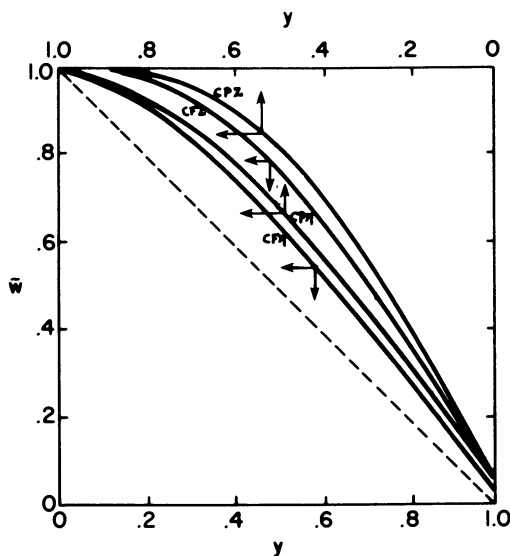
Figure 4.   Dimensionless velocity distribution for all four configurations at "standard" conditions

where $\varepsilon = a_2/a_1$ and $\delta = a_3/a_1$. In deriving Eqn. (60), we have unified the CRFR and CFRF equations by defining $z = 1 - z_{CF}$ for CFRF. Consequently, the plus and minus signs in front of δ in Eqn. (60) indicate CPRF and CFRF configurations, respectively; and the unified boundary conditions become, $\bar{w}_1(o) = 0$; $\bar{w}_1(1) = 1$. Expanding $\bar{w}_1$ in a series in ε and δ and substitute into Eqn. (60), one obtains

$$\bar{w} \sim z - \frac{z}{6} (z^2-1) \ (\varepsilon \pm \delta) \qquad (61)$$

where the positive and negative signs in front of δ correspond to CPRF and CFRF, respectively. For Eqn. (61), a perfectly uniform radial flow profile results in simply $\bar{w}_1 = z$. Thus the second term in Eqn. (61) actually represents the first order approximation of the deviation from uniformity. If both ε and δ are positive, one expects CFRF to yield a smaller deviation from uniformity than CPRF. Here $\delta = a_3/a_1$ is positive for all cases. However, ε is positive for $\xi < 1$. In summary, for $\varepsilon < 1$, i.e., viz. when the cross sectional area of the center pipe is smaller than that of the outer annulus, one expects CF-π to be the best flow configuration. For $\xi < 1$, on the other hand, CP-π is the superior configuration. Another interesting case occurs for $\xi > 1$. Since ε is negative in this case, the second term of Eqn. (61) can also be negative, which actually represents a negative deviation from perfectly uniform flow; i.e., a concave relationship between $\bar{w}_1$ and y, rather than convex.

The preceding analysis shows that certain general conclusions concerning flow distribution can be made using simple approximations. Eqn. (61) is especially useful as an analytical solution to the flow equations. However, perturbation techniques are only valid in regions where ε and δ are small. Outside this region, the conclusion stated above can be verified only with numerical techniques. A fourth-order (3,8) Runge-Kutta shooting technique was used to solve Eqns. (55) and (56). The "standard" set of parameters, derived in part from Genkin et al. (1,2), was chosen as a basis (see ref. (16)). Some of the results for these parameters and systematic variations thereof are summarized in Figure 4. Significant deviations from the ideal profile (represented by the dashed 45° line) are evident. In all the cases examined, the π-flow distribution was always closer to ideal than the corresponding Z-flow distribution (e.g., as shown in Figure 4). In addition, CFRF is superior to CPRF for $\xi < 1$ as predicted. The interesting concave behavior of the π-flow configuration for $\xi > 1.0$ is also witnessed in the numerical study. In conclusion, all the predictions derived from the perturbation analysis are substantiated by the results from numerical integration.

Cell Model Simulation

A two-dimensional cell model from an earlier publication (10) is utilized here to verify some of the results obtained from the analyses in the previous sections. This approach includes mixing in the fluid phase and interphase resistance to heat and mass transport. Consequently, it is a more sophisticated model than the models used in the preceding analyses. However, the equations must be solved numerically. The numerical techniques and the parameters used can be found in our previous works (10,16). Some typical two-dimensional particle temperature profiles are presented in Figures 5-7. The effect of flow maldistribution is evident in Figures 6 and 7. Both these cases were calculated for the same conditions except for the outer reactor radius, which was changed from the "standard" value of R_o = 0.12 m (Fig. 6) to R_o = 0.11 m (Fig. 7). This causes the distribution to become concave but closer to a perfect distribution. Thus for a very modest change in outer reactor radius, a significant improvement in exit temperature uniformity is achieved, in addition to increasing the overall conversion by 6.1% (see Table I). Of an even more dramatic nature is the improvement in fluid distribution and overall conversion caused by changing from CF-Z to CF-π flow as shown in Figure 5 and 6, respectively. For the same "standard" conditions, the change to π-flow increased overall conversion by 49.9% (See Table I). Total conversion results for various flow distributions are presented in Table I.

From the preceding analysis, the importance of radial flow distribution predicted in the previous section is substantiated. From the analysis for a perfect radial flow profile CPRF yields a higher conversion than CFRF for a highly exothermic, first order, irreversible reaction (see Fig. 2). This result is also evident in Case B of Table I. The isothermal cases, G and H, exhibit little dependence on flow direction, again confirming the results of the analysis. In general, flow maldistribution predominates and determines total conversion. However, for practically identical radial flow profiles for all flow configurations, the effects of flow direction become more evident.

The effect of axial flow in the catalyst bed is indicated in Cases I and J in Table I, where axial flow is shown to decrease conversion in all four reactor configurations. In fact, axial flow decreases conversion because it mixes fluid of different ages throughout the bed, introducing a backmixing effect. The magnitude of the axial velocity component is generally small relative to the radial component.

Conclusion

Generally, π-flow produces the most uniform radial profile at near perfect distribution or if the ratio of the area of the center pipe to outer annulus, ξ, is unity. If, however, $\xi \neq 1$, then
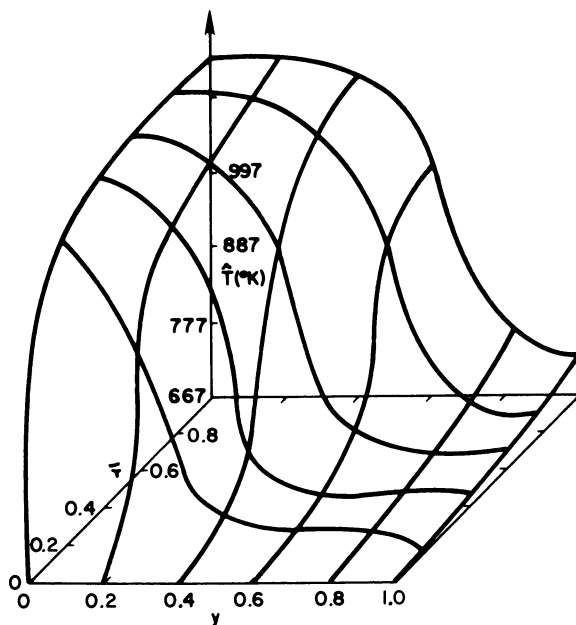
Figure 5.   Particle temperature profile in a CF-Z reactor operating at standard conditions
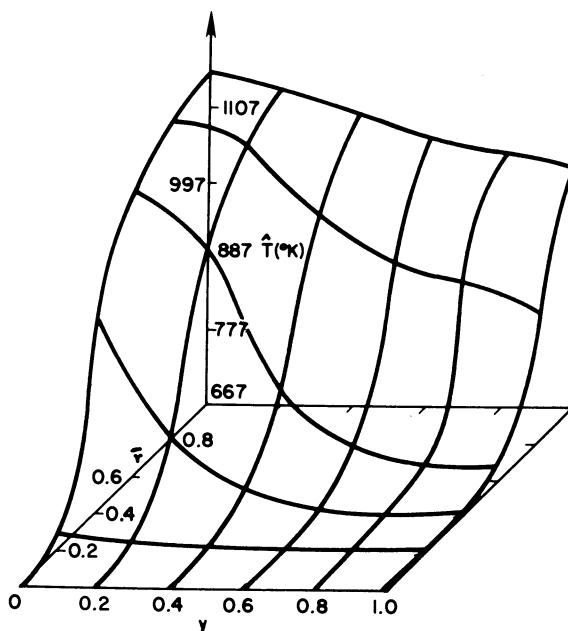
Figure 6.   Particle temperature profile in a CF-π reactor at standard conditions
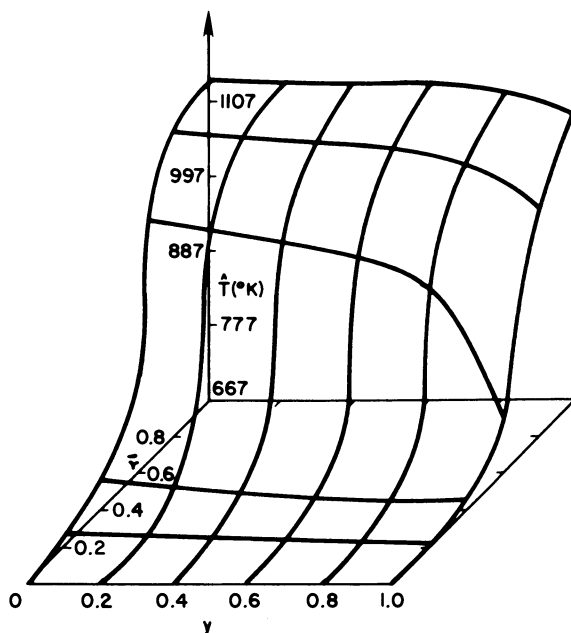
Figure 7.   Particle temperature profile in a CF-π reactor ($R_o = 0.11$ m)

TABLE I

Total Conversion, χ (%)

Parameter Values*	CF-π	CP-Z	CF-Z	CP-π
A. "Standard"	75.4	41.8	50.	72.6
B. Perfect distribution	82.8	88.8	82.8	88.8
C. $\ell = 0.9$	69.4	43.1	47.7	66.7
D. $R_o = 0.11$ m	80.0	35.0	37.4	89.1
E. $\phi_1 = 0.1$	75.4	41.3	50.1	72.6
F. $w_{o_{c_E}} = 2.54$ m/s	97.4	96.2	94.4	98.3
G. Isothermal (1111 K, $w_{o_{c_E}} = 2.54$ m/s)	99.3	98.8	98.9	99.2
H. Isothermal (667 K, $w_{o_{c_E}} = 2.54$ m/s)	14.9	12.6	13.9	14.4
I. $r_2 = 0.25$ m. $T_o = 583$ K	18.7	15.9	19.1	15.7
J. $r_2 = 0.25$, $T_o = 583$ K (without axial flow)	20.3	19.0	20.2	19.0

*All parameter values are "standard" except those designated.

CF-π is preferable for ξ<1 and CP-π is superior for ξ<1. When maldistribution is absent, the effects of flow direction become evident, and for highly exothermic, irreversible reaction, CPRF is preferred. Based on this argument, CP-π would be the best flow configuration since it gives the best profile and also enjoys the advantageous effects of flow direction for highly exothermic reactions. In any case, the effects of all the factors at a certain reaction condition can be determined from the analysis presented here.

Legend of Symbols

b*	friction factor in catalyst bed
B	dimensionless Heat of Reaction
c	dimensionless concentration
D	diffusivity
Da	Damkohler number
f	friction factor in the feed and outlet channels
ℓ	height of reactor
Le	Lewis number Pe_H/Pe_M
Pe	Peclet number
r	radial coordinate
r_1	inner radius of catalyst basket
r_2	outer radius of catalyst basket
R_o	outer radius of outer annulus
T_o, C_o	feed temperature and concentration
$\underline{v}$	dimensionless radial velocity
$\underline{w}$	dimensionless axial velocity
y	dimensionless catalyst bed dept
z	dimensionless axial coordinate, or strained y
θ	dimensionless temperature
ρ	aspect ratio r_1/r_2
ϕ	fractional free surface area of catalyst basket

Literature Cited

1. Dil'man, V.V.; Sergeer, S.P.; Genkin, V.S. <u>Teor. Osn. Khim. Tekhn</u> 1971, <u>5</u>, 564.
2. Genkin, V.S.; Dil'man, V.V.; Sergeev, S.P. <u>Int. Chem. Eng.</u> 1973, <u>13</u>, 24-8.
3. Kaye, L.A. AIChE 71st Annual Meeting, Paper No. 12E, Nov. 12-16, 1978, Miami Beach.
4. Raskin, A.Ya.; Sokolinskii, Yu. A.; Mukosei, V.I.; Aeror, M.E. <u>Teor. Osn. Khim. Tekhn.</u> 1968, <u>2</u>, 220.
5. Raskin, A. Ya.; Sokolinskii, Yu. A.; <u>Khim. Prom.</u> 1969, <u>45</u>, 520.
6. Hlavacek, V.; Kubicek, M. <u>Chem. Eng. Sci.</u> 1972, <u>27</u>, 177.
7. Dudukovic, M.P.; Lamba, H.S. 80th AIChE National Meeting, Paper No. 576, 1975, Boston.

8. Ponzi, P.R.; Kaye, L.A. AIChE J. 1979, 25, No. 1, 100.
9. Calo, J.M. "Chemical Reaction Engineering - Houston"; V.W. Weekman, Jr., and Dan Luss, ACS Symposium Series 65, Washington, D.C., 1979, pp. 550-61.
10. Chang, H.-C.; Calo, J.M. Proceedings of the 1978 Summer Computer Simulation Conference Newport Beach, July, 1978, p.272.
11. Carberry, J. "Chemical and Catalytic Reaction Engineering"; Ch. 3, McGraw-Hill, 1976.
12. Ray, W.H.; Marek, M.; Elnashaie, S. Chem. Eng. Sci. 1972, 27, 1527.
13. Syceva, A.M.; Abrosimov, B.Z.; Mel'nikov, S.M.; Fadeev, I.G. Int. Chem. Eng. 1970, 10, No. 1, 66.
14. Vanderveen, J.W.; Luss, D.; Amundson, N.R. AIChE J. 1968, 14, No. 4, 636-43.
15. Rhee, H.-K.; Foley, D.; Amundson, W.R. Chem. Eng. Sci. 1973, 28, No. 2, 607.
16. Chang, H.-C. Ph.D. Thesis, Princeton University.

Moving Bed Coal Gasifier Dynamics Using MOC and MOL Techniques

RICHARD STILLMAN

IBM Scientific Center, P.O. Box 10500, Palo Alto, CA 94304

The method of characteristics and both method of
lines techniques, continuous-time discrete-space and
continuous-space discrete-time, were used to solve
the system of hyperbolic partial differential
equations representing the dynamics of a moving bed
coal gasifier with countercurrent gas-solid heat
transfer. The adiabatic plug flow model considers
17 solids stream components, 10 gas stream compo-
nents and 17 reactions. The kinetic and thermody-
namic parameters were derived for a Wyoming subbitu-
minous coal. The inherent numerical stiffness of
the coupled gas-solids equations was handled by
assuming that the gas stream achieved steady state
values almost instantly. Calculated dynamic
responses are shown for step changes in reactor
pressure, blast temperature, steam flow rate, and
coal moisture. Both steady state convergent and
limit cycle responses were obtained.

The chemical industry is beginning to shift away from depen-
dence on natural gas and petroleum to the use of coal as the basis
for some of their hydrocarbon feed stocks. Examples can be found
in ammonia manufacture, methanol production, acetic anhydride
synthesis and synthetic gasoline production. Electric utilities
are also looking at coal for use in combined cycle and fuel cell
based power plants. A common first step in many of these plants
is the gasification of coal, and since gasifier operation can
impact the operation of other units in the plant, it is useful to
predict the dynamic behavior of a coal gasifier reactor using a
simulation model. The mathematical model can help to provide a
better understanding of the complex dynamic behavior exhibited by
the actual gasifier when subjected to simple and multiple distur-
bances. The extent of dynamic testing that can be performed on a
simulation model, as well as the type of information which can be

obtained, often goes much beyond that which would be allowable or even possible in a given commercial installation.

Some work has already been done on the simulation of transient behavior of moving bed coal gasifiers. However, the analysis is not based on the use of a truly dynamic model but instead uses a steady state gasifier model plus a pseudo steady state approximation. For this type of approach, the time response of the gasifier to reactor input changes appears as a continuous sequence of new steady states.

Yoon, Wei and Denn (1, 2, 3) consider the time response of a gasifier to small changes in operating conditions such as might occur during normal operation of the reactor. They regard the time required to reach a new steady state, following a step change in operating conditions, as the most useful measure of transient response. For small step changes, they estimate this response time, and the changes in reactor variables during a transient, using a psuedo steady state technique. Their technique involves removal of the time variable from the system of dynamic equations by assuming that the space origin moves at the same velocity as the velocity of the thermal wave for the maximum bed temperature. They give detailed calculated results for small step changes in coal feed rates for both ash discharge and slagging gasifiers.

The gasifier modeling technique used by Hsieh, Ahner and Quentin (4) is based on the construction of a data space representing steady state reactor conditions using the University of Delaware steady state model described in Yoon, Wei and Denn (1). They made an analysis of the chemical reaction rates and thermal capacitance effects to develop the dynamic algorithms used to simulate the dynamic trends between the steady state points. Their dynamic responses are thus estimated by using the quasi steady state data bank, a linear interpolation routine and the derived dynamic algorithms. No actual details of their model are given. However, they do show a short 9 minute gasifier transient response for exit gas composition and temperature resulting from a ramp decrease in steam, air and coal feed rates. Daniel (5) has used a simplified method to develop a short time scale transient model for a moving bed gasifier.

Wei (6) presents a very brief discussion of coal gasification reactor dynamics. He describes the transient response to a small step change as a soft transience in which the movement from one steady state to another one nearby takes place as a wave through a series of pseudo steady states. He points out that the hard transience of start up and major upset in reactor operation are not well understood. One of the purposes of this paper is to increase this understanding.

Although the pseudo steady state approximation provides a useful tool for estimating some aspects of gasifier dynamics, it does not provide the means to examine the full range of dynamic behavior that one would expect to find for a gasifier. Therefore, a different approach has been taken here in that a nonlinear

dynamic model representing moving bed gasifier dynamics is solved directly so that the global aspects of the dynamic behavior can be examined.

One further note, the University of Delaware gasifier model used in the pseudo steady state approximation assumes that the gas and solids temperatures are the same within the reactor. That assumption removes an important dynamic feedback effect between the countercurrent flowing gas and solids streams. This is particularly important when the burning zone moves up and down within the reactor in an oscillatory manner in response to a step change in operating conditions.

Process Description

A moving bed gasifier is a vertical reactor with countercurrent flowing gas and solids streams. Coal enters the top of the reactor and ash (and/or clinker or molten slag) is removed from the bottom. A mixture of steam and oxygen (or air) enters the bottom of the reactor and the raw product gas exits from the top.

An adiabatic steady state plug flow model has been developed by Stillman (7, 8) for this type of gasifier. For that model, the following sequence of physical and chemical events was assumed to take place in the reactor. Heat was extracted from the hot exiting gas by the entering solids stream so that the coal temperature was increased and the coal moisture was evaporated. A further increase in the coal temperature caused the coal volatile matter to be released, leaving a char. In the gasification zone, some of the char reacted with the carbon dioxide, water and hydrogen gas stream components. The oxygen in the feed gas burned all or almost all of the remaining char to provide the heat necessary to run this endothermic process. An ash residue was left from the combustion reaction. Some or all of this ash melted and then either solidified to form clinkers or else remained in a molten state, depending on the reactor operating conditions. The water gas shift reaction and the methanation reaction were also assumed to take place in the gas stream.

The model considered 17 components in the solids stream: water, hydrogen, nitrogen, oxygen, carbon, sulfur, ash, slag, clinker, water(vs), hydrogen(vs), carbon dioxide(vs), carbon monoxide(vs), methane(vs), hydrogen sulfide(vs), ammonia(vs), tar(vs),

where (vs) indicates a volatile solid component. The gas stream had 10 components:

water, hydrogen, nitrogen, oxygen, carbon dioxide, carbon monoxide, methane, hydrogen sulfide, ammonia, tar.

A set of 17 reactions was written to simulate the reactor events and they included 1 reaction for drying, 8 parallel reactions for devolatilization, 5 reactions for gasification and 3 reactions for combustion. The kinetic and thermodynamic parameters for these reactions were derived for a Wyoming subbituminous coal.

The same model description will be used as the basis for deriving the gasifier dynamic model. All of the kinetic and thermodynamic parameters will be taken from Stillman (7, 8).

Dynamic Model

The continuity equations for mass and energy will be used to derive the hyperbolic partial differential equation model for the simulation of moving bed coal gasifier dynamics. Plug flow (no axial dispersion) and adiabatic (no radial gradients) operation will be assumed.

The mass balance dynamic equations for the solids stream are given by

$$\frac{\partial C_jS}{\partial t} + \frac{\partial F_jS}{\partial z} = \sum_i a_{ij} \, r_i \qquad \begin{array}{l} i=1,2,\ldots,17 \\[4pt] j=1,2,\ldots,17 \end{array}$$

where C_jS is the concentration of solids component j and F_jS is the molar flux of solids component j defined as

$$F_jS \equiv C_jS \, u_S \qquad j=1,2,\ldots,17.$$

The a_{ij} values are the stoichiometric coefficients for component j in reaction i, r_i is the rate of reaction i, u_S is the local solids stream velocity, t is real time, and z is distance measured from the bottom of the reactor.

The corresponding mass balance dynamic equations for the countercurrent flowing gas stream are given by

$$\frac{\partial C_jG}{\partial t} - \frac{\partial F_jG}{\partial z} = \sum_i a_{ij} \, r_i \qquad \begin{array}{l} i=1,2,\ldots,17 \\[4pt] j=18,19,\ldots,27 \end{array}$$

where the molar flux of gas component j is defined as

$$F_jG \equiv C_jG \, u_G \qquad j=18,19,\ldots,27.$$

The energy balance dynamic equation for the solids stream is

$$\frac{\partial \phi S}{\partial t} + \frac{\partial \psi S}{\partial z} = h_{GS} \, A_{GS}(T_G - T_S) - \sum_i r_i \, \Delta H_i$$

$$i=1,2,\ldots,12,15,16,17$$

where the energy density and energy flux functions for the solids are defined by

$$\phi S \equiv c_{pS} \, C_S \, T_S$$

and

$$\psi S \equiv \phi S \ uS,$$

respectively. The solids absolute temperature is denoted by TS and cpS is the molar heat capacity of the solids.

On the right-hand side of the solids energy balance, the first term represents the gas-solids heat transfer, and the second term is the heat gain and loss from the solids reactions. Exothermic reactions have a negative heat of reaction and endothermic reactions have a positive heat of reaction. The local gas-solids heat transfer coefficient is indicated by hGS, AGS is the local gas-solids heat transfer area, TG is the gas stream absolute temperature, and ΔHi are the heats of reaction.

The corresponding gas stream energy balance dynamic equation is

$$\frac{\partial \phi G}{\partial t} - \frac{\partial \psi G}{\partial z} = -hGS \ AGS(TG - TS) - \sum_i ri \ \Delta Hi \qquad i=13,14$$

where the energy density and energy flux functions for the gas are

$$\phi G \equiv cpG \ CG \ TG$$

and

$$\psi G \equiv \phi G \ uG,$$

respectively.

Gas and solids equations of state, and a reactor pressure equation, are needed to complete the definition of the dynamic model. Pressure drop as a linear function of coal bed height is used for the gasifier pressure equation and the ideal gas law is used for the gas equation of state. The solids equation of state is expressed in terms of both the bulk and raw densities. These equations are given in Stillman (7, 8).

The required initial conditions for the dynamic model are the temperature and flux profiles of the gas and the solids streams down the entire length of the gasifier at time zero.

$$
\begin{array}{llll}
FjS(t,z) & j=1,2,\ldots,17 & t=0 & z=0,\ldots,L \\
FjG(t,z) & j=18,19,\ldots,27 & & \\
\psi S(t,z) & & & \\
\psi G(t,z) & & & \\
TS(t,z) & & & \\
TG(t,z). & & &
\end{array}
$$

The boundary conditions needed for the model are the input molar fluxes and the temperatures of the solids and gas feed streams, and the inlet gas pressure. At the top of the reactor:

$F_jS(t,z)$ $j=1,2,\ldots,17$ $t=t$ $z=L$
$TS(t,z)$.

At the bottom of the reactor:

$F_jG(t,z)$ $j=18,19,\ldots,27$ $t=t$ $z=0$
$TG(t,z)$
$P(t,z)$.

   This set of hyperbolic partial differential equations for the
gasifier dynamic model represents an open or split boundary-value
problem. Starting with the initial conditions within the reactor,
we can use some type of marching procedure to solve the equations
directly and to move the solution forward in time based on the
specified boundary conditions for the inlet gas and inlet solids
streams.
   However, it is important to note that there is an inherent
numerical stiffness in the coupled gas-solids equations because
the gas stream moves through the reactor much more rapidly than
the solids stream. In a typical example, while it only takes the
gas about 7 seconds to move through the reactor, it takes the
solids stream about a 1000 times longer.
   Typical ratios of gas velocity to solids velocity are about
400, 4200, 1200, at the top of the reactor, in the burning zone,
and at the bottom of the reactor, respectively. The solids and
gas velocities represent the two characteristic directions for our
hyperbolic system. If we plot these velocity curves on a reactor
length versus time graph, the characteristic curves for the gas
will be essentially horizontal in comparison to the solids stream
characteristic because of the large gas to solids velocity ratios.
   Making the assumption that the gas stream characteristic
curves are indeed horizontal for all practical purposes, is
equivalent to setting the time partial derivatives for the concen-
trations and the energy density equal to zero in the original
system of partial differential equations for the gas. Using this
approximation reduces the gas equations to a set of steady state
equations.
   Thus our final dynamic model for a moving bed coal gasifier
consists of a set of hyperbolic partial differential equations for
the solids stream coupled to a set of ordinary differential
equations for the gas stream. Shampine and Gear (9) caution that,
for systems containing elements with different time scales,
removing stiffness by changing the model may be risky because it
might be difficult to relate the solution of the modified model to
that of the original model. In our case, no such difficulty was
found.   The steady state conditions predicted by the modified
dynamic model were monitored by the steady state model (7, 8).

Distance Method of Lines

The distance method of lines (continuous-time discrete-space) technique is a straightforward way for obtaining the numerical solution of time dependent partial differential equations with one spatial variable. The original system of partial differential equations is transformed into a coupled system of time dependent ordinary differential equations by using spatial finite difference formulas to replace the spatial differentiation terms for a discrete set of spatial grid points. The number of ordinary differential equations produced by this operation is equal to the original number of partial differential equations multiplied by the number of grid points used. Thus, although we now have a larger number of equations to consider, usually the augmented system of ordinary differential equations is easier to solve numerically than the original smaller system of partial differential equations.

First order hyperbolic differential equations transmit discontinuities without dispersion or dissipation. Unfortunately, as Carver (10) and Carver and Hinds (11) point out, the use of spatial finite difference formulas introduces unwanted dispersion and spurious oscillation problems into the numerical solution of the differential equations. They suggest the use of upwind difference formulas as a way to diminish the oscillation problem. This follows directly from the concept of domain of influence. For hyperbolic systems, the domain of influence of a given variable is downstream from the point of reference, and therefore, a natural consequence is to use upstream difference formulas to estimate downstream conditions. When necessary, the unwanted dispersion problem can be reduced by using low order upwind difference formulas.

The Lagrange interpolation polynomial was used to develop the spatial finite difference formulas used for the distance method of lines calculation. For example, the two point polynomial for the solids flux variable $F(t,z)$ can be expressed by

$$F(t,z) = \left(\frac{z - z(k)}{z(k-1) - z(k)} \right) F(t,k-1) + \left(\frac{z - z(k-1)}{z(k) - z(k-1)} \right) F(t,k)$$

where k represents the grid point index number. The index number increases in value from top to bottom of the reactor. If we take the partial derivative of the two point polynomial with respect to z at index point k, we obtain

$$\frac{\partial F(t,z)}{\partial z} = \frac{F(t,k) - F(t,k-1)}{\Delta z}$$

which is the two point upwind formula for the solids stream. The local grid spacing is indicated by Δz.

In a similar fashion, more accurate higher order formulas can be developed. The four point upwind formula is

$$\frac{\partial F(t,z)}{\partial z} = \frac{11F(t,k) - 18F(t,k-1) + 9F(t,k-2) - 2F(t,k-3)}{6\Delta z}.$$

The four point upwind biased formula is given by

$$\frac{\partial F(t,z)}{\partial z} = \frac{2F(t,k+1) + 3F(t,k) - 6F(t,k-1) + F(t,k-2)}{6\Delta z}$$

and the four point downwind biased formula is

$$\frac{\partial F(t,z)}{\partial z} = \frac{-F(t,k+2) + 6F(t,k+1) - 3F(t,k) - 2F(t,k-1)}{6\Delta z}.$$

Different combinations of spatial finite difference formulas were tried to determine the best set for our system of equations. The two point upwind formula was found to be best for the solids component molar fluxes. The low order formula was used because most of the gasifier reactions turn off abruptly when a component disappears and this creates sharp discontinuities. Higher order formulas tend to flatten out discontinuities, and in some cases, this causes material balances to be lost which then leads to numerical instability problems. Maintaining component material balance is an important aid to preserving numerical stability in the calculations. The low order formulas minimized these difficulties.

The four point upwind biased formula worked best for the solids stream energy flux calculation. Some downstream information was useful because of the countercurrent flow of the gas and solids streams. To keep the same order, the four point downwind biased formula was used at the top of the reactor and the four point upwind formula was used at the bottom.

Accuracy and calculation time are highly dependent on the number of spatial grid points used. More grid points give better accuracy but calculation time increases accordingly. To resolve this dilemma, a variable grid structure was used in the calculations. In the top part of the reactor, where the drying and devolatilization reactions were taking place, a coarse grid was used. In the bottom part of the reactor, where the gasification and combustion reactions were occurring, a finer mesh was used. A total of 82 grid points was used for the method of lines calculations. With the variable grid structure, the top third of the reactor had 13 nodes, the middle third had 21 nodes, and the bottom third had 48 nodes.

Grid spacing has no effect on the use of the two point upwind formula but it does effect the use of the four point formula. Therefore, grid reduction was done in a prescribed manner. For any one change, the grid spacing could only be cut in half and the grid change had to remain in effect for at least 3 node points.

This restriction allowed the coefficients for the four point upwind biased formula to sequence through the following values for one grid spacing change

2.0	3.0	-6.0	1.0	full step size
3.2	-1.5	-2.0	0.3	half step size
2.25	2.0	-4.5	0.25	half step size
2.0	3.0	-6.0	1.0	half step size

which is then repeated for each succeeding change.

The variables needed in the dynamic model calculations are the solids molar and energy fluxes. However, in the distance method of lines technique, when we replace the spatial differential terms by finite difference formulas, the time derivative in the remaining differential equation is in terms of either component concentration or energy density, which we do not want. Therefore, the following change was made in the distance method of lines model. Replacing C_jS with its equivalent F_jS/uS and taking the partial derivative with respect to time gives

$$\frac{\partial}{\partial t}\left(\frac{F_jS}{uS}\right) = \frac{1}{uS}\frac{\partial F_jS}{\partial t} - \frac{F_jS}{uS\,uS}\frac{\partial uS}{\partial t} \quad .$$

Neglecting the acceleration term, we have the approximation

$$\frac{\partial C_jS}{\partial t} \simeq \frac{1}{uS}\frac{\partial F_jS}{\partial t}$$

which gives us the desired flux variable in the model. A similar change was used to convert from energy density to energy flux.

Time Method of Lines

The time method of lines (continuous-space discrete-time) technique is a hybrid computer method for solving partial differential equations. However, in its standard form, the method gives poor results when calculating transient responses for hyperbolic equations. Modifications to the technique, such as the method of decomposition (12), the method of directional differences (13), and the method of characteristics (14) have been used to correct this problem on a hybrid computer. To make a comparison with the distance method of lines and the method of characteristics results, the technique was used by us in its standard form on a digital computer.

The original system of partial differential equations is transformed into a system of ordinary differential equations by replacing the time differential terms with time finite difference formulas. The number of equations in the new system is the same as the original number of equations. However, it is necessary to store intermediate results at spatial nodes for both current and previous time increments.

The Lagrange interpolation polynomial was again used to develop the finite difference formulas. To avoid additional iterations, only upwind differences were used. The two point upwind formula for the solids stream concentration variable at any location z within the reactor for time t is given by

$$\frac{\partial C(t,z)}{\partial t} = \frac{C(t,z) - C(t-1,z)}{\Delta t}$$

where Δt is the time increment. The three point upwind formula is

$$\frac{\partial C(t,z)}{\partial t} = \frac{3C(t,z) - 4C(t-1,z) + C(t-2,z)}{2\Delta t}$$

and the four point upwind formula is

$$\frac{\partial C(t,z)}{\partial t} = \frac{11C(t,z) - 18C(t-1,z) + 9C(t-2,z) - 2C(t-3,z)}{6\Delta t}.$$

The same 82 point variable grid structure was used in the time method of lines calculations as was used for the distance method of lines calculations. Also, the three and four point upwind formulas were found to attenuate the calculated step responses too much and they were discarded.

Method of Characteristics

The method of characteristics (15) is a natural way for solving hyperbolic partial differential equations. The technique is based on locating the characteristic propagation paths or directions for the partial differential equations and integrating the resulting ordinary differential equations along these directions. Thus, as with the method of lines, this technique transforms our problem from solving partial differential equations to solving ordinary differential equations.

For the gasifier dynamic model, the characteristic directions are given by the solids and gas stream velocities:

$$\frac{dz}{dt} = uS \qquad + \text{direction}$$

$$\frac{dz}{dt} = -uG \qquad - \text{direction.}$$

These two families of curves cross each other at a number of common nodes. However, the assumption was made earlier that only the steady state equations would be used for the gas stream calculations. Therefore, we only need to consider the application of the method of characteristics to the solids stream partial differential equations.

To use the technique for our system of equations, we first make the assumption that the solids stream velocity is piecewise constant for very small axial sections of the reactor, i.e., for the local integration step. The solids velocity still varies significantly within the gasifier, but its change is assumed piecewise rather than continuous.

If this is done, then the solids stream energy balance dynamic equations can be rewritten as

$$\frac{1}{uS}\frac{\partial \psi S}{\partial t} + \frac{\partial \psi S}{\partial z} = RHS$$

where RHS is the right-hand side of the original equation. Since solids velocity has been assumed piecewise constant, the total differential for the energy flux is given by

$$dt\frac{\partial \psi S}{\partial t} + dz\frac{\partial \psi S}{\partial z} = d\psi S.$$

Putting the above two equations into vector-matrix notation,

$$\begin{bmatrix} \dfrac{1}{uS} & 1 \\ dt & dz \end{bmatrix} \begin{bmatrix} \dfrac{\partial \psi S}{\partial t} \\ \dfrac{\partial \psi S}{\partial z} \end{bmatrix} = \begin{bmatrix} RHS \\ d\psi S \end{bmatrix}$$

we have a system of simultaneous linear algebraic equations in terms of the first partial derivatives. The characteristic solution for these equations is obtained when the determinant of the matrix vanishes. From linear equation theory, the determinant must then also vanish when the column vector on the right-hand side of the vector-matrix equation is substituted for either of the columns in the matrix on the left.

Substituting for the second column and setting the determinant to zero gives

$$\frac{1}{uS}\frac{d\psi S}{dt} = RHS.$$

Likewise, substituting for the first column gives

$$\frac{d\psi S}{dz} = RHS.$$

Both of these equations are ordinary differential equations for the energy flux along the solids velocity characteristic curve. Either one can be used, but we chose to implement the second

equation for our method of characteristics dynamic model. A
similar derivation can be done to develop the corresponding solids
stream mass balance equations.

The integration of these equations is carried out for fixed
time slices along the various characteristic curves within the
reactor. Since the solids velocity varies down the reactor, this
fixed time slicing gives the effect of a variable grid structure
with a variable number of nodes. The location of the last node is
determined by the bottom of the reactor rather than by the time
slice. At any given time during a transient response calculation,
nodes can be either added or subtracted to handle the changing
conditions within the reactor.

A time slice of 1.5 minutes was used for most of the method
of characteristics calculations. This time slice gave a total of
79 nodes for the base case initial condition steady state. With
the variable solids velocity, the top third of the reactor had 13
nodes, the middle third had 15 nodes, and the bottom third had 51
nodes. This is very similar to the variable grid structure used
in the method of lines calculations.

Numerical Considerations

As the gas and solids streams move through the gasifier,
different reactions are slowly starting and abruptly stopping as
components disappear at different locations in the various zones.
While some reactions are proceeding vigorously, other reactions
are just starting at very low rates. Extremely steep axial
temperature and molar flux gradients are present in the burning
zone area. Also, the zone locations are continually shifting up
and down the reactor during a transient period. Thus , we would
expect the gasifier differential equations to exhibit a high
degree of numerical stiffness.

To examine the extent of this problem, an eigenvalue analysis
was done for many different reactor transient and steady state
time profiles. The range of stiffness ratios (absolute value of
ratio of largest to smallest eigenvalue, real parts only) observed
for the different reactor zones was as follows:

drying zone	10E5 – 10E10
devolatilization zone	10E2 – 10E8
gasification zone	10E1 – 10E4
burning zone	10E2 – 10E9
ash zone	10E0 – 10E1.

This indicates that the equations are extremely stiff with a
constantly changing stiffness ratio throughout the reactor. Thus,
the equations might be very stiff for a time, then moderately
stiff for a while and then mildly stiff at various other locations
within the reactor.

The eigenvalue mix was found to be very similar for all of

the profiles. On the average, 36.54% of the eigenvalues were negative real, 3.26% were positive real, 1.39% were negative complex, 0.16% were positive complex and the remaining 58.65% were zero. Also, the full Jacobian was singular at all locations within the reactor. With the presence of positive real eigenvalues and positive and negative complex eigenvalues, we would hope to find a few oscillatory transient responses, and indeed, some limit cycle responses were obtained. The ratio of the imaginary to the real part of the positive complex eigenvalue seemed to be the deciding factor between steady state convergent or limit cycle responses. This ratio was never observed to go above about 5 for the steady state results, but it went as high as 22 for the limit cycle runs.

Stiffness is not a problem for the transient part of the calculations since in the transient region integration step size is limited by accuracy rather than by stability (9). Nonstiff integration codes would be expected to perform better than stiff codes in this case. For the time method of lines and the method of characteristics, the differential equations are numerically in a transient state for the integration code even though the reactor is in a steady state condition. This is due to the reactions turning on and off at various locations as the integration proceeds along the reactor.

However, for the distance method of lines technique where integration is done at fixed distance nodes, stiffness could be a problem as we approach steady state conditions. Jacobian based stiff codes can not handle the integration in its present form because the Jacobian is always singular. In many sections of the reactor, the number of active differential equations is continually increasing or decreasing. Codes based on variable order multistep methods are very inefficient under these conditions because they must be restarted whenever a change occurs. This means that we would be using higher order code for some parts of the reactor and lower order code in the more rapidly changing sections. A fixed higher order method would probably be better. Also, for multistep methods, the integrator work- space has to be saved for each of the nodes.

Another possibility would be to use a multirate code which integrates each differential equation individually using different step sizes. Orailoglu (16) and Gear (17) discuss this approach but their procedure uses multistep Jacobian methods which are not efficient for our system of equations. What we need is a fixed order single step multirate method.

We finally decided to solve the problem by using a simple sifting procedure similar to the one used by Emanuel and Vale (18). Before the integrator was called, the derivatives were determined for the solids stream molar flux equations. Any flux equation that had a derivative below the value of the sift parameter was considered to be inactive at that time. The energy flux equation was always considered active. Only the active equations

were then integrated for the given time step. This procedure was repeated for each node at each integrator time step. In this way the stiffness ratio could be reduced to less than 100 in the drying zone, less than 10 in the devolatilization zone and to about 1 in the gasification, burning, and ash zones, while still maintaining calculated results very close to those obtained for unsifted runs.

Various integration methods were tested on the dynamic model equations. They included an implicit iterative multistep method, an implicit Euler/modified Euler method, an implicit midpoint averaging method, and a modified divided difference form of the variable-order/variable-step Adams PECE formulas with local extrapolation. However, the best integrator for our system of equations turned out to be the variable-step fifth-order Runge-Kutta-Fehlberg method. This explicit method was used for all of the calculations presented here.

The initial conditions within the reactor needed to start the dynamic model calculations were established by using the steady state model (7, 8) to calculate a first estimate. This estimate was adjusted for use with the distance method of lines, time method of lines, and method of characteristics programs by running the individual programs to a steady state condition without changing input conditions.

The dynamic model calculations are done in a two phase process. In the first phase, the solids stream dynamic equations are integrated for the reactor while keeping gas stream conditions constant. When necessary, intermediate gas stream values are obtained by interpolation between storage nodes. These calculations proceed down the reactor for the distance and time method of lines, and back up the reactor for the method of characteristics. In the second phase, the gas stream steady state equations are integrated from the bottom to the top of the reactor while keeping the solids stream conditions constant. Intermediate solids stream values are obtained by interpolation between storage nodes.

The numerical stability requirement for the coupling of the gas-solids calculations in the distance method of lines model was estimated to be

$$uS \ \Delta t/\Delta z \leq 0.028.$$

This establishes the upper limit on the solids stream integration time step size for any specified grid spacing. Likewise, for the time method of lines model, the stability requirement was estimated as

$$uS \ \Delta t/\Delta z \geq 1.67$$

which sets the time grid size based on the specified storage node spacing.

An IBM 370/158 computer was used for all of the calculations. As would be expected, the calculation speed was different for each of the three dynamic models. The distance method of lines model ran at a speed of 0.23 times real time (4.3 times slower than real time) which was very slow. For short time transient calculations, the speed could be increased to real time speed, but long term numerical stability required the slower speed. The time method of lines model ran 3.92 times faster than real time. However, the calculated transient responses were incorrect and the model could not be used for that purpose. For a time slice of 1.5 minutes, the method of characteristics model ran 1.56 times faster than real time. If the time slice was increased to 5.0 minutes (fewer nodes), the speed increased to 4.75 times real time but the gas stream accuracy was reduced. Therefore, the 1.5 minute time slice was used for the calculations shown here.

Simulation Results

Based on the dynamic model presented in the previous sections, three computer programs were written to simulate moving bed gasifier dynamics using the method of characteristics and both method of lines techniques. Table I lists the ash (Lurgi) gasifier operating data for the base case initial conditions. Except for the multiple steady state runs, all of the step change response calculations were made using these initial condition values. The proximate, ultimate and simulation model analysis of the Roland seam subbituminous coal used in the calculations are given in Stillman (7).

Figure 1 shows the exit gas temperature time response to a step change in coal moisture from 34.67 to 27.00 wt % for the three dynamic models. This is a large step change involving a solids material wave moving through the reactor and it was intended to provide a severe test for the three methods.

The upper curve was calculated by the method of characteristics program and it exhibits a true limit cycle or sustained oscillation response (19). The middle curve was calculated by the distance method of lines program. The response is attenuated and stretched out. The final long term oscillations had random unequal periods and they were out of phase with the MOC results. The lower curve was calculated by the time method of lines program. The initial part of the response is similar to the DMOL results but then the temperature incorrectly levels out to a steady state condition. Thus, it was evident that the distance and time method of lines techniques were not as accurate as the method of characteristics procedure for calculating the gasifier step responses and they were discarded.

All of the remaining calculations were done by the MOC program. The solids temperature at the 0.3 m (1 ft) level will be used to display the step change responses. That location was chosen because it is initially slightly above the burning zone

Table I.   Base Operating Data for Ash Discharge (Lurgi) Reactor

Reactor Bed Height	2.74 m (9.00 ft)
Reactor Internal Diameter	3.70 m (12.14 ft)
Exit Gas Pressure	2.84 MPa (28.0 atm)
Dry Coal Feed Rate	2067.7 kg/h-m-m (423.5 lb/h-ft-ft)
Coal Moisture Content	34.67 wt %
Dry Coal/Oxygen Ratio	2.80 wt/wt
Steam/Oxygen Ratio	8.20 mol/mol
Inlet Coal Temperature	78.0 °C (172.4 °F)
Inlet Gas Temperature	360.6 °C (681.0 °F)
Exit Gas Temperature	275.6 °C (528.1 °F)
Exit Solids Temperature	372.8 °C (703.0 °F)
Solids T at 0.3 m (1 ft)	912.6 °C (1674.6 °F)

Dry Exit Gas mol %	
Hydrogen	40.83
Carbon Dioxide	31.47
Carbon Monoxide	14.53
Methane	10.88
Nitrogen, Ammonia,	2.29
Hydrogen Sulfide, Tar	
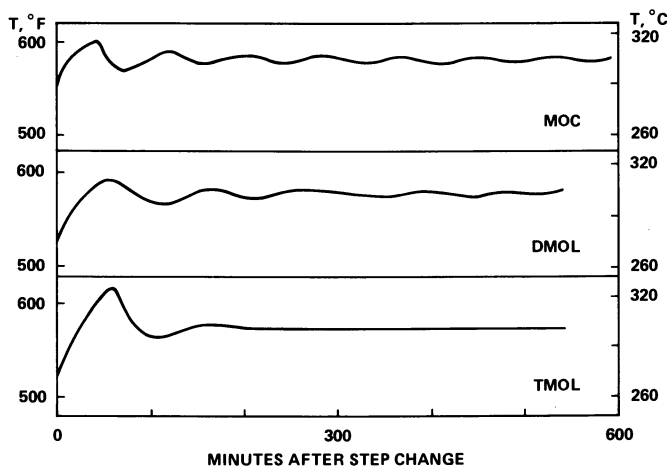
Figure 1.   Exit gas temperature response, coal moisture reduced to 27.00 wt %

where large temperature fluctuations can occur when the burning zone shifts back and forth in the reactor.

Inlet Gas Temperature. A few step response runs were made for changes in inlet gas (blast) temperature. Only steady state convergent responses were observed and the final results are summarized in Table II. Figure 2 shows the solids temperature response when the inlet gas temperature is reduced from 360.6 $\circ$C (681.0 $\circ$F) to 305.0 $\circ$C (581.0 $\circ$F). This change puts less heat into the reactor which slows down the reactions in the gasifier above the burning zone. This causes the burning zone to shift down the reactor a short distance producing the rapid temperature drop exhibited in Figure 2.

Figure 3 shows the response when the inlet gas temperature is increased to 416.1 $\circ$C (781.0 $\circ$F). Since more heat is available in the gasifier, the reaction rates are increased, the burning zone shifts slowly up the reactor a short distance, and the solids temperature at the 0.3 m (1 ft) level gradually increases as the burning zone moves a little closer.

Coal Moisture. The results for changes in coal moisture content are given in Tables III, IV and V, and Figures 4 and 5. In addition to steady state convergent results, we now have underdamped (decaying oscillation) and limit cycle responses. Figure 4 shows the solids temperature response when the inlet coal moisture is reduced from 34.67 to 32.91 wt %. There is a 66 minute delay in the response which represents the transport time for the solids stream wave to reach the 0.3 m (1 ft) level. As the burning zone begins to shift up the reactor, the solids temperature peaks and starts back down during the next 50 minutes which is the time it takes the solids wave to move out of the gasifier. The solids temperature oscillates a few more times as the location of the burning zone shifts up and down before settling out to a steady state position slightly above its initial location.

The underdamped steady state results for reducing the coal moisture content to 31.05 wt % are given in the third data column of Table III. The solids temperature response starts out similar to the Figure 4 results except the temperature rises to a higher peak value of 1133 $\circ$C (2072 $\circ$F). Starting with an amplitude of about 50 $\circ$C (90 $\circ$F), the temperature response then oscillates in a decaying manner for the next 2300 minutes until it reaches a final steady state value. The final location of the maximum solids temperature is slightly below the 0.3 m (1 ft) level.

The limit cycle response caused by decreasing the coal moisture content to 27.00 wt % is shown in Figure 5. Again there is a steep solids temperature rise as the solids material wave reaches the 0.3 m (1 ft) level, but in this case, the decaying temperature oscillations only last about 200 minutes before the gasifier settles into a sustained oscillation mode with an esti-

Table II.   Inlet Gas Temperature, Final Steady State Results

Inlet Gas Temperature	°C	305.0	388.3	416.1
	°F	581.0	731.0	781.0
Exit Gas Temperature	°C	269.4	276.7	277.6
	°F	517.0	530.0	531.7
Exit Solids Temperature	°C	330.9	398.1	424.3
	°F	627.7	748.6	795.7
Solids T at 0.3 m (1 ft)	°C	778.7	951.4	986.4
	°F	1433.6	1744.6	1807.5
Dry Exit Gas	mol %			
Hydrogen		40.92	40.82	40.82
Carbon Dioxide		32.08	31.45	31.43
Carbon Monoxide		13.83	14.56	14.59
Methane		10.88	10.88	10.87
Nitrogen, Ammonia,		2.29	2.29	2.29
Hydrogen Sulfide, Tar				
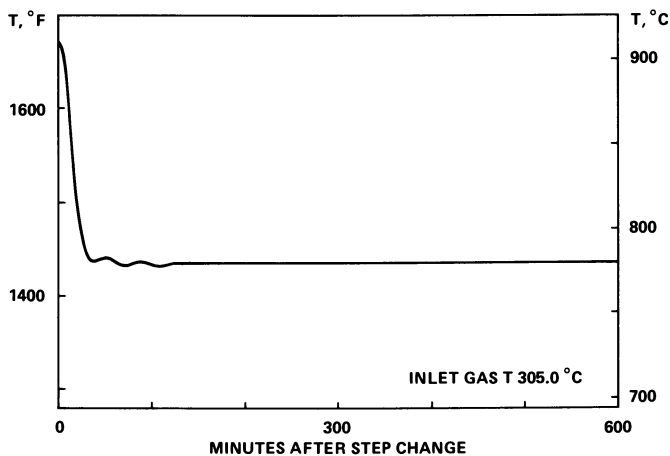
Figure 2.   Solids temperature at 0.3 m, inlet gas temperature reduced to 305.0°C
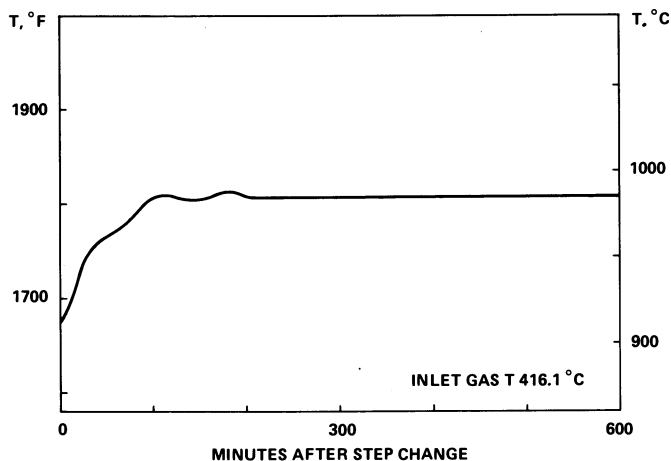
Figure 3.   Solids temperature at 0.3 m, inlet gas temperature increased to 416.1°C

Table III.   Coal Moisture Change, Final Steady State Results

Coal Moisture	wt %	33.80	32.91	31.05
Exit Gas Temperature	°C	276.0	281.2	290.4
	°F	528.8	538.1	554.8
Exit Solids Temperature	°C	375.1	372.1	368.1
	°F	707.1	701.7	694.6
Solids T at 0.3 m (1 ft)	°C	838.6	928.5	1112.9
	°F	1541.5	1703.3	2035.2
Dry Exit Gas	mol %			
Hydrogen		41.06	41.08	41.11
Carbon Dioxide		31.91	31.95	32.02
Carbon Monoxide		13.85	13.79	13.69
Methane		10.90	10.90	10.90
Nitrogen, Ammonia,		2.28	2.28	2.28
Hydrogen Sulfide, Tar				

Table IV.   Coal Moisture 30.08 wt %, Limit Cycle Results

		Max	Min
Exit Gas Temperature	°C	297.4	291.7
	°F	567.3	557.1
Exit Solids Temperature	°C	367.3	366.4
	°F	693.1	691.6
Solids T at 0.3 m (1 ft)	°C	1126.1	1070.4
	°F	2058.9	1958.8
Dry Exit Gas	mol %		
Hydrogen		41.00	41.22
Carbon Dioxide		31.78	32.27
Carbon Monoxide		14.06	13.31
Methane		10.88	10.92
Nitrogen, Ammonia,		2.28	2.28
Hydrogen Sulfide, Tar			

Estimated Limit Cycle Period 81.4 minutes

Table V.   Coal Moisture 27.00 wt %, Limit Cycle Results

		Max	Min
Exit Gas Temperature	°C	306.9	303.3
	°F	584.4	577.9
Exit Solids Temperature	°C	367.2	366.6
	°F	693.0	691.9
Solids T at 0.3 m (1 ft)	°C	1123.6	1095.8
	°F	2054.5	2004.5
Dry Exit Gas	mol %		
Hydrogen		41.25	41.36
Carbon Dioxide		32.30	32.57
Carbon Monoxide		13.27	12.86
Methane		10.91	10.94
Nitrogen, Ammonia,		2.27	2.27
Hydrogen Sulfide, Tar			

Estimated Limit Cycle Period 82.8 minutes
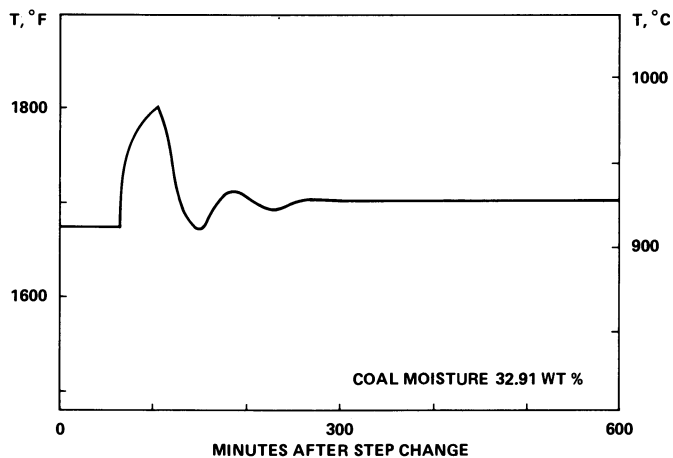
Figure 4. Solids temperature at 0.3 m, coal moisture reduced to 32.91 wt %
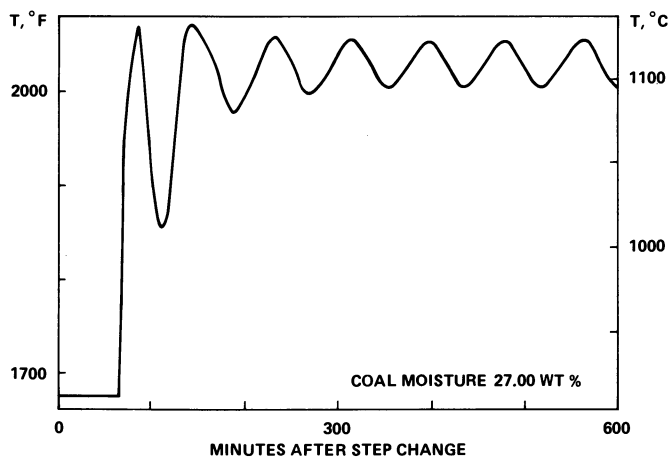
Figure 5. Solids temperature at 0.3 m, coal moisture reduced to 27.00 wt %

mated period of 82.8 minutes. The location of the solids peak burning zone temperature moves up and down in rhythm with the oscillations but always remains slightly above the 0.3 m (1 ft) level. The decaying type response means that the limit cycle surface, which encloses an equilibrium or steady state point, was approached from the outside direction.

Steam Flow. The steam/oxygen feed ratio is an important variable for controlling the gas and solids temperatures in the burning zone and changing this ratio has a significant effect on gasifier operation. The simulation results for steam flow rate step changes are given in Tables VI-X and Figures 6, 7 and 8. Besides having steady state convergent, underdamped steady state, and limit cycle responses, we also have an underdamped limit cycle response.

Figure 6 shows the steady state convergent results for reducing the steam flow rate by 1.875%. Since the oxygen flow rate remains constant at its initial value, this step change reduces the steam/oxygen molar ratio from 8.20 to 8.05. The response shows a small almost linear temperature rise for about 40 minutes, and then a heavily damped oscillatory drop to the final steady state condition. Even though reducing the steam flow rate raises the gas peak temperature, the increase in this run is not enough to overcome the effect of the reduced gas stream flow which puts less heat into the upper part of the reactor. This shifts the burning zone down the reactor and causes the final solids temperature at the 0.3 m (1 ft) level to drop by about 41 °C (74 °F).

The underdamped steady state results for a 2.25% decrease in steam feed rate are given in the third data column of Table VI. This step change reduces the steam/oxygen molar ratio to 8.02. The underdamped response starts out very similar to the Figure 6 results and appears to be headed for a steady state condition. However, beginning at about the 305 minute point, the burning zone begins to move back up the reactor. Thus, during the period of 305 to 365 minutes, the solids temperature at the 0.3 m (1 ft) level rises from 868 °C (1594 °F) to 962 °C (1763 °F). The response then settles back into a decaying oscillation mode until steady state conditions are reached 445 minutes later.

The underdamped limit cycle results for a 2.50% decrease in steam feed rate (8.00 steam/oxygen molar ratio) are given in Table VII. Once again, the response starts out like the Figure 6 response but then goes into a decaying limit cycle mode. However again, beginning at about the 340 minute point, the burning zone shifts back up the reactor. During the next 60 minutes, the solids temperature at the 0.3 m (1 ft) level goes from 860 °C (1580 °F) to 956 °C (1752 °F). The response then returns to the decaying limit cycle mode for the next 935 minutes until a very small stable limit cycle is reached.

The limit cycle responses for a 5.0% decrease and a 5.0%

Table VI.   Steam Feed Change, Final Steady State Results

Steam Feed Rate Change	%	-1.25	-1.875	-2.25
Exit Gas Temperature	°C	273.2	271.9	271.3
	°F	523.8	521.5	520.3
Exit Solids Temperature	°C	374.1	374.8	372.4
	°F	705.3	706.7	702.4
Solids T at 0.3 m (1 ft)	°C	886.9	872.3	952.3
	°F	1628.5	1602.1	1746.2
Dry Exit Gas	mol %			
Hydrogen		40.66	40.58	40.53
Carbon Dioxide		31.36	31.31	31.28
Carbon Monoxide		14.74	14.84	14.90
Methane		10.94	10.97	10.99
Nitrogen, Ammonia, Hydrogen Sulfide, Tar		2.30	2.30	2.30

Table VII.   Steam Feed Rate Change -2.5%, Limit Cycle Results

		Max	Min
Exit Gas Temperature	°C	271.0	270.8
	°F	519.9	519.5
Exit Solids Temperature	°C	372.8	372.7
	°F	703.0	702.8
Solids T at 0.3 m (1 ft)	°C	948.8	945.6
	°F	1739.8	1734.1
Dry Exit Gas	mol %		
Hydrogen		40.50	40.51
Carbon Dioxide		31.24	31.27
Carbon Monoxide		14.96	14.92
Methane		11.00	11.00
Nitrogen, Ammonia, Hydrogen Sulfide, Tar		2.30	2.30

Estimated Limit Cycle Period 82.0 minutes

Table VIII.   Steam Feed Rate Change -3.75%, Limit Cycle Results

		Max	Min
Exit Gas Temperature	°C	273.5	267.7
	°F	524.3	513.8
Exit Solids Temperature	°C	375.2	372.6
	°F	707.3	702.6
Solids T at 0.3 m (1 ft)	°C	977.8	889.4
	°F	1792.1	1632.9
Dry Exit Gas	mol %		
Hydrogen		40.15	40.53
Carbon Dioxide		30.76	31.62
Carbon Monoxide		15.74	14.47
Methane		11.03	11.08
Nitrogen, Ammonia,		2.32	2.30
Hydrogen Sulfide, Tar			

Estimated Limit Cycle Period 82.6 minutes

Table IX.   Steam Feed Rate Change -5.0%, Limit Cycle Results

		Max	Min
Exit Gas Temperature	°C	271.7	265.2
	°F	521.1	509.3
Exit Solids Temperature	°C	376.8	373.6
	°F	710.2	704.4
Solids T at 0.3 m (1 ft)	°C	958.7	860.1
	°F	1757.6	1580.2
Dry Exit Gas	mol %		
Hydrogen		39.92	40.37
Carbon Dioxide		30.52	31.53
Carbon Monoxide		16.15	14.64
Methane		11.08	11.15
Nitrogen, Ammonia,		2.33	2.31
Hydrogen Sulfide, Tar			

Estimated Limit Cycle Period 82.5 minutes

Table X.   Steam Feed Rate Change +5.0%, Limit Cycle Results

		Max	Min
Exit Gas Temperature	°C	279.8	275.3
	°F	535.7	527.6
Exit Solids Temperature	°C	374.7	372.9
	°F	706.5	703.3
Solids T at 0.3 m (1 ft)	°C	844.5	802.6
	°F	1552.1	1476.7
Dry Exit Gas	mol %		
Hydrogen		41.46	41.66
Carbon Dioxide		31.93	32.34
Carbon Monoxide		13.68	13.05
Methane		10.66	10.69
Nitrogen, Ammonia,		2.27	2.26
Hydrogen Sulfide, Tar			

Estimated Limit Cycle Period 83.5 minutes
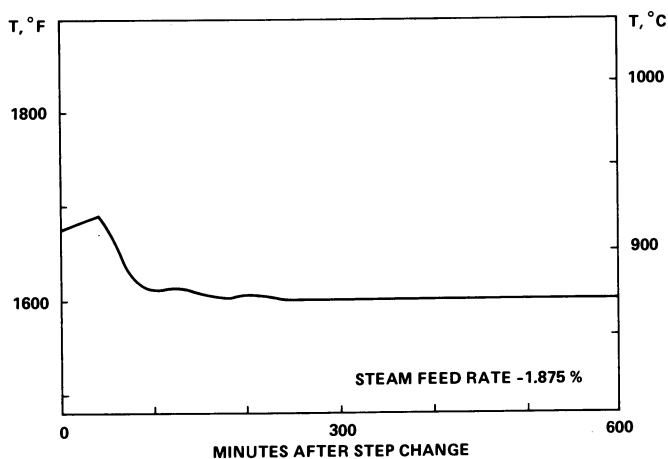
Figure 6.   Solids temperature at 0.3 m, steam feed rate reduced 1.875 %
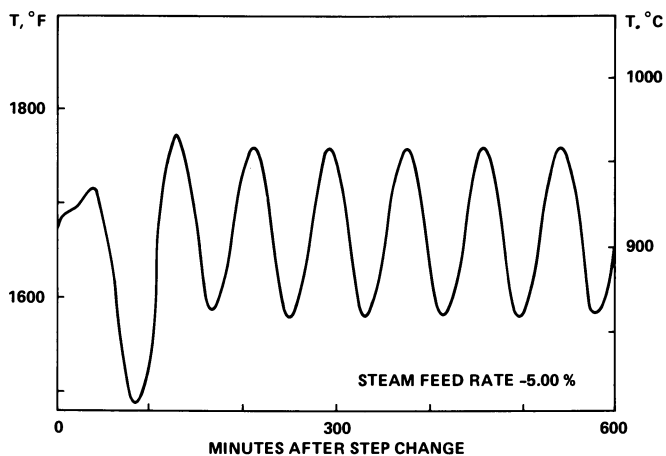
Figure 7.   *Solids temperature at 0.3 m, steam feed rate reduced 5.0 %*
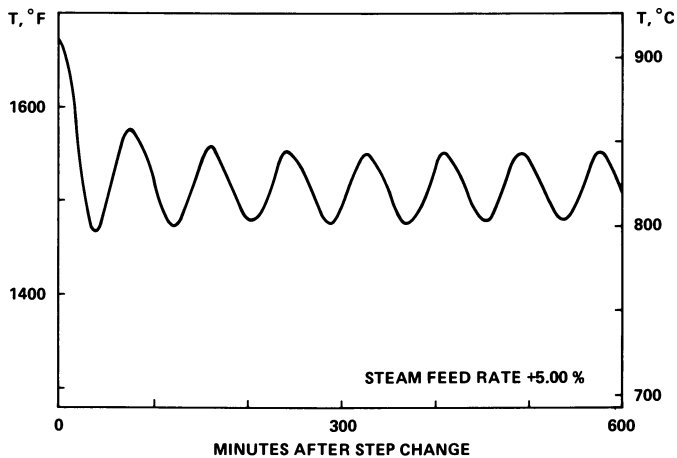
Figure 8.   *Solids temperature at 0.3 m, steam feed rate increased 5.0 %*

increase in steam feed flow rate are given in Figures 7 and 8. For these runs, the steam/oxygen molar ratios are 7.79 and 8.61, respectively. Both of the curves show a classic decaying limit cycle form which indicates that the limit cycle surface was approached from the outside.

Exit Gas Pressure. Gasifier pressure has an important effect on the composition of the exit raw gas and on the operation of the reactor. At normal operating pressure, increases in reactor pressure increase the methane and carbon dioxide content of the raw gas and decrease the hydrogen and carbon monoxide content. Decreases in pressure have the opposite effect. The reactor pressure step change results are given in Figures 9 and 10, and Tables XI, XII and XIII.

Figure 9 shows the steady state convergent results for reducing the exit gas pressure from 2.84 MPa (28 atm) to 2.53 MPa (25 atm). The pressure decrease lowers the gas density but increases the gas velocity since the molar feed rate of the inlet gas remains constant. This puts less heat into the reactor which lowers the exit gas temperature and causes the burning zone to shift down the reactor a short distance. This is reflected in the Figure 9 solids temperature response which starts out with a short false temperature rise but then exhibits a rapid temperature drop to a final steady state condition (non-minimum phase response).

Figure 10 shows the limit cycle response produced when the exit gas pressure is increased to 3.45 MPa (34 atm). This change decreases the gas velocity and shifts the burning zone up the reactor a short distance where, in this case, it oscillates up and down with a period of about 82.6 minutes. In Figure 10, the solids temperature response at the 0.3 m (1 ft) level begins with a short false temperature drop and then quickly rises and goes into an expanding oscillation mode before settling into a stable limit cycle response. The expanding oscillations indicate that the limit cycle surface was approached from the inside. The Table XII calculation had a more pronounced expanding oscillation phase as it took 846 minutes to reach a stable limit cycle response.

No experimental gasifier data was found to verify any of the simulation model results. However, limit cycle responses have been experimentally observed for the pressure in combustion chambers and boilers (20). This lends credence to our calculated results since coal combustion is an important factor in gasifier operation.

Multiple Steady States. Not only can the nonlinearity of our dynamic model equations produce limit cycle responses, it can give rise to multiple steady state conditions in which the same set of operating parameters can produce different reactor profiles. By accident, three of these multiple steady state responses were obtained and they are summarized in Table XIV.

To check the validity of the pressure step change results,
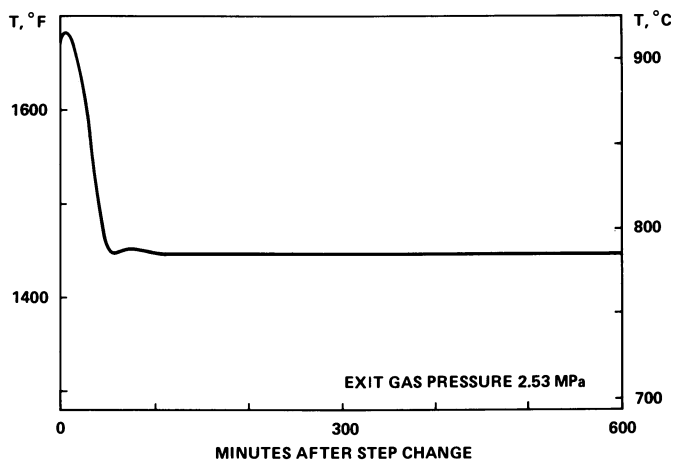
Figure 9.   Solids temperature at 0.3 m, exit gas pressure reduced to 2.53 MPa
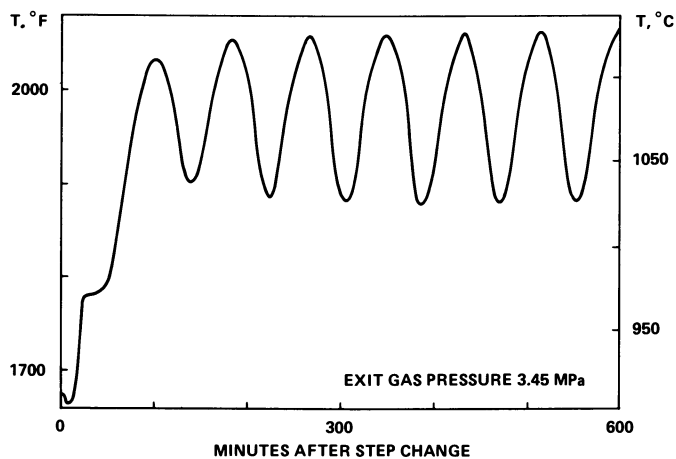
Figure 10.   Solids temperature at 0.3 m, exit gas pressure increased to 3.45 MPa

Table XI.   Exit Pressure Change, Final Steady State Results

Exit Gas Pressure	MPa	2.53	3.14
	atm	25.0	31.0
Exit Gas Temperature	°C	268.2	278.2
	°F	514.7	532.7
Exit Solids Temperature	°C	384.1	370.1
	°F	723.3	698.2
Solids T at 0.3 m (1 ft)	°C	785.2	992.8
	°F	1445.4	1819.0
Dry Exit Gas	mol %		
Hydrogen		41.23	40.44
Carbon Dioxide		31.00	32.30
Carbon Monoxide		15.00	13.58
Methane		10.50	11.37
Nitrogen, Ammonia,		2.27	2.31
Hydrogen Sulfide, Tar			

Table XII.   Exit Pressure 3.24 MPa, Limit Cycle Results

		Max	Min
Exit Gas Temperature	°C	280.7	275.6
	°F	537.2	528.1
Exit Solids Temperature	°C	370.3	368.9
	°F	698.6	696.0
Solids T at 0.3 m (1 ft)	°C	1067.7	978.9
	°F	1953.9	1794.0
Dry Exit Gas	mol %		
Hydrogen		40.10	40.35
Carbon Dioxide		32.16	32.80
Carbon Monoxide		13.90	12.95
Methane		11.52	11.59
Nitrogen, Ammonia,		2.32	2.31
Hydrogen Sulfide, Tar			

Estimated Limit Cycle Period 82.7 minutes

Table XIII.   Exit Pressure 3.45 MPa, Limit Cycle Results

		Max	Min
Exit Gas Temperature	°C	283.6	276.4
	°F	542.4	529.6
Exit Solids Temperature	°C	369.2	367.3
	°F	696.5	693.1
Solids T at 0.3 m (1 ft)	°C	1126.8	1026.6
	°F	2060.3	1879.9
Dry Exit Gas	mol %		
Hydrogen		39.66	39.98
Carbon Dioxide		32.51	33.46
Carbon Monoxide		13.61	12.21
Methane		11.88	12.03
Nitrogen, Ammonia,		2.34	2.32
Hydrogen Sulfide, Tar			

Estimated Limit Cycle Period 82.6 minutes

Table XIV.   Exit Pressure, Multiple Steady State Results

		2.84*	2.84	2.84
Exit Gas Pressure	MPa	2.84*	2.84	2.84
	atm	28.0	28.0	28.0
Exit Gas Temperature	°C	275.6	275.7	270.9
	°F	528.1	528.2	519.7
Exit Solids Temperature	°C	372.0	370.4	379.0
	°F	701.6	698.8	714.2
Solids T at 0.3 m (1 ft)	°C	918.3	1002.6	782.7
	°F	1684.9	1836.6	1440.8
Dry Exit Gas	mol %			
Hydrogen		40.83	40.83	41.03
Carbon Dioxide		31.47	31.47	31.86
Carbon Monoxide		14.53	14.53	13.93
Methane		10.88	10.88	10.90
Nitrogen, Ammonia,		2.29	2.29	2.28
Hydrogen Sulfide, Tar				

*unstable steady state results

initial conditions different from the base case values were used for some of the transient calculations. For example, if the final steady state conditions produced by increasing the exit gas pressure from 2.84 MPa (28 atm) to 3.14 MPa (31 atm) are used as the initial conditions, and the exit gas pressure is stepped back to its original value of 2.84 MPa (28 atm), we obtain a steady state convergent response which returns to the original initial condition. Likewise, if we step the exit gas pressure up to 3.45 MPa (34 atm), we obtain the same limit cycle response that we obtained in stepping from 2.84 MPa (28 atm) to 3.45 MPa (34 atm).

Next we used the 3.45 MPa (34 atm) limit cycle results at the 810 minute point for our initial conditions. If we step the exit gas pressure down to 3.14 MPa (31 atm), we obtain the same underdamped steady state result that we obtained by stepping from 2.84 MPa (28 atm) to 3.14 MPa (31 atm). However, if we step the exit gas pressure down to 2.84 MPa (28 atm), we do not return to the original initial condition state. Instead, we obtain the multiple steady state result given in the third data column of Table XIV. The exit gas temperature, the solids temperature at the 0.3 m (1 ft) level, and the raw gas carbon monoxide content are lower than the original values. The exit solids temperature, and the hydrogen and carbon dioxide content of the raw gas are higher. This condition is caused by the burning zone not being able to move back up the reactor after its initial downward shift.

We next tried stepping the exit gas pressure down to 3.14 MPa (31 atm), and then after 270 minutes, stepping on down to 2.84 MPa (28 atm). These results are given in the first two data columns of Table XIV. After about 370 minutes, the reactor reached the spurious steady state conditions given in column one, which are very close to the original initial condition values. However, the reactor only remained there for about 20 minutes, and then spent the next 330 minutes moving to the multiple steady state result given in column two. The spurious steady state results represented an unstable multiple steady state condition. The column two results show that even though the solids temperature profile down the reactor is slightly different from the original profile, the exit gas composition remains the same (to two decimal places).

Finally, the exit gas pressure was stepped down from 3.45 MPa (34 atm) to 3.24 MPa (32 atm), 3.04 MPa (30 atm), and 2.84 MPa (28 atm) in 270 minute increments. This procedure gave a steady state convergent response which corresponded to the original initial condition.

Bifurcation. Bifurcation refers to the switching or branching from one type of response behavior to another as a parameter passes through a critical value. For us, when the parameter is below the critical value, our step change responses are in the steady state convergent region. When they are above the critical value, our responses are in the limit cycle region. As the parameter values approach the critical point, we enter a transi-

tion region. Just below the critical point, even though we still have steady state convergent responses, the steady state is only reached after a long period of decaying oscillation. The closer we approach the critical point, the longer the decaying oscillation time becomes. Just above the critical point, we have long periods of either decaying or expanding oscillations which finally result in stable limit cycle responses. Thus, the approach to the critical point from either above or below is asymptotic.

Table XV provides a summary of the coal moisture, steam feed rate and exit gas pressure transient response runs showing the time required to reach the given condition. It provides a rough estimate for the values of the bifurcation points for these runs. Thus, the bifurcation point for the coal moisture step change runs lies between 30.08 and 31.05 wt % moisture. For the steam feed rate changes, it lies between -2.25% and -2.50%, and for the exit gas pressure, it is bracketed by the 3.14 MPa (31 atm) and 3.24 MPa (32 atm) values.

Summary

The continuity equations for mass and energy were used to derive an adiabatic dynamic plug flow simulation model for a moving bed coal gasifier. The resulting set of hyperbolic partial differential equations represented a split boundary-value problem. The inherent numerical stiffness of the coupled gas-solids equations was handled by removing the time derivative from the gas stream equations. This converted the dynamic model to a set of partial differential equations for the solids stream coupled to a set of ordinary differential equations for the gas stream.

The method of characteristics, the distance method of lines (continuous-time discrete-space), and the time method of lines (continuous-space discrete-time) were used to solve the solids stream partial differential equations. Numerical stiffness was not considered a problem for the method of characteristics and time method of lines calculations. For the distance method of lines, a possible numerical stiffness problem was solved by using a simple sifting procedure. A variable-step fifth-order Runge-Kutta-Fehlberg method was used to integrate the differential equations for both the solids and the gas streams.

Step change dynamic response runs revealed that the distance and time method of lines techniques were not as accurate as the method of characteristics procedure for calculating gasifier transients. Therefore, these two techniques were discarded and the remaining calculations were all done using the method of characteristics.

The nonlinear dynamic gasifier model produced a wide variety of transient response types when subjected to step changes in operating conditions. However, stepping the inlet gas (blast) temperature up and down by as much as 55.6 °C (100 °F) only gave steady state convergent responses. Varying the feed coal moisture

Table XV. Summary of Bifurcation Response Time Data

		Minutes	Type
Coal Moisture wt %	33.80	375	Steady State
	32.91	480	Steady State
	31.05	2430	Decay Steady State
	30.08	324	Limit Cycle
	27.00	315	Limit Cycle
Steam Feed % Change	−1.25	270	Steady State
	−1.875	375	Steady State
	−2.25	810	Decay Steady State
	−2.50	1335	Decay Limit Cycle
	−3.75	345	Limit Cycle
	−5.00	300	Limit Cycle
	+5.00	210	Limit Cycle
Pressure MPa(atm)	2.53(25)	270	Steady State
	3.14(31)	1890	Decay Steady State
	3.24(32)	846	Expand Limit Cycle
	3.45(34)	351	Limit Cycle

content in the range of 34.67 to 27.00 wt % gave steady state convergent, underdamped (decaying oscillation), and limit cycle (sustained oscillation) responses. Increasing and decreasing the inlet steam flow rate by up to 5 % produced steady state convergent, underdamped steady state, limit cycle, and decaying oscillation phase limit cycle responses. Perturbing the exit gas pressure in the range of 2.53 MPa (25 atm) to 3.45 MPa (34 atm) gave non-minimum phase steady state convergent, underdamped steady state, limit cycle, and expanding ocillation phase limit cycle responses. Thus, in these calculations the limit cycle surface was approached from both the inside and the outside directions.

Changing the exit gas pressure also gave three multiple steady state responses in which the same set of operating parameters produced different reactor profiles. Finally, a rough estimate for the location of the bifurcation points was given for the coal moisture, steam feed rate, and exit gas pressure transient response runs.

Nomenclature

aij	stoichiometric coefficient component j in reaction i
AGS	local gas-solids heat transfer area/volume ratio
cpG	gas molar heat capacity
cpS	solids molar heat capacity
C	concentration variable
CG	total gas concentration
CS	total solids concentration
CjG	component j concentration in gas
CjS	component j concentration in solids
F	molar flux variable
FjG	gas molar flux for component j
FjS	solids molar flux for component j
hGS	local gas-solids heat transfer coefficient
ΔHi	heat of reaction i
i	gasifier reaction index number
j	gas/solids component index number
k	distance node index number
L	top of reactor node index number
P	absolute pressure
ri	rate of reaction i
t	real time
t	time node index number
Δt	time grid spacing
TG	gas absolute temperature
TS	solids absolute temperature
uG	local gas velocity
uS	local solids velocity
z	distance from reactor bottom
Δz	local distance grid spacing

Greek Letters

ϕG   gas energy density
ϕS   solids energy density
ψG   gas energy flux
ψS   solids energy flux

Literature Cited

1. Yoon, H.; Wei, J.; Denn, M. "Modeling and Analysis of Moving Bed Coal Gasifiers"; EPRI Report No. AF-590, Vol 2, 1978.
2. _____. "Transient Behavior of Moving Bed Coal Gasification Reactors"; 71st Annual AIChE Meeting, Miami, 1978.
3. _____. AIChE J. 1979, 25, (3), 429.
4. Hsieh, B. C. B.; Ahner, D. J.; Quentin, G. H. in Vogt, W. G.; Mickle, M. H., Eds.; "Modeling and Simulation, Vol 10, Pt 3, Energy and Environment"; ISA: Pittsburgh, 1979; p 825.
5. Daniel, K. J. "Transient Model of a Moving-Bed Coal Gasifier"; 88th National AIChE Meeting, Philadelphia, 1980.
6. Wei, J. "The Dynamics and Control of Coal Gasification Reactors"; Proceedings JACC, Vol II; ISA: Pittsburgh, 1978; p 39.
7. Stillman, R. IBM J. Res. Develop. 1979, 23, (3), 240.
8. _____. "Simulation of a Moving Bed Gasifier for a Western Coal Part 2: Numerical Data"; IBM Palo Alto Scientific Center Report No. G320-3382, 1979.
9. Shampine, L. F.; Gear, C. W. SIAM Review 1979, 21, (1), 1.
10. Carver, M. B. J. Comp. Physics 1980, 35, (1), 57.
11. Carver, M. B.; Hinds, H. W. Simulation 1978, 31, (2), 59.
12. Vichnevetsky, R. Simulation 1971, 16, (4), 168.
13. Buis, J. P. Simulation 1975, 25, (1), 1.
14. McAvoy, T. J. Simulation 1972, 18, (3), 91.
15. Abbott, M. B. "An Introduction to the Method of Characteristics"; American Elsevier: New York, 1966.
16. Orailoglu, A. "A Multirate Ordinary Differential Equation Integrator"; University of Illinois Department of Computer Science Report No. UIUCDCS-R-79-959, 1979.
17. Gear, C. W. "Automatic Multirate Methods for Ordinary Differential Equations"; University of Illinois Department of Computer Science Report No. UIUCDCS-R-80-1000, 1980.
18. Emanuel, G.; Vale, H. J. in Bahn, G. S., Ed.; "The Performance of High Temperature Systems, Vol 2"; Gordon and Breach: New York, 1969; p 497.
19. Bailey, J. E. in Lapidus, L.; Amundson, N. R., Eds.; "Chemical Reactor Theory: A Review"; Prentice-Hall: Englewood Cliffs, 1977; p 758.
20. Friedly, J. "Dynamic Behavior of Processes"; Prentice-Hall: Englewood Cliffs, 1972; p 516.

Fixed Bed Reactors with Deactivating Catalysts

JAMES M. POMMERSHEIM and RAVINDRA S. DIXIT

Bucknell University, Lewisburg, PA 17837

Models are formulated and solved for the deacti-
vation of catalysts by feed stream poisons. Catalyst
deactivation effects are scaled from single pores, to
pellets to catalyst beds. Design equations were pre-
sented for fixed bed reactors with catalyst pellets
which deactivate by both pore-mouth (shell-progressive)
and uniform (homogeneous) poisoning mechanisms. Con-
version and production levels are predicted as a function
of time and reactant Thiele modulus (h). Levels
increased with increases in pellet deactivation times
(or time constants). Levels were found to increase with
Thiele moduli h for pore-mouth poisoning and decrease
for uniform poisoning. An upper limit on bed production
exists for pore-mouth and uniform irreversible poisoning,
but not for uniform reversible poisoning, where at long
times the production rate becomes constant. For uniform
poisoning the interior of the catalyst acts as an
internal guard-bed removing poison which could otherwise
inhibit reaction near the pellet surface. This effect
is most pronounced at higher h. Spherical and flat
plate pellets gave substantially equivalent results.

In order to be able to predict the chemical production from a
catalytic reactor, the kinetics of reaction must first be known.
By applying the conservation equations to a single pore, the
reaction rate for a catalyst pellet can be found. With a know-
ledge of this rate, the reactor design equations for a fixed bed
of such pellets can be solved to predict conversion levels and
chemical production. For solid catalytic reactors undergoing
catalyst deactivation, the bed design equations must also incor-
porate the kinetics of deactivation and its effect on pore, pellet
and bed transport rates. The overall models are often complex and
unwieldy, although simplifying assumptions can be made for partic-
ular cases based on the degree of uncoupling which exists between

the deactivation and reaction processes. This type of approach can lead to insights about the overall deactivation process which may lie hidden in a more complicated analysis.

In pioneering work, Wheeler (1) showed the effect that two limiting but important modes of catalyst deactivation, pore-mouth and uniform (or homogeneous) poisoning, can have on the overall activity of a catalyst pore. In pore-mouth poisoning the catalyst has a strong chemical affinity for the poison precursor and poison will be strongly adsorbed on the catalyst surface. The outer part of the catalyst is poisoned first and a moving band of totally poisoned catalyst slowly moves into the unpoisoned catalyst interior. Catalyst fouling as a result of coke deposition can also result in a moving band or shell of deactivated catalyst. Pore mouth deactivation by poisoning or fouling is more likely when precursor molecules are large and the pores are narrow and long. These factors make the Thiele modulus for poison deposition, h_s, large. In such instances the poison precursor molecules will reside in the vicinity of the pore mouth longer and be more likely to lie down there.

On the other hand, uniform or homogeneous catalyst poisoning presumes that the poison precursor species has full access to the catalyst interior before deactivation begins. There is no diffusional resistance for this species. This will be more likely to occur when the pores are large, the catalyst pellets small, and the intrinsic deactivation rate is low. In addition smaller poison precursor molecules will be able to diffuse more rapidly into the catalyst interior. Here the Thiele modulus for poison laydown h_s will be small, and in the limit, zero.

Masamune and Smith (2) examined the problem of finding conversions in a fixed bed reactor containing a deactivating catalyst. Having obtained in detail the shape of the poisoning front in a single catalyst pellet, they indicated how these results can be used with the reactor design equations to numerically predict overall conversions. Olson (3) studied the time dependence of activity in a fixed-bed reactor. Wheeler and Robell (4) combined and condensed much of the previous theory. Their results predicted the decline in activity of a fixed bed reactor. They were successful in obtaining an analytical solution which had some degree of generality. Haynes (5) extended the work of Wheeler and Robell to include a factor to account for strong intraparticle diffusion resistance to the poison precursor. The general equations were simplified by making the assumption of shell-progressive poisoning, and dimensionless plots were obtained which showed the effect of the Thiele modulus, a dimensionless time, and the number of reaction transfer units on the activity and conversion in a fixed bed reactor. In a comprehensive review on catalyst deactivation, Butt (6) has summarized a number of experimental and theoretical studies dealing with deactivation in fixed bed reactors.

Pommersheim and Dixit (7) have developed models for poisoning occurring in the pores of flat plate and spherical catalyst pellets.

They considered deactivation to occur by either pore-mouth (shell-progressive) or uniform (homogeneous) poisoning and examined the effect these types of deactivation had on overall activity and production rates for a single catalyst pellet. Analytical solutions were obtained for the production per pore by considering the time dependence of activity. Their results will be used here as the basis for the development of models for deactivation in fixed bed reactors.

In the present work, solutions are presented for fixed-bed reactors subject to the following kinds of pellet poisoning:

   (i)   pore mouth poisoning for flat plate type pellets
  (ii)   homogeneous (uniform) reversible poisoning for flat plate pellets
 (iii)   homogeneous (uniform) reversible poisoning for spherical pellets

The following assumptions are made:

1) the bed is isothermal throughout
2) concentration gradients and activity variations in the radial direction are negligible
3) no change in moles upon reaction
4) concentrations of poison species are much less than concentrations of reactant species
5) the reaction is first order and irreversible
6) reactor pressure drop does not effect reaction kinetics or flow
7) no mass transfer film external to the pellets
8) plug flow
9) the change in activity with bed length is much slower than the changes in concentration with bed length.

The last assumption is referred to as the quasi-steady-state assumption. The fraction of the bed which is poisoned is a function of time only and not of bed length, reactor space time, or the concentration of the reactant A external to the pellets. At any given time the bed activity will be constant, and only one concentration of the poison precursor species S will exist in the bed. Such a situation will be more likely to occur when deactivation rates are low compared to reaction rates. Under this condition S will spread evenly throughout the bed. Within particles, however, concentration gradients of S may still exist depending on the poisoning mechanism and the pore and pellet properties.

Bed Concentration Profiles

Feed gas or liquid enters the bottom of the packed bed with concentration $(C_{Ao})_o$. Contained within the feed is a small amount of poison precursor S in concentration $(C_{So})_o$, such as lead in

automotive exhaust gas or sulfur or metals (e.g., nickel and
vanadium) contained in a petroleum feed-stock.

Consider a differential section of a fixed bed reactor which
is packed with uniform sized catalyst particles. The plug flow
design equation for this section is (8)

$$\frac{dW}{F_{Ao}} = \frac{dX_A}{-r'_A} \tag{1}$$

where F_{Ao} is the molar flow rate of A at the bed inlet, X_A is the
(global) conversion of A, W is the weight of catalyst, and $-r'_A$ is
the moles of A reacted per second per gram of catalyst.

Pore Mouth Poisoning: Flat Plate Pellets. For flat plate
type pellets undergoing pore mouth poisoning, the moles of A
reacting per pore is given by (7)

$$-r_A = \frac{\pi r^2 \overline{C}_{Ao} D_A h \tanh h(1 - \alpha)}{L(1 + \alpha h \tanh h(1 - \alpha))} \tag{2}$$

where $\overline{C}_{Ao}$ is the intraparticle concentration of A, r is the
average pore radius, L is the pellet half width, D_A is the effec-
tive diffusivity of reactant in the pellet and h is the Thiele
modulus for the reactant A and is given by $L\sqrt{k/D_A}$. k is the
reaction velocity constant, based on pore volume, for the first
order reaction A → R. $\overline{C}_{Ao}$ varies along the bed length, but the
other model parameters will be constant.

The rate of reaction of A per unit weight of catalyst can be
related to the rate of reaction of A per pore. Thus

$$- r'_A \frac{\text{moles of A}}{\text{sec. g cat.}} = - r_A \frac{\text{moles A}}{\text{sec. pore}} \frac{\varepsilon_p}{\rho_p V_p} \tag{3}$$

where ε_p and ρ_p are the pellet porosity and density, respectively,
and V_p is the volume of one pore. The design equation then
becomes

$$-\frac{d\overline{C}_{Ao}}{dz} = \frac{V(1 - \varepsilon)\varepsilon_p \overline{C}_{Ao} D_A h \tanh h(1 - \alpha)}{HL^2 v_o(1 + \alpha h \tanh h(1 - \alpha))} \tag{4}$$

where v_o is the volumetric flow rate, H and V are the height and
volume of the reactor, respectively, and ε is the porosity of the
fixed bed. Because of assumptions number 1), 3) and 6), v_o
remains constant. Introducing dimensionless variables for con-
centration and distance:

$$\emptyset = \frac{\overline{C}_{Ao}}{(C_{Ao})_o} \qquad \text{and} \qquad \lambda = \frac{z}{H}$$

equation (4) becomes

$$\frac{d\emptyset}{d\lambda} = \frac{- V (1 - \varepsilon) \varepsilon_p D_A}{v_o L^2} \frac{h \tanh h(1 - \alpha)}{1 + \alpha h \tanh h(1 - \alpha)} \emptyset \qquad (5)$$

The boundary condition is

$$\emptyset = 1 \qquad at \qquad \lambda = 0$$

Because of assumption 9), α will be independent of λ, and equation (5) can be directly integrated to give

$$\emptyset = \exp \frac{-N_1 \lambda h \tanh h(1 - \alpha)}{1 + \alpha h \tanh h(1 - \alpha)} \qquad (6)$$

where N_1 is a dimensionless number defined as

$$N_1 = \frac{V (1 - \varepsilon) \varepsilon_p D_A}{v_o L^2} \qquad (7)$$

V/v_o is the (superficial) reactor space time. N_1 represents the ratio of reactor space time to pellet diffusion time.

The variation of α with time follows a parabolic curve (7)

$$\alpha^2 = \frac{t}{\tau_1} = \Theta \qquad (8)$$

where τ_1, the time for complete deactivation of the pellet, is equal to $\tau_1 = \omega L^2/rD_s(C_{So})_o$. ω is the intrinsic poison laydown per unit of pore surface (moles/cm^2), and D_s is the diffusivity of S. Because of the parabolic nature of equation (8), over thirty percent of the catalyst activity is already gone when $\Theta = 0.1$.

Figure 1 shows a plot of dimensionless concentration of reactant $\emptyset$ versus dimensionless time Θ, with $N_1\lambda$ fixed at unity. The Thiele modulus h is shown as a parameter. When both N_1 and λ are unity, the trace on the figure at any given modulus represents the way the output concentration from the fixed bed reactor varies with time. As time proceeds it increases towards the incoming concentration in the characteristic "S" shape shown. From this figure, it can be seen that for small values of h (less than about 0.1) there is little or no reaction and the concentration of A at the bed exit remains the same as the feed concentration.

At $t = \tau_1$ ($\Theta = 1$ in figure 1) each pore (and pellet) becomes completely deactivated. Since the bed deactivates uniformly, it will also completely lose its activity at this time. This is

shown in figure 1 by the fact that the concentration of reactant coming from the bed becomes the incoming concentration $(C_{Ao})_o$ at $\Theta = 1$. The intercept of the curves (indicated by black circles at time zero) corresponds to the initial concentration of reactant in the bed, before deactivation begins. The total production from such a deactivating fixed bed corresponds graphically to the area located above each curve and below the line $\emptyset = 1$. The area out to $\Theta = 1$ would represent the total ultimate production.

In figure 1 the parameter N_1 is fixed. This implies that the diffusivity D_A is also fixed. Thus, increases in the Thiele modulus h, shown as a parameter in figure 1, are associated with increases in the reaction rate constant k. Higher reaction rates lead to greater conversions at any given time as evidenced by the lower values of the ordinate.

Increases in temperature raise the rate constant k and raise the production. This effect becomes less and less important as the temperature increases. Figure 1 shows that there is a limit curve at very high moduli (h $\to \infty$ and $\emptyset \to \exp[N_1\lambda/\sqrt{\Theta}\,]$), above which no further increase in production appears possible. However, some further increase can occur with increases in D_A (N_1 increases), although this may be offset if D_S also increases (τ_1 drops). The intrinsic rate of poison laydown ω_o may also change with temperature, but whether it rises or falls will depend on the specific system under consideration.

Uniform (homogeneous) Reversible Poisoning: Flat Plate Pellets. The rate of reaction for uniform or homogeneous reversible poisoning in flat plate pellets is given by ($\underline{1}$)

$$-r_A = \frac{2\pi r\ L\ k_s\ \overline{C}_{Ao}\ \sqrt{1-\alpha}\ \tanh h\ \sqrt{1-\alpha}}{h} \qquad (9)$$

where k_s is the surface (pore) reaction rate constant. The concentration profiles are given by

$$\emptyset = \exp \frac{-N_2\lambda\ \sqrt{1-\alpha}\ \tanh h\ \sqrt{1-\alpha}}{h} \qquad (10)$$

where N_2 is a dimensionless number defined as

$$N_2 = \frac{2\pi r L k_s \epsilon_p\ (1-\epsilon)\ V}{V_p\ v_o} = \frac{2}{r}\ k_s\ \epsilon_p\ (1-\epsilon)\ \frac{V}{v_o} = k\epsilon_p\ (1-\epsilon)\ \frac{V}{v_o} \qquad (11)$$

N_2 represents the ratio of reactor space time to reaction time. Comparison of equations (7) and (11) shows $N_2 \sim h^2 N_1$. α, the fraction of the pore (or pellet) poisoned, is given by (7)

$$\frac{\alpha}{\alpha_e} = 1 - \exp\ (-t/\tau) = 1-\exp(-\Theta') \tag{12}$$

τ is the time constant for poison laydown for homogeneous reversible poisoning and is given by: $\tau = \omega_\infty[k_d + k_a(C_{So})_o]$, where ω_∞ is the maximum value of ω when all the adsorption sites are fully occupied, k_d is the desorption rate constant and k_a the adsorption rate constant for poison laydown, Θ' is the dimensionless time t/τ, and α_e is the equilibrium fraction of active sites on the catalyst surface which are poisoned. When $\alpha_e = 1$ the poisoning is irreversible, and all catalytic sites eventually become deactivated. Unlike pore mouth poisoning τ is not a pore burn-out time but a true first order time constant for poisoning. Thus Θ' (unlike Θ) can assume values greater than unity since some catalyst activity is always present. At $\Theta' = 1$ only 63.2% of the poisonable catalytic sites on the surface have been deactivated, while at $\Theta' = 3$ it has risen to 95%.

Equations (10) and (11) were solved for different values of Θ', α_e, h and N_2. Figure 2 shows the variation of the dimensionless concentration $\emptyset$ as a function of the dimensionless time Θ' with h as a parameter. The product $N_2\lambda$ is fixed at unity, and the poisoning is irreversible ($\alpha_e = 1$). Unlike the pore mouth poisoning case, concentrations were found to increase with increasing h. Thus the conversion decreased with increases in the Thiele modulus. With N_2 fixed, the reaction rate k will be fixed. Increases in h are then associated with decreases in reactant diffusivity, D_A, or increases in pellet dimension, L. Reaction is then confined more to the periphery of the catalyst. Since poisoning is uniform, the inside of the catalyst will be able to sponge up poison which otherwise would inhibit reaction. The inside of the catalyst acts as an internal guard bed. The lower slope of the curves in figure 2 at higher values of h is attributable to this guard-bed action.

Uniform Reversible Poisoning: Spherical Pellets. The rate of reaction for uniform reversible poisoning in spherical pellets is given by (7)

$$-r_A = \frac{3\ k\ V_p\ \overline{C}_{Ao}}{h'^2}\ (-1 + h'\ \sqrt{1 - \alpha}\ \coth h'\ \sqrt{1 - \alpha}) \tag{13}$$

where

$$h' = R\ \sqrt{k/D_A} \tag{14}$$

h' is the Thiele modulus for spherical pellets of radius R.

Figure 1. Dimensionless reactant concentration Φ vs. dimensionless time Θ for pore mouth poisoning: $N_1\lambda = 1$; parameter, h
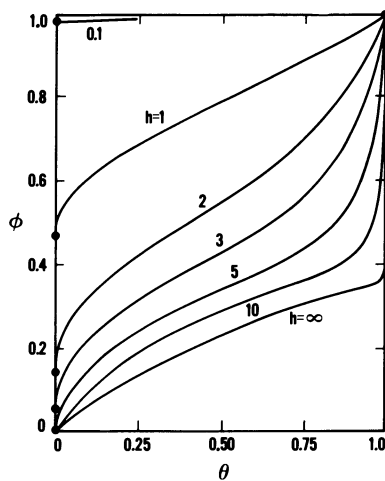
Figure 2. Dimensionless reactant concentration Φ vs. dimensionless time Θ' for uniform poisoning: $N_2\lambda = 1$; $\alpha_e = 1$; parameter, h
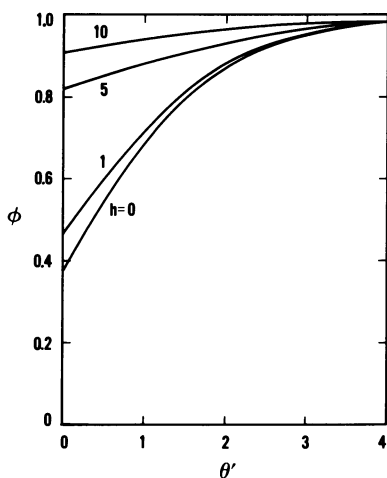
The dimensionless concentration profiles are

$$\emptyset = \exp \frac{-N_2\lambda \, (-1 + h' \sqrt{1 - \alpha} \, \coth h' \sqrt{1 - \alpha})}{3 \, h'^2} \qquad (15)$$

α, the fraction poisoned, is given by equation (12). For spherical pellets as with uniform poisoning of flat plate pellets, increasing h increases the reduced concentration resulting in lower conversions at a fixed time. As h increases, the diffusional resistance for A increases, decreasing the conversion and increasing the reduced concentration. Equation (15) can be directly compared to equation (10) if the concept of an equivalent sphere (8) is used. For flat plate pellets of width 2L, the equivalent radius is 3L. Thus, equations (10) and (15) can be made analogous to one another by replacing h' by 3h. Calculations made on this basis indicated that $\emptyset$ values were slightly less (within 3%) for the spherical case compared to the flat plate case. When h = 0 both equations (10) and (15) reduce to $\emptyset = \exp[N_2\lambda(\alpha-1)]$. For both cases a decrease in the equilibrium surface coverage of poison α_e as well as an increase in the space time to reaction time ratio N_2 results in increased conversions (lower $\emptyset$'s). Higher values of N_2 give higher initial conversions and lower values of α_e give lower deactivation rates. For these conditions the analogous curves in figure 2 would begin lower and be flatter.

Production From A Fixed Bed Reactor.

The production from a fixed bed reactor can be found by integrating the instantaneous molar flow rate of product over the time of reactor operation. The production will be equal to the total consumption of reactant when the reaction has the same number of moles of product as reactant. The total production of product R for the reaction A → R is given by

$$N_R(t) = F_{Ao} \, [t - \int_0^t \left(\frac{\overline{C}_{Ao}}{C_{Ao}}\right)_{o \, z=H} dt] = F_{Ao} \, [t - \int_0^t \emptyset \, (\lambda = 1) \, dt] \quad (16)$$

In the absence of deactivation $N_R = F_{Ao} \, [1 - \emptyset(\alpha = 0)]t$; the production varying linearly with time.

Pore Mouth Poisoning: Flat Plate Pellets.

For pore mouth poisoning of flat plate pellets, substitution of equation (6) into equation (16) yields

$$N_R(t) = 2 \, F_{Ao} \, \tau_1 \, [\frac{\theta}{2} - \int_0^{\alpha(t)} \alpha \, \exp \frac{-N_1 \, h \, \tanh h \, (1 - \alpha)}{1 + \alpha h \, \tanh h(1 - \alpha)} \, d\alpha] \qquad (17)$$

for the production coming from a fixed bed reactor. The ultimate or final total production (at $t = \tau_1$, and $\alpha = 1$) is given by

$$N_R(1) = 2 F_{Ao} \tau_1 \left[1/2 - \int_0^1 \alpha \ \exp \frac{-N_1 \ h \ \tanh h(1-\alpha)}{1 + \alpha h \ \tanh h(1-\alpha)} \ d\alpha \right] \quad (18)$$

Figure 3 shows the dimensionless production (divided by the scale factor $2F_{Ao}\tau_1$) calculated using equation (17) and expressed as a function of dimensionless time Θ with h as a parameter. The value of $N_1\lambda$ is fixed at unity. The production rises with time towards its final value at complete deactivation ($\Theta = 1$), predicted by equation (18). Low values of h give low production, while high values give high production. This is in agreement with the increased reactivity at larger moduli. At very high values of h further increase in production is not gained by higher h's. The initial slope of the curves in figure 3 represents the rate of increase of production in the absence of deactivation. The straighter curves at the higher values of h indicate that deactivation is not as important at high moduli, and that during deactivation there is not as much lost production. Raising the deactivation time τ_1, will proportionally raise the production at any time.

Figure 4 shows a plot of the fraction of the final production $N_R/N_R(1)$ vs time Θ with h as a parameter. Lower values of h result in higher values of this fraction at any fixed time, indicating that deactivation has a more pronounced effect on production at lower Thiele moduli. At high h values the curves are relatively straight and appear to approach a common asymptote at very high moduli. This is consistent with equations (17) and (18).

Uniform or Homogeneous Reversible Poisoning: Flat Plate
Pellets. Substituting equation (10) into equation (16), the total production for uniform reversible poisoning in flat plate pellets becomes

$$N_R(t) = 2F_{Ao} \tau \left[\frac{\Theta'}{2} - \int_{y*}^1 \frac{y}{y^2 - 1 + \alpha_e} \exp \frac{-N_2 \ y \ \tanh hy}{h} \ dy \right] \quad (19)$$

where the lower limit on the integral is given by

$$y* = \sqrt{1 - \alpha_e \ [1 - \exp \ (-\Theta')]} \quad (20)$$

With $\alpha_e = 1$, equations (19) and (20) reduce to the case of uniform irreversible poisoning.

For uniform poisoning in flat plate pellets, figure 5 presents a plot of the production ratio $N_R/N_R(1)$ as a function of the dimensionless time Θ' with h as a parameter. The dimensionless group N_2 was set at unity, while the poisoning was irreversible
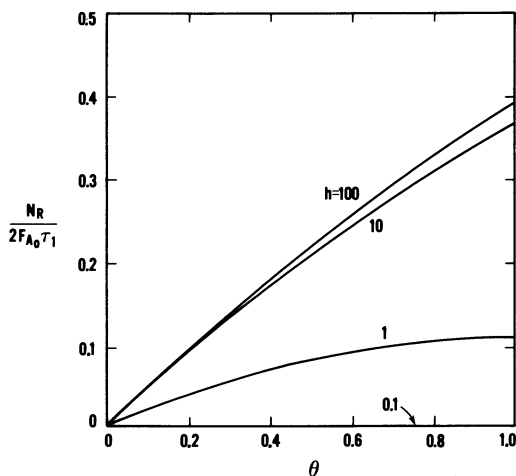
Figure 3. Dimensionless production $N_R/2F_{A_0}\tau_1$ vs. dimensionless time Θ for pore mouth poisoning: $N_1\lambda = 1$; parameter: h
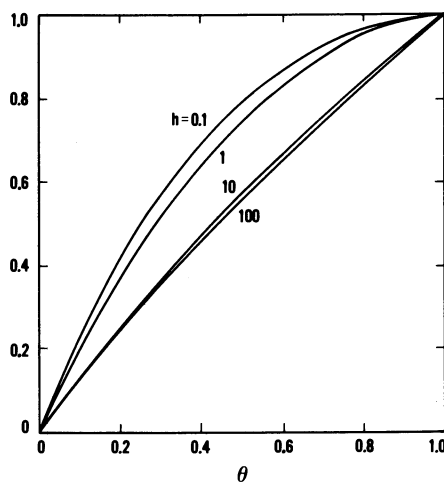
Figure 4. Fraction of final production $N_R/N_R(1)$ vs. dimensionless time Θ for pore mouth poisoning: $N_1\lambda = 1$; parameter, h

(α_e = 1). $N_R(1)$ represents the production at t = τ, the first-order time constant for deactivation. At this point 63.2% of the catalyst has become deactivated. As shown in figure 5 all curves pass through the common point Θ' = 1.

Both the production and the production ratio first rise rapidly with time and then level off at long times, generally only after the catalyst is almost completely deactivated. Thus the production is finite even though, unlike the pore mouth case, the deactivation, does not have a finite extinction time. For times less than τ, all curves are more or less common, regardless of the value of h. For times greater than τ, the production ratio levels off most rapidly for small moduli. At suitably small h, the production ratio becomes independent of h. This result can also be obtained theoretically by examining equation (17). As the value of the Thiele modulus is raised, the actual production N_R falls, as is indicated by equation (17) or by examining the relative areas above the curves in figure 2. Higher values of h are associated with severe diffusional limitations. The higher slope of the curve in figure 5 at the higher values of h is attributable to the guard bed action of the pellet interior. Because the interior of the catalyst sponges up poison, it is relatively more effective at higher moduli in raising the production ratio.

Equation (19) predicts that increases in α_e, the final fraction of the surface poisoned (as $\Theta' \rightarrow \infty$), will decrease the production of R. This effect is shown in figure 6 which presents a plot of the production ratio as a function of Θ' with the equilibrium fraction poisoned (α_e) shown as a parameter. $N_2\lambda$ and h were both set at unity. All curves cross at Θ' = 1. Comparing the curves for α_e = 0.1, 0.5 and 1.0, irreversible poisoning, α_e = 1.0, gives higher production ratios for times less than τ, but significantly lower ratios at greater times. At a low degree of poisoning, as indicated by α_e = 0.1, the production ratio curve is substantially linear. A catalyst which would not deactivate would have α_e = 0. On figure 6 this appears as a line of unit slope. The vertical distance between this line and any of the curves in figure 6 gives a measure of the production loss due to deactivation. Unlike the case of irreversible poisoning (α_e = 1), for reversible poisoning (α_e < 1) there is no upper limit on production. Note in figure 6 that only the curve for α_e = 1 becomes horizontal at longer times. With reversible poisoning at longer times Θ', $\alpha < \alpha_e$ and the production rate becomes constant. The catalyst is effectively functioning then with a reduced but constant activity, proportional to (1 − α_e).

Uniform Reversible Poisoning: Spherical Pellets. For uniform reversible poisoning in spherical pellets an expression for the instantaneous total production is obtained by substituting equation (15) into equation (16)
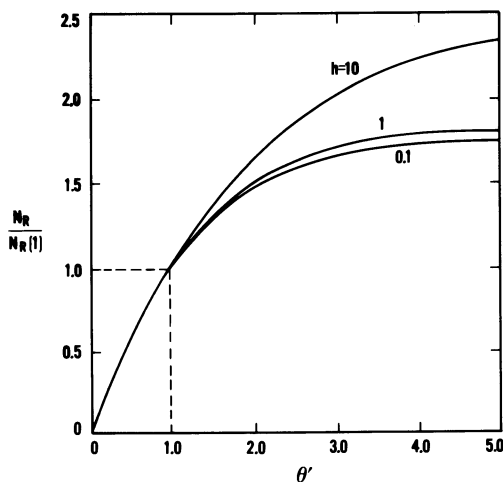
Figure 5.   Production ratio $N_R/N_R(1)$ vs. dimensionless time Θ' for uniform poisoning: $N_2\lambda = 1$; $\alpha_e = 1$; parameter, h
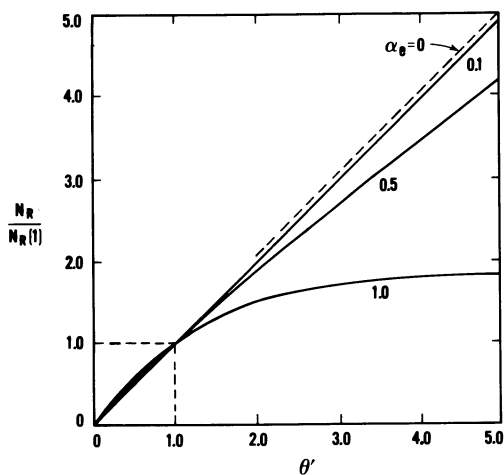
Figure 6.   Production ratio $N_R/N_R(1)$ vs. dimensionless time Θ' for uniform poisoning: $N_2\lambda = 1$; $h = 1$; parameter, α_e

$$N_R(t) = 2F_{Ao} \, \tau \, [\frac{\Theta}{2} - \int_{y*}^{1} \frac{y}{y^2-1+\alpha_e} \exp \frac{-N_2(-1 + h'y \coth h'y)}{3h'^2} \, dy] \quad (21)$$

where the lower limit on the integral is again given by equation (20).

Calculations performed with this equation gave substantially identical results with those found using equation (19) with h replaced by h'/3.

Conclusions

With either pore-mouth or uniform poisoning, fixed bed conversions and production levels are a strong function of the reactant Thiele modulus h, increasing with h for pore mouth poisoning and decreasing with h for uniform poisoning. These trends depend on the constancy of the dimensionless groups N_1 and N_2. Conversions and production levels both increased with increases in the pellet deactivation time (pore-mouth) or time constant for poison deposition (uniform).

For pore-mouth poisoning, deactivation has a more pronounced effect on production at lower moduli. At high values of h, further increases in h do not gain significant increases in production. Since pellet deactivation times decrease with increases in temperature, a best temperature may exist for maximum production.

For both pore mouth and irreversible uniform poisoning, an upper limit was found for the bed production of R, while with uniform reversible poisoning no such limit existed.

For uniform reversible poisoning, the production increased with a decrease in the equilibrium surface of the catalyst poisoned. At long times the production rate became constant.

For uniform poisoning, the interior of the catalyst acts as an internal guard-bed, removing poison which might otherwise inhibit reaction near the pellet surface. This effect is most pronounced at high values of h, where reaction is confined to the periphery of the catalyst.

Spherical and flat plate pellets give substantially equivalent conversions and production levels for uniform reversible poisoning when the Thiele moduli are put on an equivalent basis.

Legend of Symbols.

A	reactant species
$\overline{C}_{Ao}$	intrapellet concentration of A external to the pellets, moles/m^3
$(C_{Ao})_o$	concentration of A in the feed stream, moles/m^3
$(C_{so})_o$	concentration of S in feed, moles/m^3
D_A	effective diffusivity of A, m^2/s
D_s	effective diffusivity of S, m^2/s
F_{Ao}	molar flow rate of A at reactor inlet, moles/s
H	height of fixed bed, cm
h,h'	Thiele modulus for reactant A, $L\sqrt{k/D_A}$, or $R\sqrt{k/D_A}$, respectively, dimensionless
h_s	Thiele modulus for poison precursor
k	reaction rate constant, s^{-1}
k_a	adsorption rate constant, m^4/mole^2, s
k_d	desorption rate constant, m^2/mole, s
k_s	reaction rate constant of A based on surface area, m/s
L	length of catalyst pore, half width of flat plate pellets, m
N_R	production of product R, moles
$N_R(1)$	production of R at Θ (or Θ') = 1
N_1	dimensionless group for pore mouth poisoning (equation 7)
N_2	dimensionless group for uniform reversible poisoning (equation 11)
r	average or mean pore radius, m
r_A	rate of reaction of A, mole/m^3,s
r_A'	rate of reaction, moles/g catalyst,s

R   radius of spherical pellets, m; product of reaction

t   time, s

V   volume of fixed bed, m^3

V_p volume of single pore, m^3

v_o (input) volumetric flow rate, m^3/s

W   weight of catalyst, g

y*   limit in integration, $\sqrt{1 - \alpha_e(-\exp -\Theta')}$, equation (20), dimensionless

z   distance along fixed bed, m

Greek Letters.

α fraction of catalyst surface poisoned

α_e equilibrium fraction of surface poisoned

ε fixed bed porosity (interparticle)

ε_p pellet porosity (intraparticle)

Θ, Θ' dimensionless times, t/τ_1 and t/τ, respectively

λ dimensionless distance, z/H

ρ_p bulk density of catalyst pellet, g/m^3

τ time constant for poison laydown, uniform reversible poisoning, s

τ_1 pellet deactivation time, pore-mouth poisoning, s

ϕ dimensionless concentration in fixed bed, $\overline{C}_{Ao}/(C_{Ao})_o$

ω_o intrinsic poison laydown per unit of pore surface, $moles/m^2$

ω_∞ maximum value of ω_o

Literature Cited.

1. Wheeler, A., "Catalysis," P. H. Emmett, Ed., Vol. II, Reinhold, New York, 1955.
2. Masamune, S.; Smith, J. M., "Performance of Fouled Catalyst Pellets," A.I.Ch.E. Journal 1966 12, 384-394.
3. Olson, J. H., "Rate of Poisoning in Fixed Bed Reactors," Ind. Eng. Chem. Fundam. 1968 10, (2).
4. Wheeler, A.; Robell, A. J., "Performance of Fixed-Bed Catalytic Reactors with Poison in the Feed," Journal of Catalysis 1979 13, 299-305.
5. Haynes, H. W. Jr., "Poisoning in Fixed Bed Reactors," Chem. Engr. Sci. 1970 25, 1615-1619.
6. Butt, J. B., "Catalyst Deactivation," in "Chemical Reaction Engineering, Advances in Chemistry Series 109," Gould, R. F. (ed.), American Chemical Society, Washington, D.C., 1972, 259-496.
7. Pommersheim, J. M.; Dixit, R. S.; "Models for Catalyst Deactivation," 70th Annual AIChE Meeting, New York, November 1977.
8. Levenspiel, O., "Chemical Reaction Engineering," 2nd Ed., Wiley, New York, 1972.

Publication Date: September 21, 1981 | doi: 10.1021/bk-1981-0168.ix001

G

Gas
  component, molar flux of 334
  composition in experiment and
    calculation 170t
  concentration gradients 119
  dispersion coefficient 231
  dispersion and conversion with
    increasing column diameter
    and flow rate 232f
  dynamics, reactor 158
  energy balance equation 335
  holdup in bubble column 205, 209f,
                              216, 218f, 219–220
  interchange coefficients 80, 84
  –liquid
    contactors 221
    interface 206, 208
      mass transfer resistance at 234
      mass transfer coefficient 206
  -in-liquid dispersions 221, 233
  mixing in dense phase 7, 11
  mixing in emulsion phase 7, 11
  –particle system 160
  -to-particle mass transfer 4
  -phase
    degradation of maleic anhydride   56
    reactions, solid-catalyzed 14
    velocity, jet 176f
    viscosity 161
  pressure, exit 357, 361
  –solid(s)
    flow, continuum description of .. 160
    fluidized bed filter model 75–94
    fluidized bed systems
      heat transfer coefficient in ..185–200
      at low Reynolds numbers ..185–200
      mass transfer coefficient in ..185–200
    heat transfer coefficient 335
    particle mixture, thermal
      conductivity of 161
    reactions 14
      kinetics 119
      noncatalytic 118
  spargers 206
  temperature, exit 361
  transfer, interphase 11–12
  velocity 219, 234, 263, 265, 340, 357
    field 173
    and flow regime 215f
    and mass transfer coefficients 225f
    to solids velocity, ratios of 336
    superficial 203, 205, 244, 262, 269
  volume flux 161
Gasification, chemistry of 162–163
Gasification reactors, fluidized bed
  coal 157–183
Gasifier, time response of 332

Global mixing effects 229–231
Gradient(s)
  carbon concentration 100, 106, 110
    in shallow bed combustors 95
  gas concentration 119
  radical 7
  temperature 288
  thermal 4
Grid point index number 337
Grid region 14–15

H

Heat
  balance(s) 189
    equation 121, 124
  dispersion coefficients 308
  exchanger(s), specific area of 106
    bubble size and 109f, 110f
  exchanger models, packed bed ..287–304
Heat
  transfer 100
    in bubble column 231–233
    coefficient(s) 142, 282
      bed–wall 281
      in bubble columns 243–253
      gas–solids 335
        fluidized bed systems 185–200
      wall-to-suspension 234
    data 236f
    due to natural convection 62
    in fluidized beds, particle-to-gas   4
    across liquid–solid interface 244
    model 231
    in separation space 62
    in slurry reactors 234
Hermite functions, orthogonal colloca-
  tion using cubic 287–304
Heterogeneous packed bed models 281–282
Holdup in bubble columns 255
Holdup, liquid 270f
Homogeneous flow 214
  in bubble column 205–207
Homogeneous poisoning
  catalyst 368–369
  production ratio vs. time 379f
  reactant concentration vs. time 374f
  reversible 372–380
Hot flow hydrodynamics 171
Hydrodynamic(s)
  bed 3–4, 63
  hot flow 171
  mixing 177
  parameters for bubble columns ..213–241

I

IGT (Institute of Gas Technology)
  bench reactor, simulation of ..168–171